THE STRUCTURE AND KINEMATICS OF THE MAGELLANIC STELLAR PERIPHERY

Lara Rose Cullinane

A thesis submitted for the degree of
Doctor of Philosophy
of The Australian National University

Australian
National
University

September 2021

Declaration

I declare that the research presented in this thesis represents original work that I carried out during my candidature at the Australian National University, except for contributions to multiauthor papers incorporated in the thesis where my contributions are specified in the below Statement of Contribution.

- **L. R. Cullinane**, A. D. Mackey, G. S. Da Costa, S. E. Koposov, V. Belokurov, D. Erkal, A. Koch, A. Kunder and D. M. Nataf. 2020. *The Magellanic Edges Survey I: Description and first results.* MNRAS, 497, 3055.

- **L. R. Cullinane**, A. D. Mackey, G. S. Da Costa, D. Erkal, S. E. Koposov, and V. Belokurov. 2021. *The Magellanic Edges Survey II. Formation of the LMC's northern arm.* MNRAS, Submitted.

- **L. R. Cullinane**, A. D. Mackey, G. S. Da Costa, D. Erkal, S. E. Koposov, and V. Belokurov. 2021. *The Magellanic Edges Survey III. Kinematics of the disturbed LMC outskirts.* In preparation.

For each of these papers, I was the primary contributor – i.e. I performed all analysis and wrote all text – with the following exceptions. Coauthor Erkal provided dynamical models for analysis in the second and third papers, and wrote the first four pargraphs of section 4.5.3 describing the initialisation of the models. Coauthors Mackey, Da Costa, Koch, Kunder, and Nataf performed ~40% of the observations contributing to the papers. All coauthors reviewed the papers and provided feedback.

I also made contributions to the following articles during the course of the candidature:

- T. S. Li, S. E. Koposov, D. B. Zucker, G. F. Lewis, K. Kuehn, J. D. Simpson, A. P. Ji, N. Shipp, Y.-Y. Mao, M. Geha, A. B. Pace, A. D. Mackey, S. Allam, D. L. Tucker, G. S. Da Costa, D. Erkal, J. D. Simon, J. R. Mould, S. L. Martell, Z. Wan, G. M. De Silva, K. Bechtol, E. Balbinot, V. Belokurov, J. Bland-Hawthorn, A. R. Casey, **L. R. Cullinane**, A. Drlica-Wagner, S. Sharma, A. K. Vivas, R. H. Wechsler, B. Yanny, and the S^5 Collaboration. 2019. *The southern stellar stream spectroscopic survey (S^5): Overview, target selection, data reduction, validation, and early science.* MNRAS, 490, 3508

- A. P. Ji, T. S. Li, T. T. Hansen, A. R. Casey, S. E. Koposov, A. B. Pace, A. D. Mackey, G. F Lewis, J. D. Simpson, J. Bland-Hawthorn, **L. R. Cullinane**, G. S. Da Costa, K. Hattori, S. L. Martell, K. Kuehn, D. Erkal, N. Shipp, Z. Wan, and D. B.

Zucker. 2020. *The Southern Stellar Stream Spectroscopic Survey (S^5): Chemical Abundances of Seven Stellar Streams.* AJ, 160, 181

- T. S. Li, S. E. Koposov, D. Erkal, A. P. Ji, N. Shipp, A. B. Pace, T. Hilmi, K. Kuehn, G. F Lewis, A. D. Mackey, J. D. Simpson, Z. Wan, D. B. Zucker, J. Bland-Hawthorn, **L. R. Cullinane**, G. S. Da Costa, A. Drlica-Wagner, K. Hattori, S. L. Martell, S. Sharma, and the S^5 Collaboration. 2021. *Broken into Pieces: ATLAS and Aliqa Uma as One Single Stream.* ApJ, 911, 149

- T. T. Hansen, A. P. Ji, G. S. Da Costa, T. S. Li, A. R. Casey, A. B. Pace, **L. R. Cullinane**, D. Erkal, S. E. Koposov, K. Kuehn, G. F. Lewis, A. D. Mackey, N. Shipp, D. B. Zucker, J. Bland-Hawthorn, and the S^5 Collaboration. 2021. *S^5: The destruction of a bright dwarf galaxy as revealed by the chemistry of the Indus stellar stream.* ApJ, 915, 103.

- A. P. Ji, S. E. Koposov, T. S. Li, D. Erkal, A. B. Pace, J. D. Simon, V. Belokurov, **L. R. Cullinane**, G. S. Da Costa, K. Kuehn, G. F Lewis, A. D. Mackey, N. Shipp, J. D. Simpson, D. B. Zucker, T. T. Hansen, J. Bland-Hawthorn, and the S^5 Collaboration. 2021. *Kinematics of Antlia 2 & Crater 2 from The Southern Stellar Stream Spectroscopic Survey (S^5).* ApJ, Submitted.

- N. Shipp, D. Erkal, A. Drlica-Wagner, T. S. Li, A. B. Pace, S. E. Koposov, **L. R. Cullinane**, G. S. Da Costa, A. P. Ji, K. Kuehn, G. F Lewis, A. D. Mackey, J. D. Simpson, Z. Wan, D. B. Zucker, J. Bland-Hawthorn, P. S. Ferguson, S. Lilleengen, and the S^5 Collaboration. 2021. *Measuring the Mass of the Large Magellanic Cloud with Stellar Streams Observed by S^5.* ApJ, Submitted.

- A. R. Casey, A. P. Ji, T. T. Hansen, T. S. Li, S. E. Koposov, G. S. Da Costa, J. Bland-Hawthorn, **L. R. Cullinane**, A.D. Mackey, S. L. Martell, G. F Lewis, A. B. Pace, J. D. Simpson, and D. B. Zucker. 2021. *Signature of a massive rotating metal-poor star imprinted in the Phoenix stellar stream.* ApJ, Submitted.

For each of these, I both contributed to the underpinning observations and provided feedback on the resulting manuscripts.

Lara Rose Cullinane

13 September 2021

Acknowledgments

A PhD is by no means "easy peasy lemon squeezy" – it could, in fact, be considered "difficult difficult lemon difficult". My achievements, and this thesis, are thus due in no small part to those mentioned below.

First and foremost, I would like to sincerely thank my primary supervisor Dougal Mackey. From my first project working with Dougal during my undergraduate degree – completed entirely remotely at a different university! – and then subsequently throughout my PhD, he has been an incredible supervisor and mentor. Thank you for providing invaluable guidance in both my research and fledgeling academic career; always having an open door (or more recently, zoom room); and your unending encouragement and support, which have ensured I have the best possible PhD experience. I would also like to sincerely thank Gary Da Costa. As a panel member and close collaborator, Gary has provided excellent advice in navigating my PhD and beginning my future career. It's thanks to his support (financial and otherwise!) that I've been able to take up so many exciting opportunities during my PhD. It has been an absolute privilege to work with both Dougal and Gary, and I hope to continue to do so for many years to come.

Many thanks are also due to each of my collaborators, all of whom have generously shared their wisdom to improve this work.

Enormous thanks go to my family, particularly my parents. Not only have they inspired in me the confidence to follow my dreams, they have also always encouraged and assisted me in that pursuit. Words are insufficient to express how grateful I am to have always had your unconditional love and support.

I'd also like to acknowledge the financial support provided by the Joan Duffield Research Award, the Zonta Club of Canberra Breakfast Scholarship, the Alex Rogers Travelling Scholarship, and the ANU Award for Space Plasma, Astronomy and Astrophysics; each of which has provided me generous travel support allowing me to extend my research.

Finally, this thesis has made use of data from the European Space Agency (ESA) mission Gaia (https://www.cosmos.esa.int/gaia), processed by the Gaia Data Processing and

Analysis Consortium (DPAC: https://www.cosmos.esa.int/web/gaia/dpac/consortium). Funding for the DPAC has been provided by national institutions, in particular the institutions participating in the Gaia Multilateral Agreement. It is also based on data acquired at the Anglo-Australian Observatory. I acknowledge the traditional owners of the land on which the AAT stands, the Gamilaraay people, and pay my respects to elders past and present.

Abstract

The Large and Small Magellanic Clouds (LMC/SMC) are of fundamental importance in near-field cosmology. As the closest pair of interacting dwarf galaxies, they constitute the prototype system for studying the influence of tidal interactions on galaxy evolution. However, the orbital and interaction history of the Clouds – critical to understanding these influences – remains relatively unconstrained.

This thesis aims to understand the effects of past interactions between the Magellanic Clouds by performing the first dedicated kinematic study of the Magellanic stellar outskirts. Stars in these regions are strongly susceptible to external perturbations, and the resulting structural and kinematic signatures are persistent: evidenced by a wealth of substructure observed across the Magellanic periphery. To kinematically study these structures, I have developed and led the Magellanic Edges Survey (MagES), a spectroscopic study using the 2dF+AAOmega instrument on the Anglo-Australian Telescope targeting ~8700 red clump and red giant branch stars across the periphery of the Clouds. In combination with astrometric measurements and high-precision photometry from the Gaia satellite, the survey provides 3D kinematics and abundance information critical for understanding the effects of dynamical perturbations on the Magellanic system.

As a first demonstration of the efficacy of MagES data, the kinematics of two fields in the northern LMC disk are investigated. These are found to exhibit relatively undisturbed disk-like kinematics, enabling calculation of the most distant direct mass estimate for the LMC.

Focus is then directed to a large arm-like substructure to the north of the LMC. This structure is determined to be made from disturbed LMC disk material, with its discrepant kinematics relative to the disk indicative that it was strongly perturbed during a recent interaction with the Milky Way. Comparison with dynamical models reveals the feature has not been closely influenced by close passages or disk crossings of the SMC around the LMC within the past Gyr, but earlier SMC passages may have contributed to its formation. These are the first kinematic constraints on the dynamical history of the Clouds prior to their most recent pericentric passage ~150 Myr ago.

Finally, the kinematic and structural properties of the outer LMC at galactocentric radii beyond 10° are explored. The northeastern LMC disk is remarkably undisturbed, with geometry and kinematics near-identical to those at smaller radii. In contrast, the western and southern LMC disk are highly disturbed, with deviations exceeding 25 km s^{-1} from equilibrium disk kinematics, and significantly elevated velocity dispersions. Red clump stars in these regions are also significantly brighter than expected for an undisturbed disk, indicating substantial warping. It is further demonstrated that several substructures to the south of the LMC, including two claw-like features and a long arm-like structure extending around the southeastern disk, are comprised of predominantly LMC material – as opposed to SMC debris – but display strongly disturbed kinematics. Comparisons with dynamical models reveal the western LMC disk is likely significantly affected by an SMC crossing of the LMC disk plane ~400 Myr ago. However, southern substructures appear considerably more complex than observed in any models, plausibly requiring multiple previous interactions with the SMC to fully explain their observed dynamical properties.

In summary, the MagES data presented in this thesis provide a set of unprecedented empirical constraints on the interaction history of the Clouds that will be critical for guiding future numerical models aiming to accurately describe the complex evolution of the Magellanic system.

Contents

Acknowledgments v

Abstract vii

1 Introduction 1

1.1 The Clouds as probes of galaxy interaction . . . 2

1.2 The importance of tracing Magellanic interactions . . . 7

1.3 Current constraints on the orbits of the Clouds . . . 10

1.4 The Magellanic Outskirts . . . 13

1.5 Aim of this thesis . . . 18

2 LMC Disk framework 22

2.1 The systemic properties of the LMC . . . 23

2.2 The LMC disk plane . . . 24

2.3 Observed properties of a stellar tracer . . . 32

2.4 Coordinate conversions . . . 34

3 The Magellanic Edges Survey 41

3.1 Abstract . . . 41

3.2 Introduction . . . 42

3.3 Survey Design and Target Selection . . . 45

3.3.1 Target Selection . . . 45

3.3.1.1 D Fields . . . 50

3.3.1.2 M fields . . . 51

3.3.1.3 G Fields 51
3.4 Data Acquisition 52
3.4.1 Observations and Data Reduction 52
3.4.2 LOS Velocity Determination 55
3.4.3 Gaia cross-matching 59
3.5 Isolating Magellanic Stars 60
3.5.1 Contamination model 62
3.5.2 Generating membership probabilities 65
3.5.3 Determining field aggregate properties 68
3.5.4 Metallicity determination 68
3.6 Results 70
3.6.1 LMC Disk motions 75
3.6.2 Asymmetric LOS Velocity Distributions 79
3.6.3 LMC Mass estimate 85
3.7 Summary 86
3.8 Appendix: Effect of uncertainties on maximum likelihood results 88
3.8.1 Effect of uncertainties in the contamination model 88
3.8.2 Effect of uncertainties in Magellanic kinematic peak properties . . 89

4 Formation of the LMC's northern arm 90
4.1 Abstract 90
4.2 Introduction 91
4.3 Data 93
4.3.1 An arm-like coordinate system 96
4.4 Observed Properties of the Northern Arm 101
4.4.1 Metallicity 101
4.4.2 Structure 103
4.4.3 Kinematics 111
4.5 Modelling and Analysis 116

4.5.1 General methodology 116
4.5.2 *N*-body model 117
4.5.3 Simpler model suites 122
4.5.3.1 Model Caveats 128
4.5.4 Simple model kinematics along the northern arm 131
4.5.4.1 General comments 132
4.5.4.2 Effect of the MW mass 135
4.5.4.3 Effect of the SMC 136
4.5.4.4 Effect of the LMC mass 138
4.5.5 Origin of the northern arm 138
4.6 Summary 145

5 Kinematics of the disturbed LMC outskirts **147**
5.1 Abstract 147
5.2 Introduction 148
5.3 Data 150
5.3.1 Observations 150
5.3.2 Field kinematics 150
5.3.2.1 Field 3 153
5.3.3 Metallicities 154
5.3.4 Red Clump properties 154
5.4 Anchoring the LMC red clump distance scale 156
5.5 Stellar populations in the LMC outskirts 160
5.6 Kinematics in the frame of the LMC disk 162
5.6.1 Common properties and literature comparison 163
5.6.2 The relatively undisturbed north-eastern disk 167
5.6.3 The “straight-edged” western disk 168
5.6.4 The disturbed southern disk 168
5.6.5 The claw-like southern substructures 169

5.6.6 The extended southern substructure . . . 171
5.7 Discussion . . . 172
5.7.1 Dynamical models . . . 172
5.7.2 Predicted effects of interactions in the outer LMC . . . 175
5.7.3 Comparing models to observations . . . 179
5.8 Summary and Conclusions . . . 182

6 Conclusion **186**
6.1 Thesis summary . . . 186
6.2 Future Work . . . 190
6.2.1 Observations . . . 190
6.2.2 Simulations . . . 193
6.3 Final Remarks . . . 196

References **197**

List of Figures

1.1 Luminance filter image of the Magellanic Clouds 3

1.2 HI column density across the Magellanic system 5

1.3 Likelihood of the SMC remaining bound to the LMC for >2 Gyr 12

1.4 Density map of MSTO stars across the Magellanic system, selected from DECam imaging 15

1.5 DECam Hess diagram of stars in the northern LMC disk 16

1.6 Proper motions for $G \lesssim 19.5$ stars with on-sky radii $2°<R<25°$ from the LMC COM, and $R<12°$ from the SMC COM 17

1.7 Density map of red clump and RGB stars across the Magellanic system selected from Gaia data 18

1.8 Distribution of the mean G magnitudes for all Gaia EDR3 and Gaia DR2 sources 19

1.9 Hess diagram for Magellanic stars selected from Gaia with on-sky radii $6.5°<R<8°$ from the LMC COM 20

2.1 Sign value of the sine and cosine functions in each domain quadrant . . . 23

2.2 Positions of the LMC COM as measured by several literature studies . . . 25

2.3 Cartesian coordinate system used to define the plane of the sky 27

2.4 The LMC disk plane as seen by an observer 29

2.5 Predicted distance variation across the sky for the LMC disk 29

2.6 Position of a given tracer relative to the Cartesian coordinate system describing the plane of the sky 34

2.7 Projected view of the disk plane coordinate system, centered on the LMC COM 38

3.1 Location of observed 2dF MagES fields across the Magellanic system . . . 46

3.2 Colour-magnitude selections used during the target selection process for different field types . . . 49

3.3 "Quality measure" (QM) distributions . . . 53

3.4 Typical reduced spectra . . . 56

3.5 Typical quality control plots . . . 57

3.6 Typical kinematic distributions for different field types . . . 61

3.7 LMC disk velocities and dispersions in northern disk fields . . . 74

3.8 [Fe/H] distributions for stars in northern disk fields . . . 76

3.9 Azimuthal velocities in the LMC disk . . . 77

3.10 Line-of-sight velocity distributions for LMC member stars in northern disk fields . . . 81

4.1 Location of observed MagES fields across the Magellanic periphery . . . 94

4.2 Normalised density of red clump and red giant branch stars in the region surrounding the northern arm . . . 99

4.3 [Fe/H] measurements for stars in the northern arm and nearby outer LMC disk . . . 102

4.4 Colour-magnitude selection boxes used to isolate red clump stars . . . 105

4.5 Proper motion selection boxes used to isolate likely LMC stars along the northern arm . . . 106

4.6 Photometric properties of red clump stars along the northern arm . . . 107

4.7 Observed velocities and velocity dispersions for MagES fields along the northern arm . . . 112

4.8 Modelled velocities and velocity dispersions for MagES fields along the northern arm . . . 121

4.9 Total distance and out-of-plane distance of the SMC from the LMC as a function of time . . . 125

4.10 Model out-of-plane distance for fields along the northern arm . . . 133

4.11 Model velocities and dispersions for MagES fields along the arm-like feature for the simpler model suites . . . 134

4.12 Density plots of model particles for different model suites 139

4.13 Binned map of the mean ratio of the current LMC galactocentric radius to the initial particle galactocentric radius 1 Gyr ago for a single model realisation 141

4.14 Model particle distributions for base-case model realisations having experienced one or two SMC crossings of the LMC disk plane 143

5.1 Location of observed MagES fields across the Magellanic Periphery 151

5.2 Fitted red clump photometric parameters for MagES fields as a function of position angle 156

5.3 2D density plot of Gaia EDR3 proper motions for red clump stars at LMC galactocentric radii between 7 and 12° 159

5.4 [Fe/H] estimates for MagES fields as a function of position angle 161

5.5 Absolute distances $D_{\rm field}$ and out-of-plane distances z relative to the LMC disk plane for MagES fields as a function of position angle 164

5.6 Azimuthal, radial, and vertical velocities, and their associated dispersions, for MagES fields as a function of position angle 165

5.7 Kinematic predictions for four individual model realisations with differing LMC-SMC orbital histories 176

6.1 Source density distribution of 1001MC target stars 192

6.2 Parameter distribution of recent LMC/SMC interactions as a function of the present-day relative motion of the LMC and SMC COM 195

List of Tables

1.1 Properties of dwarf galaxies likely to be satellites of the Magellanic system 10

1.2 Total mass estimates for the LMC prior to its infall to the MW 13

2.1 Literature measurements of the position of the LMC centre. 26

2.2 Selected literature measurements of the LMC geometry. 30

2.3 Useful quantities and their representations in the subsequent chapters of this thesis. 40

3.1 2dF MagES fields observed as of Jan 2020 47

3.2 Number of Gaussian profiles fit to each population in Besançon Models used to describe Milky Way contamination. 63

3.3 MagES kinematic parameters and median metallicities for two northern LMC disk fields 72

3.4 Disk velocities for northern LMC disk fields 75

4.1 MagES fields along the northern arm and the nearby LMC disk 97

4.2 Feature coordinates along and across the northern arm 101

4.3 Median RC magnitude and colour for two MagES northern disk fields . . 105

4.4 Disk velocities for northern arm feature fields 113

4.5 Disk velocities for MagES fields in the northern LMC disk 119

4.6 Simulation parameters for each simpler model ensemble. 124

4.7 Model parameters for the present-day systemic properties of the LMC and SMC 126

5.1 MagES fields in the LMC outskirts analysed in this paper 152

5.2 Fitted LMC disk model parameters 160

Chapter 1

Introduction

> The time is now to grab the reigns of the world.
>
> Kaiba Seto

As the closest pair of interacting dwarf galaxies, located at respective distances of ~50 and ~60 kpc (Pietrzyński et al. 2019; Graczyk et al. 2020), the Large and Small Magellanic Clouds (LMC/SMC) constitute the prototype system for studying in detail the influence of tidal interactions on galaxy evolution. Yet despite being amongst the most well-studied objects in the southern celestial hemisphere – with Australian research on the Magellanic system dating as far back as the early 19th century (Dunlop 1828) – their orbital and interaction history remains relatively poorly constrained. Traditionally, the Clouds were thought to be on short-period orbits around the Milky Way (e.g. Gardiner and Noguchi 1996; Mastropietro et al. 2005; Bekki and Chiba 2005 and many others), with repeated pericentric passages the source of such clear apparent interaction features as the Magellanic Stream, an enormous plume of HI gas trailing the SMC for over 150° (e.g. Mathewson et al. 1974; Putman et al. 2003; Brüns et al. 2005). However, the precise proper motion measurements by Kallivayalil et al. (2006a,b), indicating that the Magellanic system is instead on its first infall to the Milky Way potential, necessatited the revision of this narrative. Whilst it is now generally agreed interactions between the two Clouds themselves must produce their characteristic features, specifics of these interactions remain uncertain.

This thesis aims to advance understanding of interactions between the Clouds by performing a detailed examination of their extreme stellar periphery. This is an area

which has only recently become accessible for comprehensive study, as the low surface brightness of these regions, in combination with the enormous on-sky area of the greater Magellanic system (>2500 deg^2) means significant survey efforts are necessary to map and study their outskirts. New and ongoing discoveries of substructures across the Magellanic periphery highlight the strong potential of the stellar outskirts as a precise and powerful probe of the interaction history of the Clouds.

In this chapter, I first present the properties of the Magellanic system which reveal its rich interaction history, and then highlight the importance of placing precise constraints on these interactions. Next, I discuss the orbital history of the Clouds as is understood today, and associated sources of uncertainty. I then introduce the Magellanic stellar periphery as a newly-accessible domain which can be used as a probe of interactions between the Clouds, before finally outlining the aims and contents of this thesis.

1.1 The Clouds as probes of galaxy interaction

The Clouds have long been recognised as cosmologically unusual, with many of their characteristic observed features thought to be the result of galaxy interactions, be those with each other or with the Milky Way.

Of the two galaxies, the LMC has more ordered structure, with a clear stellar disk, bar, and single prominent spiral arm (de Vaucouleurs and Freeman 1972): see Fig. 1.1. However, the bar is off-centre when compared to the isophotes of the disk by ~0.5 kpc (e.g. van der Marel 2001) and tilted relative to the disk plane (e.g. Subramaniam 2003; Lah et al. 2005; Choi et al. 2018b). In addition, the bar is predominantly traced by young stellar populations ($\lesssim$ 3 Gyr), with older populations having a comparatively smooth distribution (e.g. Hardy et al. 1984; Subramaniam and Subramanian 2009; El Youssoufi et al. 2019), indicating the bar must have formed relatively recently. Despite this, the bar lacks a clear gaseous counterpart (e.g. Kim et al. 2003), and the characteristic S-shaped isovelocity contours associated with funnelling of gas into the galaxy centre are not strongly observed in the LMC (Olsen and Massey 2007, see also note in Besla et al. 2012). These key characteristics have led to the LMC being categorised as the prototype for the "Magellanic Spiral" galaxy class, an extension of the Hubble sequence to the right of SAd and SBd classifications (de Vaucouleurs and Freeman 1972).

The stellar disk of the LMC can be broadly described as following an exponential density profile with scale length ~1.5 kpc (e.g. van der Marel 2001; Weinberg and Nikolaev 2001), extending to beyond 10° on-sky from the galactic centre (e.g. van der Marel 2001; Majewski et al. 2008; Nidever et al. 2019). Surveys of the kinematics in the inner ($\lesssim$ 8 kpc)

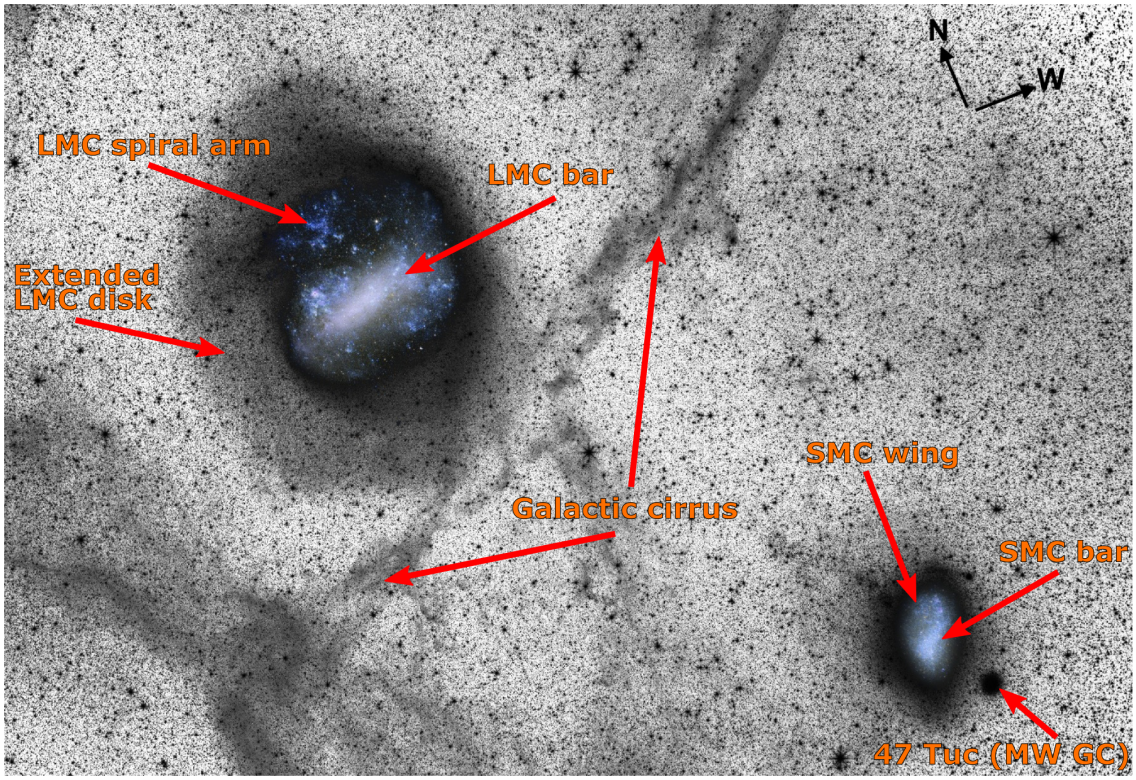

Figure 1.1: Luminance filter image of the Magellanic Clouds, with inset RGB images using Baader filters of the central regions of both Clouds, adapted from Besla et al. (2016). Features of interest in the Clouds, as well as foreground Milky Way features, are indicated.

disk reveal it displays coherent rotation, reaching a circular velocity of $\sim 80 - 90$ km s^{-1} at a radius of $\sim 2.5 - 4$ kpc (e.g. Olsen and Massey 2007; Olsen et al. 2011; van der Marel and Kallivayalil 2014). Older tracer populations such as carbon stars (e.g. Kunkel et al. 1997; van der Marel et al. 2002), red giant branch stars (e.g. Zhao et al. 2003; Cole et al. 2005; Vasiliev 2018), planetary nebulae (e.g. Feast 1968; Meatheringham et al. 1988) and star clusters (e.g. Schommer et al. 1992; Grocholski et al. 2006) are found to have larger velocity dispersions ($\sim 20 - 25$ km s^{-1}) compared to younger populations such as red supergiants (~ 8 km s^{-1}: Olsen and Massey 2007). Further, within the RGB population, more metal-poor (and, by extension, older) stars have increased dispersions by a factor of up to two relative to more metal-rich stars (Cole et al. 2005; Carrera et al. 2011).

Yet even in its relatively ordered disk, the LMC does display perturbations indicative of interactions. The disk is warped, as indicated by a change in the position angle of the line of nodes (LON) with increasing radius (Olsen and Salyk 2002; Choi et al. 2018b; Mackey et al. 2018), and flared, as indicated by an increase in the scale height of the disk with radius (Alves and Nelson 2000; van der Marel et al. 2002; Balbinot et al. 2015). The disk contains ring-like stellar overdensities (Kunkel et al. 1997; Choi et al. 2018b), as well

as a population of likely accreted SMC stars (Olsen et al. 2011).

The SMC is more disturbed than the LMC, and is classified as a "Magellanic Irregular" galaxy (with members of this class defined by their lack of rotational symmetry, but containing other structural features: e.g. de Vaucouleurs and Freeman 1972; Hunter and Gallagher 1986). Indeed, the SMC has a bar comprised of young stars (e.g. Caldwell and Coulson 1986; Zaritsky et al. 2000; Rubele et al. 2018) and gas (e.g. Martin et al. 1989; Le Coarer et al. 1993) as well as a wing-like structure (Shapley 1940) of similar composition pointing in the direction of the LMC: see Fig. 1.1. The SMC additionally has a very extended line-of-sight depth, particularly in its northeast. Here, the total depth is $\sim 20-30$ kpc: $\sim$10 kpc larger than in the southwest (e.g. Hatzidimitriou and Hawkins 1989; Crowl et al. 2001; Scowcroft et al. 2016; Ripepi et al. 2017; Tatton et al. 2021; Yanchulova Merica-Jones et al. 2021 and many others). In some regions in the northeast, the line-of-sight depth is even bimodal, potentially indicative of structures in front of the main SMC body (Nidever et al. 2013; Subramanian et al. 2017).

The kinematics of the SMC are similarly perturbed. Both young populations (Evans and Howarth 2008; Evans et al. 2015) and older RGB (e.g. Harris and Zaritsky 2006) and carbon stars (e.g. Hatzidimitriou et al. 1997), as well as star clusters (e.g. Parisi et al. 2009) have large ($\sim 25-30$ km s^{-1}) velocity dispersions, comparable to those in the outer LMC (e.g. Vasiliev 2018). Whilst most studies of stellar kinematics in the SMC do not find evidence of coherent rotation (with some exceptions, such as e.g. Dobbie et al. 2014a), there is evidence of coherent rotation of $\sim$60 km s^{-1} in the gas phase (Stanimirović et al. 2004; Di Teodoro et al. 2019). Further, the direction of the maximum velocity gradient for young stars in the bar is almost orthogonal to that for the HI bar (Evans and Howarth 2008), indicating these stars have already entirely decoupled from their parent gas – potentially due to a recent interaction. Kinematic evidence also suggests the SMC is undergoing tidal expansion due to its interactions with the LMC (Zivick et al. 2018, 2021; De Leo et al. 2020).

In addition to the two Clouds themselves, there are several extended HI features which comprise the greater Magellanic System as seen in Fig. 1.2, and are indicative of interactions between the Clouds. This includes the Magellanic Stream, trailing the Clouds and approximately tracing their orbital path for $\sim$150 degrees (e.g. Mathewson et al. 1974; Nidever et al. 2010, see also the D'Onghia and Fox 2016 review), comprised of gas stripped from both the LMC and SMC (e.g. Nidever et al. 2013; Richter et al. 2013). The Magellanic Bridge connects the two Clouds (e.g. Hindman et al. 1963; Putman et al. 2003), and the bifurcated leading arm feature (LAF) stretches for $\sim$50 degrees to the northeast of the LMC (Putman et al. 1998, 2003). A young stellar bridge, co-located

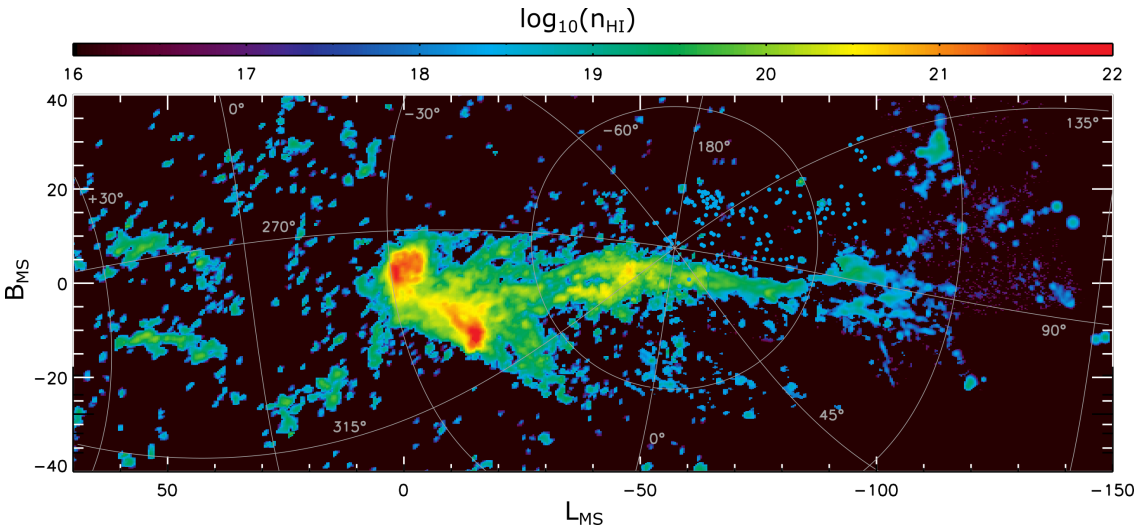

Figure 1.2: HI column density, $\log(N_{\rm HI})$, across the Magellanic system. $L_{\rm MS}$ and $B_{\rm MS}$ are Magellanic longitude and latitude respectively, as defined in Nidever et al. (2008), and define a coordinate system roughly aligned with the Magellanic Stream. In total, the leading arm feature ($L_{\rm MS}$>0), Magellanic Bridge and Magellanic Stream ($L_{\rm MS}$<0) stretch for ~200 degrees across the sky. Adapted from Nidever et al. (2010).

with the highest density regions of the gaseous bridge, also connects the Clouds (e.g. Irwin et al. 1990; Casetti-Dinescu et al. 2012; Skowron et al. 2014; Noël et al. 2015; Zivick et al. 2019; Jacyszyn-Dobrzeniecka et al. 2020b), with ongoing in-situ star-formation in the bridge region (Mackey et al. 2017; Ramachandran et al. 2021). There is also evidence for intermediate-age populations in the inter-Cloud region, with a broader and possibly more southern spatial distribution than the gaseous bridge (e.g. Noël et al. 2013, 2015; Skowron et al. 2014), suggestive of stars tidally stripped in a recent interaction. Potential stellar associations with a "counter-bridge" – a tidal counterpart to the Magellanic Bridge first predicted by Diaz and Bekki (2012) located to the north of, and at a greater distance than, the SMC – have also been identified (Dias et al. 2016, 2021; Tatton et al. 2021).

The star formation histories (SFH) of the Clouds also provide evidence of their interactions, with correlated, episodic, and spatially varying SFHs for both the LMC and SMC. Early studies of field populations in the LMC, such as those performed by Butcher (1977), Stryker (1984) and Bertelli et al. (1992) revealed that after an initial burst of star formation ~$10-12$ Gyr ago, the LMC experienced a period of relative quiescence until ~4 Gyr ago, at which point the star formation rate (SFR) across the LMC significantly increased. The more recent SFH of the LMC is characterised by multiple bursts of star formation, with spatially-resolved studies showing SFR peaks at lookback times of ~$1-2$ Gyr, ~0.5 Gyr, and ~$100-200$ Myr (e.g. Harris and Zaritsky 2009; Monteagudo et al. 2018; Ruiz-Lara et al. 2020; Mazzi et al. 2021). The peak ~$100-200$ Myr ago, which is also observed in studies of LMC Cepheids (Joshi and Joshi 2014; Joshi and Panchal

2019), is suggested to be the product of a close LMC-SMC encounter at approximately this time, with earlier bursts also potentially the result of interactions. Ongoing star formation in the LMC (i.e., within the last ~50 Myr) is predominantly confined to its bar and single spiral arm (e.g. Harris and Zaritsky 2009; Indu and Subramaniam 2011; El Youssoufi et al. 2019; Ruiz-Lara et al. 2020; Mazzi et al. 2021). The LMC also shows evidence of inside-out quenching, with recent bursts of star formation (i.e. those within the last 4 Gyr) peaking and ending at greater lookback times at larger radii (e.g. Gallart et al. 2008; Meschin et al. 2014; Ruiz-Lara et al. 2020), and some evidence of enhanced or extended SFRs in the LMC bar relative to that of the disk (e.g. Olsen 1999; Smecker-Hane et al. 2002; Rezaei kh. et al. 2014; though note Monteagudo et al. 2018 do not find significant differences in the SFHs of the bar and inner disk). This inside-out quenching is potentially the result of ram-pressure stripping (e.g. Mastropietro et al. 2005) or compression of gas in the LMC disk (e.g. Mastropietro et al. 2009) during its infall to, and interaction, with the MW's gravitational potential and associated gaseous corona.

The LMC's cluster population broadly agrees with the SFH inferred from field populations, with an abundance of clusters with ages $\gtrsim$ 12 Gyr and $\lesssim$ 3 Gyr (e.g. Mateo 1988; Da Costa 1991; Olszewski et al. 1991) consistent with the two epochs of highest SFR in the LMC, and some evidence of two "bursts" of cluster formation at lookback times of ~100 Myr and ~$1-2$ Gyr (Girardi et al. 1995). However, while the SFR of field populations in the period of relative quiescence ~$3-12$ Gyr ago is substantially non-zero (e.g. Geha et al. 1998; Holtzman et al. 1999; Mazzi et al. 2021), there are effectively zero star clusters with ages in this range. This is the LMC's cluster "age gap". The cluster ESO 121-SC03 (with an age of ~$8-9$ Gyr: Mateo et al. 1986; Mackey et al. 2006) is a sole exception, with some speculation it may have been accreted from the SMC (Bekki and Chiba 2007).

The SFH of the SMC is highly correlated with that of the LMC, suggesting the two galaxies may have been interacting for a significant period of time. The initial burst of star formation in the SMC was comparatively later (at a lookback time of ~9 Gyr: Weisz et al. 2013) and somewhat weaker than that experienced by the LMC, consistent with a younger age for the oldest SMC star clusters compared to the oldest LMC clusters (e.g. Da Costa 1991). Like the LMC, it subsequently experienced a period of relative quiescence, before a sharp global increase in the SFR ~$4-5$ Gyr ago (Noël et al. 2009; Cignoni et al. 2012; Weisz et al. 2013; Rubele et al. 2018). Intriguingly, however, formation of star clusters continued throughout this quiescent epoch, with no cluster age gap as seen in the LMC (e.g. Da Costa 1991; Rafelski and Zaritsky 2005).

The recent SFH of the SMC is, as in the LMC, characterised by repeated bursts of

star formation, with field populations experiencing episodes of increased SFR at lookback times of ~$1.5-2.5$ Gyr, ~0.5 Gyr, ~$100-250$ Myr, and ~50 Myr ago (e.g. Harris and Zaritsky 2004; Noël et al. 2007, 2009; Hagen et al. 2016; Rubele et al. 2018). The burst ~$100-250$ Myr ago, which is also evident in the age distribution of Cepheids (Joshi et al. 2016; Joshi and Panchal 2019) and star clusters (Nayak et al. 2018) is thought to be the result of the most recent close interaction between the LMC and SMC. The most recent (~50 Myr) and ongoing burst of star formation is restricted to discrete regions in the bar and wing of the SMC (e.g. Harris and Zaritsky 2004; Indu and Subramaniam 2011; Cignoni et al. 2012; Hagen et al. 2016; Strantzalis et al. 2019), with the separation between the bar and wing less apparent in slightly older (~150 Myr) populations (Rubele et al. 2018; El Youssoufi et al. 2019). In addition, the northern and eastern regions of the SMC body show enhanced star formation rates compared to the western SMC at recent times, with the 0.5 Gyr burst stronger in the northeast (Noël et al. 2007, 2009), a shift in the centroid of field populations younger than ~500 Myr in this direction (Indu and Subramaniam 2011) and a predominance of young ($\lesssim$ 100 Myr) clusters in this region (as compared to clusters in the southern SMC, which have ages predominantly between ~$0.5-1.5$ Gyr: Nayak et al. 2018).

1.2 The importance of tracing Magellanic interactions

Because of their unique status as the largest of the Milky Way's satellites, and among the nearest, the Magellanic Clouds are key laboratories for a wide variety of astrophysical processes. In particular, they are critical for understanding the importance and impact of galaxy-galaxy interactions, both in general and in the specific context of the Local Group. In this section, I discuss several key examples which motivate detailed study of the orbital and interaction histories of the Clouds.

Magellanic Spiral galaxies – of which the LMC is a prototypical example – are not uncommon (e.g. Feitzinger 1980; Odewahn 1991; Paudel and Sengupta 2017). However, the precise role of interactions with satellite companions in forming their characteristic features is debated. Odewahn (1994) find almost all Magellanic Spirals in the Third Reference Catalog of Bright Galaxies (de Vaucouleurs et al. 1991) have satellite companions, but Wilcots and Prescott (2004) find very few companion satellites for a different sample of Magellanic Spirals. In addition, Kruk et al. (2017) find no difference in the frequency of companions between Magellanic and non-Magellanic galaxy classes. As the closest Magellanic Spiral, study of the LMC offers the best opportunity to precisely constrain the interactions which can result in, and the subsequent persistence of, features which

characterise this galaxy type.

Further, interacting dwarf galaxy pairs in general are relatively common (e.g. Paudel et al. 2018). There is evidence these interactions can both enhance the star formation rates in the dwarfs (Stierwalt et al. 2015) as is observed for massive interacting galaxies (e.g. Sanders et al. 1988; Scudder et al. 2012), as well as ensuring continued star formation over longer periods of time (Pearson et al. 2016; Jahn et al. 2021; Sacchi et al. 2021). As the closest pair of interacting dwarf galaxies, and having likely interacted in isolation from massive, MW-like galaxies for many Gyr in the past, the Clouds are the ideal location to study these mechanisms in detail.

As well as providing insight into dwarf-dwarf interactions, the Clouds also offer the opportunity to study in detail the effect of dwarf galaxy accretion on more massive galaxies. Despite being on its first infall, the LMC is sufficiently massive to substantially affect the Milky Way. It is theorised to introduce both a local dark matter (DM) wake, approximately tracing its past orbit, as well as global asymmetries in (i.e. a deformation in the shape of) the Milky Way DM halo (Garavito-Camargo et al. 2019), sufficient to displace the MW centre of mass (COM) by up to ~25 kpc (Garavito-Camargo et al. 2021) on timescales of less than 0.5 Gyr (Gómez et al. 2015). Subsequent observations have confirmed these DM perturbations, manifesting as corresponding density perturbations in the stellar halo of the Milky Way (Belokurov et al. 2019; Conroy et al. 2021) as well as a global reflex motion in the outer MW stellar halo (Cunningham et al. 2020; Erkal et al. 2021; Petersen and Peñarrubia 2021) of up to 40 km s^{-1} (Petersen and Peñarrubia 2020). The LMC can also induce warps in the (stellar and gaseous) disk of the MW (Laporte et al. 2018a), and modify the strength of perturbations introduced from other satellites (such as the Sagittarius dwarf galaxy: Laporte et al. 2018b).

In addition to dynamical perturbations, the Clouds also likely affect star formation in the Milky Way. A total of $\sim 2 \times 10^9$ $M_\odot$ (combined ionized and atomic) gas is present in the extended Magellanic system, excluding that within the main bodies of the two Clouds themselves (Fox et al. 2014). This corresponds to a time-averaged gas infall rate of $4-7$ $M_\odot$ yr^{-1} (Fox et al. 2014): a value more than double the current average SFR in the MW (~2 $M_\odot$ yr^{-1}: e.g. Chomiuk and Povich 2011) assuming the gas survives interactions with the hot MW corona to reach the Galactic disk. There are suggestions this gas is already contributing to star formation, with Price-Whelan et al. (2019) finding an open cluster potentially associated with the Magellanic LAF. In addition, models suggest that when the Clouds do eventually merge with the MW, they will increase the mass of its central supermassive black hole by up to a factor of eight and the mass of the MW stellar halo by a factor of five (Cautun et al. 2019). Precisely understanding these effects are

critical for studies of the Milky Way itself (see e.g. Erkal et al. 2020), but can also be applied more generally to understand the role of dwarf satellite accretion onto massive galaxies, since mergers with MW/LMC-like mass ratios (~1:10) occur frequently across cosmic time (e.g. Stewart et al. 2008).

Finally, cosmological simulations indicate the Clouds are sufficiently massive to have their own population of smaller satellites under the hierarchical structure formation predicted by ΛCDM (e.g. D'Onghia and Lake 2008; Sales et al. 2013; Yozin and Bekki 2015; Pardy et al. 2019). The least massive of these satellites are likely to have been disrupted during the Clouds' infall to the MW potential (see e.g. Jethwa et al. 2016). However, the relatively high DM density of small satellites (Kormendy and Freeman 2016) and the limited timeframe since the accretion of the Clouds – with the Clouds crossing R_{200} of the MW ~1 Gyr ago (Besla et al. 2016)[1] – mean that more massive Magellanic satellites should remain intact and have correlated kinematics (e.g. Sales et al. 2017).

Observationally, associations between current MW satellites and a greater "Magellanic Group" were first postulated by Lynden-Bell (1976). Recent data suggests at least six current MW satellites have undergone a group infall along with the Clouds (Jethwa et al. 2016; Kallivayalil et al. 2018; Erkal and Belokurov 2020; Patel et al. 2020; Battaglia et al. 2021): a number consistent with statistics from simulations (e.g. Zhang et al. 2019; Nadler et al. 2020). Table 1.1 presents a brief overview of the most likely Magellanic satellites (i.e. those agreed upon by both Erkal and Belokurov 2020 and Patel et al. 2020), which span a wide range in luminosity. Precise constraints on the orbital history of the Clouds are required to link these satellites – and potentially others discovered in forthcoming deep photometric surveys (see e.g. Cerny et al. 2021) – to the Magellanic system.

Similarly, these constraints allow identification of satellites and stellar streams in the MW halo which have been perturbed by the infall of the Clouds. Simulations by Law and Majewski (2010) and Vera-Ciro and Helmi (2013) predicted the LMC should significantly affect the orbit of the Sagittarius stream, and the advent of precise astrometry from Gaia has allowed for observational confirmation of the influence of the LMC on this and other halo structures (e.g. Erkal et al. 2018; Koposov et al. 2019; Erkal and Belokurov 2020; Simon et al. 2020; Shipp et al. 2021; Vasiliev et al. 2021). Accounting for these effects is critical in recovering the MW's assembly history, and providing insight into the "plane of satellites" problem: group infalls such as undergone by the Clouds are one proposed mechanism through which this can be resolved (see Pawlowski 2018 for a review). In addition, measurements of the MW mass and DM halo shape derived from the orbits of these smaller satellites can be biased if the effects of perturbations by the LMC are not

[1] with R_{200} a useful proxy of a galaxy's virial radius (Reiprich et al. 2013)

Table 1.1: Properties of dwarf galaxies likely to be satellites of the Magellanic system. RA/DEC are given in J2000. M_V is the absolute V-band magnitude of the satellite.

Satellite	RA (°)	DEC (°)	M_V	Distance (kpc) from the LMC/SMC	Source
Carina II	114.107	−57.999	-4.5 ± 0.1	19/34	Torrealba et al. (2018)
Carina III	114.630	−57.900	-2.4 ± 0.2	25/42	Torrealba et al. (2018)
Hydrus I	37.389	−79.309	-4.7 ± 0.1	24/33	Koposov et al. (2018)
Phoenix II	354.993	−54.402	-2.7 ± 0.5	54/32	Jerjen et al. (2018)
Horologium I	43.868	−54.121	-3.6 ± 0.3	29/26	Jerjen et al. (2018)
Reticulum II	53.949	−54.047	-3.1 ± 0.1	23/34	Mutlu-Pakdil et al. (2018)

correctly accounted for (e.g. Erkal et al. 2020).

1.3 Current constraints on the orbits of the Clouds

Critical to the efficacy of the Magellanic system as a probe of the processes discussed above is precise knowledge of its orbital and interaction history. Accurate proper motion measurements, in combination with detailed dynamical models, have allowed for great strides forward in this area – particularly in constraining the orbit of the Clouds around the Milky Way. However, there remain significant uncertainties in the specifics of their interactions beyond this. In this section, I outline the extent of our current understanding of the history of the Magellanic system.

The current picture of the Clouds as on their first passage around the MW began with measurements of their systemic proper motions derived from Hubble Space Telescope (HST) photometry by Kallivayalil et al. (2006a,b). Compared to previous measurements of Magellanic proper motions (Kroupa and Bastian 1997; Kroupa et al. 1994; Drake et al. 2001; Pedreros et al. 2002), the Kallivayalil et al. (2006a,b) HST measurements were significantly more precise (with uncertainties <5%, compared to $>10-15\%$ in earlier studies), and also implied a substantially higher total space velocity (~378 km s^{-1}, compared to earlier estimates of ~280 km s^{-1}) – much closer to the required escape velocity for the Milky Way. Modelling by Besla et al. (2007) using these measurements revealed it is likely the Clouds are just past pericentre on their first infall to the MW potential.

A first infall scenario is consistent with several of the unusual properties of the Clouds

compared to other MW satellites. The Clouds are very gas-rich, with a total gas mass of $\sim 3.0 \times 10^9$ $M_\odot$, including $\sim 4.2 \times 10^8$ $M_\odot$ HI in the SMC (Stanimirovic et al. 1999), $\sim 5.2 \times 10^8$ $M_\odot$ HI in the LMC (Kim et al. 1998) and $\sim 2 \times 10^9$ $M_\odot$ neutral and ionised gas in the extended gas features (Fox et al. 2014). This abundance of gas also allows for ongoing star formation in the Clouds, making them bluer in colour (e.g. James and Ivory 2011; Tollerud et al. 2011) than similar-magnitude analogues around other systems. As gas from close satellites should be rapidly stripped (and thus star-formation quenched) by a massive (i.e. MW-like) host galaxy (e.g. Grcevich and Putman 2010), this implies the Clouds must have only been recently been accreted by the MW. Indeed, cosmological simulations show LMC-like satellites of MW-like hosts are generally only recently accreted (e.g. Boylan-Kolchin et al. 2011; Shao et al. 2018) – consistent with a first-infall scenario, and explaining the relatively low frequency of MW+LMC+SMC-like systems observed in large-volume surveys (with such configurations $\sim 2.7\sigma$ unusual: Robotham et al. 2012).

Presuming the Magellanic system is only recently accreted by the MW has the definite consequence that the majority of its characteristic features must be the result of interactions between the two Clouds themselves, prior to (and during) their infall to the MW potential. Although long-period ($\lesssim 3$ Gyr) orbits of the Clouds around the Milky Way are technically allowable within the PM uncertainties for light-LMC/heavy-MW combinations (e.g. Besla et al. 2007), the number of close passages of the Clouds around the MW is limited (≤ 3: Kallivayalil et al. 2013), and the associated pericentric distances are large ($\sim$400 kpc: Kallivayalil et al. 2013). At these distances, tidal influences are comparatively weaker, and ram-pressure stripping is considerably less effective (due to the associated reduction in MW halo density), than is traditionally required to produce the Magellanic stream (Besla et al. 2007). Thus, even in such a scenario, interactions between the two Clouds are necessary to form the characteristic features of the Magellanic system (Diaz and Bekki 2011, 2012).

Numerous dynamical models demonstrate interactions between the Clouds can qualitatively replicate many of their observed properties. Many models focus on reproducing the complex geometry and kinematics of the Magellanic stream (e.g. Besla et al. 2010, 2012; Guglielmo et al. 2014; Pardy et al. 2018; Wang et al. 2019; Lucchini et al. 2020; Williamson and Martel 2021) to great success. In addition, *N*-body models demonstrate that a recent close passage (or even direct collision) between the LMC and SMC can produce the tilted, offset stellar bar and single spiral arm of the LMC (e.g. Berentzen et al. 2003; Bekki 2009; Besla et al. 2012; Pardy et al. 2016) and associated bursts of star formation in both Clouds (e.g. Bekki and Chiba 2007; Yozin and Bekki 2014). Studies of the velocity field in the inner SMC reveal its current tidal disruption is likely driven by a

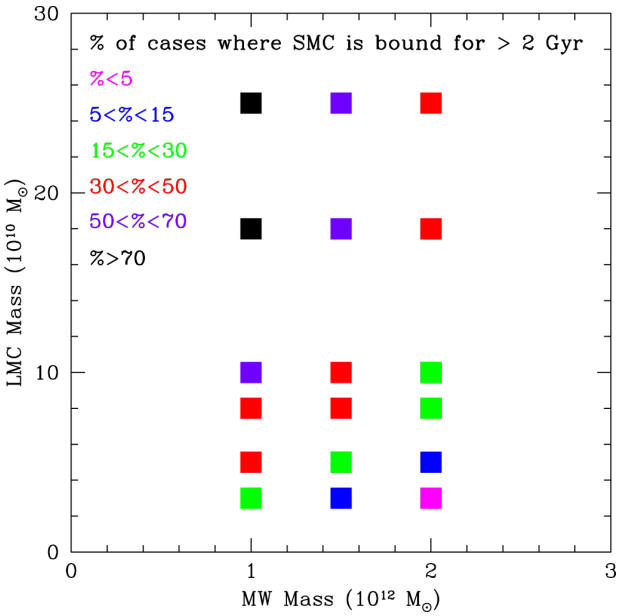

Figure 1.3: Percentage of 10000 model realisations, sampling from the current day LMC velocity uncertainty, for which the SMC has remained bound to the LMC for >2 Gyr. Higher LMC masses increase the probability of the SMC being bound for a significant period of time. Adapted from Kallivayalil et al. (2013).

close pericentric passage of the SMC around the LMC ~150 Myr ago (Zivick et al. 2018, 2021; De Leo et al. 2020), consistent with this picture. However, beyond this most recent interaction, the orbits of the two Clouds are relatively unconstrained: both long-period bound states (with repeated LMC-SMC interactions over time, as is often modelled), and the SMC being on its first infall to the LMC potential (though the presence of other likely Magellanic satellites would indicate this scenario is unlikely) are allowable within the current uncertainties (Kallivayalil et al. 2013).

One significant contributor to these uncertainties is the mass of the LMC. In addition to affecting the length of time for which the SMC has been bound to the LMC, as in Fig. 1.3, the LMC mass also influences the specifics of interactions between the Clouds which occur during this time. Traditionally, the LMC mass has been estimated based on rotation curve analysis, with van der Marel and Kallivayalil (2014) measuring an enclosed mass within 8.7 kpc of 1.7×10^{10} $M_\odot$. However, as it is clear the LMC is not tidally truncated, with evidence of LMC disk material out to much larger radii (e.g. Majewski et al. 2008; Saha et al. 2010; Besla et al. 2016), this is considered to be a strict lower limit. The total LMC mass is likely significantly higher, with different mass measurement techniques beginning to converge on a value $>10^{11}$ $M_\odot$, as in Table 1.2. However, the total LMC mass remains uncertain by a factor of ~3: sufficient to substantially change the orbit of, and thus interactions with, the SMC.

Table 1.2: Total mass estimates for the LMC prior to its infall to the MW. As the Clouds have only been recently accreted by the MW, there has been insufficient time for significant tidal stripping (e.g. Neistein et al. 2011; Sales et al. 2011), implying the total masses derived here are similar to the current LMC mass.

Value ($M_\odot$)	Source	Technique
A few times 10^{11}	Guo et al. (2010), Moster et al. (2010)	Abundance matching: applying stellar mass-halo mass (SM-HM) relations assuming an LMC stellar mass of $\sim 2.7 \times 10^9$ $M_\odot$ (van der Marel et al. 2008).
$2.5^{+0.9}_{-0.8} \times 10^{11}$	Peñarrubia et al. (2016)	Timing argument: uses the distances and velocities of galaxies in the Local Group to solve equations of motion describing their dynamics in an expanding ΛCDM Universe.
$3.4^{+1.8}_{-1.2} \times 10^{11}$	Shao et al. (2018)	Comparison to cosmological simulations, requiring the presence of an SMC-like companion.
$1.3^{+0.27}_{-0.24} \times 10^{11}$	Erkal et al. (2019)	Modelling of the track and kinematics along the length of the Orphan stream in the MW halo (see also Koposov et al. 2019).
$1.4 - 1.9 \times 10^{11}$, best estimate $1.88^{+0.35}_{-0.40} \times 10^{11}$	Shipp et al. (2021)	Modelling of perturbations to several stellar streams, with the best estimate from the combined Orphan-Chenab stream (the most strongly-perturbed of those studied).

1.4 The Magellanic Outskirts

It is clear that further investigation is necessary to better constrain the orbital and interaction history of the Magellanic system, particularly beyond the most recent LMC/SMC interaction – and the stellar outskirts of the Clouds provide the ideal location to do so. The gravitational potential well of the system is comparatively shallow in its outskirts, meaning these regions are more easily perturbed during tidal interactions. This is important in tracing interactions which occur at larger radii, that may not significantly affect the innermost regions of the Clouds – simulations by e.g. Bekki (2009) and Poggio et al. (2020) show satellite interactions which occur at small galactocentric radii much more significantly affect the host galaxy than those occurring at larger galactocentric radii. Even more critically, dynamical timescales and orbital periods in the outskirts of the Clouds are long compared to the innermost regions. This means signatures of perturbation can persist for timescales on the order of Gyr (Besla et al. 2016), allowing similarly ancient interactions to be traced today.

While dynamical models of interactions in the Magellanic system make predictions for the stellar outskirts of the Clouds, observational studies of these regions have traditionally been limited by two factors. The first of these is the low stellar density, and thus low luminosity, of the outskirts: the V-band surface brightness of these regions is as low as ~30 mag/arcsec^2 in integrated light (Mackey et al. 2016), requiring individual stellar counts to map structures. The second is the enormous (>2500 deg^2) on-sky area occupied by the Clouds. To achieve sufficient depth to count stars in the faint stellar outskirts (red clump magnitudes in these regions are at most $r \sim 18.5$, and the more populous main sequence turnoff is as faint as $r \sim 21.5$: Mackey et al. 2018) necessitates long integration times, making the total time required to survey the full on-sky area of the system prohibitively long until recently.

However, the availability of instruments with wide fields of view located on 4+m-class telescopes – which are able to survey the complete on-sky area of the Clouds in a reasonable timeframe – has increased in recent years, with several large-scale surveys dedicated to contiguously photometrically mapping the Clouds and their outskirts. In the optical, the Dark Energy Camera (DECam: Flaugher et al. 2015), with a 3 deg^2 field of view and located on the 4 m Blanco Telescope at the Cerro Tololo Inter-American Observatory in Chile, has been used to conduct a number of Magellanic surveys. This includes the Survey of the Magellanic Stellar History (SMASH: Nidever et al. 2017) and the Magellanic SatelLites Survey (MagLites: Drlica-Wagner et al. 2016), which in combination with imaging from Mackey et al. (2018) and the Dark Energy Survey (DES: Abbott et al. 2018), has provided an almost complete photometric picture of the Clouds and their surroundings, as shown in Fig. 1.4. Fig. 1.5 shows a typical Hess diagram for the associated DECam photometry, from which the main sequence turnoff (MSTO) stars used to produce Fig. 1.4 are selected. This optical photometry is complemented by near-contiguous infrared photometry provided by the Visible and Infrared Survey Telescope for Astronomy (VISTA), including both the VISTA survey of the Magellanic Clouds (VMC: Cioni et al. 2011) and the VISTA Hemisphere Survey (VHS: McMahon et al. 2013).

A key finding of these surveys is that the Magellanic periphery is very highly sub-structured, with each substructure potentially reflecting one or more interactions between the two Clouds and/or the MW. Among the first of these discoveries was the detection of a long (~10°) arm-like feature to the northeast of the LMC by Mackey et al. (2016), appearing to join the outskirts of the LMC ~13° due north of the LMC center. Since then, a plethora of new substructures have been observed. These include:

- A shell-like overdensity ("SMCNOD") ~8° northwest of the SMC, discovered by Pieres et al. (2017), and comprised of an indistinguishable stellar population to that

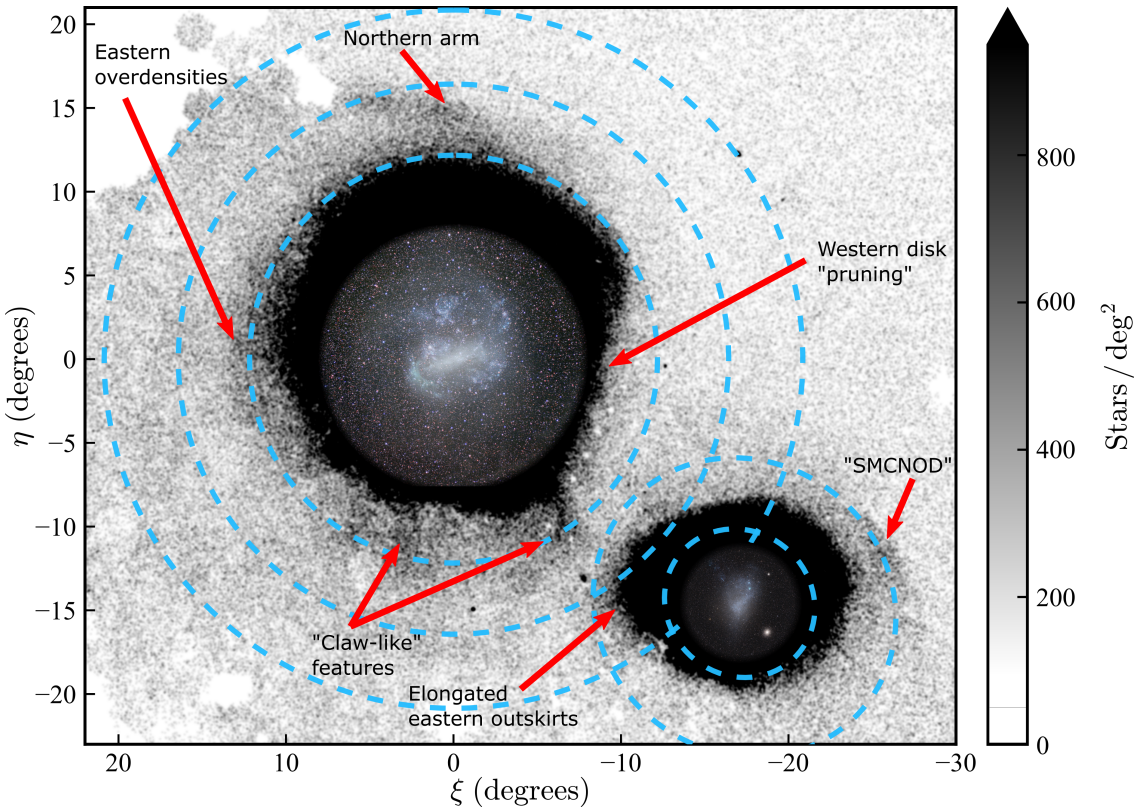

Figure 1.4: Density map of MSTO stars across the Magellanic system, selected from DECam imaging. Blue dashed lines map on-sky radii of 12°/16°/20° from the LMC centre of motion (COM), and 4°/8° from the SMC COM. A diverse array of substructures is apparent in the peripheral regions of the Clouds, with several regions of interest labelled. Adapted from Mackey et al. in prep.

of the nearby SMC body.

- Two claw-like substructures located to the south of the LMC disk discovered by Mackey et al. (2018), each appearing to join the LMC disk at ~10° from the LMC centre and extending to radii of 14°. The western-most structure is co-spatial in projection with a bridge of "old" RR Lyrae stars connecting the two Clouds located ~5° further south than the canonical HI bridge (Belokurov et al. 2017), though the strength of this bridge is debated (e.g. Jacyszyn-Dobrzeniecka et al. 2020a).

- A sharp apparent truncation or pruning of the western edge of the LMC disk from an on-sky galactocentric radius of ~10° to ~8°, stronger than expected from projection effects due to the inclination of the LMC disk (Mackey et al. 2018).

- An elongated distribution of intermediate-age populations (Mackey et al. 2018; El Youssoufi et al. 2019) and Mira variables (Deason et al. 2017) in the eastern outskirts of the SMC, pointing in the same direction as the "old" RR Lyrae bridge

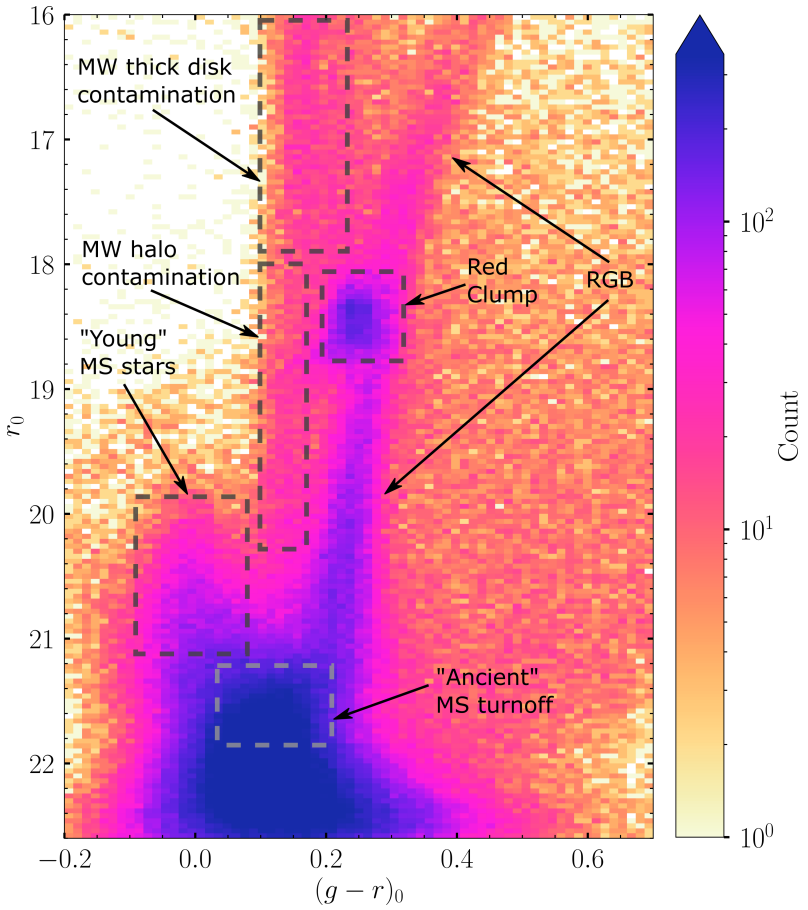

Figure 1.5: DECam Hess diagram of stars in the northern LMC disk ($7.5° \leq R \leq 8.5°$), showing the MSTO selection used to produce maps such as that in Fig. 1.4, as well as brighter Magellanic red clump stars available in Gaia photometry discussed further below.

in Belokurov et al. (2017).

- A shell-like overdensity comprised purely of young (~150 Myr) stars, located ~2° northeast of the SMC COM (Martínez-Delgado et al. 2019).

- Two potential stellar streams in the northwest outskirts of the Clouds, first discovered by Belokurov and Koposov (2016) as overdensities of blue horizontal branch (BHB) stars in DES photometry and confirmed to be kinematically distinct and associated with the Clouds by Navarrete et al. (2019).

- Multiple fragmented overdensities emanating from the eastern outskirts of the LMC disk, characterised by El Youssoufi et al. (2021).

In addition to these deep photometric surveys, the Gaia satellite (Gaia Collaboration et al. 2016) has recently provided precise astrometry for almost two billion sources across the entire sky (Gaia Collaboration et al. 2018b, 2021b), including the Magellanic Clouds.

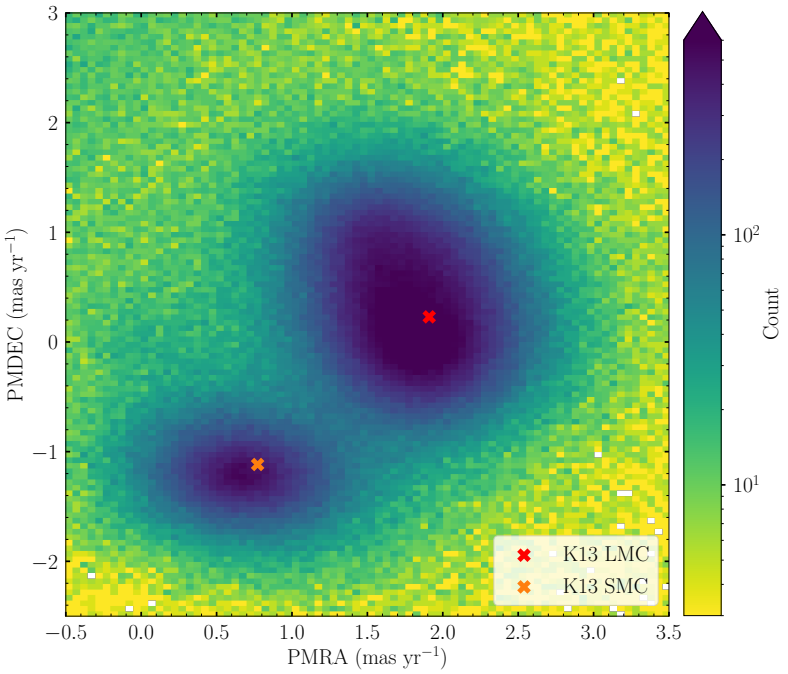

Figure 1.6: Proper motions for $G \lesssim 19.5$ stars with on-sky radii $2° < R < 25°$ from the LMC COM (stars located at $R < 2°$ are affected by crowding), and $R < 12°$ from the SMC COM. Only stars with parallax $\varpi < 0.2$ are plotted. Two clear overdensities correspond to the proper motions of the two Clouds, with that for the LMC having a greater intensity (and occupying a larger region in proper motion space) due to the LMCs factor-of-ten larger mass compared to the SMC. Red and orange crosses mark the proper motions as measured by Kallivayalil et al. (2013) for the LMC and SMC respectively, consistent with those from Gaia data.

Whilst Gaia photometry is truncated at a magnitude $G \sim 21$ (Gaia Collaboration et al. 2021b), meaning it does not cover the ancient MSTO populations traced in the deep photometric surveys discussed above, it does include Magellanic red clump and RGB stars (which have magnitudes $G \lesssim 19.5$). Further, since Gaia provides proper motion and parallax information for each star down to $G \sim 20$[2], astrometric filtering allows the clean separaion of Magellanic stars from contaminating populations (including Milky Way stars and background galaxies), as in Fig. 1.6.

The availability of Gaia data has significantly progressed the study of substructures in the Magellanic periphery, as shown in Fig. 1.7: the ability to astrometrically remove contaminants permits equally low surface-brightness levels to be achieved despite the star counts not reaching as deep as e.g. those from DECam. As a result, Belokurov and Erkal (2019) were able to trace the Mackey et al. (2016) northern arm for an additional ~10°, revealing the total length of this feature to be in excess of 23°, with Mira variables located along the full length of the feature (Deason et al. 2017). Gaia data also reveals a long arm-like structure encircling the southern LMC, which appears to join the eastern edge

[2] with stars $20 < G < 21$ predominantly having only two-parameter solutions for on-sky location.

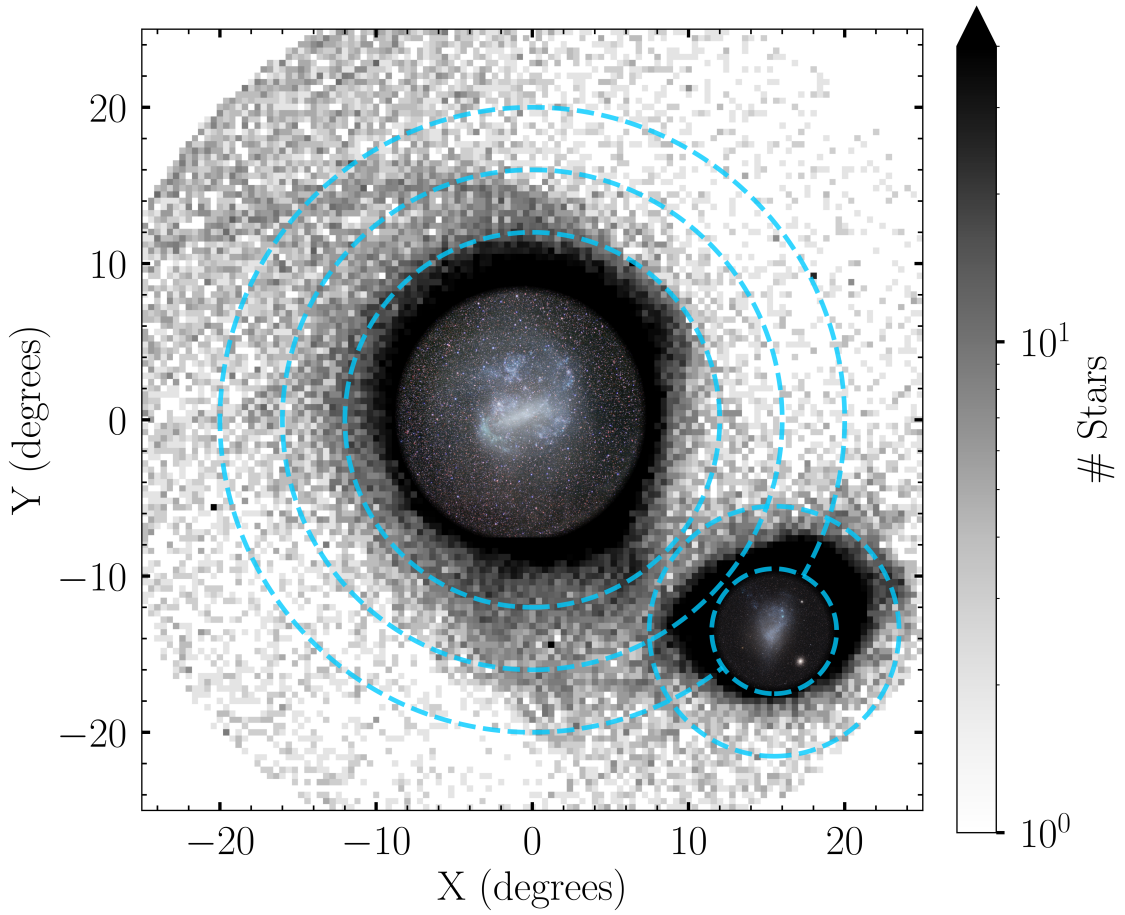

Figure 1.7: Density map of red clump and RGB stars across the Magellanic system selected from Gaia data. Blue dashed lines map on-sky radii of 12°/16°/20° from the LMC, and 4°/8° from the SMC. The substructures observed in maps made using deep MSTO photometry (as in Fig. 1.4) are not only recovered, but can often be traced to larger distances through the clean selection afforded by proper motion and parallax cuts.

of the SMC (Belokurov and Erkal 2019), subsequently detected in deep photometric data by Massana et al. (2020). In the eastern outskirts of the SMC, Subramanian et al. (2017) find a stellar substructure comprised of intermediate-aged ($2-9$ Gyr old) stars ~12 kpc in front of the SMC body, with Gaia data revealing it is kinematically distinct from the bulk motion of the SMC (Omkumar et al. 2020).

1.5 Aim of this thesis

Although precision astrometry and photometry from Gaia and the aforementioned photometric surveys have significantly advanced our understanding of the Magellanic periphery, there remains a key dimension as yet unexplored: line-of-sight (LOS) velocities. Having all three components of motion – that is, line of sight velocities along with proper motions

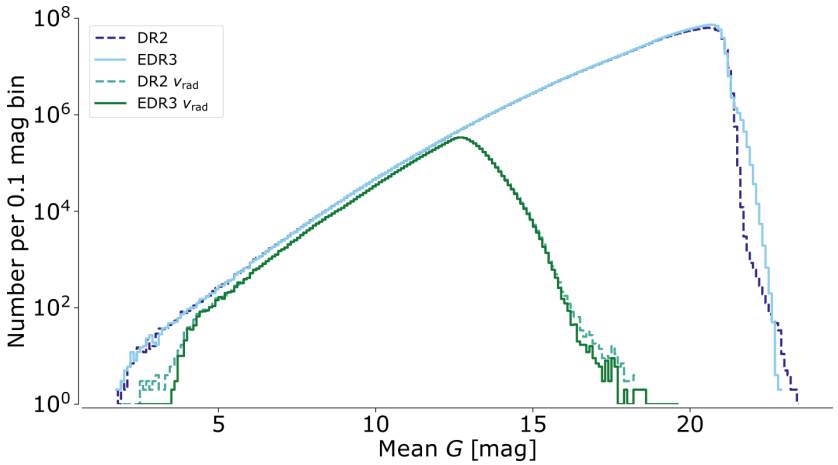

Figure 1.8: Distribution of the mean G magnitudes for all Gaia EDR3 sources (solid lines), compared to those in Gaia DR2 (dashed lines). Histogram bins are 0.1 mag wide. Sources $G \lesssim 21$ have useful proper motions, while only sources predominantly with $G \lesssim 15$ have radial velocities. Adapted from Gaia Collaboration et al. (2021b).

– is necessary to probe the full velocity field of the Clouds (see e.g. section 3 of van der Marel and Cioni 2001). This is particularly crucial for substructures in the Magellanic outskirts, as such information is necessary to place constraints on the interactions which produce them. An example for the arm-like substructure to the north of the LMC is seen in Mackey et al. (2016) and Besla et al. (2016). Both studies present dynamical models which can qualitatively replicate the shape of the feature, using different interaction mechanisms: in Mackey et al. (2016), interactions between the MW and LMC are sufficient to replicate the feature, while in Besla et al. (2016) it is formed during interactions between the LMC and SMC. Full 3D kinematics along the feature – including line-of-sight velocities – are required to differentiate between these two scenarios and elucidate the origin of the structure.

However, while there have been many spectroscopic studies – from which LOS velocities are derived – of the inner regions of the Clouds, there is a dearth of measurements in their outskirts. A handful of studies (e.g. Majewski et al. 2008; Carrera et al. 2017; Navarrete et al. 2019) have performed spectroscopy in the Magellanic periphery, but these are generally only in isolated fields, and largely do not cover the substructures discussed in section 1.4. While the Gaia satellite can supply proper motions for stars as faint as $G \sim 21$, its spectroscopic coverage is restricted to bright ($G \lesssim 15$) stars, as seen in Fig. 1.8. This omits Magellanic red clump and RGB stars entirely, as even the brightest RGB stars sit just below this cutoff, as in the Gaia CMD presented in Fig. 1.9.

A lack of spectroscopy in the outskirts of the Clouds also implies a lack of precision abundance measurements, as while photometric metallicity estimators exist (and have

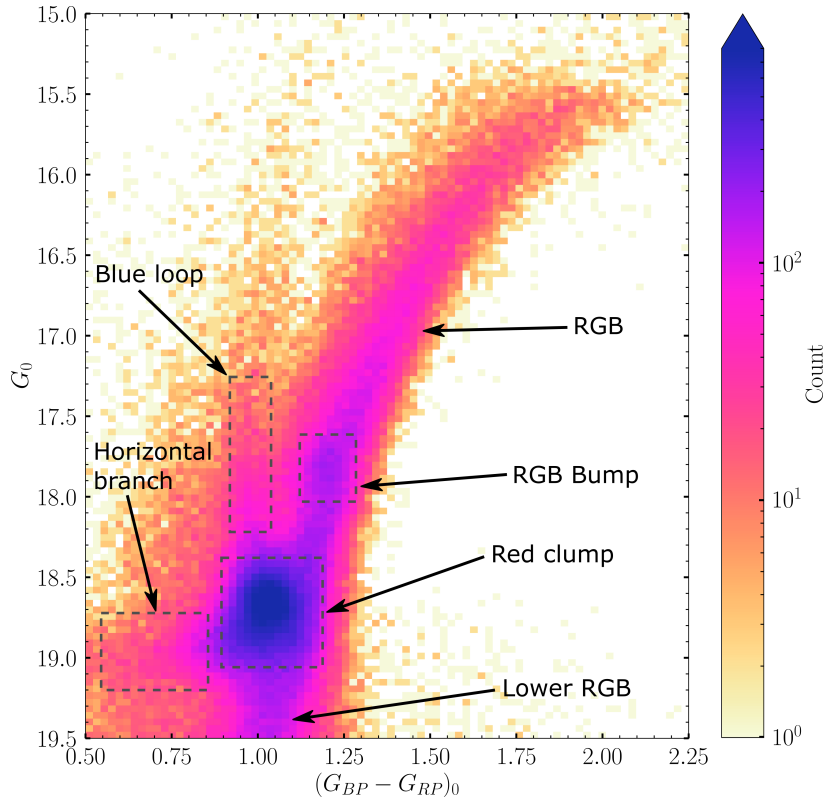

Figure 1.9: Hess diagram for Magellanic stars (i.e. with ϖ<0.2,0<μ_α<3, and −1<μ_δ<2) selected from Gaia with on-sky radii 6.5°<R<8° from the LMC COM. Red clump stars form a prominent overdensity at $G_0 \sim 19$, $(G_{BP} - G_{RP})_0 \sim 1$. Regions of interest are labelled. The brightest RGB stars are approximately $G \sim 15$: too faint for Gaia LOS velocities.

been applied to the Clouds: see e.g. Choudhury et al. 2018, 2020; Grady et al. 2021), these techniques produce aggregate metallicities for on-sky regions, not individual stars as is available from spectroscopy. Star-by-star abundances are critical in identifying substructure material as originating in the LMC or SMC (or potentially even smaller, accreted satellites). For example, Olsen et al. (2011) were able to detect a population of accreted SMC stars within the LMC using a combination of abundance and kinematic data.

Further, metallicity gradients have been observed in both Clouds. Median [Fe/H] abundances decrease from approximately −0.5 within the central ($\leq$ 6 kpc) LMC disk, to approximately −1 at larger radii (e.g. Carrera et al. 2008b, 2011), while in the SMC, [Fe/H] abundances decrease from approximately −1 in the central ($\leq$ 2°) regions, to approximately −1.5 further out (e.g. Carrera et al. 2008a; Dobbie et al. 2014b, but see also Cioni 2009). Consequently, abundance measurements can assist in determining the approximate radii from which substructure material originates, and thus the mechanisms required to perturb it.

This thesis aims to fill the spectroscopic gap in the outskirts of the Clouds by perform-

ing the first dedicated spectroscopic study of these regions. In combination with precision astrometry and photometry from Gaia, I use these data to comprehensively study the structure and kinematics of substructures in the Magellanic periphery. Comparison of my observations with dynamical models of the Magellanic system allows the placement of new constraints on the perturbations which produce these features, and thus the orbital and interaction history of the Clouds.

The thesis outline is as follows. Chapter 2 introduces a geometric framework used to describe the motion of stars relative to the plane of the LMC disk, used throughout the following analysis. Chapter 3 describes the Magellanic Edges Survey (MagES), the spectroscopic programme on which these results are based. Chapter 4 presents a detailed view of the properties and origin of the long arm-like feature to the north of the LMC. Chapter 5 explores the kinematic and structural properties of the outer LMC – including the disk outskirts, the two southern claw-like features, and the long southern arm-like structure – at galactocentric radii beyond 10°, and the dynamical interactions which can plausibly affect these. A summary of results, their implications in the context of understanding the orbital and interaction history of the Clouds, and directions for future work, are given in Chapter 6.

Chapter 2

LMC Disk framework

> Align yourself with the circling of the stars.
>
> Midorima Shintarou

In order to place constraints on the dynamical perturbations which produce substructures in the outskirts of the Clouds, physical velocities relative to their systemic motions – and for the LMC, measured in the frame of its disk – are required. However, these quantities are not observed directly: they must be inferred from measured line-of-sight velocities and proper motions in the plane of the sky. In this chapter, I outline a geometric framework which facilitates this conversion. This is based heavily on the framework presented in van der Marel and Cioni (2001 henceforth referred to as vdM01) and van der Marel et al. (2002 henceforth referred to as vdM02), which describes the inverse transformation to that discussed here (i.e. converting velocities in the frame of the LMC disk into observables). In this chapter, all angles are given in radians unless otherwise indicated.

Many of the following conversions require the use of inverse trigonometric functions in order to calculate angles. As these functions only have domains $0 \leq \theta \leq \pi$, an additional conversion factor is required in order to correctly calculate angles over the domain $0 \leq \theta \leq 2\pi$, utilising the varying sign (i.e. positive/negative) of the trigonometric functions in different quadrants, as in Fig. 2.1. The calculation prodecure for such conversions is given by the following logic. Here, `sintheta` and `costheta` represent the values of $\sin(\theta)$ and $\cos(\theta)$ respectively, each of which are calculable directly from known quantities, as indicated in the following sections.

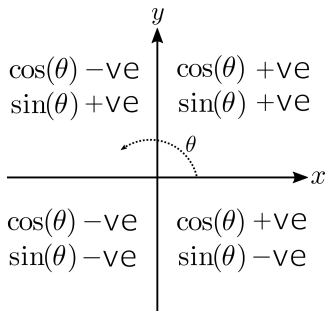

Figure 2.1: Sign value of the sine and cosine functions in each domain quadrant, utilised to identify the correct value of angles derived using inverse trigonometric functions.

```
def convtoangle(sintheta,costheta):
θ_estimate = arccos(costheta)
if (sintheta>=0 and costheta>=0) or (sintheta>=0 and costheta=<0):
θ = θ_estimate
else if (sintheta<0 and costheta>0) or (sintheta<0 and costheta<0):
θ = θ_estimate + 2(π-θ_estimate)
```

2.1 The systemic properties of the LMC

In order to calculate the motion of a tracer relative to the LMC, one must first know the systemic motion and location of the LMC centre of mass (COM), which in this thesis, are taken from literature measurements. Six parameters describe the systemic properties of the LMC:

- The on-sky position of the COM, described by right ascension (RA: α_0) and declination (DEC: δ_0) coordinates;
- The line-of-sight distance to the COM, D_0, measured in kpc;
- The heliocentric line-of-sight velocity of the COM, $V_{\mathrm{LOS},0}$ (defined as $\frac{dD_0}{dt}$), in km s^{-1}. A positive V_{LOS} indicates recession from the observer; and
- The proper motions of the COM in the plane of the sky, in mas yr^{-1}. In this thesis, the proper motion in the direction of right ascension (PMRA) is defined as $\mu_{\alpha 0} = \frac{d\alpha}{dt} \times \cos(\delta)$ such that it is perpendicular to the proper motion in the declination direction (PMDEC): $\mu_{\delta 0} = \frac{d\delta}{dt}$.

The systemic distance to the LMC has been well-characterised using variable stars, such as RR Lyrae or Cepheids, to be ~50 kpc (e.g. Freedman et al. 2001; Pietrzyński et al. 2019 and many others). In this thesis, a value of 49.59 ± 0.63 kpc from Pietrzyński et al.

(2019) is most commonly adopted[3]. In contrast, the on-sky location of the LMC COM is dependent on the technique used to define it, with photometric centres determined from stellar counts differing from kinematic centres of rotation, which themselves differ depending on the tracer population utilised in the analysis. Table 2.1 provides a summary of several literature LMC COM positions, with Fig. 2.2 highlighting the spatial variation for a subset of these estimates. As the analysis in this thesis is focussed on kinematic measurements using red clump/RGB stars (see Chapter 3), the chosen LMC COM positions are those derived using a similar technique and population. In this case, Chapters 3 and 4 use those from van der Marel and Kallivayalil 2014 (which, at the time of writing, was state-of-the-art), while Chapter 5, written subsequently, utilises updated values from Gaia Collaboration et al. 2021c. The systemic LOS velocity and proper motions of the LMC are taken from these same studies, derived from kinematic analysis of similar tracer populations to those used in the thesis, and are as follows:

- $V_{\rm LOS,0} = 261.1 \pm 2.2$ from van der Marel and Kallivayalil (2014);
- $\mu_{\alpha 0} = 1.895 \pm 0.024$ from van der Marel and Kallivayalil (2014) or 1.844 from Gaia Collaboration et al. (2021c);
- $\mu_{\delta 0} = 0.287 \pm 0.054$ from van der Marel and Kallivayalil (2014) or 0.394 from Gaia Collaboration et al. (2021c).

2.2 The LMC disk plane

As the LMC is a disk galaxy, we must next describe how the plane of its disk is oriented relative to an observer on Earth. We begin by defining a Cartesian coordinate system (x, y, z), with its origin at the LMC COM, and which describes the plane of the sky as seen in Fig 2.3. Here, the x, y-plane (where $z = 0$) is the physical plane of the sky, with the z direction perpendicular to the plane of the sky, and along the line-of-sight from the COM to the observer. The x-axis is in the direction of local west at the LMC COM (i.e. antiparallel to the unit vector in the direction of $\mu_{\alpha,0}$), the y-axis is in the direction of local north (i.e. parallel to the unit vector in the direction of $\mu_{\delta,0}$) at the LMC COM.

In this coordinate system, the systemic motion of the LMC is as shown in the left

[3] with the sole exception being the initialisation of dynamical models discussed in §4.5.3, which sample the range 50.1 ± 2.5 from Freedman et al. (2001)

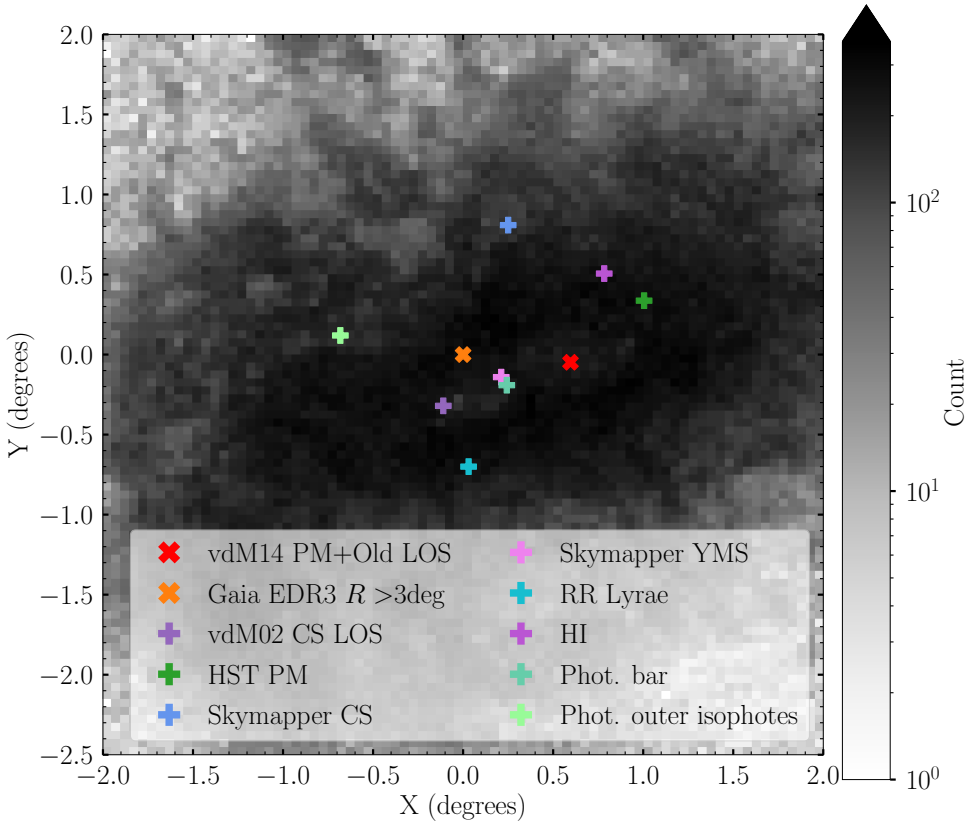

Figure 2.2: Positions of the LMC COM as measured by several literature studies. The background image shows a density map of Magellanic red clump stars in the vicinity of the LMC bar selected from Gaia EDR3. Different techniques produce significantly different positions for the COM. Centres marked are: vdM14 proper motion + "old" LOS velocity sample ("vdM14 PM+Old LOS"), Gaia Collaboration et al. (2021c) proper motions ("Gaia EDR3 R>3deg"), vdM02 LOS velocity sample ("vdM02 CS LOS"), vdM14 bulk HST proper motions ("HST PM"), W20 carbon stars ("Skymapper CS"), W20 young main sequence stars ("Skymapper YMS"), Haschke et al. (2012) RR Lyrae ("RR Lyrae"), Kim et al. (1998) HI dynamics ("HI"), de Vaucouleurs and Freeman (1972) optical centre of the bar ("Phot. bar"), and de Vaucouleurs 1957 optical centre of the outer isophotes ("Phot. outer isophotes").

Table 2.1: Literature measurements of the position of the LMC centre. Coordinates are reported as right ascension (RA) and declination (DEC) in J2000 (with conversions from J1950 applied where indicated). Highlighted rows indicate values adopted in this thesis.

RA (°)	DEC (°)	Source	Technique
83.53[a]	−69.42[a]	de Vaucouleurs (1957)	Centre of optical isophotes outside the bar region
80.89[a]	−69.74[a]	de Vaucouleurs and Freeman (1972)	Optical centre of the LMC bar
79.4	−69.03	Kim et al. (1998)	Dynamical centre of HI gas
81.91 ± 0.98	-69.87 ± 0.41	van der Marel et al. (2002)	Dynamical fit to LOS velocities for individual carbon stars
80.40	−69.00	Nikolaev et al. (2004)	Cepheid distances from combined optical MACHO (Alcock et al. 2000) and infrared 2MASS (Skrutskie et al. 1997) data
80.35	−69.68	Pejcha and Stanek (2009)	RR lyrae distances from optical OGLE-III (Udalski et al. 2008) photometry
81.5	−70.25	Haschke et al. (2012)	RR lyrae distances from optical OGLE-III (Udalski et al. 2008) photometry
78.76 ± 0.52	-69.19 ± 0.25	van der Marel and Kallivayalil (2014)	Dynamical fit to bulk HST PMs only
79.88 ± 0.83	-69.59 ± 0.25	van der Marel and Kallivayalil (2014)	Dynamical fit to bulk PMs and LOS velocities for individual "old" (carbon, AGB, and RGB) stars
80.05 ± 0.34	-69.30 ± 0.12	van der Marel and Kallivayalil (2014)	Dynamical fit to bulk PMs and LOS velocities for individual red supergiant stars
80.78	−69.30	Inno et al. (2016)	Cepheid distances from combined optical OGLE-IV (Soszyński et al. 2015) data and several infrared catalogues
80.90 ± 0.29	-68.74 ± 0.12	Wan et al. (2020)	Dynamical fit to PMs for individual carbon stars using optical Skymapper (Wolf et al. 2018) data
80.98 ± 0.07	-69.69 ± 0.02	Wan et al. (2020)	Dynamical fit to PMs for individual young main sequence stars using optical Skymapper (Wolf et al. 2018) data
81.07	−69.41	Gaia Collaboration et al. (2021c)	Dynamical fit to PMs of individual RC and RGB stars, with on-sky radii $R \leq 8°$
81.59	−69.55	Gaia Collaboration et al. (2021c)	Dynamical fit to PMs of individual RC and RGB stars, with on-sky radii $3° \leq R \leq 8°$

[a] value converted from J1950.

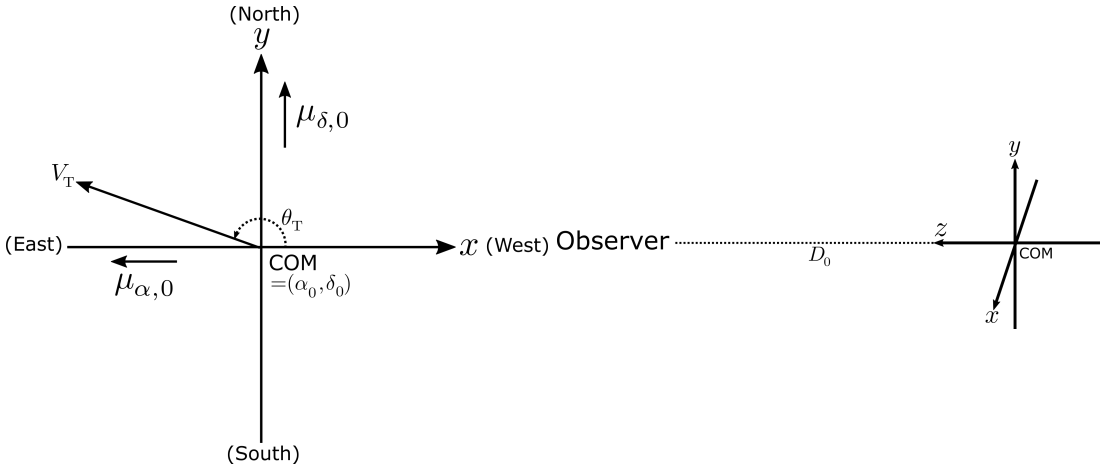

Figure 2.3: Cartesian coordinate system used to define the plane of the sky, with the origin located at the LMC centre of mass (COM). The x-axis points in the direction of local west at the LMC COM, and the y-axis points in the direction of local north at the LMC COM. The z-axis points along the LOS between the COM and the observer. Left: projected view of the sky, with the z-axis (not shown) pointing vertically out of the page. V_T is the transverse velocity of the LMC COM in the plane of the sky, and θ_T describes the angle between this vector and the positive x-axis, measured anticlockwise. Right: "side view" of the same coordinate system. Drawing perspective is used to illustrate the x-axis, which in this view actually points vertically out of the page. The distance from the observer to the LMC COM is D_0. Adapted from van der Marel et al. (2002).

panel of Fig 2.3, and can be described by Eq. 2.1 (Eq. 12 in vdM02).

$$\begin{pmatrix} V_x \\ V_y \\ V_z \end{pmatrix}_{\rm COM} = \begin{pmatrix} V_T \cos(\theta_T) \\ V_T \sin(\theta_T) \\ -V_{\rm LOS} \end{pmatrix} \tag{2.1}$$

As the positive z-axis points towards the observer, the z-velocity is simply the negative of the observed LOS velocity. V_T is the magnitude of the transverse velocity of the LMC in the plane of the sky, and θ_T is the direction of the transverse velocity vector measured anticlockwise from the positive x-axis. Eqs. 2.2 and 2.3 describe how these values are calculated from the systemic proper motions of the LMC COM, with factors of 4.7403885 producing velocity units of km s^{-1} when distances are in units of kpc and proper motions are in units of mas yr^{-1}.

$$V_T = \sqrt{(4.7403885\mu_{\delta,0} \times D_0)^2 + (4.7403885\mu_{\alpha,0} \times D_0)^2} \tag{2.2}$$

$$\begin{aligned}
\sin\left(\frac{\pi}{2}-\theta_{\mathrm{T}}\right) &= \frac{-4.7403885\mu_{\alpha,0}\times D_0}{V_{\mathrm{T}}} \\
\cos\left(\frac{\pi}{2}-\theta_{\mathrm{T}}\right) &= \frac{4.7403885\mu_{\delta,0}\times D_0}{V_{\mathrm{T}}} \\
\theta_{\mathrm{T}} &= \frac{\pi}{2} - \texttt{convtoangle}\left[\sin\left(\frac{\pi}{2}-\theta_{\mathrm{T}}\right), \cos\left(\frac{\pi}{2}-\theta_{\mathrm{T}}\right)\right]
\end{aligned} \tag{2.3}$$

If the LMC disk were entirely face-on, the (x, y) plane in this coordinate system would describe the plane of the disk. However, the LMC is inclined relative to the plane of the sky. We thus describe the disk plane using a new Cartesian coordinate system, (x', y', z'), which is rotated – first clockwise in the (x, y) plane around the z-axis, and subsequently in the (y, z) plane around the x-axis – relative to the original coordinate system, as seen in Fig. 2.4. In this new coordinate system, the (x', y') plane (where $z' = 0$) is the physical plane of the disk, with the z' direction perpendicular to the disk plane.

This rotation – and thus the plane of the LMC disk – is parameterised using two angles. The angle θ_{LON} describes the first rotation around the z-axis, which defines the orientation of the line-of-nodes (LON) – the line along which the (x', y') plane of the disk intersects the (x, y) plane of the sky – measured anticlockwise from the positive x-axis. However, by convention, the orientation of the LON is expressed as a position angle measured from north towards east (i.e. anticlockwise from the positive y-axis). Consequently, we define the position angle of the line of nodes, $\Theta = \theta_{\mathrm{LON}} - \frac{\pi}{2}$, as in Fig. 2.4.

The second angle, i, describes the subsequent rotation around the x-axis, and thus the inclination of the disk plane relative to the plane of the sky. It is defined as the angle between the (x, y)-plane of the sky, and the (x', y')-plane of the disk, measured in the direction of positive z such that a plane with inclination $0° < i < 90°$ is closer to the observer in the north, and more distant in the south. A face-on disk has an inclination of zero, while a perfectly edge-on disk has an inclination of 90°.

As is the case for the position of the COM, measurements of the LMC disk geometry (i.e. its inclination and LON position angle) vary depending on the technique (i.e. photometric or kinematic) and tracer population chosen. Table 2.2 summarises several literature values describing the geometry of the LMC disk.

Although exhibiting some variation, these measured geometries agree to the extent that the northeastern disk is closer to the observer, and the southwestern disk is further from the observer, as seen in Fig. 2.5.

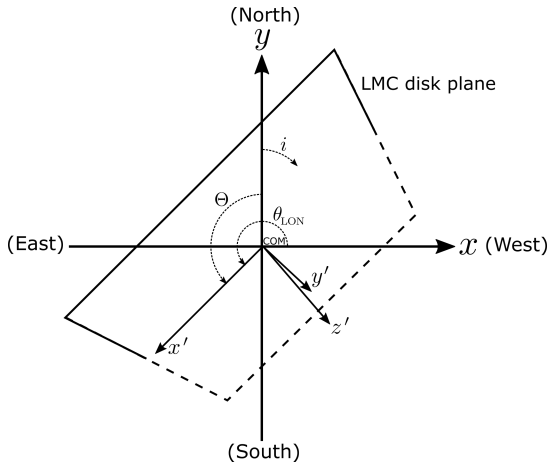

Figure 2.4: The LMC disk plane as seen by an observer. The Cartesian (x, y, z) coordinate system is the same as in Fig. 2.3, with the z-axis (not shown) pointing vertically out of the page. The (x', y', z') coordinate system describes the LMC disk, shown in drawing perspective. The x'-axis lies along the line of nodes of the LMC disk – the intersection of the (x, y)-plane of the sky and the (x', y')-plane of the LMC disk – with $\Theta = \theta_{\rm LON} - \frac{\pi}{2}$ the position angle of the line of nodes. The LMC disk plane is tilted by an angle i out of the page. Adapted from vdM02.

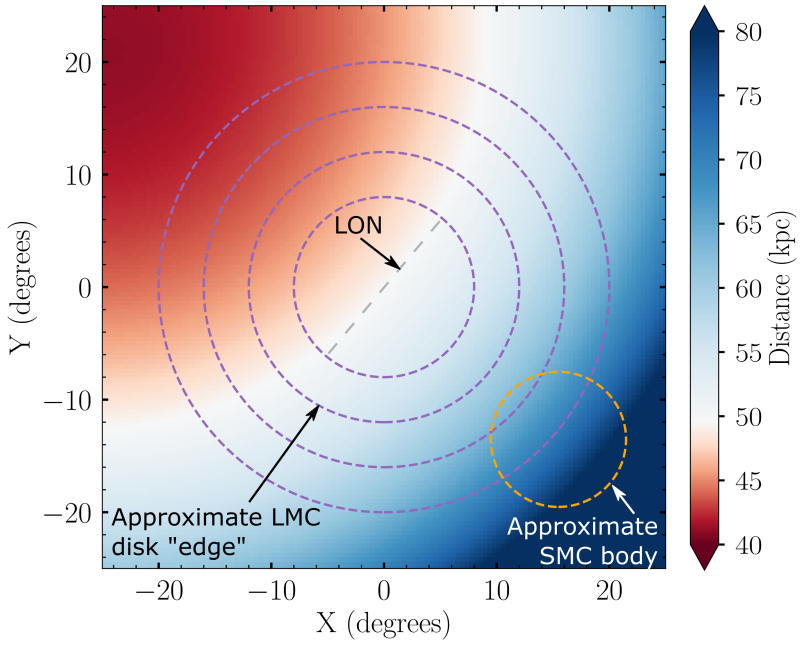

Figure 2.5: Predicted distance variation across the sky for an LMC disk with inclination and LON position angle as derived from the "PMs+Old $V_{\rm LOS}$ sample" of van der Marel and Kallivayalil (2014). White indicates the systematic LMC distance of ~50 kpc. Projection effects result in a much greater difference between the canonical and disk distance at an equivalent on-sky radius in the southwest compared to the northeast. Dashed purple lines indicate on-sky radii of 8°/12°/16°/20° from the LMC COM, and the dashed orange line indicates an on-sky radius of 6° from the SMC COM. The dashed grey line indicates the orientation of the LON. This map uses an orthographic projection centred on the LMC, as defined in Eq. 2.25.

Table 2.2: Selected literature measurements of the LMC geometry.

Inclination i (°)	LON position angle Θ (°)	Source	Technique
27 ± 2	170 ± 5	de Vaucouleurs (1957)	Optical isophotes
28.0 ± 5.9	142.4 ± 7.7	Caldwell and Coulson (1986)	Cepheid distances from optical photometry
34.7 ± 6.2	122.5 ± 8.3	van der Marel and Cioni (2001)	Photometric fit to AGB stars with on-sky radii R>2.5° using infrared 2MASS (Skrutskie et al. 1997) and DENIS (Epchtein et al. 1997) data
22.0 ± 6	~168.0	Kim et al. (1998)	Inclination from HI isophotes; LON position angle from HI dynamics
34.7 ± 6.2[a]	129.9 ± 6.0	van der Marel et al. (2002)	Dynamical fit (LOS velocities only) for carbon stars
35.8 ± 2.4	145 ± 4	Olsen and Salyk (2002)	Photometric fit to red clump stars using optical data
30.7 ± 1.1	151 ± 2.4	Nikolaev et al. (2004)	Cepheid distances using optical MACHO (Alcock et al. 2000) and infrared 2MASS (Skrutskie et al. 1997) data
37.4 ± 2.3	141.2 ± 3.7	Subramanian and Subramaniam (2010)	Photometric fit to RC stars using optical MCPS (Zaritsky et al. 2004) data
23.0 ± 0.8	163.7 ± 1.5	Subramanian and Subramaniam (2010)	Photometric fit to RC stars using optical OGLE-III (Udalski et al. 2008) data
32 ± 4	114 ± 13 102 ± 2 122 ± 32	Haschke et al. (2012)	RR Lyrae distances using optical OGLE-III (Udalski et al. 2008) data for stars with radii R<7°, 0°<R<3°, and 3°<R<7° respectively.
25.7 ± 1.6	141.5 ± 4.5	Subramanian and Subramaniam (2013)	Photometric fit to RC stars using infrared IRSF (Kato et al. 2007) data
39.6 ± 4.5	147.4 ± 10.0	van der Marel and Kallivayalil (2014)	Dynamical fit to bulk HST PMs
34.0 ± 7.0	139.1 ± 4.1	van der Marel and Kallivayalil (2014)	Dynamical fit to bulk PMs and LOS velocities for individual "old" (carbon, AGB, and RGB) stars

to be continued on the next page

Table 2.2: (continued from previous page)

Inclination i (°)	LON position angle Θ (°)	Source	Technique
26.2 ± 5.9	154.5 ± 2.1	van der Marel and Kallivayalil (2014)	Dynamical fit to bulk PMs and LOS velocities for individual red supergiant stars
44.19 ± 1.94	125.93 ± 0.29	Balbinot et al. (2015)	Photometric fit to the surface density of young main sequence stars in the northwestern LMC using optical DES data, assuming a circular disk
33.14 ± 0.09	159.59 ± 0.12	Mackey et al. (2016)	Photometric fit to the surface density of MSTO stars with on-sky radii $9°<R<13°$ in the northwestern LMC using optical DES data, assuming a circular disk
25.18 ± 0.71	185	Mackey et al. (2016)	Photometric fit to the surface density of MSTO stars with on-sky radii $9°<R<13°$ in the northwestern LMC using optical DES data, assuming an elliptical disk
25.05 ± 0.57	150.76 ± 0.09	Inno et al. (2016)	Cepheid distances from combined optical OGLE-IV (Soszyński et al. 2015) data and several infrared catalogues
$25.86^{+0.73}_{-1.39}$	$149.23^{+6.43}_{-8.35}$	Choi et al. (2018b)	Photometric fit to RC and RGB stars using optical SMASH (Nidever et al. 2017) data
$32 - 35$	$130 - 135$	Vasiliev (2018)	Dynamical fit to PMs of individual RGB stars
25.6 ± 1.1	135.6 ± 3.3	Wan et al. (2020)	Dynamical fit to PMs of individual carbon stars using optical Skymapper (Wolf et al. 2018) data
29.4 ± 0.4	152.0 ± 1.0	Wan et al. (2020)	Dynamical fit to PMs of individual young main sequence stars using optical Skymapper (Wolf et al. 2018) data
33.28 33.31	130.97 133.35	Gaia Collaboration et al. (2021c)	Dynamical fit to PMs of individual RC and RGB stars with radii $R<8°$ and $3°<R<8°$ respectively.

[a] Value not independently determined, but held fixed at that from van der Marel and Cioni (2001)

2.3 Observed properties of a stellar tracer

Having defined the global properties of the LMC disk, we are now interested in describing the position and velocity of any given star (or other tracer) relative to it. In the observable frame, this is also described by six parameters:

- the on-sky position of the tracer, described by right ascension (RA: α) and declination (DEC: δ) coordinates;
- the line-of-sight distance to the tracer, D, in kpc;
- the heliocentric line of-sight-velocity ($V_{\rm LOS}$) of the tracer, in km s^{-1};
- the proper motion of the tracer in the directions of right ascension (PMRA: μ_α) and declination (PMDEC: μ_δ), in mas yr^{-1}. Note that these proper motions are defined relative to the local directions of RA/DEC, and thus are not parallel to those measured at the LMC COM.

With the exception of the distance D to each star, these quantities can be measured directly. Direct distance measurements require parallax (ϖ) measurements for the star, as $D \propto 1/\varpi$. However, at the systemic distance of the LMC (~50 kpc), parallax values are on the order of ~0.02 mas: too small to be accurately measured by Gaia, as at the G~19 magnitudes of Magellanic red clump stars, parallax uncertainties are a factor of ~10 larger than the parallax values themselves (Gaia Collaboration et al. 2021c).

In order to estimate the distance to a star, there are thus two options. The first is to simply assume the distance of the star is such that it is located in the plane of the LMC disk, which can be calculated at any location as outlined in the following section. This is a reasonable assumption for stars at small LMC galactocentric radii, where the disk geometry is well-defined, but is less reasonable for stars at large galactocentric radii, where tidal interactions might significantly perturb the disk from the assumed plane.

A better option in the case of red clump stars is to estimate the distance using the red clump magnitude. The red clump in the Hertzsprung-Russell (H-R) diagram results from the core helium burning phase in the evolution of low and intermediate-mass stars. This phase is exceeded in duration only by the core hydrogen burning lifetime on the main sequence. While the luminosity of the red clump is dependent on population effects, such as age and metallicity, these can be allowed for making the red clump a "standardizable" candle (see Girardi 2016 for a review). Consequently, it can be used to determine distances. Given a known "reference magnitude" – i.e. the observed (apparent) magnitude (m_0) of a red clump population of the same age and abundance as the tracer of interest, at a known

distance (D_0) – the distance to the tracer can be calculated using Eq. 2.4, where m is the observed (apparent) magnitude of the tracer.

$$D = D_0 \times 10^{([m-m_0]/5.0)} \tag{2.4}$$

To perform this calculation requires the apparent magnitude of the tracer, as well as the reference magnitude, to be corrected for the reddening and extinction effects of interstellar dust, as this varies as a function of position on the sky. The specific prescription for this correction is passband-dependent, due to the wavelength dependence of the scattering and absorption of light by interstellar dust grains. In this thesis, Gaia passbands G, G_{BP}, and G_{RP} are used: Eq. 2.5 presents the assumed correction for these passbands, derived by Casagrande and VandenBerg (2018).

$$\begin{aligned} G_0 &= G - 2.740E(B-V) \\ (G_{BP} - G_{RP})_0 &= G_{BP} - 3.374E(B-V) - [G_{RP} - 2.035E(B-V)] \end{aligned} \tag{2.5}$$

Here, $E(B-V)$ is the colour excess in the photometric B and V bands. For the corrections given in Eq. 2.5, this is equal to the value measured by Schlegel et al. (1998) and corrected by Schlafly and Finkbeiner (2011): i.e. as per Eq. 2.6.

$$E(B-V) = E(B-V)_{\rm corr} = 0.86E(B-V)_{\rm SFD} \tag{2.6}$$

Note that this correction accounts only for the effects of foreground Milky Way dust between the observer and the Magellanic system, and not dust within the Clouds themselves. Accounting for intra-Cloud dust requires the effective $E(B-V)$ to be increased (e.g. Choi et al. 2018b; Bell et al. 2019, 2020; Skowron et al. 2021), as per Eq. 2.7.

$$E(B-V) = E(B-V)_{\rm corr} + E(B-V)_{\rm Clouds} \tag{2.7}$$

However, in the extreme Magellanic periphery, the contribution of intra-Cloud dust to the overall reddening is negligible (cf. Choi et al. 2018b); thus for the remainder of the thesis $E(B-V)_{\rm Clouds}$ is assumed to be zero.

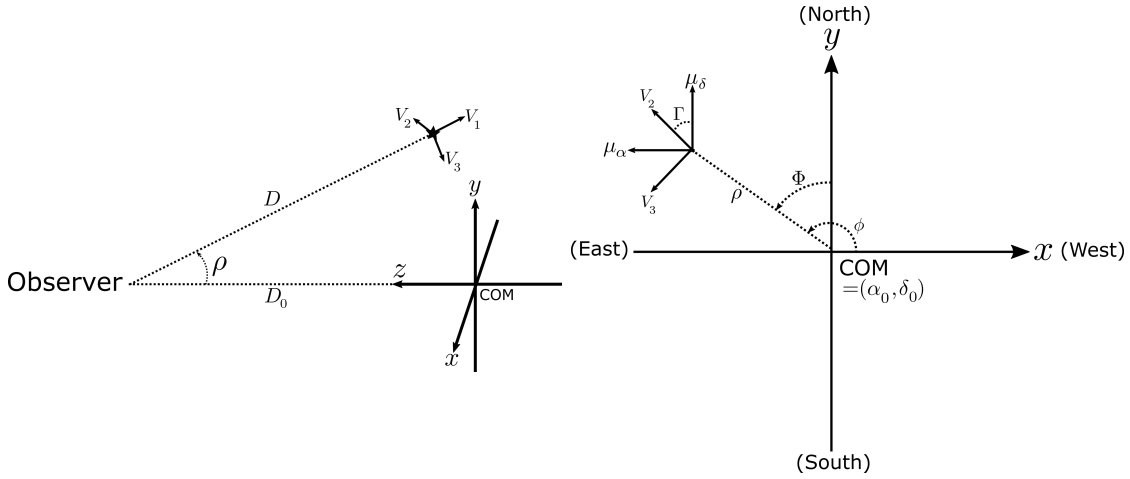

Figure 2.6: Position of a given tracer relative to the Cartesian coordinate system describing the plane of the sky, centred on the LMC centre of mass (COM) as described in §2.1. Left: "side view" of a star relative to the sky coordinate system, with drawing perspective used to illustrate the x-axis (which in this view points vertically out of the page). The velocity of a star can be decomposed into three orthogonal components: V_1, V_2, and V_3, with V_1 along the line of sight to the star. The distance along the LOS from the observer to a star is D. Right: projected view of the sky, with the z-axis (not shown) pointing vertically out of the page. All quantities are in the plane of the page (i.e. the plane of the sky). The position of a star at position (α, δ) is defined by the angle ρ – the on-sky distance between the star and the LMC COM – and the position angle $\Phi = \phi - \frac{\pi}{2}$, measured anticlockwise from the y-axis (local north at the LMC COM). The angle between the proper motion vectors (μ_α, μ_δ) of the star, and the directions of motion along the ρ and ϕ directions (V_2 and V_3), is Γ. Adapted from van der Marel et al. (2002).

2.4 Coordinate conversions

With the required coordinate systems and the observed properties of both the LMC and a given tracer now defined, I outline the conversion process required to determine the motions of a tracer – in this case a star – in the plane of the LMC disk.

We must first know the position of the star from the LMC COM in the frame of the sky, as in Fig. 2.6. We define ρ as the on-sky angular distance between the star and the LMC COM, and ϕ as the position angle of the star, which describes its direction from the LMC COM as measured anticlockwise from the local direction of west at the LMC COM. Formally, this means ϕ is defined according to vdM01 as "the angle at (α_0, δ_0) between the tangent to the great circle on the celestial sphere through (α, δ) and (α_0, δ_0), and the circle of constant declination δ_0, measured anticlockwise starting from the axis that runs in the direction of decreasing RA at constant declination δ_0".

Relations between ρ, ϕ, and the RA/DEC coordinates of the star and the LMC COM are given in Eqs. 2.8-2.9 (derived from Eqs. 1-3 in vdM01). As ρ is defined such that it is always positive, and in the domain $0° \leq \rho \leq 180°$, the inverse cosine function can be used directly. Note that whilst ϕ is utilised in the following calculations, it is not generally how

positions are reported. Instead the position angle Φ, measured anticlockwise from local north at the location of the LMC COM, is used. The relationship between ϕ and Φ is simply $\Phi = \phi - \frac{\pi}{2}$.

$$\rho = \arccos\left[\cos(\delta)\cos(\delta_0)\cos(\alpha - \alpha_0) + \sin(\delta)\sin(\delta_0)\right] \tag{2.8}$$

$$\begin{aligned} \sin(\phi) &= \frac{\sin(\delta)\cos(\delta_0) - \cos(\delta)\sin(\delta_0)\cos(\alpha - \alpha_0)}{\sin(\rho)} \\ \cos(\phi) &= \frac{-\cos(\delta)\sin(\alpha - \alpha_0)}{\sin(\rho)} \\ \phi &= \texttt{convtoangle}\left[\sin(\phi), \cos(\phi)\right] \end{aligned} \tag{2.9}$$

Were a star with coordintes ρ, ϕ located exactly in the LMC disk plane (i.e. with $z' = 0$), its LOS distance D would be given by Eq. 2.10 (Eq. 8 in vdM01).

$$D_{\text{disk}} = \frac{D_0\cos(i)}{\cos(i)\cos(\rho) - \sin(i)\sin(\rho)\sin(\phi - \theta_{\text{LON}})} \tag{2.10}$$

As the local directions of west and north (with respect to which the proper motions of a tracer are measured) vary across the sky, we must first decompose the motion of the star into entirely orthogonal coordinates. We use the position of the star relative to the LMC COM to define these as in Eq. 2.11 (Eq. 1 in vdM02).

$$V_1 = \frac{dD}{dt}, V_2 = D\frac{d\rho}{dt}, V_3 = D\sin(\rho)\frac{d\phi}{dt} \tag{2.11}$$

By definition, V_1 is thus the LOS velocity of the star. In practical terms, V_2 and V_3 are related to the observed proper motion of the star through Eq. 2.12 (the inverse of Eq. 7 in vdM02). Here, Γ is an angle that describes the rotation of the V_2/V_3 directions from the local directions of west and north, as seen in Fig. 2.6. Γ is calculated using the position of the star relative to the LMC COM as in Eq. 2.13 (Eq. 8 in vdM02).

$$\begin{pmatrix} V_1 \\ V_2 \\ V_3 \end{pmatrix} = \begin{pmatrix} V_{\text{LOS}} \\ 4.7403885D\left[\mu_\alpha\sin(\Gamma) + \mu_\delta\cos(\Gamma)\right] \\ 4.7403885D\left[\mu_\alpha\cos(\Gamma) - \mu_\delta\sin(\Gamma)\right] \end{pmatrix} \tag{2.12}$$

$$\begin{aligned}\sin(\Gamma) &= \frac{\cos(\delta_0)\sin(\alpha-\alpha_0)}{\sin(\rho)} \\ \cos(\Gamma) &= \frac{\sin(\delta)\cos(\delta_0)\cos(\alpha-\alpha_0)-\cos(\delta)\sin(\delta_0)}{\sin(\rho)} \\ \Gamma &= \texttt{convtoangle}\left[\sin(\Gamma),\cos(\Gamma)\right]\end{aligned} \tag{2.13}$$

As V_1, V_2, and V_3 are orthogonal, the total observed velocity vector of the star can be decomposed into the sum of different components, each describing the contribution of a different effect as per Eq. 2.14 (Eq. 11 in vdM02). Here, $V_{\rm total}$ is the total observed velocity of the star, $V_{\rm COM}$ is the contribution from the systemic motion of the LMC, $V_{\rm pn}$ is the contribution from disk precession and nutation (i.e. changes in the geometry of the disk over time) and $V_{\rm int}$ is the intrinsic motion of the star itself relative to the disk plane. It is this last component which is of interest.

$$\begin{pmatrix}V_1\\V_2\\V_3\end{pmatrix}_{\rm total} = \begin{pmatrix}V_1\\V_2\\V_3\end{pmatrix}_{\rm COM} + \begin{pmatrix}V_1\\V_2\\V_3\end{pmatrix}_{\rm pn} + \begin{pmatrix}V_1\\V_2\\V_3\end{pmatrix}_{\rm int} \tag{2.14}$$

The contribution of the LMC's systemic (i.e. COM) motion is given by Eq. 2.15 (Eq. 13 in vdM02), with $V_{\rm T}$ and $\theta_{\rm T}$ as defined in §2.1.

$$\begin{pmatrix}V_1\\V_2\\V_3\end{pmatrix}_{\rm COM} = \begin{pmatrix}V_{\rm T}\sin(\rho)\cos(\phi-\theta_{\rm T})+V_{\rm LOS}\cos(\rho)\\V_{\rm T}\cos(\rho)\cos(\phi-\theta_{\rm T})-V_{\rm LOS}\sin(\rho)\\-V_{\rm T}\sin(\phi-\theta_{\rm T})\end{pmatrix} \tag{2.15}$$

The contribution of precession (i.e. the change in inclination angle over time: $\frac{di}{dt}$) and nutation (i.e. the change in the position angle of the line of nodes over time: $\frac{d\Theta}{dt}$) is given by Eq. 2.16 (Eq. 16 in vdM02). However, literature measurements have indicated both $\frac{di}{dt}$ and $\frac{d\Theta}{dt}$ for the LMC are consistent with zero within uncertainty (e.g. van der Marel and Kallivayalil 2014), and thus for simplicity we assume these are zero for calculations

throughout the thesis.

$$\begin{pmatrix} V_1 \\ V_2 \\ V_3 \end{pmatrix}_{\rm pn} = \frac{D_0 \sin(\rho)}{\cos(i)\cos(\rho) - \sin(i)\sin(\rho)\sin(\phi - \theta_{\rm LON})} \times \begin{pmatrix} \frac{di}{dt}\sin(\phi - \theta_{\rm LON})\left[\cos(i)\cos(\rho) - \sin(i)\sin(\rho)\sin(\phi - \theta_{\rm LON})\right] \\ \frac{di}{dt}\sin(\phi - \theta_{\rm LON})\left[-\cos(i)\sin(\rho) - \sin(i)\cos(\rho)\sin(\phi - \theta_{\rm LON})\right] \\ \frac{di}{dt}\sin(\phi - \theta_{\rm LON})\left[\sin(i)\cos(\phi - \theta_{\rm LON})\right] + \frac{d\Theta}{dt}\cos(i) \end{pmatrix} \tag{2.16}$$

Having calculated these contributions, and the total velocity of the star, a simple subtraction thus yields its intrinsic motion. However, in this form these velocities are still relative to the plane of the sky. We must now calculate the velocities (and the position of the star) relative to the plane of the LMC disk, as defined in §2.2. The Cartesian coordinates of the star in the plane of the disk are given by Eq. 2.17 (Eq. 7 in vdM01).

$$\begin{aligned} x' &= D\sin(\rho)\cos(\phi - \theta_{\rm LON}) \\ y' &= D\left[\sin(\rho)\cos(i)\sin(\phi - \theta_{\rm LON}) + \cos(\rho)\sin(i)\right] - D_0\sin(i) \\ z' &= D\left[\sin(\rho)\sin(i)\sin(\phi - \theta_{\rm LON}) - \cos(\rho)\cos(i)\right] + D_0\cos(i) \end{aligned} \tag{2.17}$$

The intrinsic velocity of the star in the plane of the disk is given by Eq. 2.18 (the inverse of Eq. 5 in vdM02):

$$\begin{pmatrix} V_{x'} \\ V_{y'} \\ V_{z'} \end{pmatrix}_{\rm int} = \begin{pmatrix} \sin(\rho)\cos(\phi - \theta_{\rm LON}) \\ \sin(\phi - \theta_{\rm LON})\cos(i)\sin(\rho) + \sin(i)\cos(\rho) \\ \sin(\phi - \theta_{\rm LON})\sin(i)\sin(\rho) - \cos(i)\cos(\rho) \end{pmatrix} \tag{2.18}$$
$$\begin{pmatrix} \cos(\rho)\cos(\phi - \theta_{\rm LON}) & -\sin(\phi - \theta_{\rm LON}) \\ \sin(\phi - \theta_{\rm LON})\cos(i)\cos(\rho) - \sin(i)\sin(\rho) & \cos(\phi - \theta_{\rm LON})\cos(i) \\ \sin(\phi - \theta_{\rm LON})\sin(i)\cos(\rho) + \cos(i)\sin(\rho) & \sin(i)\cos(\phi - \theta_{\rm LON}) \end{pmatrix} \times \begin{pmatrix} V_1 \\ V_2 \\ V_3 \end{pmatrix}_{\rm int}$$

Whilst this gives the location and velocity of the star relative to the Cartesian disk plane, it is most informative to convert these to a cylindrical coordinate system, centred at the LMC COM and aligned with the $z' = 0$ plane, as in Fig. 2.7.

In this coordinate system, the z' position and velocity of the star is identical to that

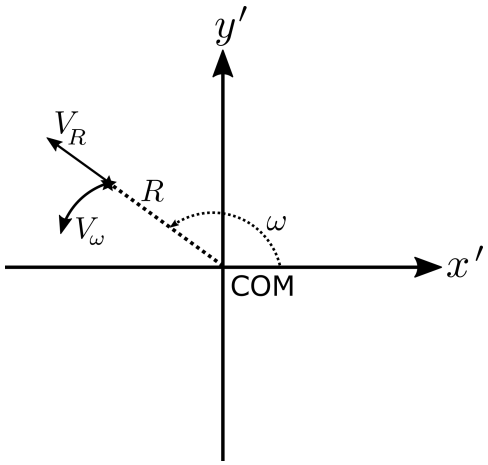

Figure 2.7: Projected view of the disk plane coordinate system, centered on the LMC COM. The z'-axis (not shown) points vertically out of the page. All quantities are in the plane of the page (i.e. the plane of the disk). The position of a star at position (x', y') is defined by the distance R – the distance in the plane of the disk between the star and the LMC COM – and the angle ω, measured anticlockwise from the positive x'-axis. The velocity of the tracer can similarly be decomposed into components in these two directions, V_R and V_ω.

of the Cartesian disk plane. However, the position of the star in the disk plane is now defined by the polar coordinates R, the *in-plane* radial distance of the star from the LMC COM, and ω, which describes its direction from the LMC COM as measured anticlockwise from the positive x'-axis. R is defined such that it is always positive. Eqs. 2.19-2.20 give the transformations from the Cartesian disk-plane coordinates to the polar disk-plane coordinates.

$$R = \sqrt{(x')^2 + (y')^2} \tag{2.19}$$

$$\begin{aligned} \sin(\omega) &= \frac{y'}{\sqrt{(y')^2 + (x')^2}} \\ \cos(\omega) &= \frac{x'}{\sqrt{(y')^2 + (x')^2}} \end{aligned} \tag{2.20}$$

$$\omega = \texttt{convtoangle}\left[\sin(\omega), \cos(\omega)\right]$$

Note that R is the in-plane radial distance; the total distance of a tracer from the LMC COM (r) must also account for the out-of-plane distance z', and is given by Eq. 2.21.

$$\begin{aligned} r &= \sqrt{(x')^2 + (y')^2 + (z')^2} \\ &= \sqrt{R^2 + (z')^2} \end{aligned} \tag{2.21}$$

Similarly, the velocity of the star in the disk plane is decomposed into two orthogonal velocities in the local directions of R and ω. V_ω describes rotation in the disk plane, and V_R describes the in-plane radial motion. A positive V_R indicates motion radially outward from the LMC COM, while a positive V_ω indicates anticlockwise rotation in the disk plane. The transformation between the Cartesian $V_{x',\mathrm{int}}$, $V_{y',\mathrm{int}}$ velocities and these orthogonal polar velocities are given in Eqs. 2.22-2.23.

$$V_R = \frac{x' \times V_{x',\mathrm{int}} + y' \times V_{y',\mathrm{int}}}{R} \tag{2.22}$$

$$V_\omega = \frac{x' \times V_{y',\mathrm{int}} - y' \times V_{x',\mathrm{int}}}{R} \tag{2.23}$$

It is important to note that the measured azimuthal velocity V_ω is different to the velocity of a tracer on a circular orbit in the equatorial plane of the disk (V_{circ}) due to the effects of asymmetric drift. Eq. 2.24 (taken from vdM02) provides the conversion between V_ω and V_{circ}, where R_d is the exponential scale length of the LMC disk (~1.5 kpc: van der Marel 2001), and σ_{LOS} is the measured LOS velocity dispersion in the disk.

$$V_{\mathrm{circ}}^2 = V_\omega^2 + \frac{R}{R_d}\sigma_{\mathrm{LOS}}^2 \tag{2.24}$$

With this final transformation, we now have the position and velocity of the stellar tracer in a useful form for analysis. However, for simplicity, in the following chapters we adopt shorthand variables to represent these quantities: Table 2.3 outlines the quantities of interest and their representation in the subsequent chapters.

It is also useful to define coordinate systems which allow the plotting of these quantities as a function of on-sky position relative to the center of the LMC. There are multiple ways to project the plane of the sky onto a flat plane suitable for this purpose, but in this thesis only two are used. The first is an orthographic projection, defined by Eq. 2.25, taken from

Table 2.3: Useful quantities and their representations in the subsequent chapters of this thesis.

Representation	Value	Description
V_θ	$-V_\omega$	Rotational velocity in the disk plane, with a positive value indicating clockwise rotation (i.e. in the same sense as the LMC).
V_r	V_R	In-plane radial velocity, with a positive value indication motion radially outward from the LMC COM.
V_z	$V_{z',\mathrm{int}}$	Out-of-plane velocity perpendicular to the disk plane. A positive value indicates motion in a direction predominantly toward the observer.
R	R	In-plane radial distance from the LMC COM.
z	z'	Out-of-plane distance of a tracer from the disk plane.
r	r	Total (radial) distance from the LMC COM.

Gaia Collaboration et al. (2018c):

$$\begin{aligned} X &= \cos(\delta)\sin(\alpha-\alpha_0) \\ Y &= \sin(\delta)\cos(\delta_0) - \cos(\delta)\sin(\delta_0)\cos(\alpha-\alpha_0) \end{aligned} \tag{2.25}$$

These coordinates are very similar to the Cartesian x, y, z coordinates which are used to describe the plane of the sky in the above framework, but do not require knowledge of the distance to a given tracer.

An alternate system is a tangent-plane (gnomonic) projection, defined by Eq. 2.26.

$$\begin{aligned} \xi &= \frac{\cos(\delta)\sin(\alpha-\alpha_0)}{\sin(\delta)\sin(\delta_0)+\cos(\delta)\cos(\delta_0)\cos(\alpha-\alpha_0)} \\ \eta &= \frac{\sin(\delta)\cos(\delta_0)-\cos(\delta)\sin(\delta_0)\cos(\alpha-\alpha_0)}{\sin(\delta)\sin(\delta_0)+\cos(\delta)\cos(\delta_0)\cos(\alpha-\alpha_0)} \end{aligned} \tag{2.26}$$

At small on-sky radii from the LMC COM, the X, Y and ξ, η coordinates are negigibly different. More significant differences are observed at larger on-sky radii.

Chapter 3

The Magellanic Edges Survey

> Evidence is everything. Without it, you have nothing.
>
> Mitsurugi Reiji

This chapter is published as **L. R. Cullinane**, A. D. Mackey, G. S. Da Costa, S. E. Koposov, V. Belokurov, D. Erkal, A. Koch, A. Kunder and D. M. Nataf, 2020. *The Magellanic Edges Survey I: Description and first results.* MNRAS, 497, 3055. The paper is reproduced here in full with minor formatting changes to make it consistent with the rest of the work in this thesis.

3.1 Abstract

We present an overview of, and first science results from, the Magellanic Edges Survey (MagES), an ongoing spectroscopic survey mapping the kinematics of red clump and red giant branch stars in the highly substructured periphery of the Magellanic Clouds. In conjunction with Gaia astrometry, MagES yields a sample of ~7000 stars with individual 3D velocities that probes larger galactocentric radii than most previous studies. We outline our target selection, observation strategy, data reduction and analysis procedures, and present results for two fields in the northern outskirts (>10° on-sky from the centre) of the Large Magellanic Cloud (LMC). One field, located in the vicinity of an arm-like overdensity, displays apparent signatures of perturbation away from an equilibrium disk model. This includes a large radial velocity dispersion in the LMC disk plane, and an

asymmetric line-of-sight velocity distribution indicative of motions vertically out of the disk plane for some stars. The second field reveals 3D kinematics consistent with an equilibrium disk, and yields $V_{\rm circ}$ = 87.7 ± 8.0 km s^{-1} at a radial distance of ~10.5 kpc from the LMC centre. This leads to an enclosed mass estimate for the LMC at this radius of $(1.8 \pm 0.3) \times 10^{10}$ M$_\odot$.

3.2 Introduction

The Large and Small Magellanic Clouds (LMC/SMC) are of fundamental importance in numerous areas of astronomy. The LMC, as the most massive Milky Way (MW) satellite – with recent estimates of its total mass exceeding 10^{11} M$_\odot$ (e.g. Kallivayalil et al. 2013; Peñarrubia et al. 2016; Shao et al. 2018; Erkal et al. 2019) – has significant effects on our Galaxy. For example, it can induce warps in the MW disk (Laporte et al. 2018a), generate overdensities in the MW dark matter halo (Garavito-Camargo et al. 2019; Petersen and Peñarrubia 2020; Erkal et al. 2020), perturb the orbits of smaller satellites and stellar streams (Koposov et al. 2019; Erkal et al. 2019; Patel et al. 2020), and has likely brought with it several dwarf satellites of its own (e.g. Bechtol et al. 2015; Kallivayalil et al. 2018; Erkal and Belokurov 2020). The Clouds are also the closest pair of interacting dwarf galaxies, at distances of 50 kpc (Pietrzyński et al. 2019) and 60 kpc (Graczyk et al. 2013) for the LMC and SMC respectively. This makes them ideally situated for a detailed study of the influence of interactions on galaxy evolution. The SMC in particular is significantly distorted, with a line of sight depth of up to 20 kpc (e.g. Crowl et al. 2001; Nidever et al. 2013; Ripepi et al. 2017) and an asymmetric, irregular morphology (e.g. Subramanian and Subramaniam 2012; El Youssoufi et al. 2019), both of which encode valuable information about its extensive interaction history.

It is evident that having precise information on the masses and orbits of the Clouds, as well as their interaction and star formation histories, is important for our understanding of both the local and more distant universe. In order to obtain information on these topics, the Clouds have been the focus of numerous surveys, with efforts intensifying as the availability of instruments able to survey quickly the large on-sky area of the Clouds increases. One example is the Dark Energy Camera (DECam; Flaugher et al. 2015), which is situated on the 4 m Blanco Telescope at the Cerro Tololo Inter-American Observatory in Chile, and has a 3 square degree field of view. Several surveys including the Survey of the Magellanic Stellar History (SMASH; Nidever et al. 2017), and the Magellanic SatelLites Survey (MagLiteS; Drlica-Wagner et al. 2016) have utilised DECam to obtain deep multi-band photometry across the Magellanic system. In combination with DECam photometry

from the Dark Energy Survey (DES; Abbott et al. 2018), and additional imaging from Mackey et al. (2018), this has provided an almost complete photometric picture of the Clouds and their surrounds (Mackey et al. in prep).

A key result from these surveys is the discovery of a wealth of low-surface-brightness substructure across the periphery of the Clouds (see e.g. Mackey et al. 2016; Belokurov and Koposov 2016; Mackey et al. 2018; Nidever et al. 2019); clear evidence of tidal interaction between the two Clouds, and/or the Clouds and the Milky Way. However, in order to piece together precise details of the interactions forming these features, kinematic information for stars in the substructures and across the Clouds, which is not provided by photometric surveys, is needed.

Spectroscopic surveys have long been used to characterise line-of-sight kinematics in the Clouds, though these have predominantly targeted stars (or star clusters) in the interior, rather than the outskirts, of the Clouds. Studies of the LMC have largely focussed on its internal rotation, with older tracer populations such as carbon stars (e.g. Kunkel et al. 1997; van der Marel et al. 2002), red giant branch stars (RGB: e.g. Zhao et al. 2003; Cole et al. 2005 and many others), and star clusters (e.g. Schommer et al. 1992; Grocholski et al. 2006) found to have larger velocity dispersions compared to younger populations such as red supergiants (Olsen and Massey 2007). Even within the RGB population, metal-poor (and, by extension, older) stars are found to have increased dispersions relative to more metal-rich stars (e.g. Cole et al. 2005; Carrera et al. 2011). Some studies have also found potential evidence for a high-dispersion halo population (Minniti 2003; Borissova et al. 2004; Munoz et al. 2006; Majewski et al. 2008) around the LMC.

In contrast to the relatively ordered motion within the LMC, studies of the SMC reveal more complex, disturbed kinematics. Both younger (Evans et al. 2015) and older populations (e.g. Harris and Zaritsky 2006; Parisi et al. 2009; De Leo et al. 2020 and many others) have large velocity dispersions and spatial velocity gradients indicative of the SMC being disrupted by the LMC (though note Dobbie et al. 2014a also find some evidence for coherent rotation within the SMC). SMC debris has been found in not only the bridge region between the Clouds (e.g. Carrera et al. 2017), but also at large distances from the Clouds (Navarrete et al. 2019), and even within the LMC itself (Olsen et al. 2011).

In addition to kinematic studies, spectroscopic measurements of the CaII triplet equivalent width (pioneered by Olszewski et al. 1991 and Armandroff and Da Costa 1991) have often been used to obtain metallicity estimates for RGB stars in the Clouds. Metallicity gradients as a function of galactocentric radius are found in both Clouds, with median [Fe/H] abundances decreasing from around -0.5 in the central ($\leq$ 6kpc) LMC disk to

around −1 further out (e.g. Carrera et al. 2011, 2008b). In the more metal-poor SMC, [Fe/H] abundances decrease from −1 in the central ($\leq 2°$) regions, to approx. −1.5 further out (e.g. Dobbie et al. 2014b; Carrera et al. 2008b; but see also Cioni 2009).

While spectroscopic studies are useful, measuring line-of-sight kinematics alone is insufficient to constrain the full 3D velocity field of the Clouds (see e.g. section 3 of van der Marel et al. 2002). This is particularly relevant when considering distant substructures, as full 3D kinematic information is required in order to distinguish between different formation mechanisms for the observed stellar substructures (see e.g. Mackey et al. 2016, 2018; Besla et al. 2016). In this respect, Gaia DR2 (Gaia Collaboration et al. 2018b) has been a boon, providing proper motion measurements down to red clump magnitudes ($G \lesssim 19$) in both Clouds. This has allowed substructures to be kinematically traced out to 25° from the centre of the Clouds (e.g. Belokurov and Erkal 2019; Belokurov et al. 2017), and detailed analyses of internal LMC dynamics based on proper motions (Gaia Collaboration et al. 2018c; Vasiliev 2018; Wan et al. 2020) to be performed. However, the Clouds are sufficiently distant that the Gaia spectrograph does not reach the faint magnitudes required to provide line-of-sight velocities for the old stellar populations in the Clouds that comprise the peripheral substructures.

As such, to date, there have been no large scale studies of 3D kinematics in the outskirts of the Clouds. The Magellanic Edges Survey (MagES) is designed to fill this gap. The core aim of the survey is to obtain spectra for large numbers of red clump and red giant branch stars that trace substructures across the Magellanic periphery, in order to derive line-of-sight velocities that can be used in conjunction with Gaia data to obtain the full 3D kinematic information necessary to unravel the interaction history of the Clouds. To do so, it utilises observations with the 2dF fibre positioner (Lewis et al. 2002) coupled with the dual-arm AAOmega spectrograph (Sharp et al. 2006) at the 3.9 m Anglo–Australian Telescope (AAT) to obtain simultaneous spectra for ~370 stars across each ~2° diameter field. The survey began in 2015, with observations taken for several nights per year to date (details provided in Table 3.1).

In this paper, we present the detailed methodology of MagES, and our first science results. §3.3 presents the survey fields and target selection procedure. §3.4 describes the reduction and data validation processes. §3.5 discusses the method used to isolate Magellanic stars and extract aggregate field kinematics. We report our first science results, a determination of the LMC disk motion using distant tracers, in §3.6, followed by our conclusions and future plans for MagES in §3.7.

3.3 Survey Design and Target Selection

As MagES is intended to shed light on interactions between the Clouds – a major signature of which is the formation tidal disturbances in the periphery – MagES fields largely target overdense regions and substructures in the outskirts of the Clouds. Over time, as the photometric coverage of the Magellanic periphery has increased, the positioning of MagES fields has evolved to continually target the most conspicuous features. To date, twenty-six 2dF fields have been observed; these are detailed in Table 3.1, with Fig. 3.1 presenting a visual representation of the targeted fields overplotted on a stellar density map of red clump stars across the Clouds.

The earliest observed fields target a large arm-like feature to the north of the LMC first discussed in Mackey et al. (2016). Subsequent runs have focussed on spoke-like features to the south of the LMC disk (discussed in Mackey et al. 2018), and extended red clump features surrounding the SMC (e.g. Mackey et al. 2018; Pieres et al. 2017). The most recent observations target another apparent tidal feature extending from the SMC which curves around the southern LMC, discussed in Belokurov and Erkal (2019), and thought to be a counterpoint to the northern arm feature.

3.3.1 Target Selection

MagES primarily targets red clump stars, as this region in colour-magnitude space has high contrast for Magellanic stars relative to background contaminants (see Fig. 3.2). Whilst even stronger contrast exists for the Magellanic main sequence turn-off population, these stars are ~2.5 magnitudes fainter than the red clump, and as such would require prohibitively long integration times to reach sufficient S/N.

In addition to the field placement evolving, the target selection procedure has also changed as new data have become available. Consequently, there are three distinct target selection procedures that have been applied during different phases of the survey:

1. Fields within the DES footprint, observed prior to the release of Gaia DR2 (2015–2016). These are denoted as **D** fields;

2. Fields outside the DES footprint, observed prior to the release of Gaia DR2 (2017); these are denoted as **M** fields; and

3. Fields observed post-Gaia DR2 release (2018+); these are denoted as **G** fields.

The three procedures are detailed in the following sections; Table 3.1 provides clas-

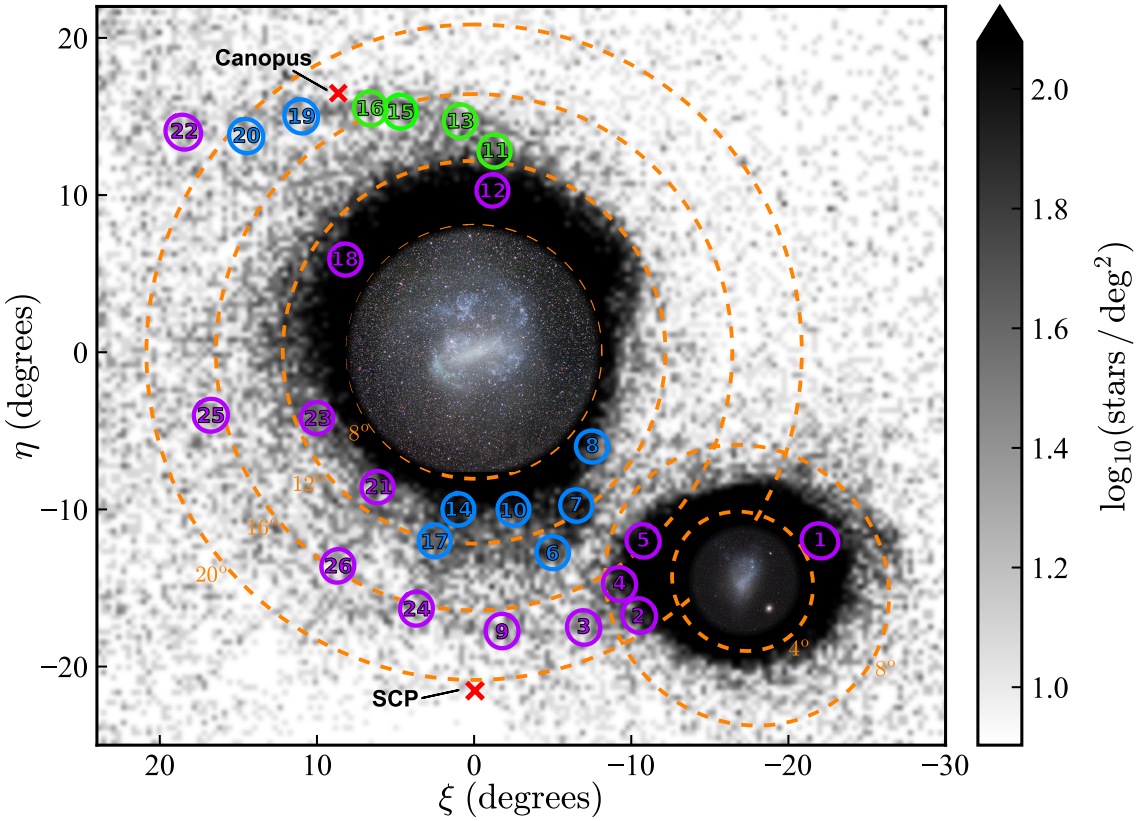

Figure 3.1: Location of observed 2dF fields across the Magellanic system; fields are predominantly located on substructures or overdensities in the periphery of the Clouds. Green circles indicate **D** fields, blue circles indicate **M** fields, and purple circles indicate **G** fields. Fields 12 and 18 are discussed in detail in this paper. The background image shows the log density of red clump and red giant stars per square degree. These were selected from Gaia DR2 according to the process outlined by Belokurov and Erkal (2019); repeated here in §3.3.1.3. On this map, north is up and east is to the left; (η, ξ) are coordinates in a tangent-plane projection centred on the LMC ($\alpha_0 = 82.25°$, $\delta_0 = -69.5°$). Orange dashed circles mark angular separations of 8°, 12°, 16°, and 20° from the LMC centre, as well as 4° and 8° from the SMC centre. Within 8° of the LMC and 4° of the SMC, wide-field optical images are displayed. The red x-signs mark the locations of Canopus (the second brightest star in the sky, which limits field placement to avoid spectral contamination from scattered light) and the south celestial pole (which limits field placement due to telescope pointing limits).

Table 3.1: 2dF fields observed as of Jan 2020. Columns give the field number; location of the field centre as RA(α), DEC(δ) in J2000.0, and ξ, η as plotted in Fig. 3.1; UT dates when the field was observed; total field exposure time; and the on-sky distance of the field from the centre of the LMC or SMC (whichever is closer, indicated by L or S respectively). Fields are numbered strictly in order of increasing right ascension across the entire survey. The fields are grouped by their classification into three categories based on the target selection procedure used (see §3.3): **D** fields are within the DES footprint and observed prior to Gaia DR2, **M** fields are outside the DES footprint and observed prior to Gaia DR2, and **G** fields are observed post Gaia DR2. Within each grouping the fields are listed in order of increasing right ascension.

Field	RA	DEC	ξ	η	Dates observed	Total exposure time (s)	Galactocentric distance (°) from LMC/SMC
					D fields		
11	05 19 42.63	−56 53 06.88	−1.30	12.80	19 Aug 2015[1], 20 Aug 2015, 21 Aug 2015, 4 Feb 2016, 5 Feb 2016	27000	12.7 (L)
13	05 35 05.69	−55 06 03.11	0.90	14.70	19 Aug 2015[1], 1 Feb 2016	18380	14.6 (L)
15	06 00 07.40	−54 17 53.14	4.70	15.30	20 Aug 2015	8700	16.0 (L)
16	06 12 13.07	−53 52 32.45	6.60	15.50	3 Feb 2016, 4 Feb 2016, 5 Feb 2016	16200	16.8 (L)
					M fields		
6	03 22 33.00	−80 40 55.00	−5.00	−12.75	14 Dec 2017, 1 Oct 2018	12600	13.1 (L)
7	03 26 04.00	−77 26 18.00	−6.50	−9.75	1 Dec 2017	10800	11.0 (L)
8	03 39 15.00	−73 43 48.00	−7.50	−6.00	15 Dec 2017, 16 Dec 2017	10800	8.8 (L)
10	04 36 23.00	−79 07 17.00	−2.50	−10.00	12 Dec 2017	9000	9.9 (L)
14	05 50 22.00	−79 21 18.00	1.00	−10.00	13 Dec 2017	10800	10.0 (L)
17	06 32 16.00	−80 59 36.00	2.50	−12.00	30 Sep 2018	12600	12.2 (L)
19	06 40 29.00	−53 29 04.00	11.00	15.00	12 Dec 2017	10800	18.6 (L)
20	07 04 01.00	−53 37 01.00	14.50	13.75	14 Dec 2017	12600	19.9 (L)
					G fields		
1	00 56 26.00	−67 43 32.00	−22.00	−12.00	30 Sep 2018, 1 Oct 2018	10800	5.4 (S)

to be continued on the next page

Table 3.1: (continued from previous page)

Field	RA	DEC	ξ	η	Dates observed	Total exposure time (s)	Galactocentric distance (°) from LMC/SMC
2	00 59 30.00	−79 10 57.00	−10.50	−16.75	2 Oct 2018	10800	6.1 (S)
3	01 20 00.00	−82 30 00.00	−6.97	−17.51	3 Mar 2019, 4 Mar 2019, 7 Mar 2019	11600	9.5 (S)
4	01 45 11.00	−79 15 22.00	−9.25	−14.75	30 Sep 2018	12600	6.9 (S)
5	02 06 32.00	−76 29 09.00	−10.75	−12.00	1 Oct 2018, 2 Oct 2018	16200	6.0(S)
9	03 40 00.00	−86 17 13.12	−1.78	−17.73	5 Mar 2019, 6 Mar 2019, 8 Mar 2019	14410	17.1 (L)
12	05 20 00.00	−59 18 00.00	−1.17	10.29	27 Feb 2019, 28 Feb 2019	10800	10.3 (L)
18	06 40 00.00	−62 30 00.00	8.19	5.89	27 Feb 2019, 28 Feb 2019	12200	10.7 (L)
21	07 17 12.00	−76 36 00.00	6.14	−8.58	2 Mar 2019, 5 Mar 2019	14600	10.9 (L)
22	07 25 34.00	−52 04 52.00	18.50	14.00	1 Oct 2018, 2 Oct 2018	9000	22.8 (L)
23	07 36 00.00	−71 00 00.00	9.99	−4.19	6 Mar 2019, 7 Mar 2019	14400	11.4 (L)
24	07 58 48.00	−84 12 00.00	3.67	−16.31	4 Mar 2019	9300	16.4 (L)
25	08 32 00.00	−67 00 00.00	16.74	−4.01	3 Mar 2019	11300	17.5 (L)
26	08 48 00.00	−79 00 00.00	8.67	−13.59	1 Mar 2019	9000	16.1 (L)

[1] on 19 Aug 2015, these pilot fields were observed with only the red arm of AAOmega; subsequent observations were taken in the typical setup with both arms of the spectrograph, as discussed in §3.4.1.

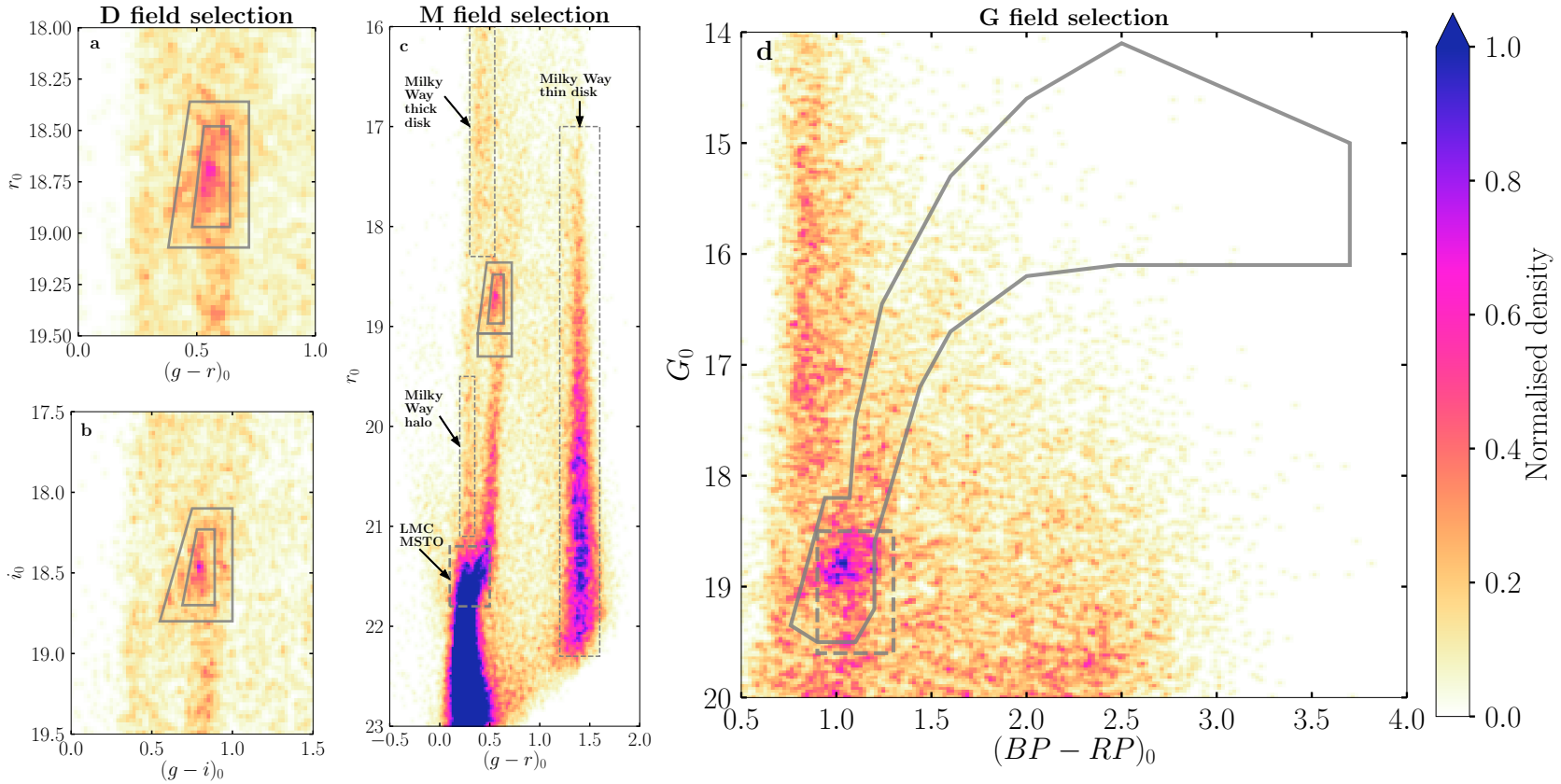

Figure 3.2: Colour-magnitude selection boxes (grey) used in target selection for each field type. These are overlaid on observed Hess diagrams of field 12, located in the northern LMC disk; the Magellanic main sequence turnoff and regions of strong Milky Way contamination are marked in panel *c*. The selection boxes are designed to select red clump stars, and in the case of **G** fields, RGB stars also. **D** fields (left panels) use joint selection from $(r_0, (g-r)_0)$ (panel *a*) and $(i_0, (g-i)_0)$ (panel *b*) CMDs; **M** fields (centre panel *c*) employ $(r_0, (g-r)_0)$ photometry only; **G** fields (right panel *d*) employ only Gaia $(G_0, (G_{\rm BP}-G_{\rm RP})_0)$ photometry, even when DES photometry exists in these regions; cuts are also placed in proper motion space as described in §3.3.1.3.

sification of each field into one of these three groups, in addition to the location of the field's centre, dates observed and total exposure time. **D** fields are listed first, followed by **M** and **G** fields; this is in approximately chronological order of observations. Within each grouping, fields are listed in order of increasing right ascension.

Once a list of possible targets is compiled for each field, they are assigned various priorities between 1 and 9 (with 9 being the highest). Higher priorities are given to stars most likely to be of Magellanic origin, though how this is defined varies based on the specific selection procedure, and is discussed in the following sections. The 2dF allocation software CONFIGURE (Miszalski et al. 2006) uses the priorities to inform fibre allocation: higher ranked targets are more likely to be observed. By design, the selection procedure is such that there are almost always more possible targets than available 2dF fibres – as such, prioritisation strongly influences which stars are observed in any given field.

All three procedures involve target selection and prioritisation based on cuts in extinction-corrected colour-magnitude space. Where DECam photometry is used, the de-reddening is done using Schlegel et al. (1998) dust maps and updated coefficients from Schlafly and Finkbeiner (2011). Where Gaia DR2 photometry is used, the correction uses the procedure described in Belokurov and Erkal (2019): the first two terms of Eq. 1 from Gaia Collaboration et al. (2018a) are used in conjunction with the Schlegel et al. (1998) dust maps. No correction is made for reddening internal to the Clouds as this is not expected to be significant in the low-density peripheral regions targeted by MagES (cf. Choi et al. 2018b).

3.3.1.1 D Fields

Initial fields observed by MagES were located entirely within the photometric footprint of DES year one (as reduced by Koposov et al. 2015); target selection is thus based on $(r_0, (g-r)_0)$ and $(i_0, (g-i)_0)$ colour magnitude diagrams. Within each colour magnitude diagram, an inner and outer box are defined, centred on the red clump, as in panels *a* and *b* of Fig. 3.2. Priorities for each star are defined based on their location on the two diagrams: stars in the inner box in both diagrams are given the highest priority, with decreasing priority given to stars located in the outer boxes, or located within box boundaries on only one of the diagrams.

Note that the boundaries of selection boxes for **D** fields are defined based on photometry of the northern disk of the LMC, where the position of the red clump in colour-magnitude space is well defined; the same box is then applied to fields covering fainter substructures. Selection boxes are designed to be sufficiently generous that small changes

in CMD position of the red clump (due to, for example, field-to-field differences in line-of-sight distance), do not affect target selection.

3.3.1.2 M fields

Fields designated **M** are located outside of the DES survey footprint, and are selected based on g- and r-band DECam photometry obtained by Mackey et al. (2018). We refer interested readers to Koposov et al. (2018) for details of the data reduction and photometric analysis. Three boxes are defined on the $(r_0, (g-r)_0)$ colour magnitude diagram, as in panel c of Fig. 3.2: an inner and outer box surrounding the red clump, similar to those used for the **D** fields, as well as a lower box designed to capture any faint red clump extension. As with **D** fields, these CMD boxes are defined based on photometry of the northern LMC disk. Highest priority is assigned to stars in the inner box; followed by the outer box. Stars in the third box are assigned lowest priority as, while useful, this region of the CMD has higher Milky Way contamination than the canonical red clump.

3.3.1.3 G Fields

Fields observed after the release of Gaia DR2 utilise these data exclusively in the selection procedure; even in regions where DECam photometry exists. Unlike previous selections, a combination of photometry and astrometry are used. Highest priority is given to stars that pass the selection procedure presented in Belokurov and Erkal (2019). This uses Gaia photometry to select red clump and RGB stars (see panel d of Fig. 3.2). **G** fields are the only fields to contain RGB stars, though these are few in number compared to red clump stars. In addition, parallax ($\varpi < 0.2$) and proper motion ($-0.6 < \mu_B$ (mas yr^{-1})< 1.4, $0.9 < \mu_L$ (mas yr^{-1})< 2.8)[4] cuts are applied to isolate Magellanic stars. Lower priority is given to stars within a slightly offset selection box surrounding the red clump, with the same parallax cut and more generous proper motion cuts ($-1.0 < \mu_\alpha$ (mas yr^{-1})< 4.0 and $-4.0 < \mu_\delta$(mas yr^{-1})< 4.0)[5] which increase the selection area in proper motion space by a factor of 25. This lower-priority selection is used when the number of target stars passing the initial, higher-priority selection criteria is significantly lower than the number of 2dF fibres available – while less efficient, we have confirmed additional Magellanic stars are captured through this second, less restrictive selection.

[4] L and B are Magellanic longitude and latitude respectively, as defined in Nidever et al. (2008). μ_L is the proper motion in the $L\cos(B)$ direction, such that it is perpendicular to μ_B.

[5] μ_α refers to proper motion in the α direction with the usual $\cos(\delta)$ correction, i.e. `PMRA` from the Gaia source catalogue.

3.4 Data Acquisition

3.4.1 Observations and Data Reduction

All observations were taken using the 2dF/AAOmega instrument on the AAT at Siding Spring Observatory. 2dF (Lewis et al. 2002) is a multi-object fibre positioner which allows for target placement within a two-degree field on the sky. It has a total of 400 fibres, of which ~365 are available for science targets (the remainder being dedicated to guide stars and sky observations, detailed later in this section). AAOmega (Sharp et al. 2006) is a dual beam optical spectrograph; for these observations, the light was split using the 580V dichroic (i.e. at 5800Å). On the blue arm, the 1500V grating was utilised, obtaining a spectral resolution of R~3700, and wavelength coverage of $4910 - 5615$Å[6]. This is designed to cover the 5167Å, 5172Å and 5183Å MgIb lines to provide precise line-of-sight (LOS) velocity estimates.

On the red arm, the 1700D grating was used, providing a resolution of R~10000 and wavelength coverage $8370 - 8790$Å[6]. This is designed to cover the 8498Å, 8542Å and 8662Å CaII triplet at sufficiently high resolution to both allow for an estimation of metallicity (as in e.g. Da Costa 2016), as well as provide a second LOS velocity estimate complementary to that obtained from the blue arm of the spectrograph.

In general, our survey strategy was to observe fields for between $10800 - 12600$ s, split into 1800 s exposures to avoid skyline saturation and mitigate cosmic ray contamination. This results in typical signal to noise (S/N) values of ~10 per pixel in both the red and blue data (at least in spectral regions not heavily contaminated by night sky emission; poor sky subtraction during the data reduction process degrades the S/N in some regions of the red spectra). In practice, total exposure times vary in accordance with observing conditions, with shorter exposures acceptable in very good conditions, but additional repeated exposures required when conditions were poor.

Fig. 3.3 shows histograms of "quality measure" (QM: an empirical S/N indicator covering spectral regions of interest, described further in §3.4.2) for both red and blue arms of the spectrograph in representative **M** and **G** fields. **D** fields have distributions comparable to **M** fields. Red clump stars have similar QM values in both red and blue spectra. In contrast, RGB stars (found only in **G** fields) have significantly higher QM values in the red spectra: this is the source of the second "bump" in the QM distribution in panel *d* of Fig. 3.3. As RGB stars are much redder than clump stars, this increase in QM is not prominent in the blue spectra.

[6] The design of AAOmega is such that the wavelength coverage varies between individual fibres; the quoted range includes only those wavelengths that are accessible in every fibre.

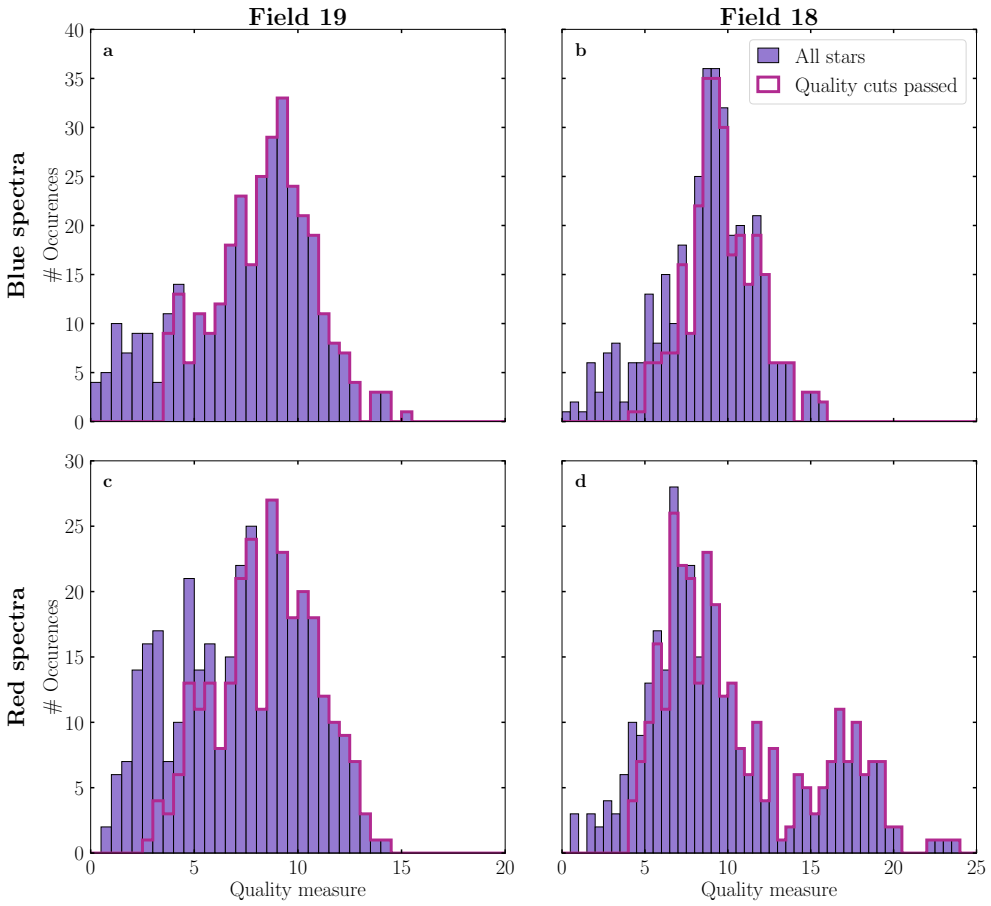

Figure 3.3: Typical "quality measure" (QM) distributions for blue (panels *a* and *b*) and red (panels *c* and *d*) spectra. Left panels show results for field 19, a typical **M** field, and right panels show results for field 18, a typical **G** field. Purple filled histograms show the distribution for all stars observed in a field (as discussed in §3.4.1); red unfilled histograms show the distribution after quality cuts are performed (as discussed in §3.4.2). Bright RGB stars (found only in **G** fields) have significantly higher QM values in the red than fainter red clump stars, but this difference is not present in blue spectra.

Data are reduced using the `2dFDR` pipeline (AAO Software Team 2015), which undertakes the subsequent steps. First, all observations are debiased using bias frames taken at the start of each night. Next, spectral traces are located with a fibre-flat field, taken immediately prior to each set of science exposures. These traces are used to extract the data for each fibre. The extracted spectra are then divided by corresponding normalised trace from the fibre-flat to correct for pixel-to-pixel variations along the CCD for each fibre. Wavelength calibration is performed using traces from an arc frame also obtained immediately prior to each set of science exposures, via a least-squares polynomial fit. A secondary wavelength calibration tweak, based on night sky emission features and utilising a lower-order polynomial fit, is also performed after the initial calibration.

Because the target stars are faint, the subtraction of signal from the night sky – both

continuum and line emission – is a crucial part of the reductions. To facilitate this, within each 2dF field, 25 dedicated fibres are used to measure the night-sky flux across the observed spectral range. Sky fibre locations are selected by CONFIGURE from a list of 150 possible locations in each field, which were cross-checked against the photometric catalogues available at the time of observation (DES or Gaia) to ensure no sources are located within a radius of 10 arcsec from the fibre position. During the reduction process, we discard any sky fibres where there are indications of non-sky signal present.

The sky-subtraction process must take into account fibre-to-fibre throughput variations; in `2dFDR`, the relative throughputs of each fibre are determined using night sky emission features. Several features are identified within each fibre, and the total flux within each feature measured. The median flux of the feature is taken across all dedicated sky fibres in the field; the ratio between this median, and the total flux of the feature measured in each target fibre, gives the relative throughput of the fibre. This procedure is repeated for several night sky emission features; the median throughput is used as the final value. In the blue spectra, as there is only a single strong night sky emission feature (at 5577Å), the throughput derived from this feature is used directly. The median sky spectrum, obtained from all sky fibres in each field, is then normalised by the relative fibre throughputs and subtracted from each fibre.

Finally, all science exposures for a given field on a given night are combined. However, in order to account for variations in data quality (caused by, for example, variable seeing) or exposure time differences between observations, the relative weight each exposure will contribute to the final combined frame must first be determined. This is calculated using the FRAMES flux weighting algorithm in `2dFDR`; which compares the total flux summed across each object spectrum to that expected (calculated by `2dFDR` based on the supplied object magnitude and the total exposure time across all exposures). The median offset between the observed and expected flux for all objects in a given exposure is calculated, and subsequently inverted and scaled such that the "best" exposure (i.e. with the smallest offset) is given a weight of unity, with shorter or poorer-quality exposures given commensurately reduced weights.

Once the relative weight of each exposure is determined, all exposures are combined into a single frame according to the following process in `2dFDR`. The weighted median value of each pixel is taken across all exposures to create an initial estimate of the combined frame. Each individual exposure is compared to this median estimate; if the value of any pixel in an individual frame exceeds the corresponding median pixel value by 10σ, that pixel is flagged as contaminated by a cosmic ray in the individual exposure. The final combined frame is calculated by taking the weighted mean of each pixel in each exposure,

excluding those flagged as contaminated by cosmic rays. In this way, pixel values where exposures are flagged as contaminated are effectively "filled-in" by the equivalent pixels in exposures which are not flagged as contaminated by cosmic rays. When a given field was observed over multiple nights, frames for each night were reduced separately, with LOS velocity estimates combined later (see §3.4.2).

Examples of typical reduced spectra are presented in Fig. 3.4. The faint target magnitudes, combined with the relatively low S/N of the spectra, preclude the determination of detailed abundance estimates for individual stars, with the exception of [Fe/H] as based on the CaII triplet (described in §3.5.4). However, the quality of the spectra is sufficient to derive LOS velocity estimates as described in §3.4.2.

3.4.2 LOS Velocity Determination

LOS velocity estimates for each star were obtained by cross-correlation of the spectra against velocity templates using the IRAF FXCOR routine. A synthetic template from the Munari et al. (2005) library, using stellar parameters appropriate for LMC red clump stars[7] and rebinned to the same dispersion as the observed spectra, was used for cross-correlation of the blue spectra. For the red spectra, observations of the star HD 160043 (a standard star observed as part of the program described in Da Costa and Coleman 2008, which used an identical setup to our observations) was used for cross-correlation. Only portions[8] of the entire observed spectrum were used for cross-correlation; these were selected to avoid regions with substantial night-sky residuals. The RVCORRECT routine was used to convert the obtained velocities to the heliocentric frame.

A number of quality cuts are subsequently performed to identify and eliminate any targets with poor or untrustworthy velocity measurements. Plots combining a bespoke "quality measure" (QM: defined as the ratio of median signal to standard deviation in a relatively flat region of the spectrum[8], after performing a single 3σ clip to remove any remaining night-sky residuals), velocity uncertainty and cross-correlation peak height (both as reported by FXCOR) are inspected to determine field-by-field thresholds on each of these parameters, for both red and blue spectra; non-static thresholds are required to account for variation in data quality over the course of the survey. The QM we describe is effectively an empirical signal-to-noise measurement across a truncated region of each spectrum – and is therefore different to analytical S/N ratios calculated for the spectra on a per-pixel or per-Angstron basis. Fig. 3.5 demonstrates an example of the cuts made for the spectra observed in field 20; a similar number of stars are retained for both red and

[7] T= 5000 K, $\log(g) = 2.5$, [Fe/H]= -0.5, $[\alpha/\mathrm{Fe}] = 0$.

[8] $5100 - 5400$Å for the blue spectra, and $8470 - 8740$Å for the red spectra.

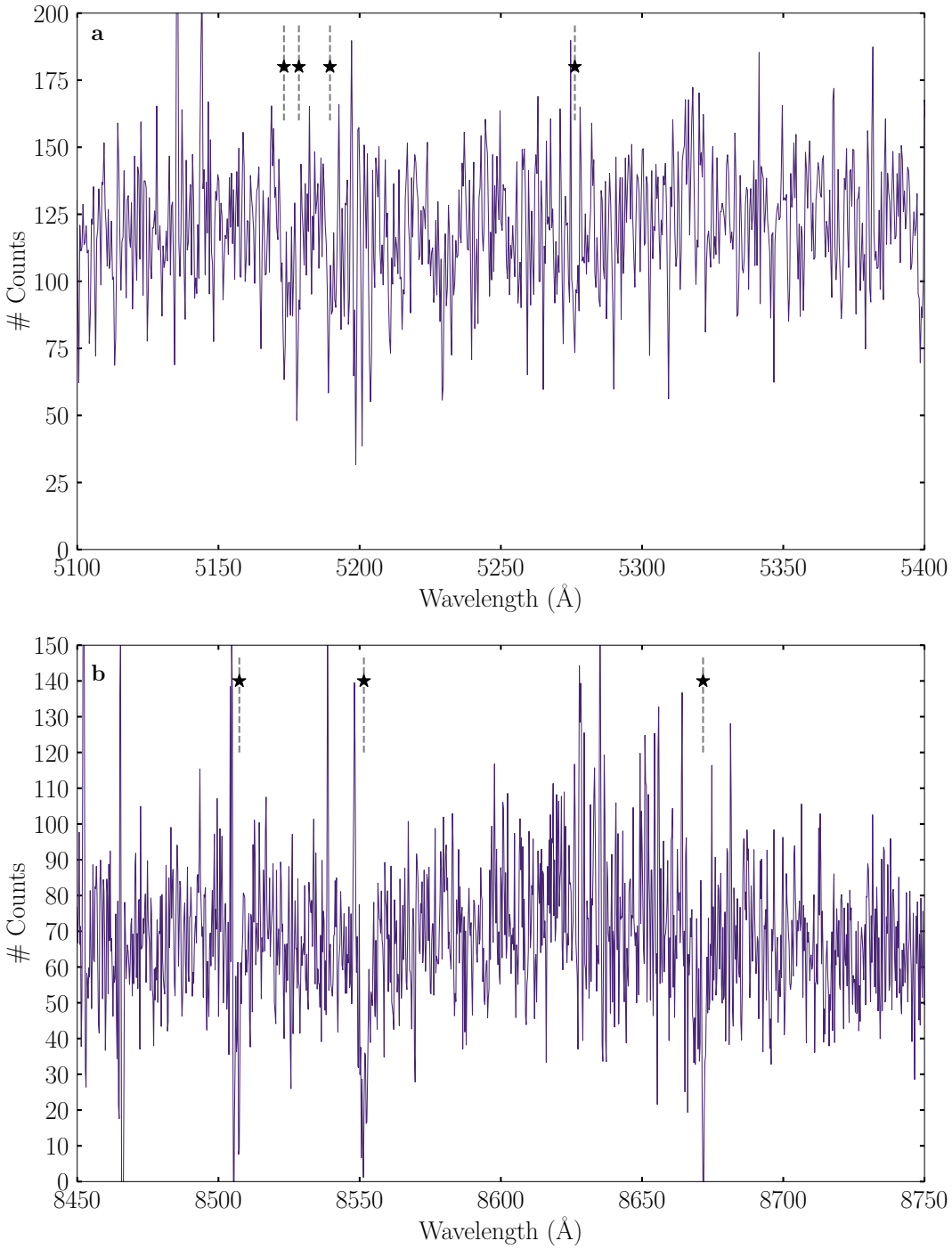

Figure 3.4: Typical reduced blue (panel *a*) and red (panel *b*) spectra. Panel a shows a star in field 19, with a heliocentric LOS velocity of ~344 km s^{-1}; MgIb lines (with rest wavelengths of 5167.3Å, 5172.6Å, and 5183.6Å) and a FeI/CaI blend (with rest wavelength 5270.2Å) are marked with stars and dashed grey lines. Panel b shows a star in field 18, with a heliocentric LOS velocity of ~334 km s^{-1}; the CaII triplet (with rest wavelengths of 8498Å, 8542Å, and 8662Å) is marked with stars and dashed grey lines. Clear sky subtraction residuals are apparent in both spectra. The relatively low S/N of the spectra allows for derivation of LOS velocity estimates, but precludes detailed elemental abundance analysis.

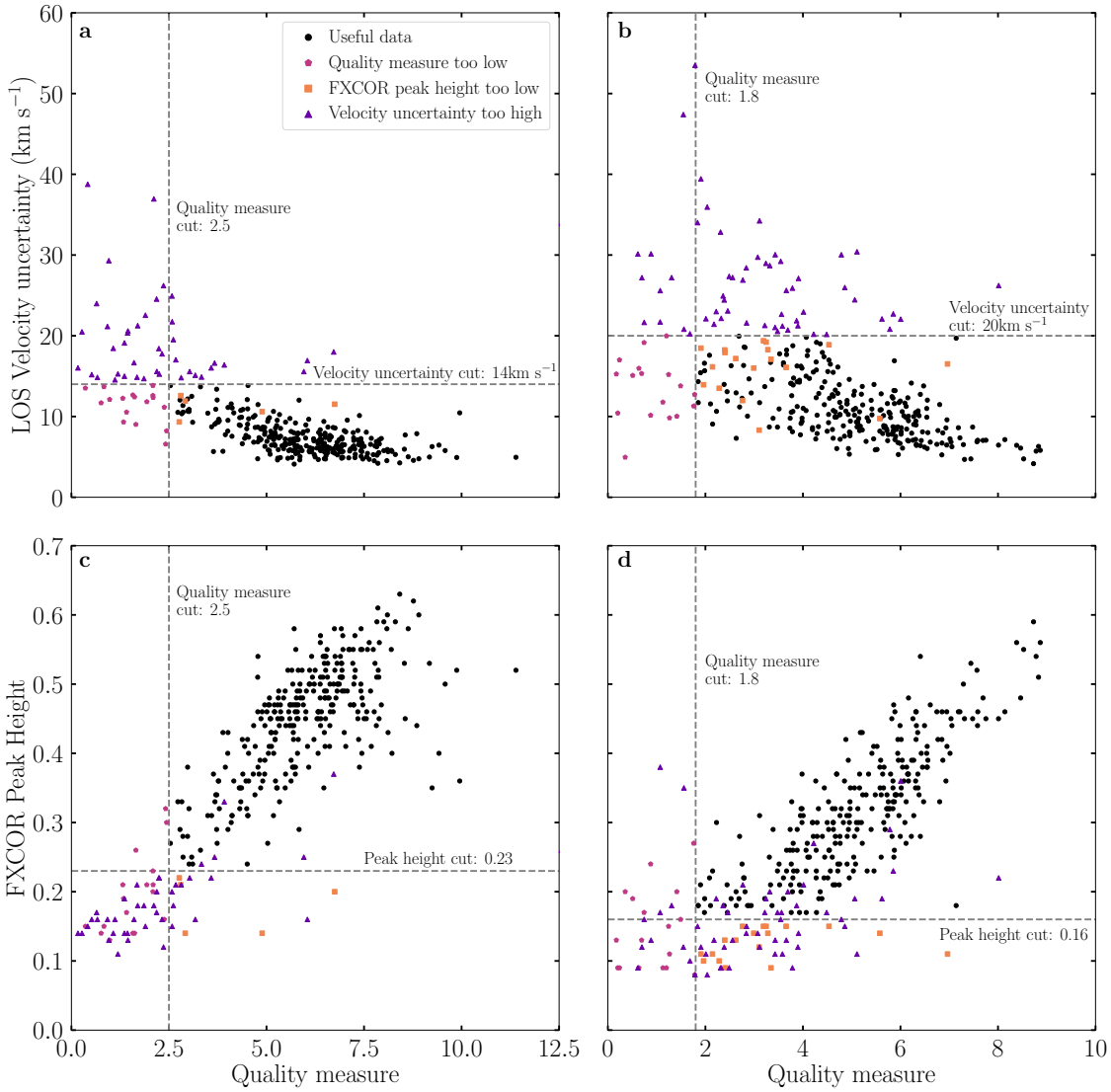

Figure 3.5: Quality control plots for field 20, showing "quality measure" vs. line of sight velocity uncertainty (top row) and "quality measure" vs. FXCOR cross-correlation peak height (bottom row), for blue (left column) and red (right column) spectra. Note that FXCOR peak height values are discrete, as this is reported by the software to only two decimal places. Stars passing quality cuts are marked in black. Stars that fail quality cuts are coloured according to the cut that is failed; where multiple cuts are failed, stars are coloured by the criterion which is failed by the largest value. Dashed lines indicate the values of cuts applied.

blue spectra, but the cut values applied are substantially different. Stars where at least one spectrum passes the quality cuts are retained for further analysis. Representative QM distributions for stars passing quality cuts are presented in Fig. 3.3: stars with low QM are preferentially removed by all quality cuts applied.

For stars where both red and blue spectra pass the quality cuts, LOS velocities obtained from the two spectra are compared. We confirm for each field that no systematic

offsets are observed, with the median velocity difference between the two associated velocities consistent with zero for all fields. Additionally, we calculate the standard deviation of the velocity difference distribution, and compare this to the median uncertainty in the difference (calculated as the quadrature sum of the uncertainties in both associated velocities). We find these are comparable for all fields, indicating the FXCOR velocity uncertainties are reflective of the true velocity uncertainty.

The average of the two derived velocities, weighted by the inverse of the velocity uncertainty (taken directly as the velocity error reported by FXCOR), is taken as the final LOS velocity, provided that the difference between the two individual velocities is less than 100 km s^{-1}. Stars where the difference in the two associated velocities exceeds 100 km s^{-1} are excluded from further analysis, as such large differences indicate a failure in the cross-correlation process. Typically <5 stars per field are excluded under this condition. Stars where the difference in the two associated velocities exceeds 50 km s^{-1} (which are also very few in number) are manually inspected; in every case, these stars have LOS velocity estimates that preclude them from being Magellanic, and are subsequently de-weighted in §3.5 such that they do not contribute to field aggregate properties. These large velocity differences are typically associated with either:

1. Unusually low signal, likely associated with small fibre misalignments (see Appendix A of Li et al. 2019 for a more detailed discussion) which, for the relatively red stars targeted in this survey, predominantly affects the blue spectrum; or, more commonly,

2. Poor skyline subtraction in the red spectrum, when prominent skylines overlap the 8498Å and 8542Å CaII lines and result in an incorrect velocity determination. Magellanic stars have LOS velocities that shift these CaII lines sufficiently far from the problematic skylines that this overlap occurs only for non-members.

For stars where only one associated spectrum passes the quality cuts, the LOS velocity derived from this spectrum is used directly as the final LOS velocity.

An additional step was applied to fields observed over multiple nights. When stars pass the aforementioned quality cuts on more than one night, the LOS velocities determined from each night are compared. Again, no systematic offsets are observed. The average of each derived velocity, weighted by the inverse of the velocity uncertainty, is taken as the final LOS velocity, provided that the difference between each of the individual velocities is less than 100 km s^{-1}. Stars where the difference in the two associated velocities exceeds 100 km s^{-1} are excluded from further analysis. Again, any stars where the difference in the two associated velocities exceeds 50 km s^{-1} are manually inspected; typically $10-20$ stars per field meet this condition. In every case, these stars have LOS velocity estimates that

preclude them from being Magellanic, and are subsequently de-weighted in §3.5 such that they do not contribute to field aggregate properties. We calculate the median velocity differences between stars observed on multiple nights, and find this is on the order of the median velocity uncertainty on each individual night, indicating the FXCOR velocity uncertainties are reflective of the true velocity uncertainty. When stars are observed over multiple nights, but only satisfy quality requirements on a single night, the LOS velocity derived from that night is used as the final LOS velocity.

The above process results in typical LOS velocity uncertainties of $5-10$ km s^{-1} per star in all observed fields. Velocity uncertainty distributions in each field do have tails to higher values, which result from stars where only single observations or spectra are analysed. The largest velocity uncertainty retained is 30 km s^{-1}; although, by design, such stars contribute very little information to the field aggregate properties described in §3.5.3.

3.4.3 Gaia cross-matching

In addition to LOS velocities, proper motions are required to obtain full 3D kinematics. To obtain these, we cross-match all MagES stars with heliocentric velocities against the Gaia DR2 catalogue (Gaia Collaboration et al. 2018b). A match radius of one arcsec is used; every star returns a single Gaia match under this condition.

The resulting sample is further filtered by requiring Gaia parameters `phot_bp_rp_excess_factor`<1.5 and `astrometric_excess_noise` (AEN)<1.0. These criteria act to remove any blended or extended sources, and unresolved binaries (see e.g. Iorio and Belokurov 2019), which may have erroneous proper motions or LOS velocities. While the AEN cut is more lenient than that used to select Magellanic stars in e.g. Vasiliev (2018), MagES fields are located in diffuse regions where blending/crowding is not expected to be significant, and most non-stellar sources or unresolved binaries are expected to be removed through the quality cuts already applied to the LOS velocities. This is supported by the fact that very few stars are removed by applying these criteria. In addition, we test alternate quality criteria (such as those in Arenou et al. 2018); doing so leaves our results essentially unchanged.

The median proper motion uncertainty, per component, is ~0.5 mas yr^{-1}, across all observed fields. As no cuts are applied to the sample based on proper motion uncertainties, some individual stars have significantly higher uncertainties (in the worst cases, up to 2 mas yr^{-1}). However, such stars are few in number, and contribute very little information to the aggregate field measurements described in §3.5.3.

The outcome of this overall process is a sample of ~7000 stars across twenty-six fields that have both line-of-sight velocities and proper motions. These include both true Magellanic stars, and some foreground contaminants (which are removed as described in §3.5). Note that no explicit parallax cuts are applied to remove contaminants at this stage. Any foreground stars with large parallaxes that survive the reduction process (for **D** and **M** fields; target selection in **G** fields precludes any stars with parallax > 0.2 mas yr^{-1}) have sufficiently different LOS and proper motions compared to other Magellanic stars that they are removed in §3.5.

3.5 Isolating Magellanic Stars

Though the target selection procedures outlined in Section 3.3 are designed to isolate candidate Magellanic stars, there remains some level of contamination from the Milky Way. This particularly affects **D** and **M** fields, which were observed prior to the release of Gaia DR2. An example is shown in Fig. 3.6, which shows LOS velocities and proper motions for stars in fields 11 (a typical **D** field, located in a low-surface-brightness substructure to the north of the LMC) and 12 (a typical **G** field, located in the northern LMC disk). In panel *a*, showing the LOS velocity distribution of stars in field 11, there is a strong kinematic peak in the LOS velocities at ~280 km s^{-1} associated with the LMC, but also a large population of contaminants at lower LOS velocities which are foreground Milky Way stars. In contrast, the LOS velocity distribution of stars in field 12 (shown in panel *c*) lacks Milky Way contaminants almost entirely. In proper motion space, there is a clear clustering of proper motions between $0<\mu_\alpha$ (mas yr^{-1})<3 and $-2<\mu_\delta$ (mas yr^{-1})<2, corresponding to stars with LOS velocities ~300 km s^{-1} in both fields. However, in field 11 (panel *b*), this is embedded in a broader proper motion distribution associated with the Milky Way. This component is missing in panel *d* for field 12, as **G** fields have proper motion cuts applied during target selection.

These two fields sit on opposite ends of a contamination spectrum: field 11 was observed with less efficient target selection criteria, and is also located in a low-surface-brightness substructure where the density of true Magellanic stars is low. In contrast, field 12 is located in the LMC disk, where the density of Magellanic stars is high, and was observed using the strictest target selection criteria. Most MagES fields have levels of MW contamination between these two extremes. Consequently, in order to reliably determine kinematics for the Magellanic system, we need to remove the Milky Way contamination to generate a sample of stars that are likely genuinely associated with the Clouds. We utilise a probabilistic method to do this, rather than applying hard cuts – although the

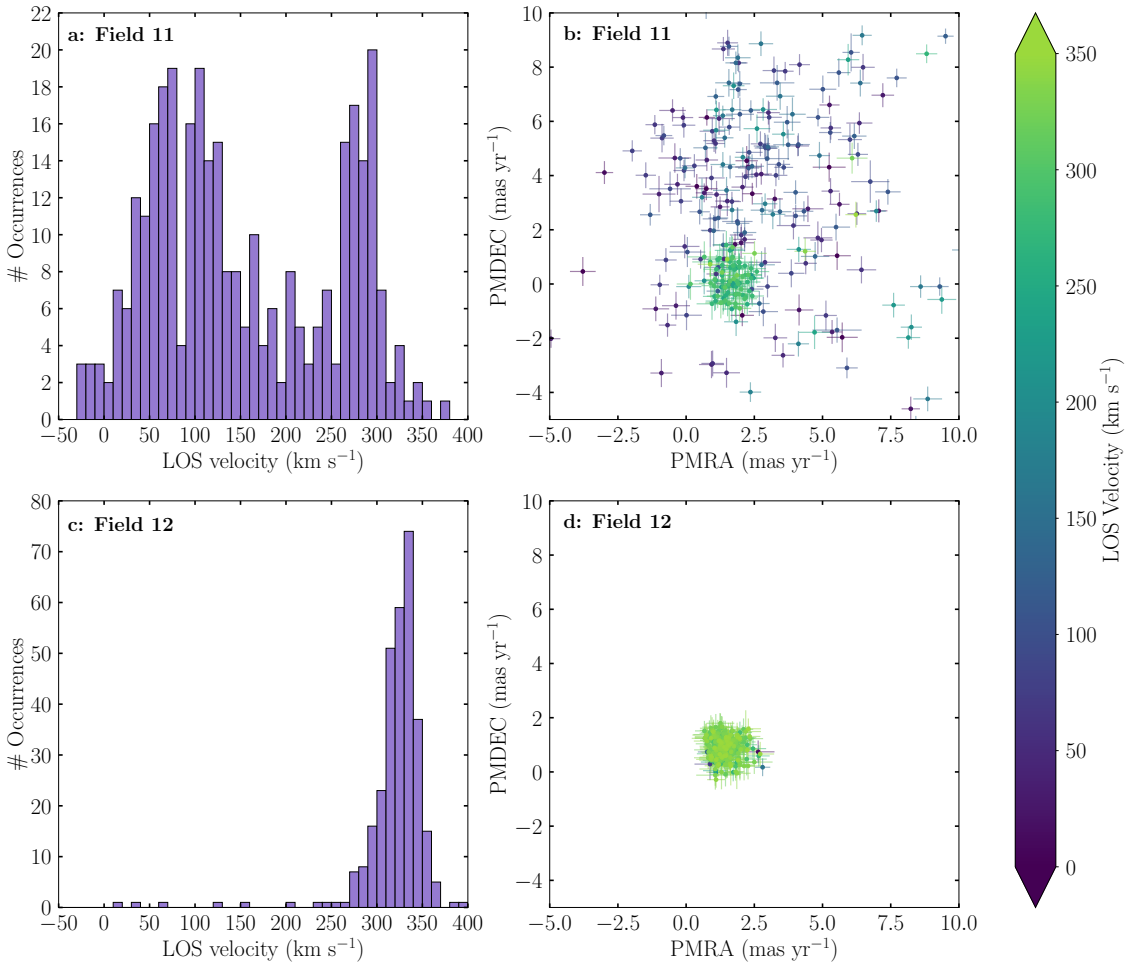

Figure 3.6: Kinematics of stars in field 11 (upper row) and field 12 (lower row). Field 11 is located in the low-surface-brightness substructure to the north of the LMC discussed in Mackey et al. (2016), and is typical of **D** and **M** fields. Field 12, discussed in greater detail in this paper, is a typical **G** field located in the northern disk of the LMC. Left panels show the distribution of heliocentric LOS velocities in each field: strong peaks exist between ~$280 - 350$ km s^{-1}; these are associated with the LMC. The large population of stars with LOS velocities <200 km s^{-1} in panel *a* are Milky Way contaminants that nonetheless pass the target selection criteria for **D** fields. Right panels show proper motions from Gaia DR2; stars with LOS velocities consistent with the Magellanic peak, coloured green, cluster in proper motion space within the box $0<\mu_\alpha$ (mas yr^{-1})<3 and $-2 < \mu_\delta$ (mas yr^{-1})<2.

LOS kinematic peak associated with the LMC is well-separated from the Milky Way contamination in Fig. 3.6, this is not the case for all observed fields. A probabilistic method is thus better suited for those fields where Magellanic and contaminant populations more closely overlap, while still allowing a homogeneous algorithm to be applied across the entire sample. We now discuss the processes used to select stars that have a high probability of Magellanic Cloud membership, and how this information is used to determine aggregate kinematics for each observed field.

3.5.1 Contamination model

In order to differentiate between Magellanic stars and contaminants, an empirical representation of the observed Milky Way contaminant profile in each field is required. As the observed contaminant profile varies across the large footprint of MagES, it is generated on a field-by-field basis using the Besançon Model of the Galaxy (described in Robin et al. 2003, and accessed as version 1603 through the web service [9]). The process used to generate the empirical model for each field is as follows.

The Besançon model is used to generate mock stars located within a 1° radius surrounding the field centre (the same field-of-view size as each observed 2dF field). The appropriate selection cuts for the field (as described in §3.3, including photometric cuts for **D** and **M** fields, and both photometric and kinematic cuts applied to **G** fields), are subsequently applied in order to obtain lists of mock Milky Way stars, within each priority band, that could conceivably have been observed in the field. This process is repeated for ten unique iterations of the Besançon model, and the results aggregated, to ensure the kinematic parameter space is sufficiently sampled.

We rescale the number of stars in each priority list by repeating each priority list n times, where n is the number of stars actually observed in that priority bin in the field. This effectively weights the contribution of each priority bin to the combined kinematic distribution of all priority bins, by the fraction of stars actually observed in that bin in the field. This process is equivalent to repeated sampling of each bin n times, and accounts for the preferential selection implemented by CONFIGURE used to generate the observed target lists.

The final list of model stars, of all priorities, is subsequently split into separate lists based on the population (disk[10] or halo) each star belongs to, as defined by the Besançon model itself. These have significantly different kinematic distributions, and we therefore found it easiest to treat these separately when generating empirical models. Once each population is defined, we generate a simple representation of the distribution of each population in velocity space using a Gaussian mixture model. We later use these analytical descriptions to inform the probability of individual stars being associated with either a contaminant population, or the Magellanic Clouds.

The log-likelihood of the mixture model for each population is described by Eq. 3.1, where $P(\mathbf{x}_j|\mathrm{MW}_{\mathrm{pop}})$ is the likelihood of each individual star in the population belonging to any Gaussian within the mixture model. Each of the J individual stars in the pop-

[9] https://model.obs-besancon.fr/

[10] No thin disk stars survive the selection criteria applied to the Model; thus all "disk" stars are defined as being associated with the thick disk of the Milky Way.

Table 3.2: Number of Gaussian profiles fit to each population in Besançon Models used to describe Milky Way contamination.

	D & **M** fields		**G** Fields	
	Disk	Halo	Disk	Halo
LOS velocities	2	1	1	1
Proper motions	1	2	1	1

ulation has kinematics $\mathbf{x}_j$ (comprising a LOS velocity v_j, and proper motions $\mu_{\alpha,j}$ and $\mu_{\delta,j}$). Note that μ_α always refers to proper motion in the $\alpha\cos(\delta)$ direction, such that it is perpendicular to μ_δ.

$$\begin{aligned}\log(\mathcal{L}) &= \sum_{j=1}^{J} \log\left(P(\mathbf{x}_j|\mathrm{MW}_{\mathrm{pop}}, \phi)\right) \\ &= \sum_{j=1}^{J} \log\left[\sum_{k=1}^{\kappa}\left(\eta_k \mathcal{N}(\mathbf{x}_j|\mathbf{m}_k, \mathbf{C}_k)\right)\right]\end{aligned} \tag{3.1}$$

Here, $\mathcal{N}(\mathbf{x}_j|\mathbf{m}_k, \mathbf{C}_k)$ is the probability density function of each Gaussian comprising the mixture model: each of which has means $\mathbf{m}_k$ and a covariance matrix $\mathbf{C}_k$. The probability density function of each component is given in Eq. 3.2.

$$\mathcal{N}(\mathbf{x}_j|\mathbf{m}_k, \mathbf{C}_k) = (2\pi)^{-d/2}\det(\mathbf{C}_k)^{-1} \times \exp\left[-\frac{1}{2}(\mathbf{x}_j - \mathbf{m}_k)^\intercal \mathbf{C}^{-1}(\mathbf{x}_j - \mathbf{m}_k)\right] \tag{3.2}$$

Here, d is the dimensionality of the Gaussians comprising the mixture model. Whilst it is possible to fit LOS velocities and proper motions simultaneously (implying a dimensionality of 3), we choose to fit these separately, as this allows us to fit a varying number of Gaussians to each kinematic component in order to best describe the overall population. For example, if disk stars have an asymmetric LOS velocity distribution, we parameterise this using two Gaussians; however in proper motion space, these stars may be sufficiently described by a single Gaussian. The total number κ of Gaussians fit to each kinematic component and population is given in Table 3.2. We note that **G** fields require fewer Gaussian components compared to **D** and **M** fields as fewer Milky Way stars survive the stricter target selection criteria applied to **G** fields. For populations where multiple Gaussians are fit, the parameter η_k is used to describe the relative fraction of stars in each Gaussian: $\sum_k^\kappa \eta_k = 1$.

The mean and covariance matrices for each kinematic component are given in Eqs. 3.3-3.4. LOS velocity Gaussians have systematic velocities of v_k and dispersions of σ_k, while proper motion Gaussians have systematic velocities of μ_k and $\mu_{\delta,k}$, dispersions of $\sigma_{\alpha,k}$ and $\sigma_{\delta,k}$, and covariance parameters of ρ_k. As we fit the LOS velocity and proper motion distributions separately, an underlying assumption of our method is that there is no correlation between the LOS velocity, and either of the proper motion components.

$$\mathbf{m}_{k,\mathrm{PM}} = \begin{pmatrix} \mu_{\alpha,k} \\ \mu_{\delta,k} \end{pmatrix} \qquad \mathbf{m}_{k,\mathrm{LOS}} = \begin{pmatrix} v_k \end{pmatrix} \tag{3.3}$$

$$\mathbf{C}_{k,\mathrm{PM}} = \begin{pmatrix} \sigma^2_{\alpha,k} & \rho_k \sigma_{\alpha,k} \sigma_{\delta,k} \\ \rho_k \sigma_{\alpha,k} \sigma_{\delta,k} & \sigma^2_{\delta,k} \end{pmatrix} \qquad \mathbf{C}_{k,\mathrm{LOS}} = \begin{pmatrix} \sigma^2_{v,k} \end{pmatrix} \tag{3.4}$$

To determine the best-fitting parameters for each of the κ Gaussians within the mixture model for each population, we sample the posterior distribution of the model parameters – which we abbreviate as $\phi = (\mathbf{m}_k, \mathbf{C}_k, \eta_k)$ – using the Markov Chain Monte Carlo ensemble sampler EMCEE (Foreman-Mackey et al. 2013) in order to maximise the log-likelihood given in Eq. 3.1. In this process, 50 walkers each take 2000 steps, with the burn-in phase of the first 1000 steps discarded when computing the final parameter values and their associated uncertainties. Uniform priors are applied to all parameters. Note that in subsequent analysis, we always use only the best-fitting parameter estimates ($\hat{\phi}$), as the effect of drawing from the confidence intervals calculated by EMCEE is negligible, as demonstrated in Appendix 3.8.

Once the best-fitting parameters for each population are known, the likelihood functions for both disk and halo populations are summed as per Eq. 3.5 to give the overall likelihood function for a given model star to belong to any of M Milky Way components within a given field. By definition, $M = \kappa_{\mathrm{disk}} + \kappa_{\mathrm{halo}}$. Here, γ refers to the relative fractions of disk and halo stars per field in the Besançon model: $\gamma_{\mathrm{disk}} + \gamma_{\mathrm{halo}} = 1$. Unlike each η_k, which are fit using EMCEE for each Gaussian within each population, γ_{disk} and γ_{halo} are calculated explicitly. The overall relative weighting of each Milky Way component is η_m.

$\mathbf{m}_m$ and $\mathbf{C}_m$ are identical in form to Eqs. 3.3-3.4.

$$\begin{aligned} P(\mathbf{x}_j|\mathrm{MW}, \hat{\phi}) &= \gamma_{\mathrm{disk}} P(\mathbf{x}_j|\mathrm{MW}_{\mathrm{disk}}, \hat{\phi}) + \gamma_{\mathrm{halo}} P(\mathbf{x}_j|\mathrm{MW}_{\mathrm{halo}}, \hat{\phi}) \\ &= \gamma_{\mathrm{disk}} \sum_{k_{\mathrm{disk}}=1}^{\kappa_{\mathrm{disk}}} \left[\eta_{k,\mathrm{disk}} \mathcal{N}\left(\mathbf{x}_j|\mathbf{m}_{k,\mathrm{disk}}, \mathbf{C}_{k,\mathrm{disk}}\right)\right] \\ &+ \gamma_{\mathrm{halo}} \sum_{k_{\mathrm{halo}}=1}^{\kappa_{\mathrm{halo}}} \left[\eta_{k,\mathrm{halo}} \mathcal{N}\left(\mathbf{x}_j|\mathbf{m}_{k,\mathrm{halo}}, \mathbf{C}_{k,\mathrm{halo}}\right)\right] \\ &= \sum_{m=1}^{M} \left[\eta_m \mathcal{N}\left(\mathbf{x}_j|\mathbf{m}_m, \mathbf{C}_m\right)\right] \end{aligned} \tag{3.5}$$

3.5.2 Generating membership probabilities

The outcome of the above process is a list of fitted parameter values, with uncertainties, which specify an approximate analytic form for the predicted Milky Way contamination within a given field. This is used in conjunction with the observed data, in a procedure similar to that outlined in Collins et al. (2013), to assign probabilistic Magellanic membership to each observed star in a given field.

As evident in Fig. 3.6, stars associated with the Clouds are concentrated in relatively cold (narrow) kinematic peaks, that are distinguishable from the profiles associated with Milky Way contaminants. As such, we generate probability density functions that describe the likelihood a given observed star belongs to either the Clouds, or one of the Milky Way contaminant profiles: under our parameterisation, if a star does not belong to the Milky Way, it must belong to a separate kinematic peak, which we associate with the Magellanic Clouds.

Unlike stars generated using the Besançon models, observed stars have associated uncertainties in their kinematics, with LOS velocities $v_i \pm u_{v,i}$ and proper motions $\mu_{\alpha,i} \pm u_{\alpha,i}$ and $\mu_{\delta,i} \pm u_{\delta,i}$. In addition, the uncertainties in the two proper motion directions are correlated: ρ_i (as obtained directly from the Gaia source catalogue using the column `PMRA_PMDEC_CORR`) describes this correlation. These uncertainties must be included in the calculation of probability density functions, in order to separate the intrinsic dispersion of the fitted Gaussians from observational broadening due to measurement error. The kinematics of each observed star $\mathbf{x}_i$ and its uncertainties $\mathbf{C}_i$ are described by Eqs. 3.6-3.7. As we calculate the probability density functions for the LOS velocities and proper motions of the stars separately, we inherently assume the LOS velocity uncertainties of the stars are uncorrelated with the uncertainties in either proper motion component.

$$\mathbf{x}_{i,\mathrm{PM}} = \begin{pmatrix} \mu_{\alpha,i} \\ \mu_{\delta,i} \end{pmatrix} \qquad \mathbf{x}_{i,\mathrm{LOS}} = \begin{pmatrix} v_i \end{pmatrix} \tag{3.6}$$

$$\mathbf{C}_{i,\mathrm{PM}} = \begin{pmatrix} \sigma^2_{\alpha,k} & \rho_i \sigma_{\alpha,i} \sigma_{\delta,i} \\ \rho_i \sigma_{\alpha,i} \sigma_{\delta,i} & \sigma^2_{\delta,i} \end{pmatrix} \qquad \mathbf{C}_{i,\mathrm{LOS}} = \begin{pmatrix} \sigma^2_{v,i} \end{pmatrix} \tag{3.7}$$

The likelihood for a given observed star to be a Milky Way contaminant is defined in Eq. 3.8. Here, the total likelihood is the sum of the probabilities of the star being associated with any of the M Milky Way components used to fit the Besançon models. $\mathbf{m}_m$ and $\mathbf{C}_m$ are as described in Eq. 3.5, and use the best-fitting parameters derived for each component fit to the Besançon model.

$$P(\mathbf{x}_i|\mathrm{MW}, \hat{\phi}) = \sum_{m=1}^{M} \left[\eta_m \mathcal{N}\left(\mathbf{x}_i|\mathbf{m}_m, [\mathbf{C}_m + \mathbf{C}_i]\right)\right] \tag{3.8}$$

If a star does not belong to the Milky Way, then under our parameterisation it must belong to a separate kinematic peak, which we associate with the Magellanic Clouds, and assume to be Gaussian in nature. The likelihood for a given observed star to be associated with such a peak is given by Eq. 3.9. Note that in this parameterisation, only a single peak associated with the Clouds is fitted; however, particularly for fields located between the two Clouds, it is possible multiple separate populations associated with the Clouds are present. In such cases, the procedure can be generalised to allow the fitting of multiple Gaussians associated with Magellanic peaks, as necessary.

$$P(\mathbf{x}_i|\mathrm{MC}, \varphi) = \mathcal{N}\left(\mathbf{x}_i|\mathbf{m}_{\mathrm{MC}}, [\mathbf{C}_{\mathrm{MC}} + \mathbf{C}_i]\right) \tag{3.9}$$

$\mathbf{m}_{\mathrm{MC}}$ and $\mathbf{C}_{\mathrm{MC}}$ describe the properties of the means and covariances of the Magellanic peak respectively, and are given in Eqs. 3.10-3.11. Here, v_{MC} is the systemic LOS velocity of the peak; $\mu_{\alpha,\mathrm{MC}}$ and $\mu_{\delta,\mathrm{MC}}$ are the systemic proper motions of the peak; $\sigma_{v,\mathrm{MC}}$ is the velocity dispersion of the peak; $\sigma_{\alpha,\mathrm{MC}}$ and $\sigma_{\delta,\mathrm{MC}}$ are the proper motion dispersions of the peak; and ρ_{MC} describes the covariance of the proper motion dispersions. We assume there is no correlation between the LOS velocity dispersion and the proper motion dispersions of the peak.

$$\mathbf{m}_{\mathrm{MC,\ PM}} = \begin{pmatrix} \mu_{\alpha,\mathrm{MC}} \\ \mu_{\delta,\mathrm{c}} \end{pmatrix} \qquad \mathbf{m}_{\mathrm{MC,\ LOS}} = \begin{pmatrix} v_{\mathrm{MC}} \end{pmatrix} \tag{3.10}$$

$$\begin{aligned} \mathbf{C}_{\mathrm{MC,\ PM}} &= \begin{pmatrix} \sigma^2_{\alpha,\mathrm{c}} & \rho_{\mathrm{MC}}\sigma_{\alpha,\mathrm{MC}}\sigma_{\delta,\mathrm{MC}} \\ \rho_{\mathrm{MC}}\sigma_{\alpha,\mathrm{MC}}\sigma_{\delta,\mathrm{MC}} & \sigma^2_{\delta,\mathrm{MC}} \end{pmatrix} \\ \mathbf{C}_{\mathrm{MC,\ LOS}} &= \begin{pmatrix} \sigma^2_{v,\mathrm{MC}} \end{pmatrix} \end{aligned} \tag{3.11}$$

In order to identify the characteristics of the Magellanic kinematic peak, we use EMCEE to sample the posterior distribution of each of the peak parameters – which we abbreviate as $\varphi = (\gamma_{\mathrm{MC}}, \mathbf{m}_{\mathrm{MC}}, \mathbf{C}_{\mathrm{MC}})$ – in order to maximise the log-likelihood function given in Eq. 3.12. Here, N is the total number of observed stars, γ_{MW} describes the fraction of observed stars in a given field that are associated with the Milky Way (as opposed to being Magellanic in origin), and γ_{MC} describes the fraction of observed stars in a given field that are associated with the Magellanic Clouds (as opposed to being associated with any component of the Milky Way). By definition, $\gamma_{\mathrm{MW}} + \gamma_{\mathrm{MC}} = 1$. Note that the value of the kinematic peak parameters derived in this process are not the final kinematic properties of the Clouds at this location: they simply indicate a region in velocity space, roughly consistent with the expected motions of the Clouds, where an excess of stars above the Milky Way contamination baseline exists.

$$\log\left(\mathcal{L}\right) = \sum_{i=1}^{N} \log\left[\gamma_{\mathrm{MC}} P(\mathbf{x}_i|\mathrm{MC}, \varphi) + \gamma_{\mathrm{MW}} P(\mathbf{x}_i|\mathrm{MW}, \hat{\phi})\right] \tag{3.12}$$

Once the initial properties of the Magellanic kinematic peak ($\hat{\varphi}$) are known, these are used in Eq. 3.13 to calculate the individual probability that a given observed star belongs to the peak, and is therefore associated with the Clouds. Separate independent probabilities are generated based on (1) the LOS velocity distribution $P(\mathrm{MC}|i, \hat{\varphi}, \hat{\phi})_{\mathrm{LOS}}$ and (2) the 2D proper motion distribution $P(\mathrm{MC}|i, \hat{\varphi}, \hat{\phi})_{\mathrm{PM}}$. These are multiplicatively combined as per Eq. 3.14 to determine an overall probability $P(\mathrm{MC}|i, \hat{\varphi}, \hat{\phi})$ that each observed star is associated with the Clouds.

$$P(\mathrm{MC}|i, \hat{\varphi}, \hat{\phi})_{\mathrm{LOS/PM}} = \frac{\gamma_{\mathrm{MC}} P(\mathbf{x}_i|\mathrm{MC}, \hat{\varphi})}{\gamma_{\mathrm{MC}} P(\mathbf{x}_i|\mathrm{MC}, \hat{\varphi}) + \gamma_{\mathrm{MW}} P(\mathbf{x}_i|\mathrm{MW}, \hat{\phi})} \tag{3.13}$$

$$P(\mathrm{MC}|i,\hat{\varphi},\hat{\phi}) = P(\mathrm{MC}|i,\hat{\varphi},\hat{\phi})_{\mathrm{LOS}} \times P(\mathrm{MC}|i,\hat{\varphi},\hat{\phi})_{\mathrm{PM}} \tag{3.14}$$

3.5.3 Determining field aggregate properties

Once each star in a field has been assigned an aggregate association probability $P(\mathrm{MC}|i,\hat{\varphi},\hat{\phi})$, these are used to calculate the aggregate 3D motion of the Clouds, and the dispersion in each of the three velocity components, across the field. A single Gaussian with mean $\mathbf{m}_{\mathrm{MC}}$ and covariance $\mathbf{C}_{\mathrm{MC}}$, taking identical form to those given in Eqs. 3.10 and 3.11, is used to describe the field kinematics. EMCEE is used to sample the posterior distribution of each of these parameters to maximise the log-likelihood function given in Eq. 3.15; each term of which is weighted by $P(\mathrm{MC}|i,\hat{\varphi},\hat{\phi})$. In this way, stars that are very unlikely to be associated with the Clouds contribute minimally to the calculated field aggregate properties. The resulting parameters describe the field aggregate properties of the Clouds at each location. We report the 68 per cent confidence interval as the 1σ uncertainty in each parameter.

$$\log(\mathcal{L}) = \sum_{i=1}^{N} \log\Bigg(P(\mathrm{MC}|i,\hat{\varphi},\hat{\phi})\gamma_{\mathrm{MC}}\mathcal{N}(\mathbf{x}_i|\mathbf{m}_{\mathrm{MC}},[\mathbf{C}_{\mathrm{MC}}+\mathbf{C}_i]) + \left[1-P(\mathrm{MC}|i,\hat{\varphi},\hat{\phi})\right]\gamma_{\mathrm{MW}}P(\mathbf{x}_i|\mathrm{MW},\hat{\phi})\Bigg) \tag{3.15}$$

3.5.4 Metallicity determination

In addition to field kinematics, [Fe/H] estimates are also determined for stars with high probability of being associated with the Clouds (defined here as having $P(\mathrm{MC}|i,\hat{\varphi},\hat{\phi}) > 50\%$). The procedure used broadly follows that outlined in Da Costa (2016), although with some modifications. In Da Costa's method, the equivalent widths of the 8542Å and 8662Å CaII lines, present in the red-arm spectra of each star, are first measured by fitting a combined Gaussian plus Lorentzian function, and summed (see Da Costa 2016 for further details of the measurement technique). Next, the reduced equivalent width, W', is calculated as per Eq. 3.16.

$$W' = EW - (-0.660 \pm 0.016) \times (V_0 - V_{\mathrm{HB},0}) \tag{3.16}$$

Here, -0.660 ± 0.016 is the slope of the $EW - W'$ relation derived in Da Costa (2016). V_0 is the de-reddened V-band magnitude of the star; this is calculated from the Gaia

photometry of the star using the transformations given in Evans et al. (2018). $V_{\mathrm{HB},0}$ is the horizontal branch magnitude, which we take as equal to the median red clump magnitude in the surrounding field. This median is calculated by taking the median Gaia G_0 magnitude for stars in a selection box surrounding the Magellanic red clump on the Gaia $(G_0, (G_{\mathrm{BP}} - G_{\mathrm{RP}})_0)$ CMD. The boundaries of the selection box are drawn on a field-by-field basis, but in all cases covering only a narrow $(G_{\mathrm{BP}} - G_{\mathrm{RP}})_0$ range to minimise contamination from Milky Way stars, many of which are located near to the Magellanic red clump (as seen in Fig. 3.2). The median G_0 magnitude is then converted to a V-band magnitude using the relations given in Evans et al. (2018). Finally, the reduced equivalent width is transformed into an [Fe/H] estimate using Eq. 2 in Da Costa (2016), reproduced here as Eq. 3.17. This equation is valid in the range $-2.4 \lesssim [\mathrm{Fe/H}] \lesssim 0.1$ dex.

$$[\mathrm{Fe/H}] = (0.528 \pm 0.017)W' - (3.420 \pm 0.077) \tag{3.17}$$

However, the 8662Å line used in the above calculation is within a region of the spectrum relatively heavily contaminated by night-sky emission, which is often poorly-subtracted during the data reduction process. This, in combination with the relatively faint magnitudes of the observed red clump stars, can result in inaccurate measurements of the line's equivalent width. The 8542Å line is not as strongly affected, but is still difficult to accurately measure in lower-S/N spectra. In order to mitigate this effect, and prevent biasing of the derived metallicities, we implement two modifications to the method in Da Costa (2016).

The first of these is that spectra for red clump stars, after being shifted into the rest frame using their observed LOS velocities, are stacked in groups of at least ten. This increases the contrast of the two CaII absorption features relative to the residual night-sky emission (which is stochastically either over- or under-subtracted, and is therefore suppressed when multiple spectra are stacked). This allows for more accurate determination of the equivalent widths of the lines. Note that as red clump stars only occupy a small magnitude range (and relatively small ranges in other stellar parameters) (Girardi 2016), stacking spectra is not expected to bias the resulting equivalent widths. It will, however, result in metallicity estimates that tend toward the mean metallicity of the field. As such, we only use stacked spectra when analysing aggregate metallicity properties across an entire field, and do not include results from stacked spectra when analysing the metallicity distribution within a given field.

Unfortunately, even when considering stacked spectra, it remains impossible to determine accurate equivalent widths for the 8662Å line for ~50 per cent of spectra. In order to

derive metallicities for these spectra, we implement a similar process as described above, but which does not utilise the equivalent width of the 8662Å line. Instead, the slope of the $EW - W'$ relation, and the coefficients in Eq. 2 of Da Costa (2016), are recalculated using only the equivalent width of the 8542Å line. The resulting relations are provided in Eqs. 3.18 and 3.19.

$$W' = EW - (-0.366 \pm 0.036) \times (V_0 - V_{\mathrm{HB},0}) \tag{3.18}$$

$$[\mathrm{Fe/H}] = (0.884 \pm 0.001)W' - (-3.336 \pm 0.004) \tag{3.19}$$

The propagated uncertainty in each individual metallicity value is dominated by systematic and photometric uncertainties in the $W' - EW$ relation. Whilst the uncertainty in the equivalent width of each line decreases as the S/N of the spectrum increases, brighter stars – which have higher S/N spectra – have a correspondingly larger value of $(V_0 - V_{\mathrm{HB},0})$, which results in a larger uncertainty in this term of the $W' - EW$ relation than that contributed by the equivalent width itself. As a result, the overall metallicity uncertainty does not correlate strongly with either spectrum S/N, or [Fe/H] value.

For stars where both CaII lines can be measured accurately (which are typically the brightest stars in any given field) we compare the [Fe/H] values derived using the single and double-line methods. We find the [Fe/H] values derived have an ~0.2 dex scatter around the 1:1 relation, with no systematic offset between the derived values. This scatter is significantly larger than the propagated uncertainty in each individual metallicity value. We therefore take 0.2 dex as the total uncertainty on the metallicity value of each individual star, regardless of which method is used.

3.6 Results

The result of MagES data processing is a set of six kinematic parameters for each 2dF field, describing the apparent systemic velocity and dispersion of the Clouds in 3D at that location, and a set of metallicity estimates for each location. Detailed analysis of these data, covering various substructures in the Magellanic periphery, will be presented in forthcoming papers. Here, we focus on initial results from two fields (12 and 18) in the northern outer disk of the LMC: both to verify our approach, and to provide a basis for future comparison with more distant fields. Table 3.3 provides the observed kinematic properties of these two fields (LOS velocity and dispersion, and the two components of proper motion and their dispersions), their median metallicities, and the standard

deviation of their [Fe/H] distributions. The reported uncertainty on the median metallicity is the standard error of the mean, equal to the standard deviation of the distribution divided by the square root of the number of stars with metallicity determinations.

Whilst Table 3.3 reports 3D kinematics in observable units, it is more informative to consider these in the reference frame of the LMC disk itself. As such, the framework presented in van der Marel and Cioni (2001) and van der Marel et al. (2002) is used to describe the LMC disk velocity field, and transform the observed components into velocities in a cylindrical coordinate system. This coordinate system is aligned with the LMC disk, and has its origin at the LMC centre of mass (COM). This transformation includes the subtraction of the systemic motion of the LMC COM, as projected at each field location.

However, various studies of the Clouds have reported COM positions which differ by up to a degree on the sky, depending on the chosen tracer (see e.g. Wan et al. 2020 henceforth referred to as W20). Given that our sample is primarily red clump stars, for consistency we adopt the COM position reported by van der Marel and Kallivayalil (2014 henceforth referred to as vdM14), for their "PMs+Old $v_{\rm LOS}$ Sample": i.e. $79.88^\circ \pm 0.83^\circ$, $-69.59^\circ \pm 0.25^\circ$. This is a kinematic centre, derived from a simultaneous fit of HST field-aggregate proper motions, combined with LOS velocities for an "old"[11] stellar sample. This is as similar as possible to the data used in the present work. We further adopt the associated bulk motion reported by vdM14 applicable for this choice of centre: i.e. $\mu_{\delta,0} = 0.287 \pm 0.054$ mas yr^{-1}, $\mu_{\alpha,0} = 1.895 \pm 0.024$ mas yr^{-1}, and $v_{\rm LOS,0} = 261.1 \pm 2.2$ km s^{-1}. The bulk proper motions reported are, within uncertainty, consistent with those reported by Gaia Collaboration et al. (2018c).

The geometry of the LMC disk must also be assumed during this coordinate transform. When considering estimates derived using relatively old tracers (similar to the population observed with MagES) the inclination of the LMC disk has traditionally been reported as ~35° (e.g. van der Marel and Kallivayalil 2014; Vasiliev 2018); though some more recent studies suggest ~25° (e.g. Wan et al. 2020; Choi et al. 2018b). However, all such measurements have been derived using stars at much smaller radial distances from the LMC COM than even the innermost of our fields. Moreover, warps (e.g. Choi et al. 2018b; Olsen and Salyk 2002 Mackey et al. in prep.) and a twisting of the position angle of the line of nodes (LON; represented as Θ)[12] (e.g. Choi et al. 2018b Mackey et al. in prep.) have been found in the LMC disk. Given this, the behaviour of the LMC disk at radii commensurate with our fields is largely unconstrained; so the most appropriate

[11] Comprised of carbon stars, AGB and RGB stars that are predominantly older than 1-2 Gyr and therefore similar in age to the red clump population.

[12] The axis along which the plane of the inclined LMC disk intersects the plane of the sky.

Table 3.3: MagES kinematic parameters (described in §3.6) and median metallicities for two northern LMC disk fields.

Field	Distance (°) from LMC COM	$V_{\rm LOS}$ (km s^{-1})	$\sigma_{\rm LOS}$ (km s^{-1})	μ_α(mas yr^{-1})	σ_α (mas yr^{-1})	μ_δ(mas yr^{-1})	σ_δ (mas yr^{-1})	Median [Fe/H]	$\sigma_{\rm [Fe/H]}$
18	10.7	324.8 ± 1.1	19.8 ± 0.8	1.45 ± 0.02	0.13 ± 0.02	0.96 ± 0.01	0.11 ± 0.02	-1.0 ± 0.1	0.3
12	10.3	287.5 ± 1.5	24.3 ± 1.0	1.77 ± 0.02	0.13 ± 0.02	0.19 ± 0.02	0.21 ± 0.02	-1.1 ± 0.1	0.5

choice of geometry for these fields is not obvious.

In this work, we therefore decided to test two different LMC disk geometries, spanning the range of recent measurements reported in the literature. The first is taken from the same vdM14 field-aggregate proper motion and old stellar LOS measurements as used for the LMC COM properties (with $i = 34.0°$, $\Theta = 139.1°$). The second is taken as the best-fitting model from Choi et al. (2018b) ($i = 25.86°$, $\Theta = 149.23°$), which is derived solely from photometric data[13]. Future work (e.g. Mackey et al. in prep) should provide direct disk geometry measurements at the locations of several MagES fields, which can be used to validate the assumptions made here. For simplicity, in what follows we assume no precession or nutation of the LMC disk, consistent with the measurements of vdM14.

For each of the assumed geometries, the observed kinematic parameters for our two fields are transformed into physical velocities and dispersion in the LMC disk frame. We calculate V_θ, the azimuthal streaming or rotation velocity; V_r, the radial velocity in the disk plane; and V_z, the vertical velocity perpendicular to the disk plane, as well as dispersions in each of these components. Fig. 3.7 displays these velocities for the two northern LMC disk fields. Error bars on each point are obtained by using Monte Carlo error propagation to simultaneously propagate uncertainty in the observed velocity components, the LMC disk geometry, and the bulk motion of the LMC COM. Uncertainty in the location of the LMC COM is not propagated as this is found to be negligible compared to the other uncertainty sources.

As is apparent from Fig. 3.7, the calculated velocities and dispersions are, within uncertainty, the same for both tested disk geometries. This is partly due to the relatively large uncertainties in the disk geometry parameters themselves. For example, the vdM14 model has a large uncertainty in the inclination ($\pm 7°$), while the Choi et al. (2018b) et al. model has a large uncertainty in the position angle of the line of nodes ($\pm 8.35°$). Nevertheless, the lack of substantial sensitivity to the parameters of the tested disk geometries indicates that the conclusions drawn in the following analysis are robust to differences between the actual LMC disk geometry at these locations, and the values assumed in this paper. Consequently, in subsequent discussion, we adopt disk velocities and dispersions assuming the geometry of vdM14, for consistency with our adopted COM position and bulk velocity. These disk measurements are reported in Table 3.4, which presents the azimuthal, radial, and vertical velocity components, and their dispersions.

[13] We do not use the model parameters derived using only the outermost radial bin in the Choi et al. (2018b) analysis as that data comes only from a small portion of the southern LMC disk; at this stage, it is not clear if the reported warping of the disk in the south has a counterpart in the northern LMC.

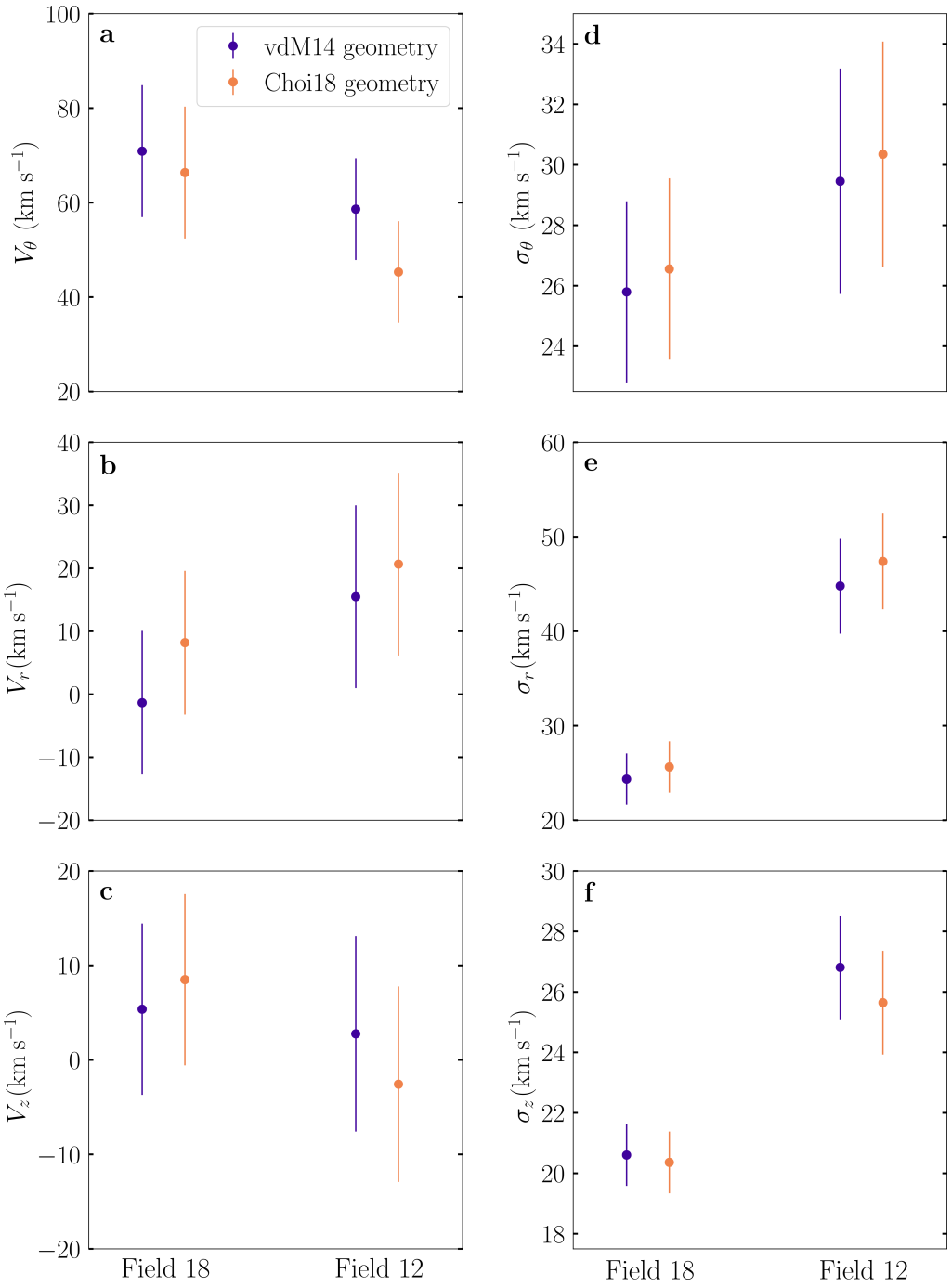

Figure 3.7: LMC disk velocities and dispersions in fields 18 and 12, calculated using both vdM14 and Choi et al. (2018b) disk geometries. Top panels show the azimuthal velocity component (panel *a*) and its dispersion (panel *d*); positive values indicate clockwise rotation. Middle panels show the radial velocity component (panel *b*) and its dispersion (panel *e*); positive values indicate movement outward from the LMC COM in the LMC disk plane. Bottom panels show the vertical velocity component (panel *c*) and its dispersion (panel *f*); positive values indicate movement perpendicular to the disk plane, in a direction primarily towards the observer. For each velocity component, the values within a given field are the same within uncertainty, regardless of the assumed geometry.

Table 3.4: Disk velocities for northern LMC disk fields, derived using vdM14 geometry.

Field	V_θ (km s^{-1})	σ_θ (km s^{-1})	V_R (km s^{-1})	σ_R (km s^{-1})	V_Z (km s^{-1})	σ_Z (km s^{-1})
Field 18	70.9 ± 14.0	25.8 ± 3.0	-1.3 ± 11.4	24.4 ± 2.7	5.4 ± 9.6	20.6 ± 1.0
Field 12	58.6 ± 10.8	29.5 ± 3.7	15.5 ± 14.5	44.8 ± 5.1	2.8 ± 10.3	26.8 ± 1.7

The [Fe/H] distributions for the two fields are presented in Fig. 3.8. The median metallicity in both fields ([Fe/H]= -1.0 ± 0.1 for field 18, and [Fe/H]= -1.1 ± 0.1 for field 12) is consistent with literature spectroscopic metallicity determinations for stars at similar distances from the LMC COM (Majewski et al. 2008; Carrera et al. 2011). Both distributions have tails to lower metallicities, with this tail being most pronounced in field 12; this inflates the standard deviation of the distribution. We look for evidence that any stars we observe may form part of a halo-like component by comparing the kinematics of stars in the metal-poor tails of the [Fe/H] distributions (defined here as having [Fe/H]<–1.5) to those stars with higher [Fe/H] values. While there are only few "metal-poor" stars, simple Kolmogorov–Smirnov (K–S) tests indicate no significant differences in the kinematics of lower- and higher-metallicity stars in either field.

3.6.1 LMC Disk motions

In this section, we discuss the derived velocities and dispersions of two fields observed in the northern LMC disk. We remind readers that these values are derived assuming the geometry, and associated bulk velocity, of vdM14; uncertainties in these values, and in the distance to the LMC, are propagated through and contribute to the uncertainty in the values reported here.

Fig. 3.9 shows the azimuthal velocity (V_θ) for the two MagES disk fields, relative to similar measurements obtained by vdM14. It should be noted that the vdM14 proper motions are based on Hubble Space Telescope (HST) astrometry, and as such, represent the mean proper motion of all stellar populations in each given field. It is known from LOS velocity measurements (see e.g. van der Marel and Kallivayalil 2014) that younger stellar populations in the Magellanic Clouds rotate more quickly than older populations. As such, the rotation velocity derived from HST proper motions (which combine both populations) is higher than that derived using just LOS velocities for older stars. Also plotted are rotation velocities derived from Vasiliev (2018), W20, and Gaia Collaboration et al. (2018c). These are derived using the proper motions of large samples of individual Magellanic RGB and carbon stars.

The azimuthal velocities for the two MagES fields (70.9 ± 14.0 km s^{-1}, and $58.6 \pm$

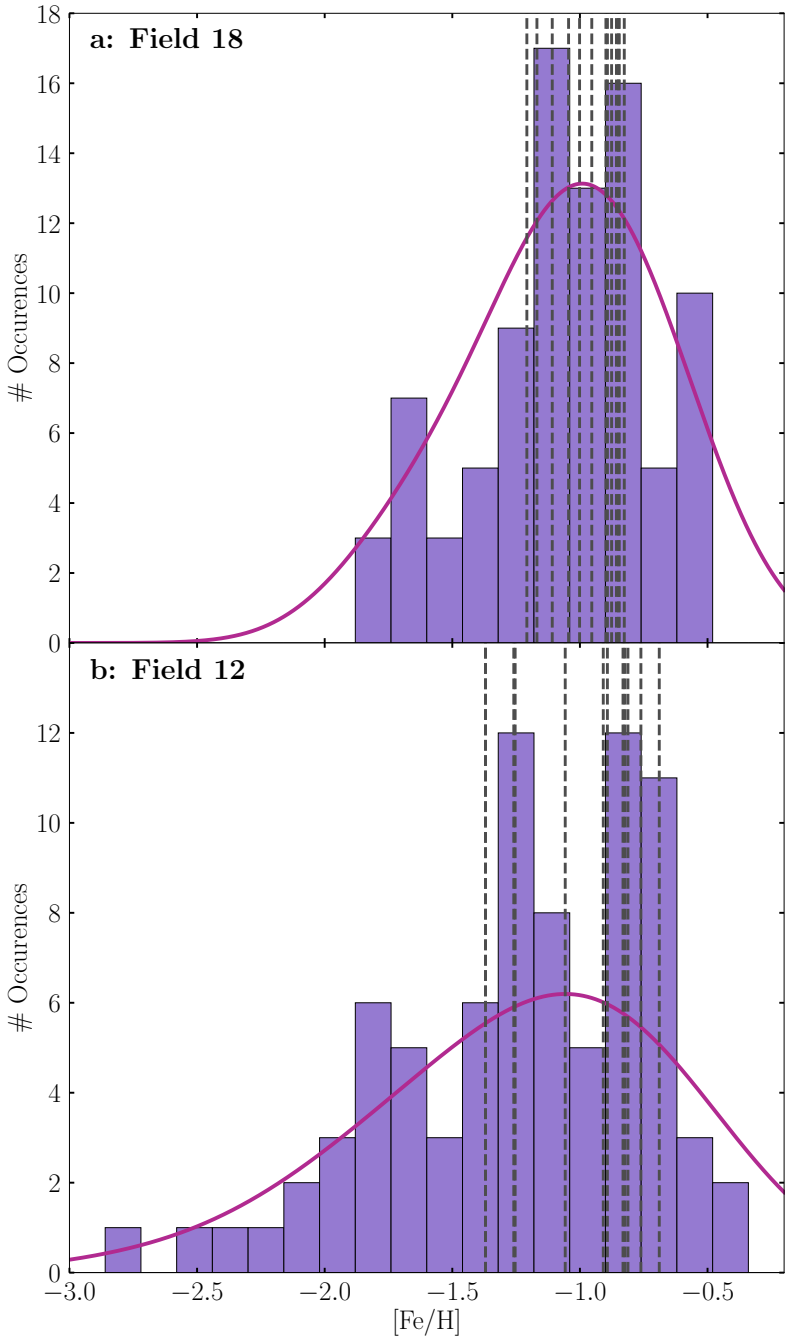

Figure 3.8: [Fe/H] distributions for stars in Fields 18 (panel *a*) and 12 (panel *b*). In both fields, the median metallicity is consistent that expected for stars in the outer LMC disk, with a tail to lower [Fe/H] values. Vertical dashed lines indicate metallicities derived from stacked spectra, which tend to the median metallicity of the field; the histogram comprises only measurements from individual stars. The smooth curves overplotted in red were derived via kernel density estimation using a Epanechnikov kernel, convolved with the median metallicity uncertainty.

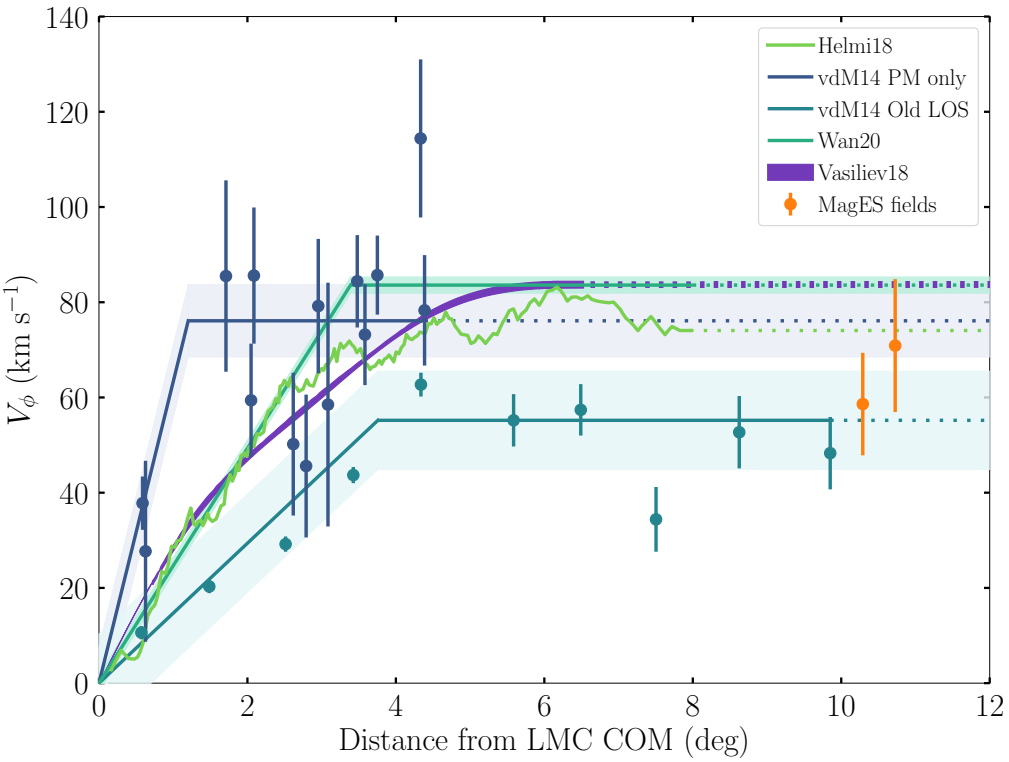

Figure 3.9: Azimuthal velocities in the LMC disk as a function of distance from the LMC COM. Orange points indicate measurements for the two MagES fields in the northern LMC disk; error bars include propagated uncertainties from all parameters. Dark blue points show vdM14 values derived from HST proper motion measurements of mixed young and old populations, while light blue/aqua points show vdM14 values derived from line-of-sight observations for their "old" stellar population. Error bars on these points only include uncertainty in the observed motions, and not disk geometry or COM location, and are thus smaller than those for the MagES fields. The solid lines reflect the best-fitting rotation models derived from Vasiliev (2018 labelled Vasiliev18), W20, Gaia Collaboration et al. (2018c labelled Helmi18) and vdM14. Surrounding shaded regions indicate 1σ uncertainty propagated from all parameters; these are thus comparable to the errorbars of the MagES fields. Dashed continuations of the solid lines indicate where these models have been extrapolated outwards in order to facilitate comparison with the two MagES points: the observations used to derive the velocities shown are generally located much closer to the LMC COM than the MagES fields.

10.8 km s^{-1} for fields 18 and 12 respectively) are both consistent with one another within uncertainty, and consistent with all other sets of measurements in Fig. 3.9. This is unsurprising; the old stellar populations used to derive each literature rotation curve are similar to the population observed by MagES; and therefore should have similar kinematics, as is observed.

It is worth noting these northern-LMC MagES fields provide an estimate of the LMC rotation at radii more distant from the LMC COM (>10° on-sky) than all previous estimates (which typically have data confined to <10° of the LMC COM). As these measurements are consistent with measurements derived at more central locations, this indicates

the LMC rotation curve remains flat even at very large distances from the LMC COM, where external perturbations (e.g. due to the SMC) might be expected to disturb the disk motion. For example, at comparable radii on the southern side of the LMC disk, clear substructures are seen (Mackey et al. 2018).

The azimuthal velocity dispersion (σ_θ) within the two MagES fields (25.8 ± 3.0 km s^{-1} and 29.5 ± 3.7 km s^{-1} for fields 18 and 12 respectively) are moderately lower than that measured by W20 (37.1 ± 0.7 km s^{-1}). This difference can at least partially be attributed to the fact that W20 assume a constant velocity dispersion at all radii. As their data are relatively centrally concentrated (with data at radii predominantly within 6°), the recovered dispersion is predominantly reflective of the large dispersion in the inner LMC. However, there is evidence that the azimuthal velocity dispersion decreases with radius in disk galaxies (see e.g. Vasiliev 2018; Guiglion et al. 2015; Noordermeer et al. 2008). As the MagES fields are situated at substantially larger galactocentric radii (~10.5° from the LMC COM) than the W20 data, it is reasonable that the azimuthal velocity dispersion in the MagES fields is correspondingly smaller.

By this reasoning, it might also be expected that the azimuthal velocity dispersion in the MagES fields should be smaller than that measured by Vasiliev (2018) (~20 km s^{-1} at ~8° from the LMC COM). However, the aforementioned decrease in azimuthal velocity dispersion with radius is strongest in the inner regions of the disk, and levels off (implying a relatively constant dispersion as a function with radius) in the disk outskirts (Vasiliev 2018; Noordermeer et al. 2008). Accordingly, consistency between the dispersions measured in the MagES fields, and that measured by Vasiliev (2018), is not surprising. This is true for field 18, although the dispersion in field 12 is somewhat higher than that measured by Vasiliev (2018). We note, however, that field 12 is located only a small distance radially inward from the base of the arm-like feature discussed in Mackey et al. (2016). We hypothesise that this increased dispersion may be due to the same perturbation which formed the feature. Further evidence of perturbation in field 12 is discussed below.

For both MagES fields, the vertical motion (V_z) perpendicular to the LMC disk plane is, within uncertainties, consistent with zero. This is as expected; in an equilibrium system, a roughly equivalent number of stars will, at any one time, be moving vertically in both directions, resulting in a mean motion of zero across the field. The vertical velocity dispersion for the two fields (20.6 ± 1.0 km s^{-1} and 26.8 ± 1.7 km s^{-1} for fields 18 and 12 respectively) are slightly higher, but not significantly different from, that measured by Vasiliev (2018) (~15 km s^{-1} at ~8° from the LMC COM).

As is the case for the vertical velocity, in an equilibrium system, the mean radial velocity (V_r) across a field is expected to be zero, with a roughly equivalent number of

stars moving in both directions. This is true for field 18; however for field 12, the radial velocity (15.5 ± 14.5 km s^{-1}) does not overlap zero within ~1σ. The (small) positive value suggests a mild net motion radially outward for stars in this field.

The source of the net outward motion in this field is not obvious. As noted above, field 12 is located nearby the base of an arm-like structure in the outer LMC. It is possible this radial motion is a signature of the perturbation which formed the feature. Interestingly, Gaia Collaboration et al. (2018c) also find positive radial velocities for some stars between ~$4^\circ - 8^\circ$, which they suggest may be due to non-equilibrium effects induced by interactions between the Clouds. Chapter 4 investigates the hypothesis that interactions can cause such positive radial velocities in further detail.

The radial velocity dispersion (σ_r) in field 18 (24.4 ± 2.7 km s^{-1}) is, within uncertainty, equal to the azimuthal velocity dispersion. This is consistent with the behaviour reported in Vasiliev (2018) and W20. The magnitude of the radial dispersion measured here is again somewhat smaller than that reported in W20; the difference can be attributed to the same reasons outlined above for the azimuthal velocity dispersion. However, the radial dispersion is approximately consistent with the ~20 km s^{-1} reported by Vasiliev (2018) at his most distant point. In this field, the radial and vertical velocity dispersions are also consistent with each other, within uncertainties. This is similar to the behaviour of the Milky Way thick disk (Bland-Hawthorn and Gerhard 2016; Guiglion et al. 2015).

In contrast, field 12 has a radial velocity dispersion (44.8 ± 5.1 km s^{-1}) almost double that of field 18. This is significantly higher than either the azimuthal or vertical velocity dispersions measured in the field, and, by coincidence, is closer to that measured in the inner LMC disk by Vasiliev (2018) and W20. As noted above, field 12 is located nearby the base of an arm-like structure in the outer LMC. Further, W20 use a N-body model of the interaction between the LMC and SMC to demonstrate that such events can cause increased radial velocity dispersions, particularly in the outer regions of the LMC disk. Consequently, it seems plausible that the same perturbation which formed the nearby interaction feature, might also have increased the radial velocity dispersion in the outer disk as measured here. This idea is explored in greater detail in Chapter 4.

3.6.2 Asymmetric LOS Velocity Distributions

When the LOS velocity distribution of stars in the two northern disk fields are plotted, as in Fig. 3.10, it is apparent that the distributions are asymmetric: there are clear tails to lower LOS velocities. We quantify this asymmetry by calculating the "excess" fraction of stars in the low-velocity tail. To do this, we first fit a half-normal distribution to

stars with LOS velocities exceeding the peak velocity of the field, using a least-squares fitting algorithm. The centre of the half-Gaussian is fixed to the peak velocity reported in Table 3.3; only the dispersion of the half-Gaussian is fit. This "reduced dispersion" reflects the dispersion value that would be calculated if the LOS velocity distribution were truly Gaussian in nature. Using this "reduced dispersion", we then calculate the fraction of stars with LOS velocities greater than 1σ below the peak value. If the distribution were perfectly Gaussian, 15.865 per cent of stars would have velocities further than 1σ from each side of the peak value.

If we perform this test for stars with LOS velocities exceeding the peak velocity, this is approximately true: field 18 has 16.2 per cent, and field 12 has 13.3 per cent, of stars greater than 1σ above the peak value. Given the finite size of the sample, $1-2$ per cent difference between the calculated values is expected. In contrast, if we perform the same test for stars with LOS velocities under the peak velocity, substantially different results are observed. In field 18, 21.2 per cent of stars are greater than 1σ below the peak value, while for field 18, this increases to 30.2 per cent. This is significantly more than expected for a perfectly Gaussian distribution.

This asymmetry was not accounted for when fitting Gaussians to these distributions as described in §3.5. Consequently, it is possible that the field kinematics discussed above are slightly biased. To demonstrate this is not the case, new estimates of the aggregate field kinematics are determined by repeating the process described in §3.5.3, but including in this calculation only stars with LOS velocities exceeding a particular velocity threshold, so as to effectively "exclude" the low-LOS-velocity tail from the calculation. If doing so does not change the aggregate field properties derived, we can be satisfied the analysis in §3.6.1 remains unaffected by the asymmetry in the LOS velocity distribution.

The velocity threshold imposed does not take a fixed value; instead, it is varied in 5 km s^{-1} steps for both fields. The most stringent threshold is equal to $V_{\rm LOS} - \sigma_{\rm LOS}$, as reported in Table 3.3: this corresponds to 1σ below the aggregate LOS velocity of the field. The weakest threshold imposed passes all stars with Magellanic membership probabilities $P(\mathrm{MC}|i, \hat{\varphi}, \hat{\phi}) > 30\%$.

In both fields, imposing a LOS velocity threshold introduces small changes to the LOS kinematic properties: as the LOS threshold becomes more stringent, the field aggregate LOS velocity increases, and the LOS velocity dispersion decreases. In field 18, these both change by ~5 km s^{-1}; in field 12, slightly larger shifts (~8 km s^{-1} each) are observed. This is not surprising: excluding LOS velocities below a threshold naturally increases the median LOS velocity of the remaining population; and, by reducing the range of LOS values in the surviving population, naturally decreases its dispersion.

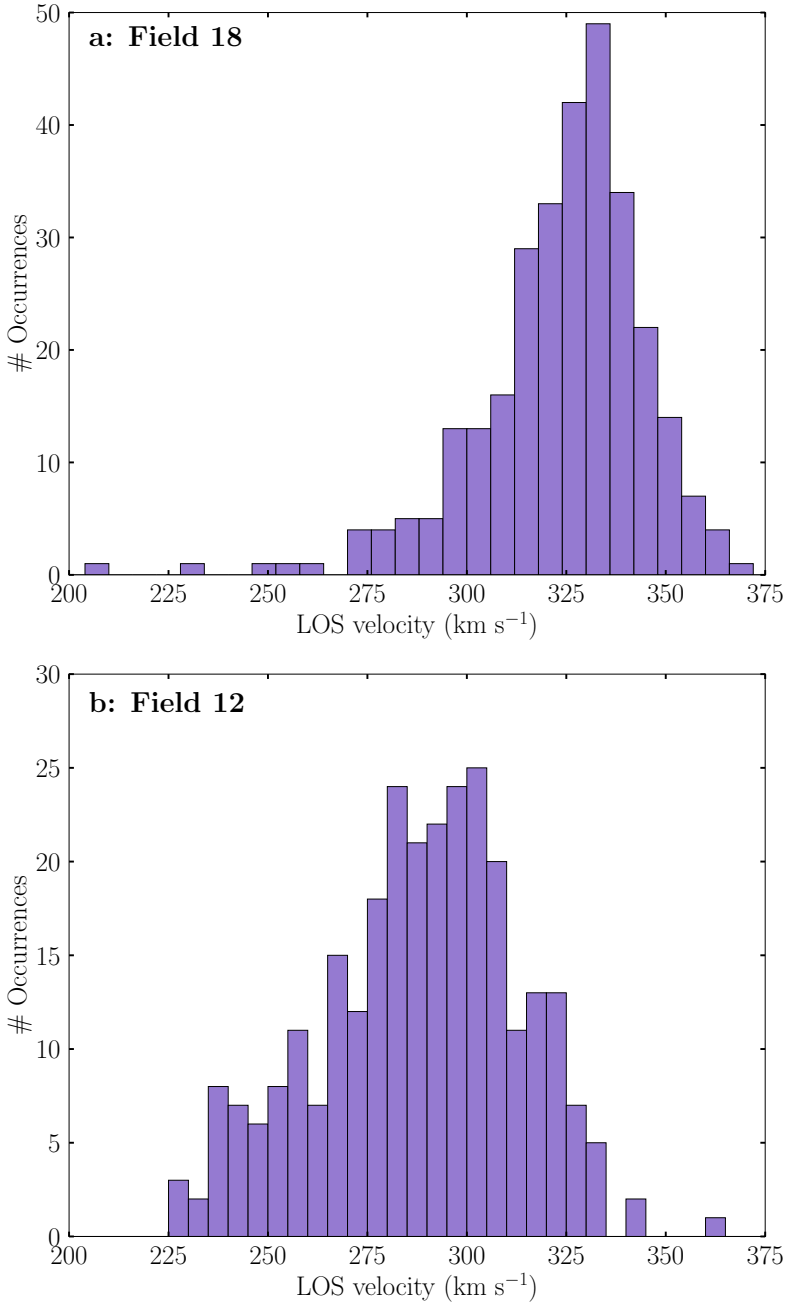

Figure 3.10: Line-of-sight velocity distributions for LMC member stars in fields 18 (panel *a*) and 12 (panel *b*). Both distributions show asymmetry, with tails to lower LOS velocities. This is particularly apparent in field 12, located near the base of a substructure in the northern LMC.

Of greater interest is any effect on the proper motions of the population. The most stringent threshold applied to field 12 (265 km s^{-1}) results in reductions to both proper motion dispersions by ~0.03 mas yr^{-1} (corresponding to differences of ~7 km s^{-1} at the distance of the Clouds). However, as the proper motion components have larger uncertainties than the LOS velocity component, these shifts remain within the 1σ uncertainty of the value obtained when no threshold is applied. In field 18, observed differences in proper motions are even smaller – on the order of ~2 km s^{-1} at the distance of the Clouds – and therefore not significant.

Of more import is whether these small shifts in observed kinematic properties engender differences when transformed into the LMC disk frame. The same transformation as described in §3.6 is performed to generate LMC disk velocities for each set of observed velocities, with uncertainties in both the observed kinematics, and the LMC disk geometry, propagated.

In field 18, the only effect of imposing a LOS velocity threshold is a reduction in the vertical velocity dispersion (σ_z), which drops by ~4 km s^{-1} at the most stringent velocity threshold of 305 km s^{-1}. Considering the dispersion derived without any threshold imposed is 20.6 ± 1.0 km s^{-1}, this represents a ~4σ reduction in the dispersion. All other disk velocities are well within the 1σ uncertainty of the original values. The same pattern is observed in field 12, with a reduction in the vertical velocity dispersion of ~6 km s^{-1} at the most stringent velocity threshold of 265 km s^{-1}. This represents a 3.5σ reduction in the dispersion. While the azimuthal and radial velocity dispersions in this field also drop by a few km s^{-1}, due primarily to the reduced dispersion in the observed proper motions, these also remain within the 1σ uncertainty of the original derived values.

It is no surprise that only the vertical velocity dispersions differ by any substantive amount; the relatively low inclination of the LMC means the LOS velocity dispersion (which is most significantly affected by imposing a LOS velocity threshold) is translated almost directly into the vertical velocity dispersion. Further, despite these reductions, the vertical velocity dispersions calculated remain consistent with the most distant estimates derived by Vasiliev (2018). Thus the conclusions drawn in §3.6.1 are unaffected by the asymmetry in the LOS velocity distribution of the stars.

Having satisfied ourselves that the results in §3.6.1 remain valid, we now turn to analysing the asymmetry itself, and its possible origins. We first check for possible correlations between LOS velocity, and other properties of individual stars, testing proper motions, Gaia G_0 magnitude, on-sky position, and metallicity where available. Unfortunately, the relatively large uncertainties on individual measurements of these quantities are sufficient to mask any such correlations if they exist. Consequently, we instead analyse

aggregate properties of stars with lower and higher LOS velocities – as these aggregate properties have smaller associated uncertainties, any significant differences in the overall kinematics of the two groups should be more clearly apparent. To do this, the same range of LOS velocity thresholds discussed above are used to divide the stars in each field into two subgroups; a "low-velocity" sample containing stars with LOS velocities below the threshold, and a "high-velocity" sample containing stars with LOS velocities that exceed the threshold.

However, each individual star has an uncertainty in its LOS velocity, and this could change how each star is classified between the two subsamples. This would consequently affect the aggregate properties of the two groups. In order to account for this, the observed kinematics of each star are drawn randomly from a Gaussian distribution with width equal to the 1σ uncertainty in its velocity. This process is repeated in order to generate a set of 500 "low-velocity" and "high-velocity" groups for any given threshold, the aggregate properties of which can be compared to one another.

K–S tests are used to determine whether the properties of the high- and low-LOS velocity groups are statistically similar. Tests are performed on the median proper motions, $(G_{\rm BP} - G_{\rm RP})_0$ colour, Gaia G_0 magnitude, on-sky position, metallicity, and fibre number (to confirm no systematic differences linked to the observational setup are present). Two-dimensional K–S tests are used to compare the positions and proper motions of the groups, as these properties are correlated; all other tests are one-dimensional. The dispersions of the two groups are not compared as there are always significantly fewer stars in the low-velocity group; the dispersion calculated is therefore not likely to be representative of the true dispersion of the population. For the properties which are tested, each of the 500 distribution sets is compared, and the median of the resulting p-value distribution assessed. In all cases, this p-value is >0.05, indicating there is no significant difference in the properties of the stars comprising the two subgroups (apart from, by definition, their mean LOS velocities).

In order to better understand the implications of the LOS velocity asymmetry, we transform the aggregate properties of the two groups into the LMC disk frame using the procedure outlined in §3.6. We find that differences exist between the vertical and azimuthal velocity components of the two groups, but the radial velocity of the two groups remains consistent within uncertainty, regardless of the threshold used to separate the groups. This is true of both fields analysed.

By far the most significant difference is in the vertical velocity component (V_z); in both fields, the low-LOS-velocity group has V_z values of ~40 km s^{-1}, indicating motion perpendicular to the disk plane, in a direction roughly towards the Earth. This is primarily

a consequence of the relatively low inclination of the LMC disk, such that differences in LOS velocity naturally correspond to differences in the vertical velocity. Compared to the behaviour of the high-LOS-velocity sample (which has median vertical velocities consistent with 0 km s^{-1}, as expected for an equilibrium stellar disk), the large vertical velocity of the low-velocity sample is indicative of mean motion away from the disk for these stars.

There are also differences in the azimuthal velocity of the two groups. In both fields, the low-velocity group rotates ~25 km s^{-1} more slowly than the high-velocity group, though this difference is barely significant at the 1σ level. The large uncertainties in the azimuthal velocities, which may mask the significance of this difference, are a direct consequence of the large uncertainties in the proper motions of the stars from which the azimuthal velocity is derived. Future Gaia releases, with reduced proper motion uncertainties, will likely clarify whether this small difference is genuinely significant.

The difference in azimuthal velocity of the two groups bears similarities to the signature of a kinematically distinct population of stars discussed in Olsen et al. (2011), which they attribute to infalling SMC stars either moving counter to LMC disk rotation, or located in a plane strongly inclined relative to the LMC disk. However, it is unlikely our low-velocity group is part of the same population. At the large radii of our fields, we would expect any difference in distance associated with the stars being located in very different planes to result in a detectable difference in red clump magnitude, which is not observed. Further, the difference in azimuthal velocity between the two groups is identical in both fields, despite these being located more than 10° apart, suggesting that both groups are likely linked to the LMC disk. At the large galactocentric radii of our fields, the median LMC [Fe/H] abundance of approx. −1 is less easily distinguishable from typical SMC metallicities (Dobbie et al. 2014b).

We speculate that the low-velocity tail of the LOS velocity distribution may be the result of an external perturbation. This is consistent with the fact that there is a higher relative fraction of stars in the low-velocity group in field 12 (which, as discussed above, shows other indications of being perturbed) compared to field 18. While there are other possibilities, it is certainly plausible that an interaction, with either or both of the SMC or Milky Way, could begin to pull stars out of the LMC outer disk in one direction preferentially, generating the non-zero vertical velocity observed for these stars. Numerical models of interactions in the Magellanic system are required to test the veracity of this signature, and its possible links with the northern arm. The MagES collaboration is actively working to follow up this avenue of investigation.

3.6.3 LMC Mass estimate

Under the assumption that stars in the outer LMC disk are following equilibrium or near equilibrium motions[14], it is possible to calculate an estimate for the dynamical mass of the LMC using the azimuthal rotational velocities derived in the preceding analysis. This assumption is likely valid for field 18; but, as discussed above, there are indications of possible non-equilibrium behaviour in field 12. As such, despite the fact that azimuthal velocities for both MagES disk fields are consistent within uncertainty, only information derived from field 18 is used in the following analysis. To determine the dynamical mass, Eq. 3.20 is used.

$$M_{\rm enc} = \frac{RV_{\rm circ}^2}{G} \tag{3.20}$$

Here, $M_{\rm enc}$ is the enclosed mass of the LMC within R kpc of the LMC COM; $G = 4.3007 \times 10^{-6}$ kpc $\mathrm{M}_\odot^{-1}(\mathrm{km\ s^{-1}})^2$; and $V_{\rm circ}$ is the circular velocity (in km s^{-1}) at distance R from the LMC COM. Note that the azimuthal rotation velocity is not $V_{\rm circ}$, the velocity of a tracer on a circular orbit in the equatorial plane; to determine this first requires correction for asymmetric drift. To make this correction, we use Eq. 3.21, taken from van der Marel et al. (2002), which relates azimuthal velocity V_θ to $V_{\rm circ}$.

$$V_{\rm circ}^2 = V_\theta^2 + \frac{R}{R_d}\sigma_{\rm LOS}^2 \tag{3.21}$$

Here, R_d is the disk scale length (which we take as 1.5 kpc from van der Marel et al. 2002) and $\sigma_{\rm LOS}$ is the line of sight velocity dispersion of stars in the field. Note that Eq. 3.21 only applies to the simplified case of an axisymmetric exponential disk system embedded within an isothermal dark halo. Although, as is apparent from Fig. 3.1, axisymmetry breaks down at large distances from the LMC COM in the south, at the location of field 18 in the northern LMC disk, this remains a reasonable assumption.

The circular velocity calculated using the above procedure is 87.7 ± 8.0 km s^{-1}. This is consistent with values reported by vdM14 (91.7 ± 18.8km s^{-1}) and Vasiliev (2018) (~90 km s^{-1}), but moderately lower than the circular velocity reported by W20 (123.6 ± 1.9 km s^{-1}). However, as discussed in §3.6.1, the radial velocity dispersion measured by W20 is $10 - 15$ km s^{-1} larger than those measured by MagES, and more closely reflects inner disk kinematics. By extension, when this is used in the asymmetric drift correction, it results in a significantly larger circular velocity than that derived from the MagES data.

[14] i.e. that the mean V_r and V_z in a field are identically zero.

Using the MagES circular velocity in Eq. 3.20 results in a total enclosed LMC mass, within 10 kpc, of $(1.8 \pm 0.3) \times 10^{10} M_\odot$. To compare this mass to that derived in vdM14, we project their enclosed mass estimate (determined within a radius of 8.7 kpc) out to a distance of 10 kpc. The resulting mass of $(2.1 \pm 0.7) \times 10^{10}$ $M_\odot$ is consistent with our estimate. Assuming that this radius is sufficient to encompass the majority of light from the LMC, a mass-to-light (M/L) ratio for the LMC can be calculated. We calculate the V-band luminosity of the LMC using its absolute magnitude (taken as -18.1 from McConnachie 2012) relative to the absolute magnitude of the Sun (taken as 4.81 from Willmer 2018). Using this with our enclosed mass estimate implies a M/L ratio of 12.5 ± 2.3 $M_\odot/L_\odot$.

The derived mass is low compared to mass measurements derived using more indirect methods, such as perturbations to stellar streams ($\sim 1.4 \times 10^{11}$ $M_\odot$; Erkal et al. 2019), the timing argument ($\sim 2.5 \times 10^{11}$ $M_\odot$; Peñarrubia et al. 2016), or cosmological simulations of similar systems ($\sim 3.4 \times 10^{11}$ $M_\odot$; Shao et al. 2018). This difference is to be expected, as each of the above methods provides the total infall mass of the LMC, including its dark halo. In contrast, the MagES field considered here, despite being at a greater distance from the LMC COM than most previous kinematic estimates, is still located well within the LMC dark halo: studies such as Navarrete et al. (2019) or Munoz et al. (2006) have found likely LMC-associated stars at distances almost three times greater than field 18. As such, the enclosed mass derived simply does not capture a significant fraction of the total LMC mass. If, however, the assumption is made that the LMC rotation curve remains flat out to 29 kpc (the furthest distance LMC-associated stars have been found to date as per Navarrete et al. 2019), and that the LMC is embedded in a typical dark matter halo, the inferred LMC enclosed mass would be $(1.1 \pm 0.2) \times 10^{11}$ $M_\odot$, which is more in line with total infall mass estimates, and the mass calculated under similar assumptions in Wan et al. (2020). In this scenario, the implied M/L ratio of the LMC rises to 58.2 ± 6.8 $M_\odot/L_\odot$.

3.7 Summary

In this paper, we have described the Magellanic Edges Survey (MagES), a spectroscopic survey that, in conjunction with Gaia astrometry, is designed to obtain and interpret 3D stellar kinematics across the Magellanic periphery. Conducted using 2dF+AAOmega at the AAT, it primarily targets red clump stars and will ultimately yield 3D velocities for ~7000 stars in twenty-six two-degree diameter fields in the outskirts of the Clouds, and metallicities for a limited subset with sufficiently high S/N spectra. It will constitute the

largest sample of Magellanic stars with homogeneous 3D velocity information to date, in fields at larger galactocentric radii than most previous studies. In combination, this will provide significant insight into the evolution and interaction history of the Magellanic system.

As an early science demonstration, we present results for two MagES fields in the outer northern disk of the LMC. One field is located near the base of an arm-like feature to the north of the LMC first discovered by Mackey et al. (2016), and has 3D kinematics indicative of perturbation from an equilibrium disk. It has a non-zero radial velocity outwards in the LMC disk plane, in the direction towards the substructure, and an elevated azimuthal velocity dispersion. Further, it has a significant (~44 km s^{-1}) radial velocity dispersion; which, as illustrated by W20, can be caused by LMC/MW/SMC interactions. The other field, located ~10° from any known photometric substructures, behaves as expected for an equilibrium disk. Its kinematics are consistent with literature values derived from similar populations closer to the LMC centre, indicating the rotation curve of the LMC remains flat even at very large radii. The kinematics derived for both fields are robust against moderate changes to the assumed geometry of the LMC disk.

Both fields display an asymmetric LOS velocity distribution, with tails to low LOS velocities, though this is more pronounced in field 12. The asymmetry does not affect the field-aggregate properties discussed in §3.6.1, and K–S tests confirm no statistically significant differences exist between stars with lower and higher LOS velocities. However, when transformed into the LMC disk frame, stars with low LOS velocities are found to have vertical velocities of ~40 km s^{-1}, indicative of a subset of stars being perturbed away from the assumed LMC disk plane. As the asymmetry is strongest in the field nearest the arm-like substructure, we hypothesise that it is a signature of interaction. Further analysis in conjunction with dynamical models is required to fully understand this behaviour.

The kinematics of the "undisturbed" field are used to estimate the LMC mass; one of the most distant estimates derived using stellar kinematics. The derived circular velocity of the stars is 87.7 ± 8.0 km s^{-1}, with a resulting enclosed mass of $(1.8 \pm 0.3) \times 10^{10}$ $M_\odot$ within ~10 kpc. This is consistent with other enclosed mass values derived using stellar kinematics (e.g. vdM14); but, as is typical for such estimates, is lower than masses derived using more indirect methods, for example perturbations to orbits of MW stellar streams, which are sensitive to the total halo mass.

3.8 Appendix: Effect of uncertainties on maximum likelihood results

In Section 3.5, several maximum likelihood steps are used to determine fit parameters; each of which, in addition to returning parameter values that maximize the given likelihood function, also provide 1σ confidence intervals for the fit parameters. In the main analysis, we always utilise the best-fit values for each parameter in subsequent steps, with the inherent assumption that the effect of these uncertainties is negligible. Here, we confirm this assumption is reasonable.

3.8.1 Effect of uncertainties in the contamination model

The calculation in §3.5.2, to determine initial estimates for the properties of Magellanic kinematic peaks, requires the use of parameters that describe the expected Milky Way foreground contamination, derived from the Besançon models in §3.5.1. However, each of these Milky Way contamination parameters – i.e. those within $\hat{\phi}$, comprised of v_m, $\mu_{\delta,m}$, $\mu_{\alpha,m}$, $\sigma_{v,m}$, $\sigma_{\delta,m}$, $\sigma_{\alpha,m}$, ρ_m, and η_m – has an associated 1σ uncertainty. The effect of varying these parameters within their uncertainties on the initial estimate of the parameters defining the Magellanic peak is tested to ensure it is negligible.

We do this by calculating the Magellanic peak parameters 500 times, each time using Milky Way contamination parameters drawn randomly from Gaussian distributions centred on the best-fitting parameter values, with width equal to the 1σ equivalent uncertainty in the parameter. The resulting distributions of each Magellanic peak parameter are inspected, and the standard deviation calculated as an estimate of the uncertainty introduced by varying the Milky Way contamination parameters.

In every case, we find the distributions of Magellanic peak parameters introduced by varying the contamination model input parameters, are much narrower than the 1σ uncertainties in the Magellanic peak parameters when determined using the best-fitting contamination model as input. In other words, the dominant source of uncertainty in the Magellanic peak parameters is that driven by observational uncertainties in the stellar kinematics, and not uncertainties associated with the parameters of the model contaminant population; validating the assumption made in the text.

3.8.2 Effect of uncertainties in Magellanic kinematic peak properties

The initial estimates for the Magellanic peak properties are used to calculate the probability of each star being associated with the Clouds; which is subsequently used to calculate the aggregate kinematics of each field in §3.5.3. As discussed in §3.8.1, each of these parameters has associated uncertainty. We test the effect of varying these parameters within their uncertainties on the membership probability of each star, and the field aggregate properties, to ensure this is negligible.

To begin, the membership probability $P(\mathrm{MC}|i, \varphi, \hat{\phi})$ of each star is calculated 500 times, each time using Magellanic peak parameters within φ – that is, v_{MC}, $\mu_{\delta,\mathrm{MC}}$, $\mu_{\alpha,\mathrm{MC}}$, $\sigma_{v,\mathrm{MC}}$, $\sigma_{\delta,\mathrm{MC}}$, $\sigma_{\alpha,\mathrm{pk}}$, and ρ_{MC} – drawn randomly from Gaussian distributions centred on the best-fitting parameters, with width equal to the 1σ uncertainties on the parameters. As $P(\mathrm{MC}|i, \varphi, \hat{\phi})$ requires information from both LOS velocity and proper motion, these values are varied simultaneously. The resulting $P(\mathrm{MC}|i, \varphi, \hat{\phi})$ distributions are all relatively narrow; we characterise the width of these distributions as half the difference between the minimum and maximum $P(\mathrm{MC}|i, \varphi, \hat{\phi})$ values calculated for each star.

We then calculate the field aggregate properties as per Eq. 3.15 500 times. Each time, membership probabilities for all stars are drawn randomly from a Gaussian distribution centred on the original $P(\mathrm{MC}|i, \hat{\varphi}, \hat{\phi})$ value assigned to each star, with width equal to the characteristic width of the $P(\mathrm{MC}|i, \varphi, \hat{\phi})$ distributions.

In every case, we find that the distributions of each field aggregate property introduced by varying the membership probability, are much narrower than the 1σ uncertainties in the aggregate properties when determined using the best-fitting membership probabilities as input. In other words, the dominant source of uncertainty in the field aggregate parameters is that driven by observational uncertainties in the stellar kinematics, and not uncertainties associated with the membership probabilities of each individual star, or initial peak parameter estimates.

Chapter 4

Formation of the LMC's northern arm

> It seems I have encountered a conundrum... We have no choice but to find out the truth of the matter ourselves.
>
> Sarutobi Sasuke

This chapter is submitted to The Monthly Notices of the Royal Astronomical Society, and is currently under (re-)review, as **L. R. Cullinane**, A. D. Mackey, G. S. Da Costa, D. Erkal, S. E. Koposov, and V. Belokurov, 2021. *The Magellanic Edges Survey II. Formation of the LMC's northern arm.* The paper is reproduced here in full with minor formatting changes to make it consistent with the rest of the work in this thesis.

4.1 Abstract

The highly-substructured outskirts of the Magellanic Clouds provide ideal locations for studying the complex interaction history between both Clouds and the Milky Way (MW). In this paper, we investigate the origin of a $>20^\circ$ long arm-like feature in the northern outskirts of the Large Magellanic Cloud (LMC) using data from the Magellanic Edges Survey (MagES) and Gaia EDR3. We find that the arm has a similar geometry and metallicity to the nearby outer LMC disk, indicating that it is comprised of perturbed disk material. Whilst the azimuthal velocity and velocity dispersions along the arm are consistent with those in the outer LMC, the in-plane radial velocity and out-of-plane vertical velocity are significantly perturbed from equilibrium disk kinematics. Comparison

with a new suite of dynamical models of the Magellanic/MW system reveals the tidal force of the MW during the LMC's infall is likely responsible for the observed increasing out-of-plane velocity along the arm. Our models indicate close LMC/SMC interactions within the past ~Gyr, particularly the SMC's pericentric passage ~150 Myr ago and a recent SMC crossing of the LMC disk plane ~400 Myr ago, likely do not perturb stars that today comprise the arm, but are instead potentially responsible for structures in the western LMC disk. Historical interactions with the SMC prior to ~1 Gyr ago may be required to explain some of the observed kinematic properties of the arm, in particular the observed strongly negative in-plane radial velocity.

4.2 Introduction

The Large and Small Magellanic Clouds (LMC/SMC), as the closest pair of interacting dwarf satellites of the Milky Way (at distances of ~50 and ~60 kpc respectively: Pietrzyński et al. 2019; Graczyk et al. 2020), are ideally situated for detailed study of the influence of tidal interactions on galaxy evolution. The SMC has long been known to be heavily distorted, with a line of sight depth of up to 20 kpc (e.g. Hatzidimitriou and Hawkins 1989; Ripepi et al. 2017) which varies as a function of position angle. It possesses an asymmetric, irregular morphology exhibiting striking differences between the locations of young and old stars (e.g. El Youssoufi et al. 2019; Mackey et al. 2018), and kinematic evidence for tidal expansion (e.g. De Leo et al. 2020; Zivick et al. 2021). The LMC, although more kinematically ordered than the SMC, also displays substantial deviations from a simple rotating disk structure. It has multiple warps (Olsen and Salyk 2002; Choi et al. 2018b), sharp truncations in the outer disk (Mackey et al. 2018), ring-like overdensities (Kunkel et al. 1997; Choi et al. 2018a), and an off-centre stellar bar (e.g. van der Marel and Cioni 2001). Each of these features encodes valuable information about the extensive interaction history of the Clouds.

Precise measurements of the masses and orbits of the LMC and SMC, and their internal kinematics, are key to understanding how interactions between both Clouds, and the Milky Way, form the disturbed features observed. While the Clouds are strongly suspected to have experienced a close passage ~150 Myr ago (Zivick et al. 2018), and are likely just past pericentre on their first infall into the Milky Way potential (Kallivayalil et al. 2013), particulars of their interactions beyond this remain relatively unconstrained. Recent studies of the star-formation history of the Clouds provide evidence of potential past interactions, with spikes in the global star formation rate of both Clouds ~$1-2$ Gyr ago (e.g. Rubele et al. 2018; Ruiz-Lara et al. 2020). However, these studies have lower

time-resolution than dynamical studies, and alone provide limited constraints on, for example, the impact parameter or the relative location and orientation of the Clouds during close interactions.

One useful method to explore past dynamical interactions is to study stars in the outskirts of the Clouds. These stars are most strongly susceptible to external perturbations, and the resulting structural and kinematic signatures are more persistent compared to the central regions, where dynamical timescales are much shorter. Recent studies of the Clouds using deep photometric data (e.g. Mackey et al. 2016, 2018; Pieres et al. 2017) and multi-dimensional phase-space information from Gaia (e.g. Belokurov and Erkal 2019; Gaia Collaboration et al. 2021c) have revealed a wealth of substructure in the periphery of the Magellanic system. Many of these features are thought to be due to dynamical perturbation and, as a result, are ideal targets for studying the history of interactions between the LMC and SMC, and between the Clouds and the Milky Way.

Of particular interest is a large arm-like feature to the north of the LMC discovered in first year data from the Dark Energy Survey (DES) by Mackey et al. (2016 henceforth referred to as M16). The feature begins ~13° due north of the LMC centre where it appears to join the northern outskirts of the LMC disk, and has an on-sky width of ~2°. Initial photometric analysis, limited by the extent of the DES footprint, traced the substructure for ~12.5° eastward. Utilising astrometric proper motion and parallax information provided by Gaia DR2, Belokurov and Erkal (2019) were also able to recover the feature, tracing it for at least an additional ~10° beyond the initial discovery.

Several papers have attempted to elucidate the origin of the feature using dynamical models, with varying conclusions. M16 present an N-body model of the LMC undergoing infall over ~2 Gyr into a three-component MW potential as described in Gómez et al. (2015). That simulation produces a qualitatively similar stream of debris in the northern outskirts of the LMC disk, due solely to the tidal influence of the Milky Way (i.e., without requiring the presence of the SMC). In contrast, Besla et al. (2016) present N-body models of an LMC and SMC interacting in isolation for 6 Gyr, before undergoing infall into a MW halo potential for 1 Gyr. Even prior to entering the MW potential, qualitatively similar asymmetrical spiral structures, formed in the LMC disk after repeated SMC passages, are seen in the LMC's northern outskirts; these persist during infall to the MW potential. Belokurov and Erkal (2019) also show a number of simpler models of tracer particles within high-mass and low-mass LMC potentials, undergoing infall for 1 Gyr into the three-component MW potential described in Bovy (2015). Models both with and without the presence of an SMC potential form qualitatively similar features in the northern outskirts of the LMC, with the best qualitative match occurring due to the combined influence of

both the SMC and MW. With multiple scenarios each reproducing qualitatively similar structures to that observed, the origin of the feature remains uncertain.

However, these studies have been fundamentally limited by a lack of kinematic data along the arm. This restricts analysis to only qualitatively reproducing the feature's shape which – as demonstrated above – results in ambiguity regarding its origin. Indeed, M16 note that line-of-sight (LOS) velocities would assist in distinguishing between material tidally stripped from the LMC, and overdense features in the extended LMC disk. An investigation into the kinematics of the northern arm is therefore critical.

In this paper, we present a comprehensive analysis of the LMC's northern arm using data from the Magellanic Edges Survey (MagES: Cullinane et al. 2020). This spectroscopic survey targets red clump (RC) and red giant branch (RGB) stars in the extreme Magellanic periphery, using the 2dF/AAOmega instrument (Lewis et al. 2002; Sharp et al. 2006) on the 3.9 m Anglo-Australian Telescope (AAT) at Siding Spring Observatory. In conjunction with Gaia astrometry, it is the first large-scale survey to study 3D kinematics in the outskirts of the Clouds. MagES fields are specifically selected to cover low-surface-brightness substructures in the Magellanic periphery – including the northern arm. With seven fields located across the length of the feature, providing 3D kinematics for hundreds of individual stars, detailed study of the arm's dynamical properties becomes possible.

The paper is arranged as follows. Section 4.3 presents an overview of the data, and §4.4 describes the derived kinematic, structural, and abundance properties of the feature. In §4.5 we present new dynamical models of the LMC and SMC undergoing infall into the Milky Way potential, aimed at quantitatively reproducing the kinematics of the northern arm, and discuss the main implications for the origin of this structure. Our conclusions are presented in §4.6.

4.3 Data

MagES utilises the 2dF multi-object fibre positioner, and the dual-beam AAOmega spectrograph on the AAT. The 2dF positioner allows for the observation of ~350 science targets per 2 degree diameter field. As described in Cullinane et al. (2020 henceforth referred to as Paper I), we configure the blue arm on AAOmega with the 1500V grating, to give coverage of the MgIb triplet with resolution R~3700, and the red arm with the 1700D grating to give coverage of the near-infrared CaII triplet with R~10000. Paper I also outlines in detail the target selection procedures, observation characteristics, and data reduction pipeline for MagES; here we briefly present details of the observations specific to the northern arm.

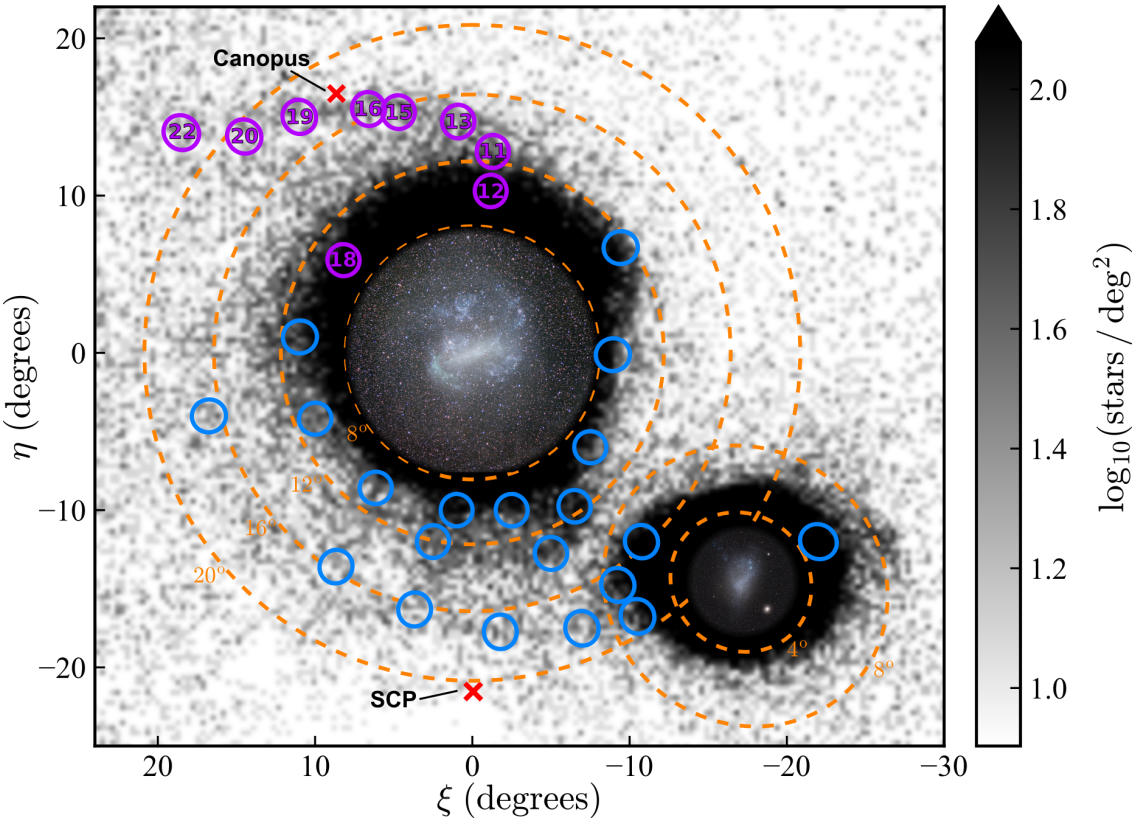

Figure 4.1: Location of observed MagES fields across the Magellanic periphery. Purple circles indicate fields along the LMC's northern arm analysed in this paper, with blue circles indicating other MagES fields. The background image shows the log density of Magellanic red clump and red giant stars per square degree, selected from Gaia DR2 (the target catalogue from which most MagES stars are drawn) as per Belokurov and Erkal (2019). On this map, north is up and east is to the left; (η, ξ) are coordinates in a tangent-plane projection centred on the LMC ($\alpha_0 = 82.25°$, $\delta_0 = -69.5°$). Orange dashed circles mark angular separations of 8°, 12°, 16° and 20° from the LMC centre and 4°, 8° from the SMC centre. The red x-signs mark the location of Canopus – the second brightest star in the sky, which limits MagES field placement on the northern arm to avoid spectral contamination from scattered light – and the south celestial pole.

Seven MagES fields are located along the arm; field positions are shown in Fig. 4.1. We note that with the exception of field 22 (as well as fields 12 and 18 located in the northern LMC disk) all fields along the arm were observed prior to the release of Gaia DR2, and thus selection for those fields was performed without using parallax and proper motion information. As a consequence, the selection efficiency for true Magellanic members in these fields is relatively low – these correspond to **D** and **M** fields as defined in Paper I. We discuss the implications of this in greater detail below.

Reduction of the spectra using the `2dFDR` pipeline, and derivation of LOS velocities, are described in Paper I. Stars with heliocentric velocity estimates are cross-matched

against the Gaia EDR3 catalogue[15], and further quality cuts based on Gaia parameters `ruwe`<1.4 and $C^*<4\sigma_{C^*}$[16] applied.

The resulting sample of stars includes both true Magellanic stars, and foreground contaminants. We use a statistical framework, described in detail in Paper I, to probabilistically associate stars, based on their kinematics, to either the Clouds, or one of several possible Milky Way contaminant populations. These association probabilities are used to weight the fitting of a multi-dimensional Gaussian distribution describing the aggregate Magellanic kinematic properties of each field: the LOS velocity ($V_{\rm LOS}$) and dispersion ($\sigma_{\rm LOS}$), plus the two components of proper motion (μ_α, μ_δ)[17] and their dispersions (σ_α, σ_δ). We assume there is no covariance between the LOS velocity and either proper motion component, but do account for covariance between the two proper motion components as presented in Gaia EDR3. Fitting is performed using the Markov Chain Monte Carlo ensemble sampler EMCEE (Foreman-Mackey et al. 2013) in order to maximise the log-likelihood of the Gaussian model given the data; we report the 68 per cent confidence interval as the 1σ uncertainty in each of the six fitted parameters. As part of this process, we additionally obtain a fitted estimate of the total fraction of likely Magellanic stars per field.

Table 4.1 provides the inferred kinematic properties for each of the seven fields along the northern arm, as well as the number of stars in the field with an individual probability $P_i \geq 50\%$ of being associated with the Clouds. This number is typically very similar ($\pm 1-2$ stars) to that inferred from the fitted total fraction of Magellanic stars. In each case, the number of likely Magellanic stars is significantly lower than the total number of stars observed in the field. This is primarily due to the relatively inefficient target selection used in all fields except field 22 (and disk fields 12 and 18 as discussed above). These fields were observed prior to the release of Gaia DR2, and thus target selection was based only on colour-magnitude diagram (CMD) position. As there is moderate Milky Way contamination within the selection boxes used to isolate Magellanic red clump stars (see Fig. 3.2), a significant fraction of the targets observed in these fields are not genuinely Magellanic members. Fields observed later in the survey, after the release of Gaia DR2 (**G** fields), use updated target selection procedures that incorporate kinematic priors, and consequently suffer far less from contamination by non-members. This is demonstrated in field 22, which uses the updated selection procedure. Despite being located near the end of the arm – where the density of Magellanic stars is intrinsically low, and the density of

[15] While Paper I describes cross-matching against Gaia DR2, we have updated our procedures to incorporate the latest astrometry from Gaia EDR3 (Gaia Collaboration et al. 2021b).

[16] C^* and σ_{C^*} are defined using Eqs. 6 and 18 of Riello et al. (2021) respectively.

[17] μ_α refers to proper motion in the α direction with the usual $\cos(\delta)$ correction, i.e. `PMRA` from the Gaia EDR3 source catalogue.

contaminants is high due to the field's proximity to the Galactic plane – a comparable number of Magellanic stars are detected as in e.g. field 15, located much closer to the LMC disk in areas where the density of members is significantly higher. Table 4.1 also provides kinematic data for two fields in the northern LMC disk located close to the northern arm, previously discussed in Paper I and re-analysed using Gaia EDR3 data.

Notable in Table 4.1 is field 20, which contains no stars with a significant probability of being Magellanic. In addition to using the relatively inefficient CMD-only selection procedure, the field centre is ~1° offset from the feature track. This offset was not apparent when the field was initially observed in 2017, as at the time it was located at the extreme limit of the known structure. It is only with astrometric cuts as afforded by Gaia that the feature could be traced further, revealing the offset. As a result, no stars in this field are convincingly Magellanic in origin, and we therefore exclude this field from further analysis.

In addition to kinematic properties, MagES also reports [Fe/H] estimates for sufficiently bright red giant branch stars, derived from the equivalent width of the 8542Å and 8662Å CaII triplet lines (see Paper I and Da Costa 2016 for details). However, such stars are only included in the target selection for field 22 along the arm (as well as fields 12 and 18, previously described in Paper I). For the fainter red clump stars observed in the remaining fields along the arm, the S/N for any individual star is too low to accurately measure the equivalent width of the two lines, particularly as the 8662Å line is within a region of the spectrum relatively heavily contaminated by night sky emission. Therefore, in order to derive metallicity estimates for these fields, spectra for likely ($P_i \geq 50\%$) Magellanic stars are shifted into the rest frame using their (geocentric) LOS velocities and then stacked to create a single "representative" RC spectrum for the field. This increases the contrast of the two CaII lines relative to the (stochastically over- or under-subtracted) residual night-sky emission, allowing for equivalent width measurements to be performed. As the stacked clump stars only occupy a small magnitude range, stacking spectra is not expected to substantially bias the derived equivalent widths, and the resulting [Fe/H] estimates are expected to tend towards the mean metallicity within a given field. All metallicity estimates are assumed to have uncertainties of 0.2 dex (we refer the interested reader to Paper I for details).

4.3.1 An arm-like coordinate system

For the following analysis, it is convenient to have a coordinate system in which the northern arm, as projected on the sky, is straight – similar to coordinate systems used

Table 4.1: MagES fields along the northern arm and in the nearby northern LMC disk. Columns give the field number and classification as described in Paper I; location of the field centre as RA(α), DEC(δ) in J2000.0; on-sky distance of the field from the centre of the LMC ($R_{\rm LMC}$), number of likely Magellanic stars per field, and aggregate kinematic parameters (described in §4.3).

Field (Class)	RA	DEC	$R_{\rm LMC}$ (°)	$N_{\rm Magellanic}$ (P_i>50%)	$V_{\rm LOS}$ (km s^{-1})	$\sigma_{\rm LOS}$ (km s^{-1})	μ_α (mas yr^{-1})	σ_α (mas yr^{-1})	μ_δ (mas yr^{-1})	σ_δ (mas yr^{-1})
11 (D)	05 19 42.63	−56 53 06.88	12.7	75	280.8 ± 2.2	17.2 ± 2.0	1.72 ± 0.03	0.13 ± 0.03	0.06 ± 0.04	0.24 ± 0.03
13 (D)	05 35 05.69	−55 06 03.11	14.6	38	294.3 ± 1.7	8.0 ± 1.9	1.58 ± 0.04	0.12 ± 0.06	-0.03 ± 0.04	0.16 ± 0.06
15 (D)	06 00 07.40	−541753.14	16.0	32	311.9 ± 2.7	12.6 ± 2.1	1.50 ± 0.04	0.09 ± 0.06	0.12 ± 0.04	0.06 ± 0.05
16 (D)	06 12 13.07	−535232.45	16.8	25	323.2 ± 2.0	8.3 ± 1.7	1.50 ± 0.05	0.11 ± 0.07	0.24 ± 0.04	0.07 ± 0.06
19 (M)	06 40 29.00	−532904.00	18.6	13	351.3 ± 4.8	14.5 ± 4.5	1.16 ± 0.09	0.23 ± 0.10	0.57 ± 0.07	0.13 ± 0.09
20 (M)	07 04 01.00	−533701.00	19.9	0	-	-	-	-	-	-
22 (G)	07 25 34.00	−520452.00	22.8	27	372.9 ± 1.6	7.1 ± 1.3	1.15 ± 0.03	0.06 ± 0.04	0.71 ± 0.02	0.04 ± 0.03
18 (G)	06 40 00.00	−623000.00	10.7	299	324.5 ± 1.2	20.3 ± 0.9	1.49 ± 0.01	0.11 ± 0.01	1.00 ± 0.01	0.12 ± 0.01
12 (G)	05 20 00.00	−591800.00	10.3	284	287.1 ± 1.5	24.8 ± 1.1	1.78 ± 0.01	0.12 ± 0.01	0.20 ± 0.01	0.19 ± 0.01

to describe stellar streams in the MW halo. However, while coordinate systems for most halo streams can be derived by assuming that the stream follows a great circle on the sky, this is not the case for the northern arm. Consequently, in this section we describe derivation of a custom coordinate system which follows the track of the structure on the sky, with the origin of the feature nearest the LMC disk. In this derivation, we neglect uncertainties on the position of each individual star, as these are negligibly small (~0.15" in each component).

To locate the feature, we use a catalogue of Magellanic red clump and red giant branch stars selected from Gaia DR2 according to Belokurov and Erkal (2019), which incorporates astrometric, photometric, and quality cuts. This catalogue provides a relatively clean selection of Magellanic stars with contiguous coverage across the entire length of the arm. We calculate an orthographic projection of the stars into Cartesian X, Y coordinates, as per Eq. 2 of Gaia Collaboration et al. (2018c), repeated here as Eq. 4.1. Here, $(\alpha_0, \delta_0 = 79.88°, -69.59°)$: the LMC centre-of-mass (COM) position reported by van der Marel and Kallivayalil (2014 henceforth referred to as vdM14) for their "PMs+Old vLOS Sample". This is a kinematic centre, derived from a simultaneous fit of HST field-aggregate proper motions, combined with LOS velocities for an "old"[18] stellar sample. This is as similar as possible to the data used in the present work.

$$\begin{aligned} X &= -\cos(\delta)\sin(\alpha - \alpha_0) \\ Y &= \sin(\delta)\cos(\delta_0) - \cos(\delta)\sin(\delta_0)\cos(\alpha - \alpha_0) \end{aligned} \tag{4.1}$$

To describe the feature, we select stars in the region $-20<X<0.8$ and $10<Y<18$, as seen in Fig. 4.2. In addition to containing stars associated with the northern arm feature, this region also includes a significant number of stars associated with the outer LMC disk, the high density of which necessitates masking before fitting the northern arm itself. All stars within the solid selection box in panel *a* of Fig. 4.2 are masked. Additionally, we mask stars within a two-degree diameter circle centred on the Carina dwarf galaxy $(\alpha_C, \delta_C = 100.40°, -50.97°)$, just north of the feature; many stars associated with the Carina dwarf pass the selection criteria described in Belokurov and Erkal (2019).

Remaining stars are binned into $0.4° \times 0.4°$ bins to smooth their distribution; smaller bins contain too few stars near the low-density end of the feature, while larger bins do not sufficiently resolve the feature. We describe the resulting binned distribution Z by a Gaussian profile in Y, as in Eq. 4.2, where the peak height (A_Y), centre (Y_T), and width

[18] Comprised of carbon stars, AGB and RGB stars that are predominantly older than 1-2 Gyr and therefore similar in age to the red clump population.

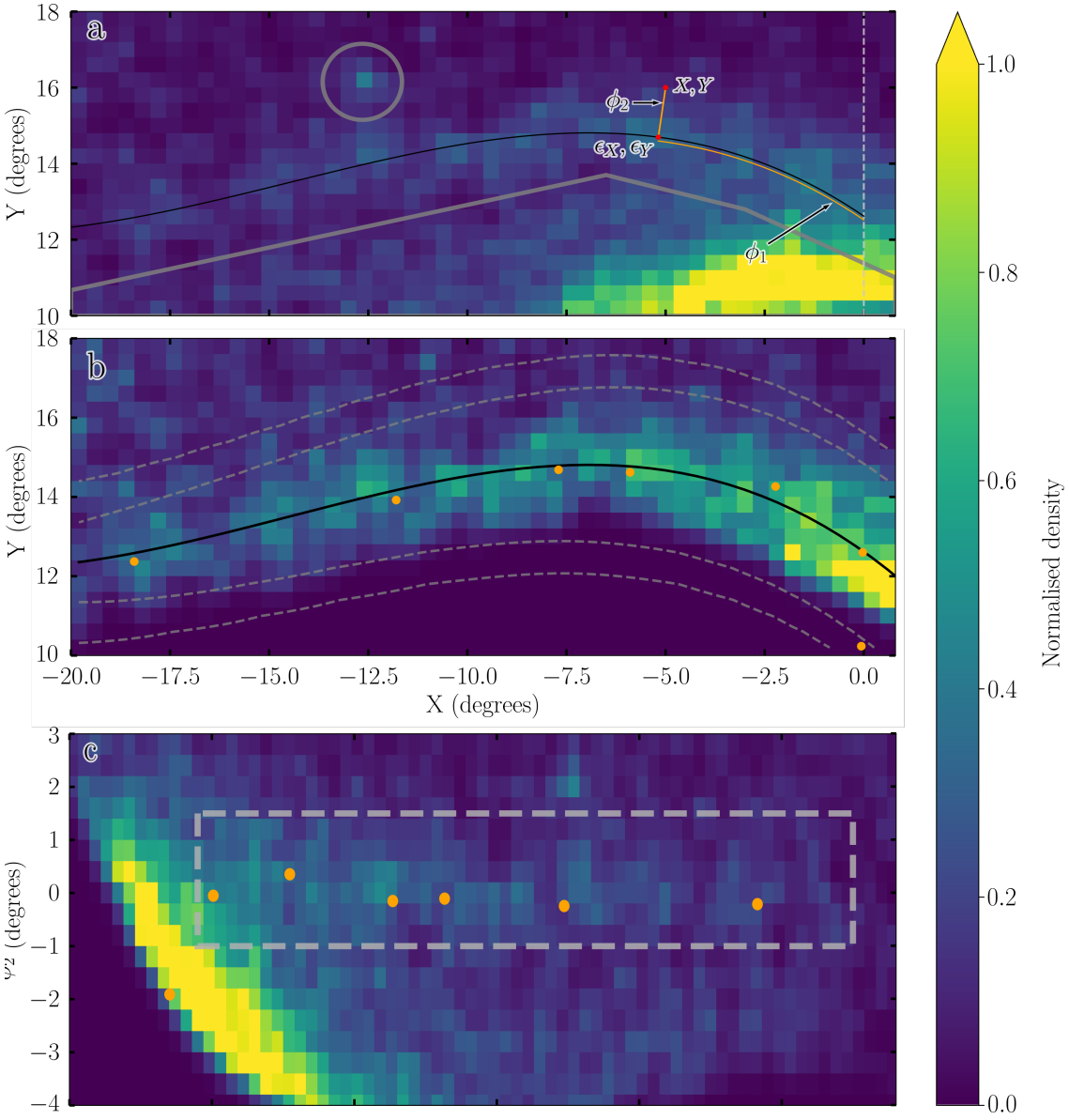

Figure 4.2: Normalised density of red clump and red giant branch stars, selected as per Belokurov and Erkal (2019), in the region surrounding the northern arm, used to derive a feature coordinate system. Panels *a* and *b* have data binned in $0.4° \times 0.4°$ squares within an orthographic projection in Cartesian coordinates. Panel *a* shows the full selection of stars, with solid grey lines indicating the regions surrounding the LMC disk and the Carina dwarf galaxy masked prior to fitting the feature track. Also shown is an example demonstrating the calculation of the two feature coordinates (ϕ_1 and ϕ_2) for any point (X, Y) in the feature; (ϵ_X, ϵ_Y) is the nearest point on the feature track. Panel *b* shows the post-masking data used in the fitting routine. The best-fitting polynomial (as described in Eq. 4.3) is shown in solid black, with fitted 1σ and 2σ contours represented by dashed grey lines. Centres of MagES fields along the arm are overplotted in orange; the fitted feature track passes close to the centre of each field. Panel *c* shows the full data selection after transformation into the feature coordinates. In this coordinate system, the feature track is a straight line at $\phi_2 = 0°$. The selection box used to describe the feature location is shown in dashed grey.

(σ_Y) are each allowed to vary as an nth-order polynomial as a function of X.

$$
\begin{aligned}
Z(X,Y) &= A_Y(X)\exp\left[\frac{-\left(Y-Y_\mathrm{T}\left(X\right)\right)^2}{2\left(\sigma_Y\left(X\right)\right)^2}\right] \\
A_Y(X) &= a_nX + a_{n-1}X^{n-1} + ... + a_0 \\
\sigma_Y(X) &= b_nX + b_{n-1}X^{n-1} + ... + b_0 \\
Y_\mathrm{T}(X) &= c_nX + c_{n-1}X^{n-1} + ... + c_0
\end{aligned}
\tag{4.2}
$$

We perform a least-squares fit to the polynomial coefficients, for all combinations of nth-order polynomials up to a maximum of 2$^{\mathrm{nd}}$ order in A_Y, 2$^{\mathrm{nd}}$ order in σ_Y, and 5$^{\mathrm{th}}$ order in Y_T; polynomials of higher orders overfit the data, resulting in unrealistic contours particularly near the ends of the feature. The set of coefficients with the lowest sum-of-square residuals are taken as the final track parameters for the arm: Eq. 4.3 gives the resulting best-fit equations describing the on-sky feature track.

$$
\begin{aligned}
A_Y(X) &= 2.642\times10^{-2}X + 0.7229 \\
\sigma_Y(X) &= 8.198\times10^{-3}X + 1.168 \\
Y_\mathrm{T}(X) &= -3.386\times10^{-6}X^4 - 1.669\times10^{-3}X^3 \\
&\quad - 6.825\times10^{-2}X^2 - 0.7099X + 12.62
\end{aligned}
\tag{4.3}
$$

We note coefficients describing the variation in width and peak height are, for the process of deriving the feature track, nuisance parameters; it is the polynomial describing the centre position that is of interest. However, we do find the peak height (A_Y), indicative of the stellar density, decreases by ~70%, and the feature width (σ_Y) decreases by ~14% along the length of the structure. The track and 1σ width contours from the fit are shown in panel *b* of Fig. 4.2, with the MagES field centres marked in orange. Whilst the polynomial fit is not at all constrained by the locations of MagES fields – which were deliberately selected to be centred on the feature – it nonetheless passes very closely to each field centre. We define the origin, where the arm appears to meet the LMC disk, to sit at $X = 0°$.

We use the best-fit track to define a coordinate system for the arm, with components denoted ϕ_1 and ϕ_2, in which the central track is a straight line at $\phi_2 = 0$. For each star, we determine the nearest point on the track given by Eq. 4.3 (which we refer to as ϵ). The coordinate ϕ_1 is defined as the distance (or line integral) along Eq. 4.3 from $X = 0$ to

Table 4.2: Orthographic Cartesian coordinates centred on the LMC COM, and feature coordinates along and across the northern arm (calculated as in §4.3.1) for MagES fields.

Field	X (deg)	Y (deg)	ϕ_1 (deg)	ϕ_2 (deg)
11	−0.03	12.60	0.05	−0.05
13	−2.23	14.26	2.74	0.36
15	−5.89	14.62	6.35	−0.15
16	−7.70	14.68	8.17	−0.10
19	−11.80	13.92	12.36	−0.24
22	−18.40	12.37	19.15	−0.21

$X = \epsilon_X$. We calculate the direction normal to Eq. 4.3 at ϵ, and define ϕ_2 as the distance along the normal vector from ϵ to the star's location[19]. The outcome of this process is a set of ϕ_1, ϕ_2 coordinates for each star; the resulting density plot for stars along the northern arm is shown in panel *c* of Fig. 4.2. For convenience, we also transform the MagES field centres into the feature coordinate system. Table 4.2 presents the location of MagES fields along the arm in both Cartesian and feature coordinates. When selecting member stars later in our analysis, we define a box of width 2.5° in ϕ_2, between $-0.5° \leq \phi_1 \leq 25°$ as in panel *c* of Fig. 4.2, which describes the location of the feature.

4.4 Observed Properties of the Northern Arm

4.4.1 Metallicity

[Fe/H] measurements for MagES fields along the arm, as a function of both LMC galactocentric radius (R) and ϕ_1 distance along the feature, are presented in Fig. 4.3. We find very weak ($<2\sigma$) evidence for a negative metallicity gradient along the feature when performing a least-squares fit to the stacked field measurements, which are expected to trend to the field mean. The gradients we derive (-0.015 ± 0.007 dex per degree in R, and -0.025 ± 0.014 dex per degree in ϕ_1) both imply a drop from [Fe/H]~−0.9 at the base of the feature, to [Fe/H]~−1.2 at the most distant measured point (R~23°, ϕ_1~20°). Whilst only fields 22 and 12 have multiple metallicity measurements, we do note in these fields a relatively large scatter in [Fe/H], with metallicity measurements covering an ~0.5 dex range even in the outermost field 22. We discuss the implications of the potential decrease in mean [Fe/H] along the feature on estimates of its structure using RC photometry in

[19] We note this procedure does not result in a 1:1 mapping of X, Y to ϕ_1,ϕ_2 across the entire X, Y domain, as due to the shape of the feature normal vectors to Eq. 4.3 for negative values of ϕ_2 eventually intersect. However, these intersections only occur at relatively large negative values of ϕ_2, within the LMC disk where ϕ_1,ϕ_2 coordinates are not meaningful. In the vicinity of the northern arm X, Y locations are mapped to unique ϕ_1,ϕ_2 coordinates.

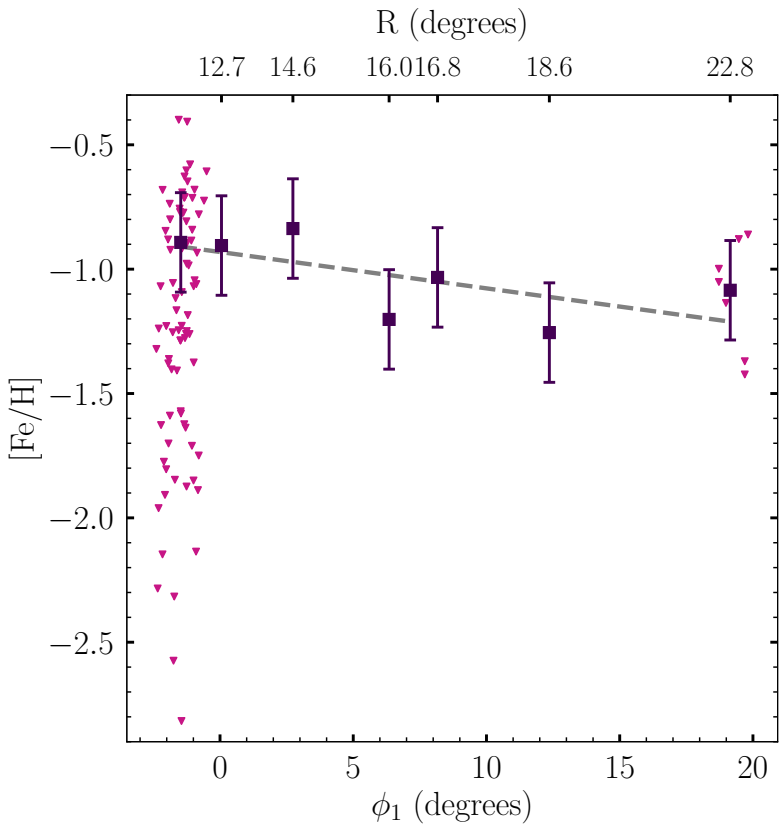

Figure 4.3: [Fe/H] measurements for stars in the northern arm and nearby outer LMC disk, as a function of LMC galactocentric radius (R: top) and ϕ_1 distance along the feature (bottom). Red triangles indicate MagES measurements for individual stars, while squares indicate metallicities derived from stacked spectra, which tend to the mean metallicity of the field. The dashed grey line shows the best-fitting metallicity gradient along the feature.

§4.4.2.

Whilst literature [Fe/H] measurements in the outskirts of the LMC are sparse, they are generally consistent with our results. Grady et al. (2021) reports photometric metallicities along the feature utilising Gaia DR2 photometry of RC/RGB stars, finding similar [Fe/H] values along the feature to our spectroscopic measurements. Any potential gradient along the feature, however, is masked by a large dispersion (defined in that paper as the difference between the 10^{th} and 90^{th} percentile of the distribution) of up to ~0.6 dex within each square degree pixel. Both Majewski et al. (2008) and Carrera et al. (2011) find a decrease in the mean metallicity of RGB stars beyond a LMC galactocentric radius of ~7°, with mean [Fe/H]~−1 at distances of $\geq 10°$, with a scatter of ~1 dex at these large distances. We also note that Munoz et al. (2006) measure a mean [Fe/H]= −0.67 and a dispersion of 0.62 dex – somewhat higher than our measurements – for a group of 15 stars in the vicinity of the Carina dwarf (located near the armlike feature at ϕ_1~12.5°) with heliocentric velocities indicating a potential LMC association. However, cross-matching these stars

against Gaia EDR3 returns at least three stars with proper motions strongly inconsistent with being associated with the LMC, suggesting their reported mean metallicity could be too high (assuming the non-Magellanic stars are metal-rich Galactic contaminants). Unfortunately, Munoz et al. (2006) do not report individual [Fe/H] measurements so we cannot calculate a corrected value.

Our [Fe/H] measurements indicate the feature is likely comprised of disturbed LMC disk material. The median metallicity near the base of the feature is consistent with measurements in the nearby outer LMC disk fields (Paper I), and given the negative metallicity gradient at smaller LMC radii (Majewski et al. 2008; Carrera et al. 2011), a mild negative metallicity gradient could be expected under the assumption that the feature is an overdensity in the extreme LMC disk outskirts, such that stars currently located at large distances along the feature had their origin at larger radii than stars currently located at smaller galactocentric radii. We explore formation mechanisms for the feature using models to test this idea in §4.5.

We can, however, rule out the feature being the disrupted remains of an accreted dwarf satellite of the LMC as discussed in M16. Considering the mass-metallicity relation for dwarf galaxies (as presented in Kirby et al. 2013; Hidalgo 2017), a stellar mass of $\geq 10^{7.6}$ $M_\odot$ is required for a mean [Fe/H]$\gtrsim -1.2$, corresponding to an integrated luminosity $M_V \lesssim -11.5$ (McConnachie 2012). In contrast, M16 find the integrated luminosity of the feature is only $M_V \sim -7.4$. Even accounting for the increased spatial extent of the feature traced using more recent data, and uncertainties in the mass-metallicity relation, this is still $\gtrsim 30$ times fainter than the luminosity of the required satellite.

4.4.2 Structure

In order to place constraints on the geometry of the feature, we carefully analyse Gaia EDR3 photometry of stars along its length. Although Gaia parallaxes lack the precision to provide useful distances for the Clouds (Gaia Collaboration et al. 2021c), the apparent magnitude of the red clump can instead be used as a standardizable candle to provide information about the relative geometry of the feature. However, the apparent magnitude of the red clump is not purely distance dependent: population effects including the age and metallicity of clump stars affect their intrinsic luminosity (see Girardi 2016 for a review), and interstellar extinction along the line-of-sight also affects the measured clump magnitude. To determine the relative geometry of the feature therefore requires dereddened photometry, as well as assumptions about its constituent stellar populations.

Following the procedure described in Gaia Collaboration et al. (2021a), we deredden

our photometry utilising the Schlegel et al. (1998) dust maps, corrected as described in Schlafly and Finkbeiner (2011), in conjunction with the mean extinction coefficients for the Gaia passbands described in Casagrande and VandenBerg (2018). No correction is made for reddening internal to the Clouds as this is not expected to be significant in the low-density peripheral regions targeted by MagES (c.f. Choi et al. 2018b henceforth referred to as C18). We correct the Gaia G-band photometry for the 6-parameter solution as described in Riello et al. (2021) prior to applying the dereddening procedure.

In order to effectively utilise the clump magnitude as a distance estimator along the feature, we initially assume that the stellar population comprising the clump does not vary, and is identical to that in the nearby LMC outer disk. This implies any magnitude differences observed along the feature are due entirely to distance effects. However, as discussed in §4.4.1, there is weak evidence for a mild negative metallicity gradient along the feature. In the Gaia G passband (which substantially overlaps the optical V-band investigated in Girardi and Salaris 2001), this is expected to result in an increase in clump luminosity along the feature, as well as a shift to bluer colours. We discuss the scale of this potential population effect and its implications on our results in detail below.

To determine an appropriate CMD selection box for RC stars, we utilise dereddened Gaia EDR3 photometry within the northern LMC disk, where the clump is well-populated. We select stars within a 1° radius of two MagES disk fields (fields 12 and 18: see Fig. 4.1), with parallax $\varpi < 0.2$ and proper motions within a box of full width five times the dispersion of the field median motions reported in Table 4.1 (i.e. $\pm 2.5\sigma_{\alpha/\delta}$), and passing the quality cuts `ruwe`<1.4 and $C^{*}<4\sigma_{C^{*}}$. Fig. 4.4 shows the resulting Hess diagrams for the two fields. We define a selection box of $0.85<(G_{\rm BP}-G_{\rm RP})_0<1.05$, and $18.0<G_0<19.25$, to select red clump stars. The selection is designed to minimise contamination from the RGB and potential RGB bump (which, at a similar magnitude to the RC, could bias estimation of the clump magnitude), whilst being sufficiently wide in magnitude range to accommodate potential distance variations along the northern arm. The resulting median clump magnitude and colour, and associated dispersion calculated as the standard deviation, are provided for the two fields in Table 4.3. Note the observed ~0.1 mag difference in median G_0 for these fields is expected due to the inclined disk geometry of the LMC. We test small (~0.25 mag) adjustments to the selection box (including stricter blue and bright magnitude cutoffs to minimise contamination from horizontal branch and blue loop stars respectively) and find these do not significantly affect our results.

We apply the same CMD, parallax, and quality cuts to stars within the feature selection box in ϕ_1/ϕ_2 coordinates presented in §4.3.1. Unlike in an individual disk field, the mean proper motion varies along the length of the feature, and therefore a simple

Table 4.3: Median RC magnitude $\langle G_0 \rangle$ and colour $\langle (G_{\rm BP} - G_{\rm RP})_0 \rangle$, and associated dispersion, for two MagES northern disk fields. Standard errors on both the median and dispersion are reported.

Field	$\langle G_0 \rangle$	σ_{G_0}	$\langle (G_{\rm BP} - G_{\rm RP})_0 \rangle$	$\sigma_{(G_{\rm BP}-G_{\rm RP})_0}$
18	18.66 ± 0.02	0.24 ± 0.01	0.975 ± 0.004	0.052 ± 0.002
12	18.75 ± 0.02	0.23 ± 0.01	0.972 ± 0.004	0.052 ± 0.002

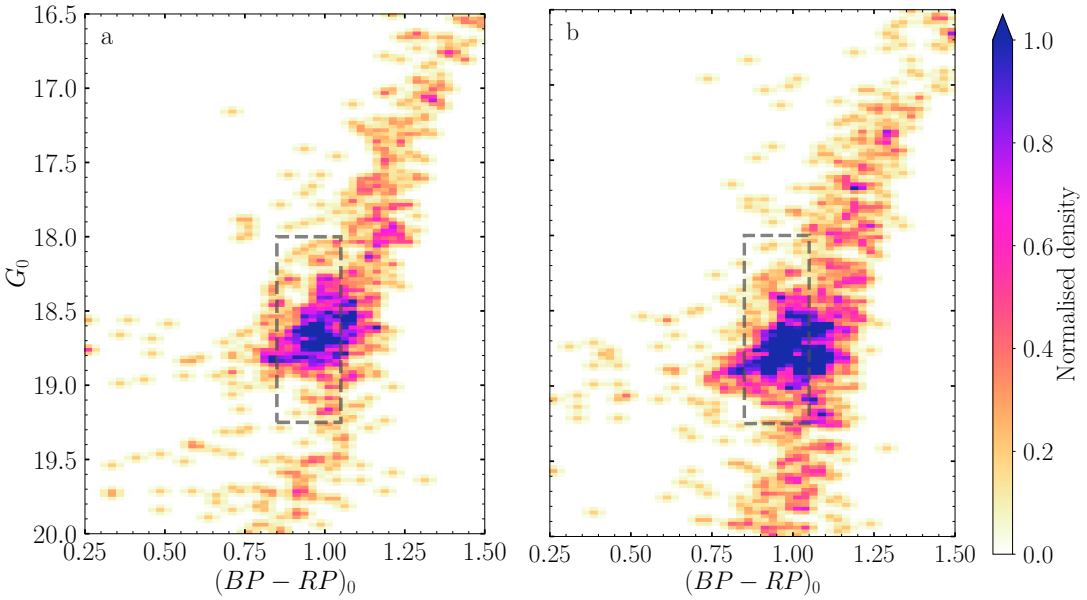

Figure 4.4: Colour-magnitude selection boxes used to isolate red clump stars, overlaid on Hess diagrams of stars within 2° diameter fields centred on MagES fields 18 (panel *a*) and 12 (panel *b*), located in the northern LMC disk. Only stars passing proper motion, parallax, and quality cuts as described in the text are included. The RC selection box (dashed grey line) is designed to minimise contamination from non-RC populations (including RGB, horizontal branch, and blue loop stars) whilst allowing for colour and magnitude shifts along the arm.

global proper motion cut is insufficient to minimise contamination. As such, we perform a least-squares fit to each of the two proper motion components measured for the MagES fields along the feature as a function of ϕ_1, weighted by the proper motion uncertainty. We define each proper motion selection to be a box centred on the resulting fit, with a full width five times the mean proper motion dispersion of all MagES fields along the arm (i.e. $\pm 2.5 \left\langle \sigma_{\alpha/\delta} \right\rangle$). The resulting selections are presented in Fig. 4.5, overlaid on 2D histograms of the underlying proper motion distribution (limited to stars with proper motions $0 < \mu_\alpha < 3$ and $-2 < \mu_\delta < 2$); the fitted relations follow the underlying overdensities in proper motion space associated with the feature. Our final selection includes only stars which pass the selection in both proper motion components.

We bin our final selection into segments of 2.5° in ϕ_1, and determine the median $(G_{\rm BP} - G_{\rm RP})_0$ colour, G_0 magnitude, and associated dispersions (calculated as the stan-

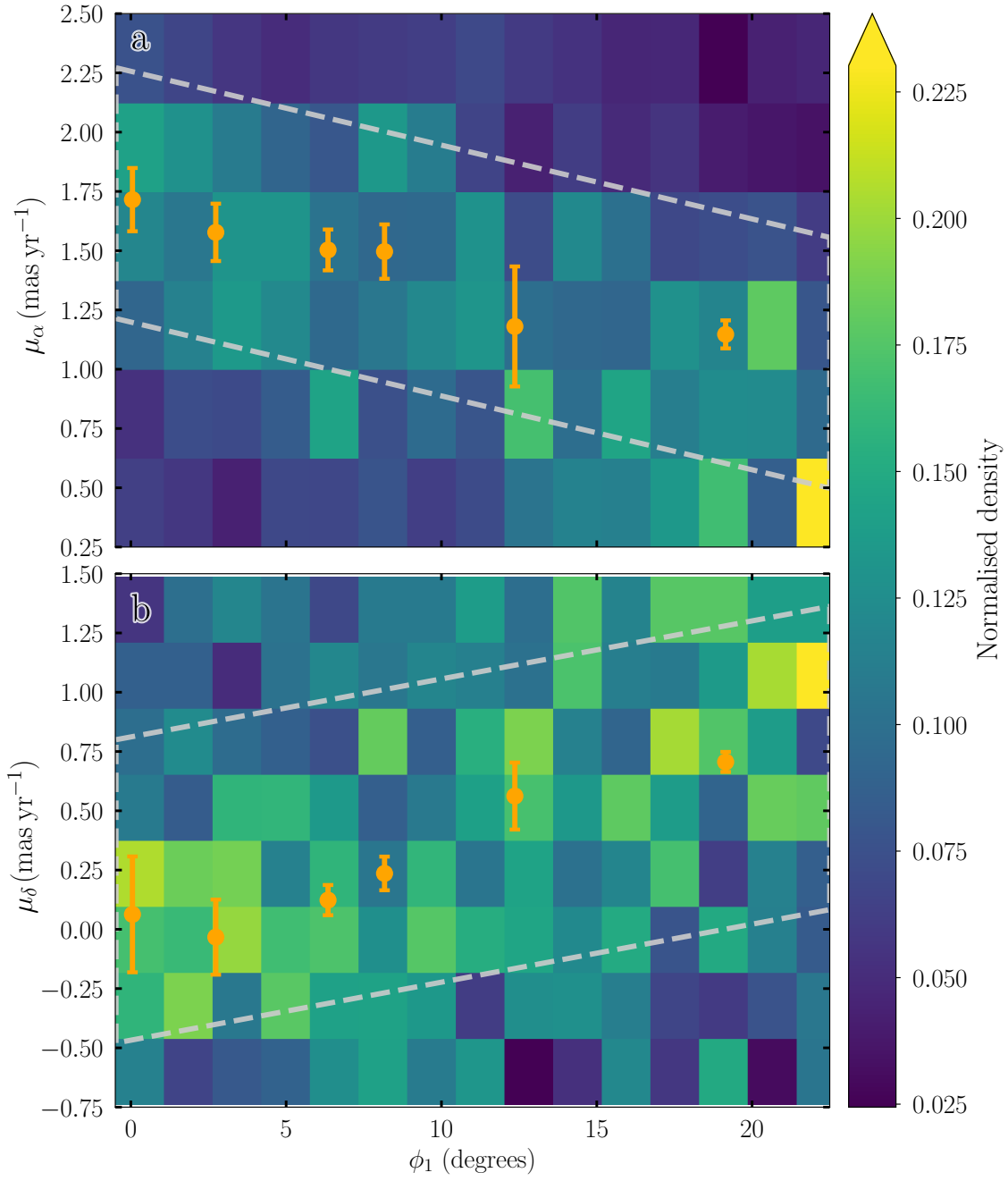

Figure 4.5: Proper motion selection boxes (dashed grey) used to isolate likely LMC stars along the northern arm. Orange points indicate MagES field aggregate motions, with error bars representing the field aggregate 1σ dispersion. These are overlaid on 2D histograms of μ_α (panel *a*) and μ_δ (panel *b*) as a function of ϕ_1 location along the feature for RC stars in the vicinity of the northern arm.

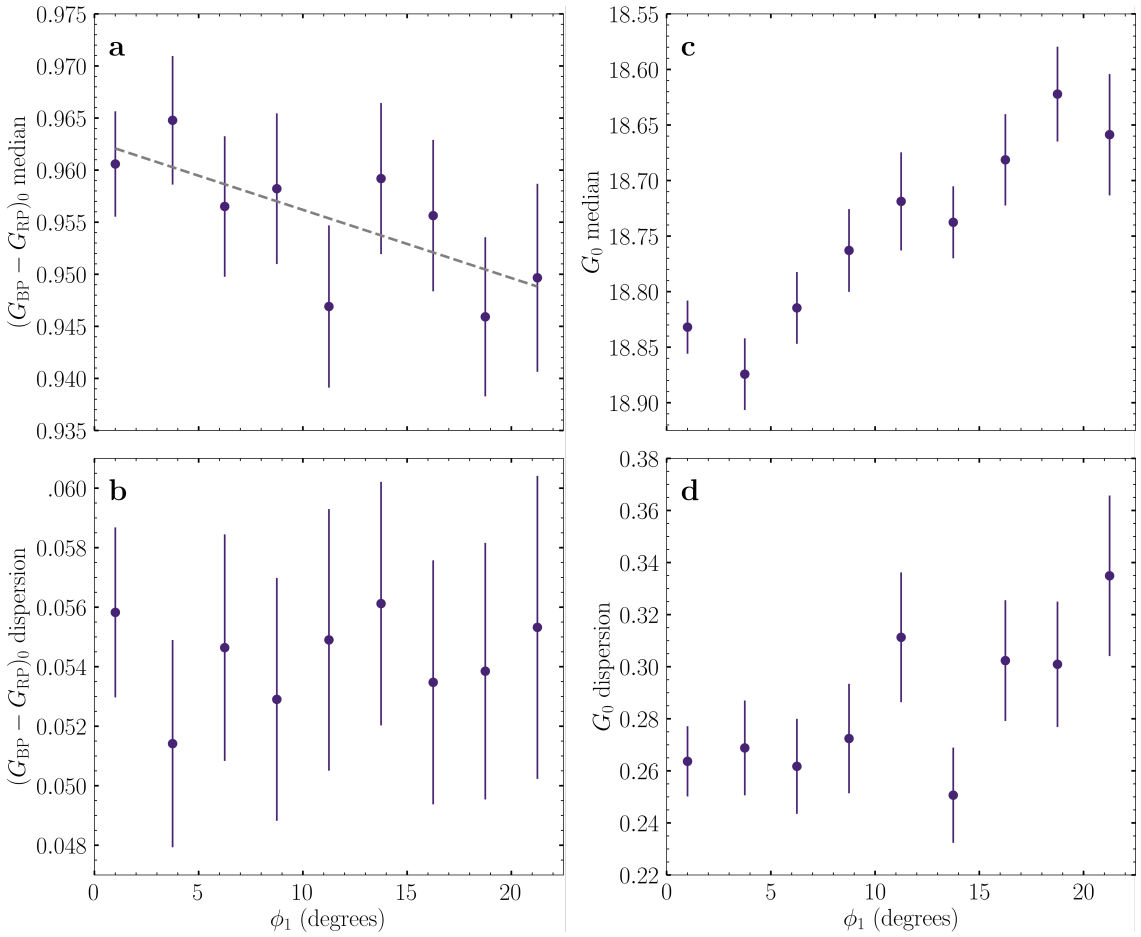

Figure 4.6: Photometric properties of red clump stars calculated within 2.5° bins in ϕ_1 distance along the feature. Panels show (*a*) median $(G_{BP} - G_{RP})_0$ colour, (*b*) standard deviation in the $(G_{BP} - G_{RP})_0$ distribution, (*c*) median G_0 magnitude, and (*d*) standard deviation in the G_0 distribution. The dashed grey line in panel *a* shows a linear least-squares fit to the median colour as a function of ϕ_1.

dard deviation of the distribution) for each bin. Bins are chosen such that at least sixty stars are present in each bin, in order to provide robust estimates of the colour-magnitude distributions. Fig. 4.6 shows the resulting photometric trends as a function of the ϕ_1 distance along the feature; error bars represent the standard error on each parameter. The standard error on all quantities increases along the feature due to the decreasing density of Magellanic stars further from the LMC disk.

An underlying assumption of the following analysis of the structure's photometric properties is that any underlying contaminant (i.e. non-Magellanic) population of stars within our final selection is uniformly distributed within the CMD selection box along the length of the feature. To test this, we utilise the Besançon Model of the Galaxy (Robin et al. 2003)[20]. We generate an empirical representation of the observed Milky

[20] Accessed as version 1603 through the web service https://model.obs-besancon.fr/

Way contaminant profile within the feature selection box by applying the same CMD, position, parallax, and proper motion selection cuts as our observed sample to the Model. We find the underlying MW population is distributed relatively uniformly within the CMD selection box, and remains so along the length of the feature, indicating this does not bias either the median RC colour or magnitude inferred from our final selection. The number of contaminant stars within the selection does increase along the length of the feature; we discuss this in further detail below.

As seen in Fig. 4.6, there is a mild (~0.01 mag) trend to bluer colours as the ϕ_1 distance along the feature increases, such that the mean colours at either end of the feature differ by approximately 1σ. A linear least-squares fit, weighted by the standard error on the median colour, has a slope of $(-6 \pm 2) \times 10^{-4}$ mag/degree. Such a trend is qualitatively consistent with the mild trend to lower metallicities with increasing ϕ_1 as observed in §4.4.1: red clump stars become bluer at lower metallicities (Girardi 2016). We test whether the magnitude of this colour shift is consistent with that expected from the metallicity gradient along the feature using PARSEC isochrones (Bressan et al. 2012)[21], assuming the default parameters for IMF and mass loss, in Gaia EDR3 passbands. For isochrones of an 11 Gyr old population[22], at metallicities of [Fe/H]= −0.9 and [Fe/H]= −1.2 (the maximum inferred metallicity difference along the feature), we calculate the luminosity-weighted mean magnitude in the G, $G_{\rm BP}$, and $G_{\rm RP}$ passbands for core He-burning stars[23] as in Eqs. 3 and 4 of Girardi and Salaris (2001).

The calculated (reddening-free) $G_{\rm BP} - G_{\rm RP}$ colour difference between the two metallicities is ~0.06 mag: significantly larger than the measured ~0.01 mag difference in $(G_{\rm BP} - G_{\rm RP})_0$ along the feature. This is not unexpected: dispersion in the clump age and metallicity (~0.5 dex as measured in §4.4.1), as well as photometric uncertainties, will act to "smear out" the clump colour and reduce the measured colour difference along the feature. We also note the dispersion in $(G_{\rm BP} - G_{\rm RP})_0$ remains constant along the length of the feature, implying the underlying scatter within the RC population remains relatively constant along the arm.

Whilst the most straightforward interpretation of the shift to bluer colours along the arm is due to an underlying metallicity gradient, it is not the only possibility. Stellar age also affects the median RC colour, with young ($\lesssim 2$ Gyr) RC stars significantly bluer than older RC stars (Girardi and Salaris 2001). However, DECam CMDs in the vicinity of the feature reveal a lack of main sequence stars above an ancient (~10^{11} Gyr: Mackey et al. 2018) turnoff. We can thus infer age is not the dominant driver of the shift in RC

[21] Accessed as version 3.4 of the web form http://stev.oapd.inaf.it/cmd
[22] the best-fitting isochrone for the outer LMC disk in Mackey et al. (2018).
[23] with label "4" in the isochrone.

colour. In contrast, we cannot rule out the possibility of systematics in the reddening correction affecting the median $(G_{BP} - G_{RP})_0$ colour at the level of 0.01 mag, noting the mean $E(B-V)$ value along the feature remains relatively constant at ~0.08 between $0° < \phi_1 < 15°$, but increases to ~0.25 at $\phi_1 \sim 22.5°$. However, we do note the minimal change in $(G_{BP} - G_{RP})_0$ colour implies any systematic in the reddening correction must be small.

We now consider the gradient in G_0 observed along the northern arm. The median magnitude increases from $G_0 \sim 18.83$ at the base of the feature to $G_0 \sim 18.63$ far from the LMC disk. To check the possible effect of changing metallicity on G-band magnitude, we utilise the same isochrones as described above to quantify the maximum potential difference in G_0 from metallicity, and find only a ~0.06 mag increase in magnitude for more metal-poor populations. This is similar to the standard error on the G_0 magnitude per bin. Further, as in the case of the RC colour, the large metallicity scatter along the feature is expected to reduce the severity of the observed magnitude difference due to metallicity along the feature. We therefore conclude that the gradient in G_0 observed along the northern arm can be entirely attributed to a change in distance, with the structure becoming closer with increasing ϕ_1: as would be expected given the inclination (i) and orientation (Ω) of the LMC disk.

To investigate how closely the northern arm follows the plane of the LMC disk, we calculate the expected magnitude difference along the feature under the assumption of disk geometry. As multiple estimates of the LMC disk geometry exist, even considering only "old" stellar populations, we investigate two geometries which span the range of recent measurements reported in the literature: that from vdM14 ($i = 34.0° \pm 7°$, $\Omega = 139.1° \pm 4.1°$; similar to that reported by Gaia Collaboration et al. 2021c), and that from C18 ($i = 25.86° \pm 1.4°$, $\Omega = 149.23° \pm 8.35°$). Accounting for changes in both the LMC galactocentric radius and position angle along the feature, the expected magnitude difference along the feature is 0.16 ± 0.03 mag under the C18 geometry, and 0.21 ± 0.08 mag under the vdM14 geometry: corresponding to end-to-end changes in distance of 3.4 ± 0.6 kpc and 4.1 ± 1.4 kpc respectively. Our measured difference of 0.21 ± 0.05 mag is, within uncertainty, consistent with both of these estimates, if somewhat closer that of vdM14. We can therefore infer the feature does, to first order, follow the plane of the LMC disk, though the precision of our measurements limits our ability to isolate a preferred disk geometry at these large radii.

We also investigate the thickness of the feature using the G_0 dispersion of the RC. Within a given bin and passband, the measured dispersion σ_{G_0} can be parameterised by Eq. 4.4, where σ_{geo} is the apparent dispersion due to global distance differences along the length of the feature, σ_{int} is the intrinsic dispersion of the clump due to population

effects, $\sigma_{\rm err}$ is dispersion introduced through photometric uncertainties, $\sigma_{\rm depth}$ is due to the intrinsic thickness of the feature, and $\sigma_{\rm cont}$ is the apparent broadening of the RC due to the presence of an underlying uniformly-distributed model contaminant population within the selection box. Note that under this parameterisation, $\sigma_{\rm cont}$ only accounts for Milky Way contamination, and not contamination from non-RC Magellanic populations, such as RGB stars, discussed further below. Of interest is whether $\sigma_{\rm depth}$ within the feature is comparable to that in the outer LMC disk.

$$\sigma^2_{G_0} = \sigma^2_{\rm geo} + \sigma^2_{\rm int} + \sigma^2_{\rm err} + \sigma^2_{\rm depth} + \sigma^2_{\rm cont} \tag{4.4}$$

As we bin the data into 2.5° lengths along the feature, within each bin we expect the global distance gradient $\sigma_{\rm geo}$ to be small: assuming either C18 or vdM14 geometries results in a maximum magnitude difference of ~0.05 mag across each bin due to a global distance gradient. We expect $\sigma_{\rm geo}$ to be similar, if slightly smaller, within our two LMC disk reference fields (MagES fields 12 and 18) as these fields also have a diameter of ~2°. We subtract the predicted $\sigma_{\rm geo}$ effect from the measured G_0 dispersion both along the feature and within the disk fields prior to comparison.

As discussed above, the dispersion in RC colour remains constant along the feature, implying similar population effects along its length, and in §4.4.1 a metallicity dispersion of ~0.5 dex is measured along the feature: consistent with the dispersions measured for the two disk fields in Paper I. As such, it is not unreasonable to assume the stellar populations within the feature are similar to those in the outer LMC disk, and we can infer that $\sigma_{\rm int}$ is constant both along the feature, and within the two reference disk fields. Similarly, as we utilise the same photometric dataset and implement the same quality cuts throughout our analysis, we expect $\sigma_{\rm err}$ to be approximately constant both along the feature, and within the disk.

Under these assumptions, any difference in G_0 dispersion between the feature and the disk fields is due entirely to a difference in feature thickness, or the effects of contamination. We expect $\sigma_{\rm cont}$ to be effectively zero within the disk fields, due to the very high density of Magellanic stars compared to the expected MW contamination within the selection (a factor of $\gtrsim$ 100). In contrast, the level of predicted MW contamination within the selection increases along the length of the feature, increasing by a factor of ~3 from the disk fields to the outermost bins along the feature. We hypothesise that this increase in contamination, and associated increase in $\sigma_{\rm cont}$, is the dominant driver of the increased G_0 dispersion measured beyond 10° along the feature. In contrast, for bins within the first 10° of the feature, the predicted number of contaminant stars is significantly less

than the total number of observed stars per bin. This implies $\sigma_{\rm cont}$ is much smaller, if not zero, within these bins. When we compare the measured G_0 dispersion within these bins to that for the two disk fields, we find these are equal within uncertainty: implying the thickness of the feature is approximately the same as the thickness of the LMC disk. This is further evidence the feature is made from perturbed LMC disk material.

To test the hypothesis that contamination is responsible for the observed increase in G_0 dispersion along the arm, and to check that contamination is not adversely affecting any of the other measured parameters, we fitted a mixture model that explicitly tries to account for non-RC populations within each bin. The model assumes the density of red clump stars takes the form of a two-dimensional Gaussian on the CMD, while the background density is described by linearly varying terms in both colour and magnitude. The relative fraction of contaminants and members in a given bin is left as a free parameter. We sample the posterior probability distributions for the model parameters using the Markov Chain Monte Carlo ensemble sampler EMCEE.

Whilst this approach is more comprehensive in modelling the stellar populations within the selection box than our original method, a disadvantage is that it requires a substantial number of stars per bin to robustly converge. As a result, we can only reliably perform the fit within four bins (of length ~5°, compared to 2.5° in our original method) along the arm. Nonetheless, our results agree closely with the RC $(G_{\rm BP} - G_{\rm RP})_0$ colour and G_0 magnitude trends determined from the simple medians, as well as the $(G_{\rm BP} - G_{\rm RP})_0$ colour dispersion. The fitted RC dispersion in G_0 also remains constant along the full length of the arm, with the non-member fraction increasing by a factor of ~2 from $\phi_1 = 0$ to $\phi_1 = 20$ degrees. This supports our conclusion that it is the contaminating populations that drive the increasing G_0 dispersion along the arm in our simple measurements, while the intrinsic thickness does not substantially change.

4.4.3 Kinematics

Whilst Table 4.2 reports kinematic information in observable units, our finding that the northern arm sits close to the expected plane of the LMC disk and is likely comprised of disk material means it is more informative to consider its kinematics in the LMC disk frame. As such, the framework presented in van der Marel and Cioni (2001) and van der Marel et al. (2002) is used to transform the observed components into velocities in a cylindrical coordinate system. This coordinate system is aligned with the LMC disk, and has its origin at the LMC centre of mass (COM). As in Paper I, we choose the COM to be ($\alpha_0 = 79.88°$, $\delta_0 = -69.59°$) as reported by vdM14 for their "PMs+Old $V_{\rm LOS}$

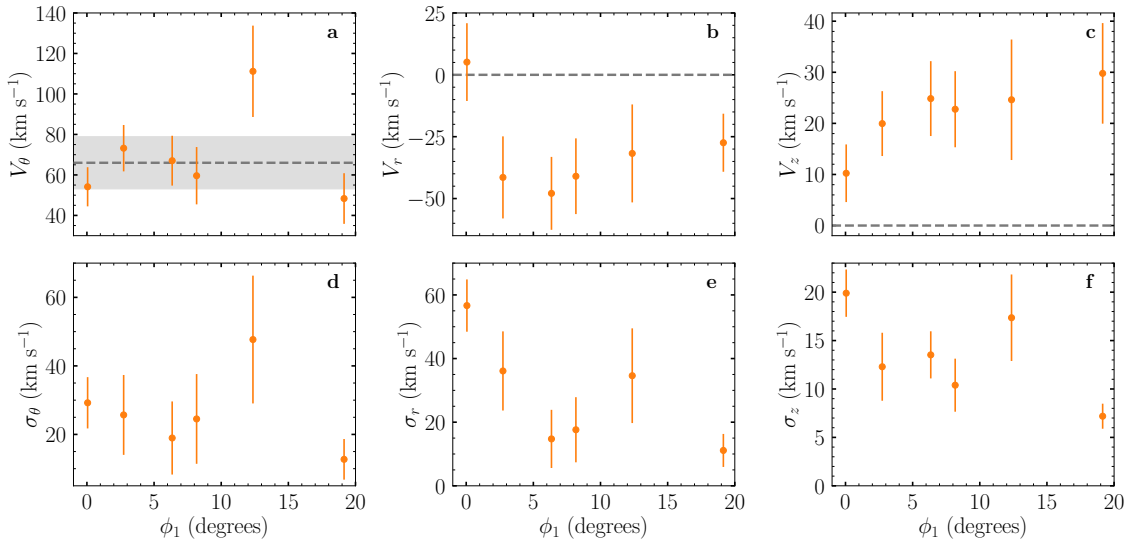

Figure 4.7: Observed velocities and dispersions for MagES fields along the northern arm as a function of ϕ_1, calculated assuming C18 disk geometry. Top panels show, in order, the azimuthal, in-plane radial, and out-of-plane vertical velocities; bottom panels show the velocity dispersions in each component. Positive azimuthal velocities indicate clockwise rotation (i.e. in a direction from North towards West), positive radial velocities indicate movement outward from the LMC COM in the LMC disk plane, and positive vertical velocities indicate movement perpendicular to the disk plane, in a direction primarily towards the observer. Grey dashed lines indicate the expected kinematics for an equilibrium disk, with the rotational velocity (and uncertainties) taken from Paper I, recalculated assuming the C18 disk geometry for consistency.

Sample", and the associated systemic motions applicable for this choice of centre: i.e. $\mu_{\delta,0} = 0.287 \pm 0.054$ mas yr^{-1}, $\mu_{\alpha,0} = 1.895 \pm 0.024$ mas yr^{-1}, and $V_{\rm LOS,0} = 261.1 \pm 2.2$ km s^{-1}.

The orientation of the LMC disk relative to the line-of-sight must also be assumed during this coordinate transform. From §4.4.2, the feature remains roughly within the plane of the LMC disk, though the moderate uncertainties in our measurement preclude distinguishing between varying literature measurements of the disk geometry. As such, for this paper we choose to utilise the C18 geometry when calculating kinematics in the plane of the LMC disk. This is motivated by preliminary results from Mackey et al. (in prep), which indicate the inclination of the LMC decreases at large radii. Using this assumed geometry, we transform the observed kinematic parameters for the feature fields into physical velocities and dispersion in the LMC disk frame. We calculate V_θ, the azimuthal streaming or rotation velocity; V_r, the radial velocity in the disk plane; and V_z, the vertical velocity perpendicular to the disk plane, as well as dispersions (σ_θ, σ_r, σ_z) in each of these components. These disk measurements are reported in Table 4.4, and Fig. 4.7 plots each component as a function of ϕ_1 position along the feature.

With the exception of field 19 (discussed below), clear trends are observed in each of the disk velocity components and their dispersions. Within uncertainty, the azimuthal

Table 4.4: Disk velocities for northern arm feature fields, calculated assuming C18 disk geometry. In V_θ, positive values indicate clockwise rotation. In V_r, positive values indicate movement outward from the LMC COM in the LMC disk plane. In V_z, positive values indicate movement perpendicular to the disk plane, in a direction primarily towards the observer: "in front" of the LMC disk. We also give the number of likely Magellanic stars per field, repeated from Table 4.2.

Field	$N_{\text{Magellanic}}$ ($P_i \geq 50\%$)	V_θ (km s^{-1})	σ_θ (km s^{-1})	V_r (km s^{-1})	σ_r (km s^{-1})	V_z (km s^{-1})	σ_z (km s^{-1})
11	75	54.2± 9.8	29.2 ± 7.5	5.7 ± 16.7	56.7 ± 8.2	9.4 ± 6.2	19.9 ± 2.4
13	38	73.4 ± 11.7	25.7 ± 11.7	-39.3 ± 16.3	36.1 ± 12.4	19.5 ± 6.0	12.3 ± 3.5
15	32	67.3 ± 12.9	19.0 ± 10.7	-47.1 ± 15.0	14.7± 9.1	24.2 ± 6.2	13.5 ± 2.4
16	25	59.2 ± 14.2	24.5 ± 13.1	-40.4 ± 15.8	17.6 ± 10.2	21.6 ± 6.6	10.4 ± 2.7
19	13	108.8 ± 22.9	47.7 ± 18.6	-30.2 ± 20.0	34.6 ± 14.9	22.4 ± 9.9	17.4 ± 4.5
22	27	47.6 ± 14.6	12.7 ± 5.9	−26.3± 9.8	11.1 ± 5.2	28.3 ± 6.1	7.2 ± 1.3

rotation velocity in each field is consistent with that derived from the two MagES disk fields 12 and 18 in Paper I, recalculated using Gaia EDR3 astrometry and the assumption of a C18 disk geometry to maintain consistency with fields along the northern arm. The dominant source of uncertainty in estimates of the disk kinematics – both in the Paper I values, and those measured here – are uncertainties in the assumed disk geometry. The measured azimuthl velocity is also within the uncertainty of that derived for RC sources in Gaia Collaboration et al. (2021c), which is approximately flat at ~70 km s^{-1} (with perhaps a very mild ~5 km s^{-1} downturn at their outermost radii of ~8 kpc).

In contrast to the relatively ordered and disk-like kinematics observed in the azimuthal velocity, the in-plane radial velocity (V_r) and out-of-plane vertical velocity (V_z) along the feature are strongly out of equilibrium. Both these values are expected to be near zero in an equilibrium disk, and measurements of these in MagES northern disk fields reported in Paper I are consistent with zero within uncertainty. However, the in-plane radial velocity drops sharply from approximately zero (in field 11) to -40 km s^{-1} by the next field ~3° away along the feature. This strongly-inward velocity remains roughly constant along the feature before a slight decrease in magnitude to approximately -30 km s^{-1} in the outermost field 22. In addition, the vertical velocity gradually increases along the feature from near zero to a maximum of nearly 30 km s^{-1} in field 22: a significant out of plane motion. Such dramatic kinematic signatures strongly suggest perturbation by an external gravitational potential: we investigate this possibility in greater detail in §4.5.

Since the geometry of the outer LMC disk is uncertain, it is possible the observed kinematic perturbations are simply reflections of incorrectly assuming C18 parameters for the disk geometry. To test this, we solve for the disk orientation required for the feature kinematics to simply be a projection of purely rotational motion within the LMC disk plane by simultaneously minimizing the sum of squares of V_r and V_z. However, we find the derived disk orientations (typically with inclinations approximately $-40°$) are strongly inconsistent with the constraints derived in §4.4.2, indicating genuinely perturbed kinematics.

In general, the velocity dispersion in each component decreases along the length of the feature. The azimuthal (σ_θ) and vertical (σ_z) velocity dispersions in field 11 nearest the outer LMC disk are similar to those observed in the nearby outer disk in Paper I; the dispersions gradually decrease to approximately half their disk values by the outermost field along the structure. As moving along the feature also increases the galactocentric radius of the fields, this is not surprising: the velocity dispersion is expected to decrease with radius for material within an axisymmetric disk potential (Gaia Collaboration et al. 2021c; Vasiliev 2018; Binney and Tremaine 2008). More interesting is the dispersion of the

in-plane radial velocity. The dispersion in the two innermost feature fields (>40 km s^{-1}) are similar to that in the nearby outer LMC disk (~45 km s^{-1}: Paper I); the innermost feature field is even larger than this value. This is in stark contrast to the canonical disk value of ~25 km s^{-1} measured at large ($\geq 8°$) radii in undisturbed fields (Cullinane et al. 2020; Gaia Collaboration et al. 2021c; Vasiliev 2018). As discussed in Wan et al. (2020), a large in-plane radial velocity dispersion can be indicative of perturbation by an external gravitational force: in their model, an interaction with the SMC can elevate the radial velocity dispersion in the outskirts of the LMC. In fields further along the feature, the radial velocity dispersion drops to values more consistent with the outer disk, continuing to drop along the length of the feature to ~10 km s^{-1} in the outermost feature field.

In Fig. 4.7, field 19 is a notable outlier when compared with the kinematic trends observed in the other fields. This is especially true of its azimuthal velocity (~1.8σ higher than the other fields) and three dispersion components (~1σ higher than the other fields). In addition, field 19 has generally larger uncertainties for all parameters. Investigation revealed that these characteristics can be traced to a combination of two issues. Firstly, field 19 has substantially fewer Magellanic members than any of the other fields – a factor of two smaller than adjacent fields 16 and 22. Secondly, it transpires that the peak of one of the contamination populations we model during our membership analysis (see Paper I) sits very close (~0.4 mas yr^{-1}) to the kinematic peak for field 19 in the proper motion plane. As a consequence, our algorithm finds it difficult to robustly distinguish between Magellanic members and non-members.

In fields where a large number of Magellanic stars are present, this is not an issue: the contamination populations are generally very broad compared to the narrow Magellanic kinematic peaks, allowing reliable association of stars with the appropriate population. However, the low number of genuinely Magellanic stars in field 19 broadens the observed Magellanic peak in proper motion space, resulting in misclassification of some genuinely Magellanic stars as belonging to the contaminant population (and potentially vice-versa, though the large difference in LOS velocity between Magellanic and non-Magellanic stars typically mitigates misclassification in this direction). This biases the derived Magellanic μ_α; indeed, most of the deviance observed in V_θ can be directly mapped to the μ_α component of proper motion. Because of these issues, we do not attribute any physical significance to the fact that field 19 appears to be a kinematic outlier, and downweight its importance when comparing our measurements with numerical models in the next section.

4.5 Modelling and Analysis

In order to interpret the observed properties of the northern arm, we have created a suite of dynamical models of the LMC+SMC+Milky Way system with which to compare our observations. These comprise an existing N-body model of the MW and LMC only, presented in M16, and five new model ensembles with varying LMC, SMC, and MW masses. Within each of the five new model ensembles, we sample from literature uncertainties in the 6D phase space properties of the LMC and SMC centres in order to investigate the allowed distribution of orbits – and hence past interactions – of the Clouds. We utilise these models to test the relative importance of tidal forces from the MW and SMC in generating structures akin to the northern arm.

4.5.1 General methodology

While we analyse several different models, calculated using two distinct numerical methods, we utilise a common procedure for making mock observations of these models. The simulations are evolved in Cartesian coordinates which are centered on the present-day location of the Milky Way. Mock observations are made on the final snapshot from the location of the Sun, which is assumed to be at a distance of 8.178 kpc (GRAVITY Collaboration et al. 2019) from the Galactic center and moving with a velocity of $(11.1, 242.5, 7.3)$ km s^{-1} (motivated by the results of Schönrich et al. 2010 and Bovy et al. 2012). These mock observations are made for the same observables as the real data, i.e. α, δ, D, μ_α, μ_δ, $V_{\rm LOS}$. We subsequently convert these observables into the same (X, Y) coordinate system as the observed data using Eq. 4.1. Note that in this transformation, we set α_0, δ_0 to be the defined LMC centre for each individual model, rather than the observed LMC centre, as the defined centre by design varies between model iterations.

To determine the model kinematics within each field for comparison with our observations, we select all particles within a one-degree radius of the central (X, Y) coordinates of each field reported in Table 4.2 – the same size as a MagES field observed with 2dF. We calculate the resulting median and dispersion of each kinematic component ($V_{\rm LOS}$, μ_α, and μ_δ), which are suitable for direct comparison with the equivalent MagES observations. We further convert the model kinematics for each field into the reference frame of the assumed LMC disk plane using the same process as for the observed data, described in §4.4.3, to facilitate comparison with the equivalent observations. However, we make one key change to this process, as unlike the observed stars, the true distance to each model particle is known. We therefore utilise the true particle distances to calculate the out-of-plane distance (z) relative to the assumed C18 LMC disk plane for each particle,

rather than making the assumption that all particles are in the LMC disk plane ($z = 0$) as required for the observations. We use the calculated out-of-plane distances to assess the accuracy of this earlier assumption (see below).

We note there are two possible approaches for comparing model fields to MagES fields. The first, which we have adopted, is to select model locations at the same (X,Y) coordinates as each MagES field. However, these positions are not always precisely co-located with any northern overdensity that may appear in a given model. An alternative is to fit a unique feature track following any northern overdensity for each model realisation, using the same method as described in §4.3.1, and compare model fields centred at the same ϕ_1/ϕ_2 coordinates as each MagES field as reported in Table 4.2. While this ensures model fields are co-located with any northern overdensity generated in the models, differences in the shape of the feature between model iterations can result in model fields located at significantly different LMC galactocentric radii and position angles.

We adopt the first approach described above as this is equivalent to selecting particles at the same projected LMC galactocentric radius and position angle as the MagES fields, ensuring particles feel comparable gravitational forces from the LMC+SMC+MW as the observed stars. In comparison, under the second approach outlined above, the different galactocentric radii of the model fields means the gravitational forces felt by particles at each field location can differ, potentially significantly, between model iterations. The derived kinematics are thus not strictly comparable, even between individual model realisations. Nonetheless, we have tested the second approach by fitting a feature track to each model realisation, selecting all particles within a one-degree radius of the ϕ_1/ϕ_2 coordinates of each MagES field, and calculating the resulting field kinematics. Comparison of the two approaches reveals the choice of field location does not significantly affect the derived model kinematics, nor the resulting conclusions regarding the origin of the feature.

4.5.2 *N*-body model

We first compare our data to an existing *N*-body simulation of an LMC flyby of the MW presented in M16. The LMC is modelled as a two-component galaxy (stellar disk and NFW halo), with a total mass of 1.4×10^{11} $M_\odot$ and stellar disk mass of 4×10^9 $M_\odot$. The disk and halo are comprised of 10^6 particles each, with a softening length of 75 and 500 pc respectively. The disk has a scale radius of 1.5 kpc, and a scale height of 0.3 kpc; the total LMC mass within 8.7 kpc is 1.8×10^{10} $M_\odot$ and has a circular velocity of ~90 km s^{-1}, consistent with vdM14. The Milky Way is modelled as a three-component system with

a bulge, disc, and dark matter halo as described in Gómez et al. (2015). The model was integrated for 2 Gyr, with initial positions and velocities of the Milky Way and LMC chosen using backward integration from the current position as in Gómez et al. (2015), and initial LMC disk orientation chosen to match that reported in vdM14. The resulting present-day LMC position and systemic velocities were within 2σ of the Galactocentric Cartesian values reported in Kallivayalil et al. (2013).

Whilst the *N*-body model was run prior to the availability of more recent (i.e. post-*Gaia*) structural and kinematic measurements in the outer LMC disk, we still perform a comparison to the *N*-body model as it surpasses our newer models in several aspects. In particular, it captures the self-gravity of the LMC disk and the deformation of the LMC dark matter halo during infall to the MW potential, both potentially significant in forming the northern arm, and follows the evolution of the LMC for twice as long as the newer models, allowing for a better understanding of the arm's formation timescale.

For the present analysis, we have shifted the final LMC position and systemic velocities to new coordinates ($\alpha_0 = 80.86°$, $\delta_0 = -69.89°$, $D_0 = 49.74$ kpc, $V_{\mathrm{LOS},0} = 262.7$ km s^{-1}, $\mu_{\alpha,0} = 1.995$ mas yr^{-1}, $\mu_{\delta,0} = 0.265$ mas yr^{-1}) in order to more closely match recent estimates of the LMC's systemic properties, and facilitate comparison with our new model suites which include realisations with these same central properties. We stress that as the true endpoint values of the simulation are different to these shifted values, the orbital history of the LMC in this *N*-body model is slightly different to that of later models which have the shifted values as their true endpoints. Some small differences are therefore expected when comparing predictions from this *N*-body model to later model suites.

In order to verify the applicability of the *N*-body model, we briefly discuss the model kinematics for the two MagES fields located in the northern LMC disk discussed in Paper I: any systematic differences between the observed and modelled kinematics in this comparison will likely also occur for fields along the arm. Table 4.5 presents the three velocity components in the plane of the LMC disk (V_θ, V_r, and V_z), as well as dispersions in each of these components, for MagES fields 18 and 12 and the corresponding *N*-body model predictions. We note the observed values are slightly different to those presented in Paper I as we re-calculate these using Gaia EDR3 astrometry and assumption of a C18 disk geometry to maintain consistency with fields along the northern arm.

From Table 4.5, one clear difference between the *N*-body model and the observations is the velocity dispersions: each of the three components are significantly lower in the model than the observations. This directly contributes to the overestimation of the azimuthal velocity (V_θ) by the model. The model does not explicitly set the azimuthal velocity; instead, the circular velocity (V_{circ}) is fixed at a singular radius by enforcing an enclosed

Table 4.5: Disk velocities for MagES fields 18 and 12, located in the northern LMC disk, derived assuming C18 disk geometry. Measurements are presented for both observed data, and for the M16 N-body model. As model particles have precisely known positions and kinematics, no uncertainties are reported for the model fields.

Field	V_θ (km s^{-1})		σ_θ (km s^{-1})		V_r (km s^{-1})		σ_r (km s^{-1})		V_z (km s^{-1})		σ_z (km s^{-1})	
	Measured	N-body	Measured	N-body	Measured	N-body	Measured	N-body	Measured	N-body	Measured	N-body
18	66.0 ± 12.9	106.8	25.6 ± 2.1	9.0	19.7 ± 8.3	20.5	25.6 ± 2.0	9.6	5.4 ± 6.8	3.0	20.8 ± 1.1	6.1
12	42.2 ± 7.3	84.9	27.5 ± 2.5	6.1	25.3 ± 14.4	-1.8	43.2 ± 3.8	23.3	-3.7 ± 5.4	1.7	25.4 ± 1.3	6.4

mass of 1.8×10^{10} $M_\odot$ at a radius of 8.7 kpc (van der Marel and Kallivayalil 2014). However, the circular velocity is higher than the azimuthal velocity due to asymmetric drift, with the difference roughly a factor of the disk velocity dispersion at the large distances of these fields. As such, the too-low velocity dispersions in the model directly contribute to its too-high azimuthal velocity. We consequently expect these same discrepancies in fields along the northern arm. In contrast, the radial and vertical velocities are generally similar in both the model and observations.

We also assess the geometry of the model, calculating the median out-of-plane distance (z)[24] at the location of the two fields. If the model geometry matches the assumed disk geometry, the median distance above the disk plane should be zero. We find the median out-of-plane distances are smaller under the assumption of C18 disk geometry (≤ 0.5 kpc for both fields, with field 18 above the disk plane and field 12 below the disk plane) than the assumption of vdM14 disk geometry ($\sim 0.8 - 1.6$ kpc below the disk plane for fields 18 and 12 respectively). The smaller out-of-plane distances calculated using C18 geometry imply this is closer to the model inclination, and supports our choice in §4.4.3 to assume this geometry when transforming observed MagES kinematics into the LMC disk plane.

Having established caveats associated with the kinematics of the model, and substantiated the assumption of C18 disk geometry in calculating these, we now compare the model kinematics to MagES fields along the northern arm. Fig. 4.8 shows the three disk velocity components, as well as dispersions in each of these, for both the N-body model (represented by magenta points) and observations within each field. The figure also shows results for the base-case suite of newer models, discussed in more detail below. To improve figure clarity, particularly when comparing several model suites to observations, we plot each field spaced equally along the x-axis, with model points slightly offset from observations. We list the LMC galactocentric radius for each field on the top axis for reference. Whilst overall kinematic trends as a function of position along the feature are similar in both the N-body model and the observations, kinematics within each individual field differ.

As expected from the analysis of the two MagES disk fields, the azimuthal and vertical velocity dispersions (panels d and f of Fig. 4.8) in all fields are substantially lower than the observations, with the in-plane radial velocity (panel e) dispersion also lower in all but two fields mid-way along the arm. This is likely a reflection of the underestimated velocity dispersions within the model more generally. The model azimuthal velocity (panel a) is

[24] Following convention we consider positive z to indicate "above" the disk and negative z to indicate "below" the disk. More informative is to note that in the van der Marel et al. (2002) framework, z increases in the direction of the observer such that "above" corresponds to "in front of" the disk plane while "below" corresponds to "behind" the disk plane relative to the observer.

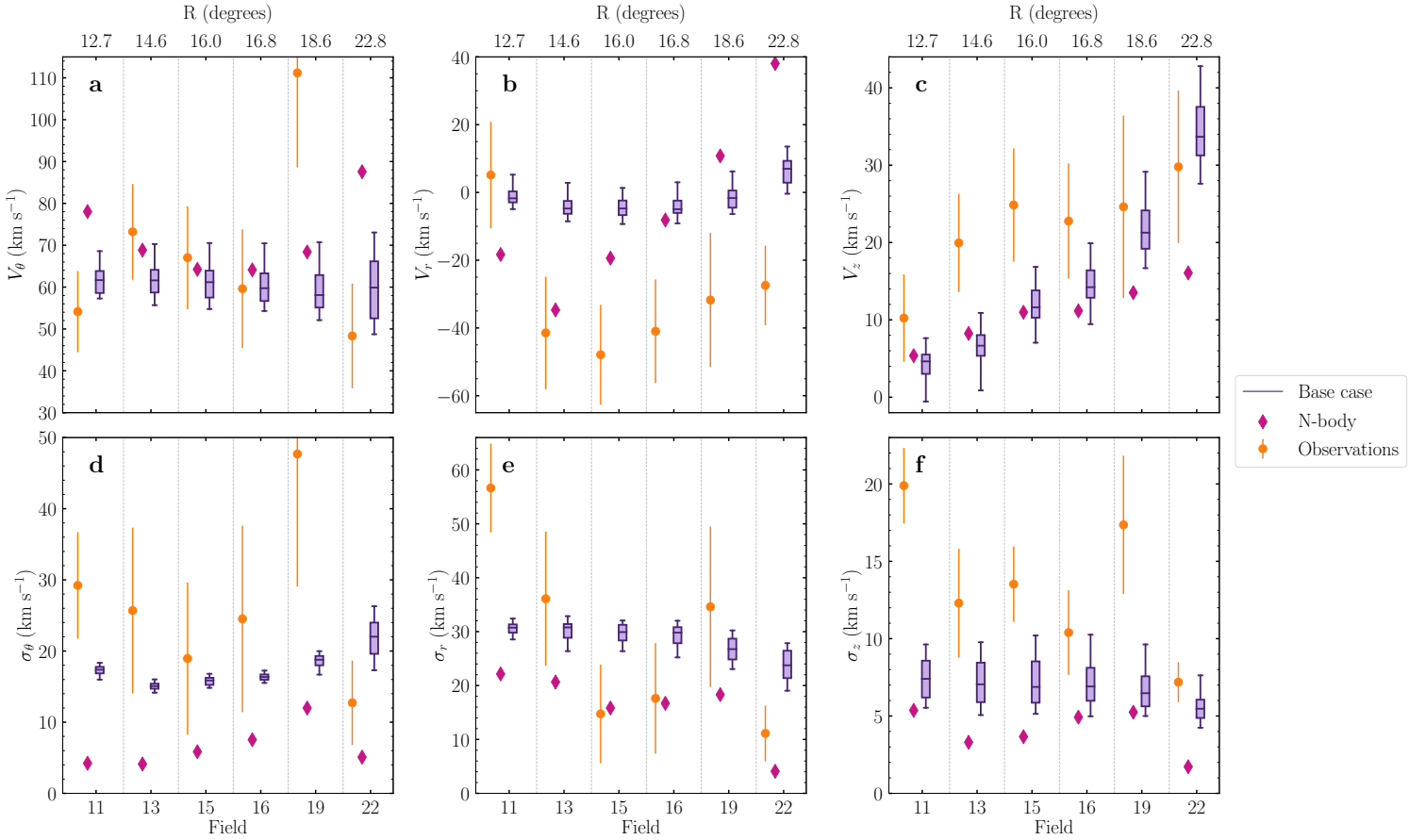

Figure 4.8: Modelled velocities and dispersions for MagES fields along the northern arm, calculated assuming a C18 disk geometry. Top panels show, in order, the azimuthal (V_θ), radial (V_r), and vertical (V_z) velocity components, with bottom panels showing the corresponding velocity dispersion in each component. Orange points show the observations and associated 1σ uncertainties, and magenta diamonds show results from the N-body model. Purple box-and-whisker plots show the distribution of the new base-case model suite across 100 realisations: the shaded box shows the 25^{th}-75^{th} percentiles of the distribution, with whiskers representing the 5^{th} and 95^{th} percentiles, and the central shaded line the 50^{th} percentile of the distribution. For clarity, fields are artificially spaced equally along the x-axis, with model points slightly offset. The top axis lists the LMC galactocentric radius R, in degrees, for each field.

also significantly higher than the observations in the innermost feature field. This is likely due to the too-low velocity dispersion of the model, as it is this field where the all three components of velocity dispersion are most significantly underestimated.

The model in-plane radial velocities (panel *b*) do show the same general shape as the observations, with a drop to approximately -35 km s^{-1} in field 13, and an increasing velocity moving further along the feature. However, the model radial velocity increases much too sharply compared to the observations, with the outermost field having a predicted radial velocity close to 40 km s^{-1}. This is clearly inconsistent with the strong negative in-plane radial velocity measured along the entire length of the arm. The vertical velocity (panel *c*) follows the same trend as the observations, but offset in magnitude: while increasing along the length of the feature, with the exception of the innermost field it is consistently lower than the observations by $\sim 10 - 15$ km s^{-1}. The overall qualitative agreement between model velocity trends and observations suggest it is plausible that the northern arm could be formed solely as a consequence of the tidal force of the Milky Way; however, the quantitative disagreements indicate there must be differences between this specific model realisation – and associated perturbation – compared to the actual LMC.

4.5.3 Simpler model suites

Whilst the *N*-body model has some qualitative agreement with the observed kinematic trends, it is nonetheless a single model that does not include the SMC. To learn more about the origin of the northern arm, a suite of models is required to (i) probe the allowed range of physical parameters, such as varying galaxy masses and the effect of SMC interactions, and (ii) account for the effects of uncertainties on the LMC and SMC central positions and systemic velocities on the orbits of the Clouds. As it is prohibitively computationally expensive to run such large model suites as full *N*-body models, we instead generate a suite of simpler models. We note that while there are limitations associated with these simpler models, which we discuss further below, they are valuable as an initial exploration of the allowable parameter space.

Our models are inspired by those presented in Belokurov and Erkal (2019) who modelled the LMC disk as a collection of test-particles initially on circular orbits in a single plane. In order to account for the velocity dispersion of the LMC disk, as well as the disk thickness, we instead initialize the LMC disk as an exponential disk made of test-particles. We model the LMC potential as an exponential disk and a Hernquist (Hernquist 1990) dark matter halo. For the exponential disk, we use a disk mass of 2×10^9 M$_\odot$, a scale radius of 1.5 kpc, and a scale height of 0.4 kpc. For the Hernquist profile, we assume a

mass of 1.5×10^{11} $M_\odot$ (motivated by the results of Erkal et al. 2019) and a scale radius of 20 kpc in our fiducial model. We also consider a lighter LMC model where the Hernquist profile mass is 1.5×10^{10} $M_\odot$ and the scale radius is 1 kpc. In both cases, the scale radius is chosen so that the circular velocity is approximately 90 km s^{-1} at 10 kpc. The disks are initialized using AGAMA (Vasiliev 2019). We note that since all of the features examined in this work are focused on the outskirts of the LMC (> 10 kpc), we only include particles with apocenters larger than 7 kpc when initializing the disk for computational efficiency.

The Milky Way is modelled as a three-component system with a bulge, disk, and dark matter halo similar to the `MWPotential2014` from Bovy (2015). We use an NFW halo (Navarro et al. 1997) with a mass of 8×10^{11} $M_\odot$, a scale radius of 16 kpc, and a concentration of 15.3. For the disk, we use a Miyamoto-Nagai potential (Miyamoto and Nagai 1975) with a mass of 6.8×10^{10} $M_\odot$, a scale radius of 3 kpc, and a scale height of 0.28 kpc. For the bulge, we use a Hernquist profile with a mass of 5×10^9 $M_\odot$ and a scale length of 0.5 kpc. We also consider a more massive Milky Way case where the NFW mass is raised to 1.2×10^{12} $M_\odot$ with all other parameters kept the same.

The SMC is modelled as a Hernquist profile with a mass of 2.5×10^9 $M_\odot$ and a scale radius of 0.043 kpc. We also consider a more massive SMC with a mass of 5×10^9 $M_\odot$ and a scale radius of 1.26 kpc. In both cases, the scale radius is chosen so that the SMC has a circular velocity of 60 km s^{-1} at 2.9 kpc (motivated by the results of Stanimirović et al. 2004). As the entire SMC mass is enclosed within this radius in our models, this results in much smaller scale radii than in e.g. Besla et al. (2012), who model an initially more massive SMC which experiences mass loss through repeated interactions with the LMC.

As in Erkal et al. (2019), we treat each system (i.e. MW, LMC, SMC), as a particle sourcing a potential. This allows us to account for the motion of the Milky Way in response to the LMC. We account for the dynamical friction of the Milky Way on the LMC using the results of Jethwa et al. (2016). The LMC and SMC are initialized at their present day locations, then rewound for 1 Gyr in the presence of each other and the Milky Way. At this time, the LMC disk (which is aligned such that its present-day geometry matches that from C18, equal to that assumed for the observations) is initialized with $\sim 2.5 \times 10^6$ tracer particles and the system is evolved to the present. No tracer particles are placed within the SMC potential. We verify that the present-day kinematics of the inner LMC ($R<10$ kpc; noting that particles with apocentres <7 kpc are not included in our simulation) remain consistent with those observed in the equilibrium LMC disk at these radii (i.e. $V_{\rm circ} \sim 90$ km s^{-1}, $V_r \sim V_z \sim 0$, $z \sim 0$, and each of $\sigma_\theta, \sigma_r, \sigma_z$ approximately constant). This indicates our simulations are suitable for comparison with our

Table 4.6: Simulation parameters for each simpler model ensemble.

Ensemble	Realisations	LMC mass ($M_\odot$)	MW mass ($M_\odot$)	SMC mass ($M_\odot$)
Base-case	100	1.5×10^{11}[a]	8×10^{11}[b]	2.5×10^{9}[c]
No SMC	12	1.5×10^{11}	8×10^{11}	-
Light LMC	12	1.5×10^{10}[d]	8×10^{11}	-
Heavy MW	12	1.5×10^{11}	1.2×10^{12}[e]	-
Heavy SMC	12	1.5×10^{11}	8×10^{11}	5×10^{9}[c]

[a] Erkal et al. 2019; [b] Bovy 2015; [c] Harris and Zaritsky 2006; [d] vdM14; [e] Bland-Hawthorn and Gerhard 2016.

observations, and that any deviations from equilibrium at larger radii in our simulations are genuinely the result of perturbations from the Milky Way, SMC, or both.

As a summary of our setup, Table 4.6 shows the properties of each set of models. For the "base-case" model set – our best estimate of realistic parameters for each of the LMC, SMC, and MW – we run 100 realisations, sampling from within Gaussian uncertainties on the LMC and SMC distances and systemic velocities as presented in Table 4.7. Also presented in Table 4.7 are the current-day relative velocities and positions of the SMC compared to the LMC, in the frame of the LMC disk, that result from our sampling of the 12-dimensional LMC/SMC parameter space.

Sampling these parameters results in a range of allowable orbits for the SMC around the LMC, and both Clouds around the Milky Way. In general, the orbit of the Clouds around the Milky Way does not vary too significantly between realisations, with the Clouds always just past their first pericentric passage around the Milky Way (c.f. Kallivayalil et al. 2013). However, the orbit of the SMC around the LMC can vary significantly. Fig. 4.9 shows both the total distance r (top panel)[25] and the height above the disk plane z (bottom panel) of the SMC from the LMC centre of mass as a function of time during each of the 100 realisations of the base-case model setup. In general, whilst the orbit of the SMC within the past ~250 Myr from today is broadly consistent across all realisations, the orbital history beyond this can diverge quite significantly depending on the specific location in parameter space of each realisation. In the following, we report statistics after running an additional 900 realisations of the base-case model setup (noting these are not full realisations initialised with test particles, but instead simply trace the orbits of the LMC and SMC COM), sampling from the present-day positions and systemic motions of the Clouds as in Table 4.7, to give 1000 total past orbits.

We find the SMC is currently in the process of crossing the LMC disk plane, with ~81% of orbits having already had a crossing at a distance of 17 ± 5 kpc, and the remaining ~19%

[25] r, the total distance, is distinct from R, which is the in-plane cylindrical radius.

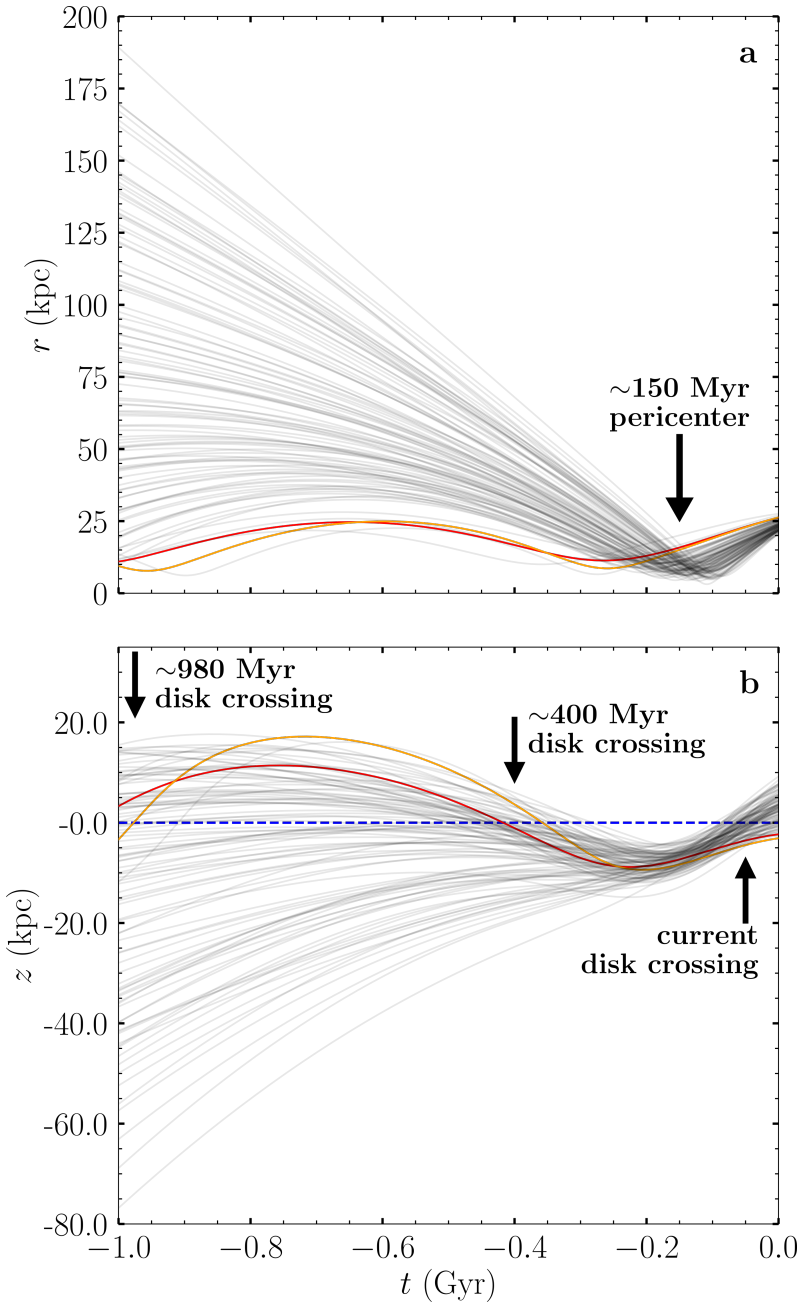

Figure 4.9: Total distance r (top) and out-of-plane distance z (bottom) of the SMC from the LMC as a function of time from the present day, up to the 1 Gyr cutoff of our models. Each grey line represents a single realisation of the base-case model suite, associated with an allowable orbit sampling from the uncertainties in the present-day systemic motions of the Clouds. Where these lines cross the dashed blue line at $z = 0$ in the bottom panel indicates an SMC crossing of the LMC disk plane. Minima in the top panel indicate SMC pericentric passages around the LMC. Red and orange lines represent individual realisations which experience, respectively, one and two SMC crossings of the LMC disk plane prior to today, which are discussed further in Section 4.5.5.

Table 4.7: Model parameters for the present-day systemic properties of the LMC and SMC. Parameters are sampled from a Gaussian distribution centred on the peak value, with a 1σ width equal to the literature uncertainty on that parameter. In the case of values taken from vdM14, results from their "PMs+Old $V_{\rm LOS}$ Sample" are used. The bottom section of the table presents the present-day distribution of the 3D position and velocity of the SMC relative to the LMC, which results from sampling the systemic properties of the Clouds reported in the upper section of the table. We report the median value, with the uncertainty values corresponding to the 1σ width of the distribution.

Variable	Value	Unit	Reference	Comment
LMC α_0	79.88	degrees	vdM14	RA of the LMC COM. Held fixed.
LMC δ_0	-69.59	degrees	vdM14	DEC of the LMC COM. Held fixed.
LMC $V_{\rm LOS,0}$	261.1 ± 2.2	km s^{-1}	vdM14	LOS velocity of the LMC COM.
LMC $\mu_{\alpha,0}$	-1.895 ± 0.024	mas yr^{-1}	vdM14	Proper motion in the $\alpha\cos(\delta)$ direction of the LMC COM.
LMC $\mu_{\delta,0}$	0.287 ± 0.054	mas yr^{-1}	vdM14	Proper motion in the δ direction of the LMC COM.
LMC D_0	50.1 ± 2.5	kpc	Freedman et al. (2001)	Distance to the LMC COM. Used in the vdM14 analysis. Whilst more recent (and precise) distance estimates are available, we permit D_0 to vary over this range in order to investigate a larger range of allowed LMC orbits.
SMC α_0	13.38	degrees	Subramanian and Subramaniam (2012)	RA of the SMC COM. Held fixed.
SMC δ_0	-73.0	degrees	Subramanian and Subramaniam (2012)	DEC of the SMC COM. Held fixed.
SMC $V_{\rm LOS,0}$	145.6 ± 0.6	km s^{-1}	Harris and Zaritsky (2006)	LOS velocity of the SMC COM.
SMC $\mu_{\alpha,0}$	0.772 ± 0.063	mas yr^{-1}	Kallivayalil et al. (2013)	Proper motion in the $\alpha\cos(\delta)$ direction of the SMC COM.
SMC $\mu_{\delta,0}$	-1.117 ± 0.061	mas yr^{-1}	Kallivayalil et al. (2013)	Proper motion in the δ direction of the SMC COM.
SMC D_0	62.1 ± 1.9	km s^{-1}	Graczyk et al. (2013)	Distance to the SMC COM.
$r_{\rm tot}$	23.5 ± 1.5	kpc	-	Total distance between the LMC and SMC centres of mass.
$V_{\rm tot}$	122.6 ± 32.0	km s^{-1}	-	Total velocity of the SMC relative to the LMC.

set to cross the plane in the very near future. This crossing is likely to affect the dynamics of the LMC disk in the future, but is sufficiently recent (with the median crossing time only 45^{+25}_{-26} Myr ago) that it will not have a significant effect on the present-day kinematics of the disk as a whole. We additionally see that in all realisations, the SMC has had a recent pericentric passage around the LMC 147^{+42}_{-31} Myr ago (in agreement with Zivick et al. 2018). However, as seen in Fig. 4.9, while these are relatively close pericenters, with $r_{\rm peri} = 8.0^{+2.4}_{-2.0}$ kpc, we also find that they occur significantly below the plane of the LMC disk, with $z_{\rm peri} = -6.8^{+2.5}_{-2.6}$ kpc.

Beyond this, the orbit of the SMC varies significantly. Approximately 51% of our realisations have a second SMC crossing of the LMC disk 398^{+84}_{-68} Myr ago, which occurs across a broad range ($28.8^{+11.4}_{-9.2}$ kpc) of distances[26]. The remaining ~49% of orbits either i) do not quite cross the disk plane but do closely approach it during this time period, or ii) remain significantly behind the LMC's disk plane for the entirety of the 1 Gyr over which our models are run. A handful of models (~9%) additionally have a third disk crossing 906^{+61}_{-163} Myr ago, though we note a much larger fraction would experience this crossing if our models were rewound for a greater length of time than the 1 Gyr for which they are currently run. Due to the increasing uncertainty in the SMC's orbit at earlier times, the particulars of this third crossing are much less robustly constrained than the ~400 Myr crossing, with a crossing distance of $53.8^{+13.1}_{-46.3}$ kpc. In fact, ~20% of these third crossings pass within 10 kpc of the LMC center (i.e. this occurs in ~2% of the total model set). At around this time, we additionally find a small fraction (~4%) of our models show a second SMC pericentric passage, again noting this fraction would be substantially increased were our models rewound further than 1 Gyr. These passages have similar pericentric distances to the most recent pericentric passage ($r_{\rm peri} = 6.2^{+3.8}_{-2.3}$ kpc), but occur at smaller out-of-plane distances ($z_{\rm peri} = 2.2^{-1.1}_{+2.5}$ kpc) due to the similarly-timed disk crossing in these realisations.

Whilst these statistics are for the base-case model setup, we find broadly similar results for the heavy-SMC model setup – that is, all realisations experience a SMC pericentre ~150 Myr ago at a reasonably large out-of-plane distance, a moderate fraction of realisations experience a second SMC crossing of the LMC disk plane ~400 Myr ago, and a modest number of realisations have additional disk crossings and pericentric passages ~1 Gyr ago (noting again the number of such realisations would increase were our models rewound for a greater length of time).

It is important to note that the relative simplicity, and in particular the lack of self-

[26] as these are disk crossings, $z = 0$ and thus the in-plane radial distance R is equal to the total distance r.

gravity of our models (see §4.5.3.1 for a detailed discussion), mean the interactions described above are only estimates; more realistic models of the Magellanic/Milky Way system will be required to confirm the precise orbit of the SMC relative to the LMC. Nevertheless, our models provide a useful first look at understanding the likely relative importance of different interactions on the northern arm. We defer detailed discussion of the overall effects of these interactions on the LMC disk, as well as which regions of parameter space correspond to different orbits of the SMC, to Chapter 5, which incorporates MagES data across a larger region of the LMC disk.

4.5.3.1 Model Caveats

Whilst the ability to explore the large allowable parameter space is a significant advantage of our simple model suites, this approach does have limitations. Particularly significant is the lack of self-gravity, which has two significant effects on the system. The first of these is that the gravitational potentials used to model the dark matter halo of each galaxy are unable to deform in response to one another (e.g. Garavito-Camargo et al. 2021). This can potentially influence both the global orbits of the Clouds, and the response of stars within them. The second is that model particles describing stars in the LMC disk cannot directly affect one another – i.e. the LMC disk potential is also fixed in shape – which can affect the response of the stellar disk to interactions (particularly those which might introduce overdensities to the disk). We discuss in turn these effects on each pair of galaxies in the MW/LMC/SMC system below.

We first discuss the effect of self-gravity on the MW/LMC pair, as we can to some extent quantify these effects through comparison of the simpler models to the *N*-body model. In the *N*-body model the gravitational potentials of both galaxies, which in the simpler models are rigid profiles, are allowed to move in response to one another (i.e. the reflex motion of the Milky Way in response to the LMC is captured Gómez et al. 2015); but this is a global shift in position as opposed to a change in shape. However, models capturing this deformation process (see e.g. Fig. 10 of Erkal et al. 2019) demonstrate the shape of the MW potential is not significantly affected even during the infall of a massive (1.5×10^{11} $M_{\odot}$) LMC; and at the distance of our outermost field ($R_{\rm LMC}$~23 kpc), the deformation of the LMC potential is also minimal.

In terms of the disk, as the stellar density is highest near the base of the feature, in the *N*-body model the higher concentration of particles here better maintains the disk kinematics. This contributes to the *N*-body having a strong negative in-plane radial velocity in field 13, but one much closer to zero in field 11: the stronger LMC gravitational

potential at smaller galactocentric radii, in combination with the stronger self-gravity of the disk, helps maintain the disk kinematics near equilibrium levels. In contrast, the lower stellar density in the outskirts of the feature mean the self-gravity of the disk contributes negligibly to the overall gravitational potential, with these regions therefore more easily perturbed. However, we find in §4.5.4.1 below that V_r is less significantly perturbed in the simpler model suites all along the arm compared to the N-body model: somewhat unexpected given the lack of self-gravity in these models should allow for larger perturbations in their kinematics. We therefore conclude the effect of self-gravity in the MW/LMC pair is not responsible for the largely negative in-plane radial velocity along the arm.

We next discuss the effect of self-gravity on the LMC/SMC pair. Several studies have investigated the effects of close interactions with a smaller satellite (like the SMC) on a larger host (like the LMC) in fully self-gravitating systems (e.g. Berentzen et al. 2003; Bekki 2009; Besla et al. 2012; Yozin and Bekki 2014; Pardy et al. 2016). These studies typically assess the effects of a near-direct collision between the two galaxies: that is, a crossing of the host's disk plane which occurs at relatively small host galactocentric radii. A common finding of each of these studies is that such interactions can introduce asymmetries in the disk of the host, and offsets of up to ~2.5 kpc between the dynamical centres of the disk and a central bar. This results in an off-centre and potentially tilted bar, as is observed in the LMC today. Of greater interest to this paper is that these crossings can also produce density waves and features similar to spiral arms out to large radii ($\gtrsim$ 10 kpc: Berentzen et al. 2003; Besla et al. 2016) relatively shortly after the crossing time (100-200 Myr: Berentzen et al. 2003; Pardy et al. 2016), with these features persisting for ~Gyr after the crossing (Berentzen et al. 2003; Yozin and Bekki 2014). Our simple models would not fully capture these effects.

However, we do note this specific type of interaction – that is, a disk plane crossing at small galactocentric radii – is not typical of the interactions observed in our models, with this only occurring in ~9% of our models and ~900 Myr ago, where uncertainties in the orbit of the SMC are very large. The more recent disk crossing observed in our models, which occurs ~400 Myr ago and in ~51% of our models, occurs at a much larger radius ($28.8^{+11.4}_{-9.2}$ kpc) than is typically modelled in these studies. In fact, Bekki (2009) finds that interactions at larger galactocentric radii distances ($R \sim 5-10$ kpc) are unable to produce an off-centre stellar bar in the LMC; and Poggio et al. (2020), while studying the impact of the Sagittarius dwarf on the Milky Way, find that disk crossings at large radii (i.e. which do not align with a simultaneous pericentric passage) affect the MW disk significantly less than crossings at smaller radii. We therefore expect the ~400 Myr disk

plane crossing will have a comparatively small effect on the LMC disk as a whole.

In addition, as discussed above, our models suggest the SMC's recent pericentric passage ~150 Myr ago, occurs at a relatively large out-of-plane distance ($-6.8^{+2.5}_{-2.6}$ kpc), with the SMC only approximately now crossing the LMC disk plane. Thus, whilst the radius of the pericentric passage is similar to the interactions modelled in the above studies, we expect its effect on the LMC disk to be commensurately reduced, though Laporte et al. (2018a), in studying the MW/LMC system, find out-of-plane pericentres may introduce mild ($z \sim 1$ kpc) warping of the host galaxy disk which would not be captured in our simpler models.

Likely a more significant effect of the SMC's recent pericentre is an indirect one: studies of the MW/LMC system (e.g. Garavito-Camargo et al. 2019) suggest pericentres produce both local and global dark matter wakes in the halo of the host galaxy. These wakes can induce torques on the satellite galaxy (Tamfal et al. 2021), thus affecting its orbit. Along similar lines, Kallivayalil et al. (2013) note that such dynamical friction effects would result in a more eccentric orbit of the SMC around the LMC, though the magnitude of this effect is not explicitly calculated. As our simple models do not capture these effects, this is a source of increased uncertainty in the orbit of the SMC, and thus its interactions with the LMC, beyond the recent pericentric passage.

Finally, we briefly discuss the effect of self-gravity on the MW/SMC pair. In contrast to the MW/LMC pair, we do not capture the effect of dynamical friction from the Milky Way on the SMC. This may affect the recent orbit of the SMC, which in turn would affect specifics of interactions between the LMC and SMC. However, we expect the direct effect of the LMC – being much closer and having likely experienced repeated interactions with the SMC prior to the current infall to the Milky Way potential – is more significant in this case.

We additionally note that the gravitational potential used to represent the SMC in our models is relatively simple, particularly given recent findings that indicate it is currently being tidally disrupted by the LMC (e.g. Zivick et al. 2018; De Leo et al. 2020). More detailed modelling which captures this disruption, as well as mass loss from the SMC over time (due to likely repeated interactions with the LMC) would be necessary to fully describe these effects and assess how such a varying potential affects the SMC's orbit.

The above simplifications mean our models do not capture all the subtleties of interactions between the Clouds, and thus cannot definitively establish the origin of substructures such as the northern arm. However, we stress our aim is qualitative, not quantitative, agreement with observations; and our simpler models do permit an exploration of the

allowable parameter space which can indicate the plausibility of various interactions in forming substructures. This ability to isolate which interactions are more or less likely to contribute to the origin of substructures is valuable, as these can be investigated using more detailed models in the future.

4.5.4 Simple model kinematics along the northern arm

We first discuss the base-case suite of 100 models (represented by purple points in Figs. 4.8-4.10). Kinematics for this suite are presented in Fig. 4.8. The distribution of results across the ensemble are represented by box-and-whisker plots, displaying the 5^{th}, 25^{th}, 50^{th}, 75^{th}, and 95^{th} percentiles within each field. For a given field, the spread in ensemble kinematics – that is, ~10 km s^{-1} in V_r and V_z, $10-20$ km s^{-1} in V_θ, and $5-10$ km s^{-1} in each velocity dispersion component – is due entirely to differences in the orbits of the Clouds parameterised by sampling from within the uncertainties in their central positions and motions. These variations can be of a similar order of magnitude to the observational uncertainties within the fields, and demonstrate the importance of sampling these parameters as compared to running a single model realisation.

We find a number of key differences between the ensemble kinematics and the *N*-body model. The azimuthal and in-plane radial velocity dispersions (panels *d* and *e* of Fig. 4.8) are up to $10-15$ km s^{-1} higher than the *N*-body model, and the vertical velocity dispersion (panel *f*) up to 5 km s^{-1} higher. This is by design, as the model suites are initialised with higher velocity dispersions to more closely match recent MagES measurements in the outer LMC disk (see Paper I). However, the velocity dispersion in each component remains underestimated in field 11 (closest to the LMC disk) relative to observations.

The ensemble azimuthal velocity (panel *a*) is lower than the *N*-body model, and remains flat at approximately the value measured in the outer LMC disk in Paper I. This is more consistent with the observations, particularly in the inner- and outermost fields along the feature where the *N*-body model is most discrepant. The vertical velocity (panel *c*) is also more consistent with observations in the three outermost feature fields. However, in the three fields closest to the LMC disk, the vertical velocity is not significantly different from the *N*-body model and remains lower than the observations.

The greatest difference in model kinematics is in the in-plane radial velocity (panel *b*). In the base-case ensemble, this remains almost flat along the length of the feature, with only a very mild (~5 km s^{-1}) drop and subsequent increase in the mean radial velocity along the feature. This is significantly different from the very negative values seen in

the observations and the inner fields of the *N*-body model. However, the lack of a steep increase in radial velocity along the feature in the model suite is a trend that is less discrepant with observations than the *N*-body model in the outermost feature fields.

In order to understand the drivers of these kinematic differences, we now compare the different simple model ensembles to assess the impact of varying galaxy masses on the kinematics of the northern arm. Fig. 4.11 shows the three disk velocity components (V_θ, V_r, and V_z), as well as dispersions in each of these components, for both the model ensembles and the observations within each field. Each point represents the median of the 12 realisations, with error bars showing the full range across each suite. We include the base-case ensemble in this comparison, but for consistency sample only the same 12 realisations as included for the other suites. Pale dashed extensions to the base-case ensemble results show the full range from all 100 realisations of the ensemble, for comparison. Fig. 4.10 shows, in the same format, the out-of-plane distance (z) for each of the model ensembles.

4.5.4.1 General comments

In general, most of the model suites follow the same overall kinematic trends, and do not provide substantially better matches to the observations than the base-case model. The largest differences between model suites typically occur in the outermost field, with the median response typically very similar for most of the length of the feature. This as expected: at smaller radii, the LMC potential dominates, and any external perturbing potential, regardless of origin, does not significantly affect the kinematics. In contrast, at large galactocentric radii the perturbing potential can dominate, leading to different kinematics depending on the origin of the perturbation.

We find the out-of-plane distances (Fig. 4.10) are typically small (<3 kpc) for each of the model suites, consistent with our findings in §4.4.2 that the northern arm roughly follows the plane of the LMC disk. We have tested utilising the median out-of-plane distance for each field in each model suite as the assumed distance for the MagES fields when deriving the observed kinematics in the plane of the disk. However, we find the resulting differences in kinematics are typically less than ~5 km s^{-1}: well within the uncertainties of the measurements calculated assuming the fields exactly follow the LMC disk plane. We also find the median distance dispersion within each field is negligibly different (~0.15 kpc) between model suites, with a mild (~0.3 kpc) decrease in the median distance dispersion along the length of the feature. This is, within uncertainty, consistent with our measurements of constant G_0 dispersion along the first half of the feature. It is

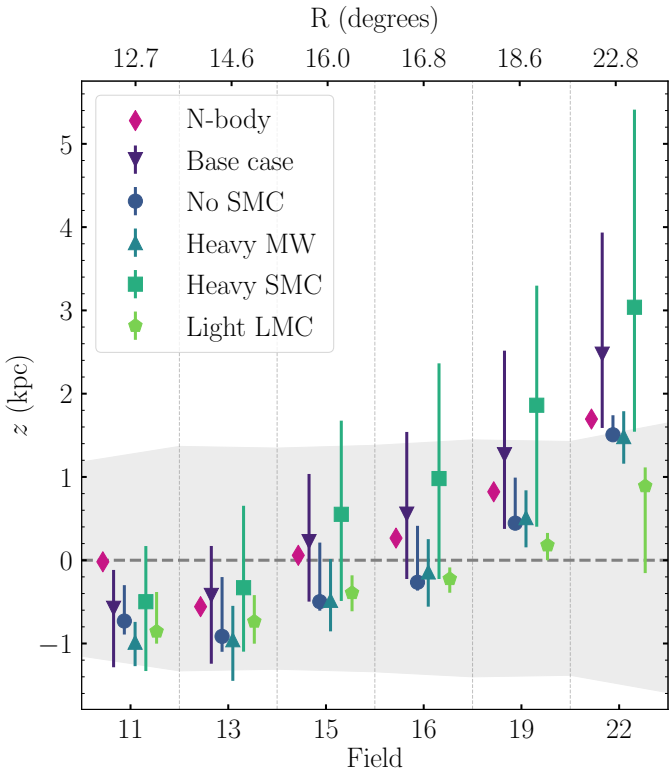

Figure 4.10: Model out-of-plane distance (z) for fields along the northern arm-like feature, calculated relative to a C18 disk geometry. Magenta diamonds show results from the *N*-body model results. Coloured model points show ensemble medians, and error bars show ensemble ranges, with each suite represented by a different colour and symbol. Points without error bars have sufficiently small ranges that these are not observable. For clarity, fields are spaced equally along the x-axis, and each suite of model points slightly offset. The top axis lists the LMC galactocentric radius of the fields. The dashed grey line indicates the $z = 0$ assumption utilised for the observed data, with the shaded grey region indicating the distance range associated with the uncertainty in the median G_0 magnitude along the northern arm as in §4.4.2.

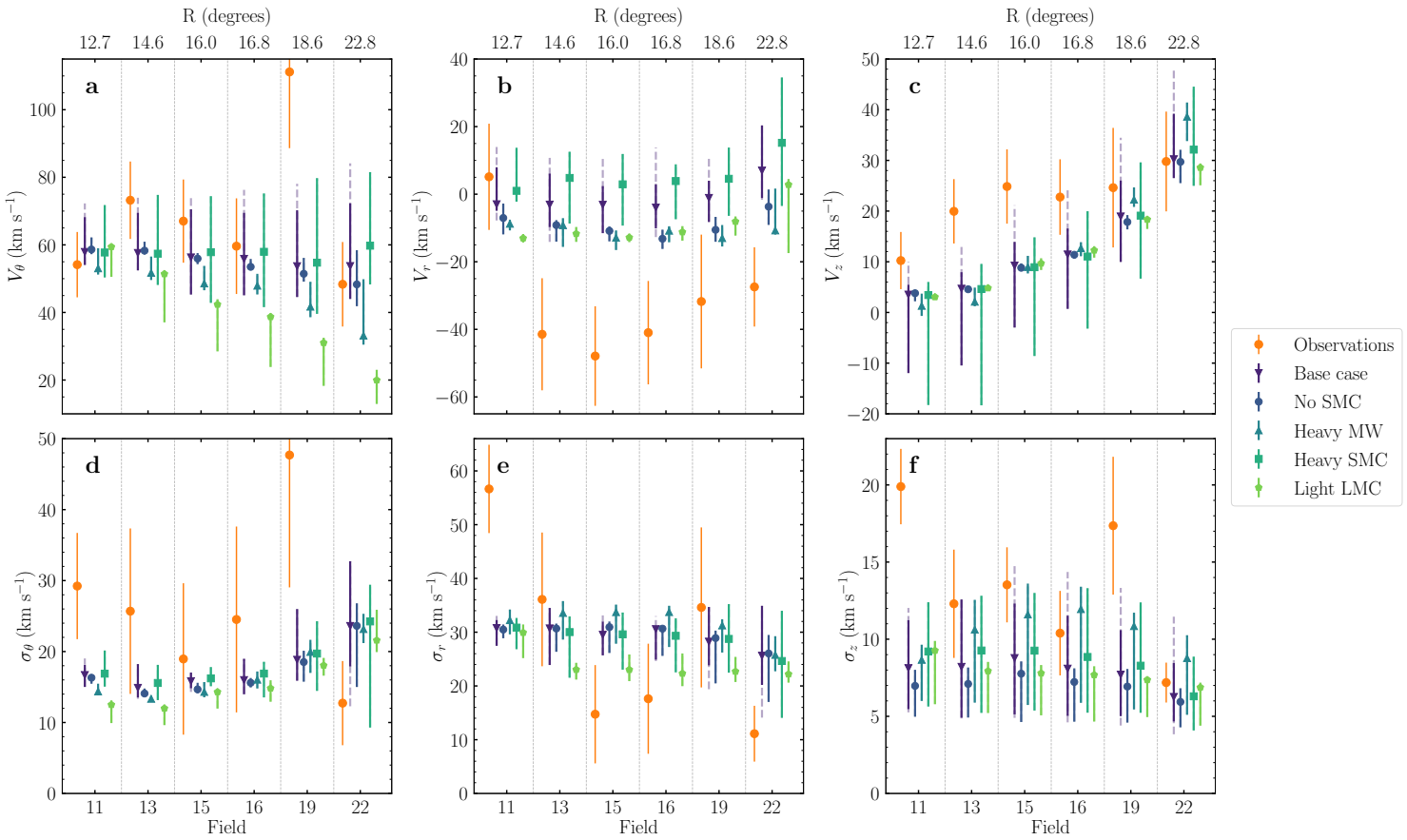

Figure 4.11: Model velocities and dispersions for MagES fields along the arm-like feature for the simpler model suites, calculated assumming a C18 disk geometry. Top panels show, in order, the azimuthal, radial, and vertical velocity component, with bottom panels showing the corresponding velocity dispersion in each component. Orange points show the observations and associated 1σ uncertainties. Coloured model points show ensemble medians, and error bars show ensemble ranges, with each suite represented by a different colour and symbol. Points without error bars have sufficiently small ranges that these are not observable. For clarity, fields are artificially spaced equally along the x-axis, and each suite of model points slightly offset. The top axis lists the LMC galactocentric radius of the fields. Dashed extensions of the error bars for the base-case ensemble (purple) show the full range of data from the 100 realisations relative to the range associated with the subsample of 12 realisations used for the other model suites.

further suggestive that the increase in the G_0 dispersion measured in the outer regions of the feature is due to contamination as speculated in §4.4.2, and not a genuine thickening of the feature – if so, we would expect the distance dispersion of the models to increase along the length of the northern arm.

Notably, regardless of model suite, each component of velocity dispersion is underestimated in the innermost feature field. In the case of the vertical velocity dispersion, this is due to the initial conditions of the model, which even within the outer LMC disk is lower than observations at ~10 km s^{-1}. This is due to the modest scale height of the disk used in our model and the relatively small contribution of the disk to the gravitational field in the outer parts of the disk. It is possible that previous encounters with the SMC may be needed to inflate this dispersion. Alternatively, the outer disk of the LMC may be thicker than assumed in our model.

We also note that whilst selection of the 12 realisations attempts to sample the full possible kinematic distribution, comparison of the set of 12 realisations to the full suite of 100 base-case models as in Fig. 4.11 reveals the full range is somewhat underestimated, with the upper limits of V_θ, V_r, V_z, and σ_z underestimated by up to 30%. In general, this does not improve the consistency between the model kinematics and observations, with the possible exception of V_z in the inner fields. Median values are not significantly different in the restricted set, and lower limits are typically well-sampled. The largest differences in median values are only on the order of ~10%, with overestimated σ_z medians and underestimated V_θ medians along the length of the arm.

4.5.4.2 Effect of the MW mass

The effect of the heavy MW (indicated by dark green points in Figs. 4.11 and 4.10) is most apparent in the azimuthal velocity (panel *a* of Fig. 4.11), with a mild decrease in the median V_θ (by ~15 km s^{-1}) along the length of the feature. However, we note this remains consistent with the observations within uncertainty. Further, the V_θ medians are typically underestimated as compared to a full suite of 100 realisations. Consequently, this does not preclude a heavy MW from matching the observations.

Comparing the in-plane radial and vertical velocities (panels *b* and *c* respectively), in the innermost fields the heavy MW suite is not significantly different from the base-case suite (indicated by purple points). A larger difference occurs in the outermost fields along the feature, with the heavy MW generating slightly higher vertical velocities, and slightly more negative in-plane radial velocities. It is not surprising the strongest effects are felt in the outermost fields: it is here where the MW gravitational potential is strongest compared

to the LMC gravitational potential, and can induce the strongest perturbations.

The heavy MW has a negligible effect on the azimuthal velocity dispersion (panel *d*), and minimally (~2 km s^{-1}) increases the in-plane radial velocity dispersion (panel *e*) – not sufficient to meet the large measured velocity dispersions in the innermost observed field. It does have an increased (~5 km s^{-1}) vertical velocity dispersion(panel *f*) in all but the innermost field, which provides a closer match to observations than any of the other model suites. The out-of-plane distance (Fig. 4.10) is also negligibly different from the no-SMC and *N*-body models, remaining within 1.5 kpc of the assumed C18 inclined disk geometry. Out-of-plane distances of this magnitude can be accommodated within our photometric uncertainties. As discussed in §4.4.2, the typical uncertainty in our median G_0 magnitudes along the feature is ~0.05 mag. At the distance of the feature, this corresponds to an ~1.5 kpc uncertainty in the derived distance.

We can understand the increased effects of the heavy MW in the *z*-direction when considering the LMC's orbit and inclination relative to the MW during its infall. The orientation of the LMC is such that the northern half of the disk is inclined closer to the MW plane. As such, there is an increasingly strong gravitational force from the MW along the length of the northern arm. Further, the orbit of the LMC is such that it is approaching the MW from underneath the MW disk plane. The force of the MW thus pulls forward in the positive *z*-direction on the LMC disk, increasing V_z particularly in the outermost fields where this pull is strongest relative to the LMC potential. This may also explain the increased vertical velocity dispersion σ_z as compared to the lighter MW models, and the increasingly positive out-of-plane distance along the feature.

As the primary effect of the MW on the LMC is in the positive *z*-direction, we hypothesise the MW is also responsible for the asymmetric LOS velocity distributions observed in the northern LMC disk in Paper I. The distribution of $V_{\rm LOS}$ for likely-Magellanic stars in MagES fields 18 and 12 were found to have tails to low LOS velocities; the low inclination of the LMC disk implies stars in these tails have positive vertical velocities of up to ~40 km s^{-1}. This is similar to the positive V_z velocities found along the northern arm. We therefore suggest stars in the northern LMC disk showing this perturbation signature are, like the northern arm, disturbed during the LMC's infall to the MW.

4.5.4.3 Effect of the SMC

We now consider the effect of the SMC, comparing the no-SMC (indicated by dark blue points in Figs. 4.11 and 4.10) and heavy SMC (indicated by turquoise points) model suites to the regular SMC base-case ensemble (indicated by purple points). The median

azimuthal and vertical velocities (panels *a* and *c* of Fig. 4.11 respectively) are negligibly affected by the presence of the SMC, although some individual realisations have quite large differences from the median. In the case of the heavy SMC, certain individual realisations have ~20 km s^{-1} higher azimuthal velocities in the outermost feature fields, and ~20 km s^{-1} lower vertical velocities in the innermost feature fields. However, those realisations are very inconsistent with observations – the associated negative vertical velocities being ~5σ inconsistent with the positive vertical velocities measured. We can conclude the strong perturbations associated with these individual realisations are not realistic, despite being within the allowed uncertainties for the central positions and systemic velocities of the SMC in particular, given these large discrepancies are only observed in model suites including the SMC. The SMC also negligibly affects the median velocity dispersion in any of the three components (panels *d-f*), with the only difference being an increased allowable range of azimuthal and radial velocity dispersions in the outermost fields compared to the no-SMC models.

Instead, the SMC has the strongest effect on the in-plane radial velocities (panel *b*), with model suites including the SMC having higher median radial velocities than the no-SMC suite, and the heavy SMC suite generating the largest increase of up to ~20 km s^{-1}. Notably, this perturbation is in the wrong direction: these median kinematics are further from the negative observed radial velocities than the no-SMC suite (although we note some individual realisations of the base-case and heavy SMC suites do overlap the range of the no-SMC suite). This suggests recent interactions with the SMC, as captured by these models, are not the source of the perturbation generating the northern arm-like feature.

In the innermost two fields along the northern arm, the base-case and heavy SMC suites have slightly smaller (~0.4 kpc) median out-of-plane distances than the no-SMC suite (Fig. 4.10). However, in fields further along the feature, these distances significantly increase, with the median out-of-plane distance ~3 kpc in front of the LMC disk in the outermost field, and some individual realisations >5 kpc from the assumed disk plane. Notably, we find the realisations which produce the largest out-of-plane distances are the same realisations that produce very negative vertical velocities in the innermost fields, strongly inconsistent with observations. Even so, the median out-of-plane distances are moderately larger than the ~1.5 kpc uncertainties in distance accommodated by our photometric uncertainties in §4.4.2. Whilst some individual realisations of these models do have out-of-plane distances within this range, a majority of these model realisations are ruled out as these geometries would result in brighter G_0 magnitudes along the arm, inconsistent with those measured. This provides further evidence that recent SMC interactions

are not responsible for formation of the northern arm.

4.5.4.4 Effect of the LMC mass

Whilst a number of recent studies have indicated the total LMC mass is large ($\geq 10^{11}$ $M_\odot$: e.g. Erkal et al. 2019; Peñarrubia et al. 2016), we additionally explore the formation of the northern arm assuming a factor-of-ten lighter LMC (indicated by light green points in Figs. 4.11 and 4.10) as used in traditional models of the LMC assuming tidal truncation (see e.g. section 2 of Garavito-Camargo et al. 2019 for a review). The most significant kinematic difference this induces is in the azimuthal velocity (panel *a* of Fig. 4.11), which displays a strong drop from ~60 km s^{-1} in the innermost field to only ~20 km s^{-1} in the outermost field. This is a result of the model setup, rather than a physical perturbative effect from the MW. As the model suites are initialised to match the rotation curve of the LMC ($V_{\rm circ}$~90 km s^{-1}) at 10 kpc, this necessitates an enclosed mass of nearly 1.5×10^{10} $M_\odot$ at this radius. In order to facilitate this, and maintain the total mass of 1.5×10^{10} $M_\odot$ for the model, there is negligible dark (or baryonic) matter beyond this radius. As a result, the azimuthal velocity drops off with approximately $1/R$ dependence as expected given the lack of matter beyond this radius. Given this is strongly inconsistent with the approximately flat azimuthal velocities measured, we can conclude the LMC is not this light, and must be at least 1.5×10^{11} $M_\odot$ in order to maintain the flat rotation curve observed across these large galactocentric radii. All other kinematic component medians do not differ significantly under the light-LMC case as compared to the other model suites.

4.5.5 Origin of the northern arm

As discussed in §4.5.4.2, the increasingly positive vertical velocity observed along the northern arm is consistent with a MW origin, with qualitatively similar trends observed along the arm in all models, including those omitting the SMC. The heavy-MW model suite also produces the closest σ_z to that observed, indicating the strength of the Milky Way's gravitational force in this direction. More difficult to understand is the strongly negative radial velocity observed along the arm, which none of our models replicate. The model suite producing the closest match to these kinematics is the heavy MW suite (indicated by dark green points in Figs. 4.11 and 4.10); individual model realisations in this suite provide the most negative radial velocities along the length of the feature, albeit significantly weaker than those observed (approximately -10 km s^{-1}, compared to approximately -40 km s^{-1}). Also notable is the *N*-body model (magenta points in

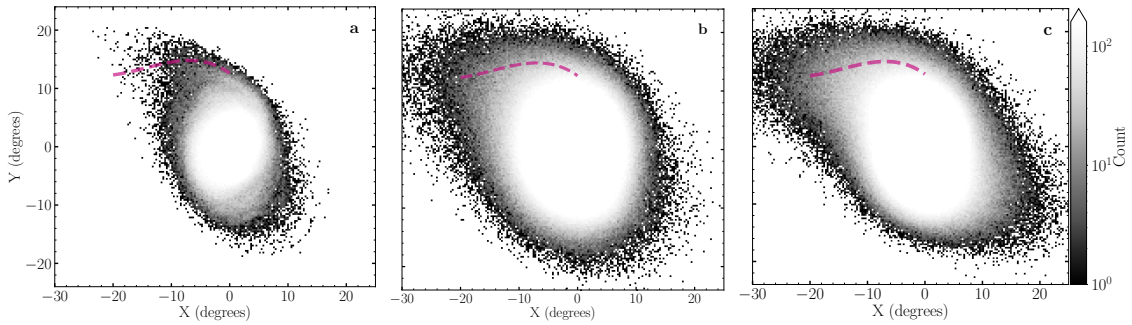

Figure 4.12: Density plots of model particles for different model suites. Panels show the *N*-body model (*a*), an individual realisation of the base-case suite (*b*), and the same realisation in the heavy MW suite (*c*). Dashed magenta lines in each panel show the observed feature track of the northern arm. The two realisations of the simpler model suites produce relatively flat northern overdensities in the Y direction, similar to that observed, while the debris track in the *N*-body model increases strongly in Y along the length of the feature, to larger values than those observed.

Figs. 4.8 and 4.10), which does have a significant negative radial velocity in field 13 (approximately -35 km s^{-1}), but which increases rapidly resulting in a strongly positive radial velocity in the outermost feature field.

As discussed in §4.5.3.1, we do not expect the lack of self-gravity between the LMC and MW in the simpler model suites to significantly affect the kinematics of the northern arm. However, we do note that the geometry of the feature differs significantly in the simpler models as compared to the *N*-body model. Fig. 4.12 shows the density of model particles for the same individual realisation of the base-case and heavy MW model suites, in addition to the *N*-body model. Notably, the debris forming the arm-like feature in the *N*-body model (panel *a*) has a significantly different geometry to the simpler model realisations (panels *b* and *c*), with the structure increasing steeply in *Y*-position along the length of the feature. This means that when comparing measurements at the same X/Y positions as the observed MagES fields, the regions compared in the *N*-body model are not along the stream of debris actually forming the arm-like structure, and as a result there are fewer model particles within each field. This is in contrast to the simpler model realisations, where the northern overdensities are not significantly different from the observed feature track, albeit without the observed gap between the northern arm and the disk. As a result, it is perhaps not surprising that the kinematics of the *N*-body model are somewhat different to those in the simpler model ensembles, and the observations: different areas of the feature, under the influence of different gravitational forces, are being compared. Nonetheless, as discussed above, when a feature track is fitted to the *N*-body model and equivalent ϕ_1/ϕ_2 locations along the northern arm are compared, the resultant kinematics are not substantially different from those derived when equivalent X/Y positions are compared.

Given individual realisations of the heavy MW ensemble produce the closest kinematics to those observed, it might be inferred that an even heavier MW is necessary in order to produce the strong observed perturbations in V_r. However, we note there is an upper limit on the MW mass beyond which the LMC and SMC become bound, and have experienced multiple previous pericentric passages around the MW. That scenario is inconsistent with results that the Clouds are only now on their first infall into the MW potential (Kallivayalil et al. 2013). Given the 50% increase in MW halo mass in our models only has a relatively small effect on V_r (reducing these by ~5 km s^{-1} compared to the no-SMC models with a regular-mass MW), the MW mass required to reproduce the observed kinematics would likely exceed that binding threshold. This implies a heavy MW likely contributes to, but is not the only required condition for, reproduction of the feature kinematics.

Further, Fig. 4.13 shows the distribution of model particles for an individual heavy MW realisation, colour-coded by the ratio of each particle's current LMC galactocentric radius $R_{\rm final}$, to its origin radius $R_{\rm initial}$. Particles in the region of the northern arm generally move outwards over the course of the simulation, with $R_{\rm final}/R_{\rm initial}$~1.2 along most of the arm. This implies particles located at large distances along the arm originate at marginally larger galactocentric radii than particles at the base of the arm: consistent with the mild negative metallicity gradient observed along the arm. However, the fact that $R_{\rm final}/R_{\rm initial}>1$ along the length of the arm indicates the MW acts to push stars that form the northern arm outwards from the LMC disk. Notably, immediately below the observed feature track and crossing its base, model particles move strongly outwards: $R_{\rm final}/R_{\rm initial}$ reaches up to ~3. This may contribute to forming an overdensity along the feature track, with particles immediately below the feature track pushed strongly outwards to form the feature and generate a gap between the feature and the observed LMC disk. This scenario, however, does not explain the strongly negative radial velocities observed along the arm – indicating models including only the Milky Way do not capture the full perturbation to the LMC.

We next consider the potential effects of recent interactions with the SMC on the northern arm, discussing first the recent pericentric passage of the SMC around the LMC ~150 Myr ago. As discussed in §4.5.3, while this is a close pericentre (with the SMC passing within $8.0^{+2.4}_{-2.0}$ kpc of the LMC centre), it is not coincident with a disk plane crossing: the SMC remains ~7 kpc below the LMC disk plane during the encounter. As such, we find the SMC does not substantially affect the LMC disk during this interaction and, as discussed in §4.5.3.1, the inclusion of self-gravity in the models is unlikely to significantly change this conclusion. In addition, we point out that for every model, the projected location of the pericentric passage is towards the southwest of the LMC: almost

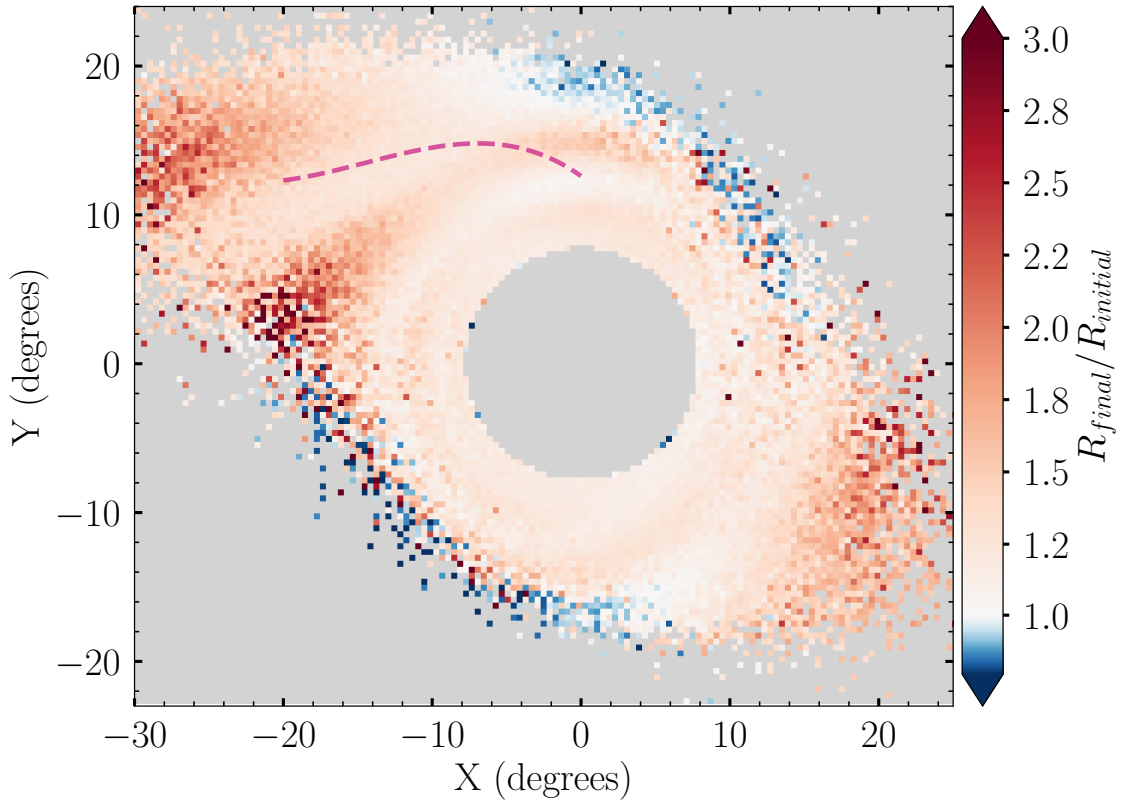

Figure 4.13: Binned map of particles within a single realisation of the heavy MW model, colour-coded by the mean ratio within each bin of the current LMC galactocentric radius ($R_{\rm final}$) to the initial particle galactocentric radius 1 Gyr ago during model initialisation ($R_{\rm initial}$). The dashed magenta line shows the observed feature track of the northern arm. The central 8° of the LMC disk is masked to emphasise the variation in $R_{\rm final}/R_{\rm initial}$ in the outskirts of the LMC.

directly opposite to the northern arm. At this radius, the circular velocity of the LMC (which as seen in §4.4.3, remains constant even along the arm) implies a timescale of ~300 Myr for the stars most strongly perturbed by this interaction to reach the north-eastern disk. This is approximately double the ~150 Myr that has passed since the pericentric passage, further indicating this interaction is unlikely to be the origin of the northern arm.

Interactions with a greater possibility of contributing to the formation of the northern arm are SMC crossings of the LMC disk plane, as these directly affect the nearby stars as the SMC passes through the disk. In the ~50% of our base-case and heavy SMC model realisations which experience disk crossings in the past 1 Gyr (beyond that which is currently occurring), we find the LMC disk is most strongly affected by the disk crossing ~400 Myr ago. This crossing can occur across a broad range of distances ($28.8^{+11.4}_{-9.2}$ kpc: see §4.5.3) from the LMC centre, but those which occur at the smallest radii have the largest effect on the LMC disk – and a much more significant effect than the recent SMC

pericentric passage in the regions of interest. A handful of models (~9%) have yet another SMC disk crossing ~900 Myr ago, which can occur across a very wide distance range (1σ limits of 7.5 and 66.9 kpc). While crossings which occur at distances toward the upper end of this range are unlikely to significantly affect the LMC, the ~20% which pass within 10 kpc of the LMC center could potentially affect the northern arm, and we consider these in addition to the ~400 Myr crossing in the discussion that follows.

Fig. 4.14 presents results from two realisations of the base case model, as highlighted in Fig. 4.9, demonstrating the effect of these disk crossings on the LMC disk. The left panels present a realisation which has only experienced the most recent ~400 Myr disk crossing – which in this model occurs at a distance of ~18 kpc from the LMC center – and the centre panels present one of the few realisations which has experienced two SMC disk crossings (excluding that which is currently occurring) within the past 1 Gyr. These occur ~360 and ~980 Myr ago, at LMC distances of ~14.5 kpc and ~8 kpc respectively. The upper panels show the original locations of these disk plane crossings, and the present-day location of the crossing, computed by rotating the location of the original disk-crossing within the LMC's disk plane assuming a circular velocity of 90 km s^{-1}. Note these are different to the present-day location of the SMC itself. Lower panels show the binned current LMC particle distribution, colour-coded by the distance of each particle from the SMC at the time of each disk crossing.

We first discuss the SMC crossing of the LMC disk plane ~400 Myr ago. Considering first the realisation which has experienced only this crossing, shown in the leftmost panels of Fig. 4.14, we find the geometry of the northern arm in this realisation is very similar to that in both the base-case and heavy MW model suite realisations in Fig. 4.12. This indicates the crossing does not significantly impact the geometry of the northern arm. Further, as seen in panels *d* and *e* of Fig. 4.14, particles which today form the northern arm are not closely perturbed by the SMC during its crossing of the LMC disk plane. The fact that this crossing typically occurs at large LMC galactocentric radii (typically double that of the recent pericentric passage) further indicates that, as discussed in §4.5.3.1, the inclusion of self-gravity in the models is unlikely to change this result. This fact, in conjunction with the fact that model realisations which experience this crossing (and indeed most realisations in both the base-case and heavy SMC model suites) do not produce negative in-plane radial velocities as observed along the northern arm, lead us to conclude the disk crossing ~400 Myr ago is likely not the origin of the northern arm.

Instead, we do note particles most closely perturbed during this disk plane crossing have in fact moved clockwise with the LMC's rotation (from red cross to red circle in panels *a* and *b* of Fig. 4.14), and are now located in the western outskirts of the LMC

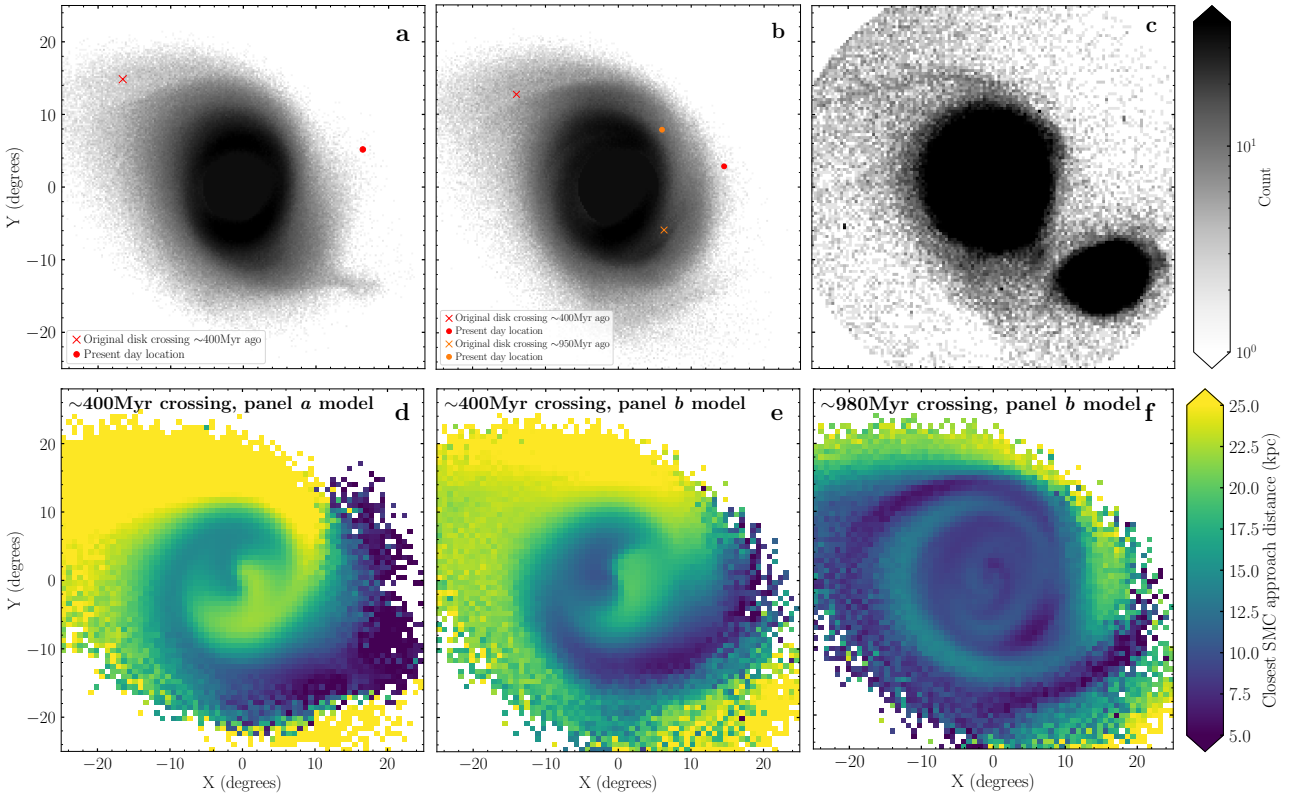

Figure 4.14: Upper panels: Density of particles for base-case model realisations having experienced one (left) or two (center) SMC crossings of the LMC disk plane, compared to the density of observed LMC stars selected using very similar criteria to Gaia Collaboration et al. (2021c) (right). Locations of crossings are marked by coloured x-signs, with the present-day location of the crossing (different to the present-day location of the SMC itself) marked with circles of the corresponding colour. Lower panels: Current model particle distribution, colour-coded by the particle distance from the SMC at the time of each SMC crossing of the LMC disk plane. In order, panels show the realisation with a single crossing ~400 Myr ago (left) corresponding to the density map in panel *a*, the ~400 Myr crossing (centre) in the two-crossing model corresponding to the density map in panel *b* and the ~980 Myr crossing in the two-crossing model (right) corresponding to the density map in panel *b*. Stars closely perturbed during the most recent SMC disk crossing ~400 Myr ago, in both realisations, now comprise the western LMC disk (which appears truncated in Gaia maps of the periphery, as in panel *c*.

disk: the same region as the observed apparent truncation in the western LMC disk at a radius of ~10° in panel *c* of Fig. 4.14. Chapter 5 investigates this truncation feature, and the potential role of the SMC in its formation, in more detail.

We next consider the model realisation which experiences disk crossings both ~400 and ~900 Myr ago, focussing on the older disk crossing which occurs in this model ~980 Myr ago. Panel *f* reveals some particles closely perturbed in this crossing are now located in the vicinity the northern arm. This is evidence that historical interactions with the SMC can potentially influence stars which now form the northern arm. We do find that the few realisations in both the base-case and heavy-SMC models which have experienced this older disk crossing still do not produce the negative in-plane radial velocities as observed along the northern arm. However, it is possible for these early disk crossings to occur at small LMC radii (see 4.5.3); and in such a case, as discussed in §4.5.3.1, our relatively simple models would not capture the full effect of the interaction due to the lack of self-gravity incorporated in the models. Notably, Besla et al. (2016) find that multiple LMC/SMC close passages over the course of 6 Gyr can produce significant overdensities and apparent spiral arms in the outer LMC disk, particularly in its northern outskirts at similar distances to the location of the arm today, though they do not report kinematics for these features. It is thus plausible that early interactions with the SMC may have perturbed stars which today form the northern arm, producing both the characteristic gap between the arm and the nearby northern LMC disk, and the strongly negative in-plane radial velocities observed, neither of which are replicated in our simpler models. More realistic models are thus required to confirm this possibility, and better constrain these early interactions between the Clouds.

In summary, we posit the following scenario for the formation of the northern arm. Prior to the Clouds' infall into the MW potential and up to ~1 Gyr ago, historical interactions between the LMC and SMC, potentially including disk crossings at small LMC galactocentric radii, perturb stars that, at the present day, comprise the northern outskirts of the LMC, inparting a strongly negative radial velocity to the stars which will eventually form the arm. Over the last ~Gyr, the Clouds have fallen into a relatively massive MW potential, which acts to further perturb these stars – particularly in the *z*-direction – whilst they rotate around the LMC, producing the arm-like feature seen today. Recent interactions between the LMC and SMC during the past Gyr, particularly the SMC's recent pericentric passage ~150 Myr ago and an SMC crossing of the LMC disk plane ~400 Myr ago, likely do not strongly affect the stars that form the northern arm, but do closely impact stars which today form a truncation in the western LMC disk.

4.6 Summary

We have performed a detailed investigation of the arm-like feature in the extreme northern outskirts of the LMC first discovered by Mackey et al. (2016). Our analysis utilises spectroscopic data for red clump and red giant branch stars from seven MagES fields located along the full length of the feature to obtain [Fe/H] abundances, and in conjunction with Gaia EDR3 data, the first 3D kinematics for individual stars within the arm. We also use Gaia photometry of the red clump to probe the structure of the arm.

We find the northern arm generally follows the inclination of the LMC disk plane, and has a similar thickness to the outer LMC disk. The median metallicity near the base of the arm is consistent with that in the nearby outer LMC disk, and we find weak evidence for a mild negative gradient in [Fe/H], decreasing from approximately -0.9 at 11 kpc from the LMC centre, to approximately -1.2 at an LMC galactocentric radius of ~22 kpc in the outermost MagES feature field. We therefore conclude the arm is comprised of LMC disk material.

The kinematics of the northern arm also indicate it is comprised of perturbed LMC material. The azimuthal velocity remains reasonably constant along the feature, at approximately ~60 km s^{-1}: similar to that measured in the outer LMC disk. In contrast, the in-plane radial velocity and out-of-plane vertical velocities are strongly perturbed. Both of these velocity components are near zero at the base of the arm, consistent with the equilibrium values in the outer LMC disk. However, the in-plane radial velocity drops to approximately -40km s^{-1} just two degrees from the base of the arm, remaining near this value along its length, and the vertical velocity steadily increases to ~30 km s^{-1} along the length of the arm. The velocity dispersion in each component decreases along the length of the arm, from values comparable to those in the outer LMC disk near the base of the arm, to roughly half this in the outermost MagES field.

In order to understand the formation of the northern arm, we develop a new suite of dynamical models, sampling from uncertainties in the LMC and SMC central locations and systemic motions, and investigating the effect of different LMC/SMC/MW masses on the structure and kinematics of the feature. We find models with a heavy MW (1.2×10^{12} M$_\odot$) and without an SMC have the closest match to the observed kinematics, reproducing the same qualitative velocity trends as those observed. In these models, the LMC's infall to the Milky Way's gravitational potential produces the increasingly positive out-of-plane velocity along the arm. However, even this model is insufficient to fully reproduce the feature kinematics: most significantly, the observed in-plane radial velocity is ~$20 - 30$ km s^{-1} more negative than in the model.

Our models suggest recent (i.e. within the past ~Gyr) interactions with the SMC do not strongly contribute to the formation of the northern arm. Model LMC particles most significantly disturbed in these interactions, including the recent SMC pericentre ~150 Myr ago and a recent crossing of the LMC disk plane by the SMC ~400 Myr ago, are today located predominantly in the southwestern LMC disk, and are far from the northern arm. Further, model realisations in which the SMC plays a more important dynamical role (particularly those including a heavy SMC) become increasingly inconsistent with observations, with positive in-plane radial velocities and negative vertical velocities (in contrast to the negative in-plane radial velocities and positive vertical velocities observed). However, as it is likely the LMC and SMC are a long-lived binary pair, it is possible that historical interactions with the SMC prior to the past ~900 Myr have perturbed LMC stars which now form the northern arm. Indeed, such interactions could be responsible for the strongly negative observed in-plane radial velocity, which is not replicated in any of our models.

In summary, we suggest the following origin for the northern arm. Prior to the Clouds' infall into the MW potential ~1 Gyr ago, interactions between the LMC and SMC perturbed the kinematics of stars in what is now the northern outskirts of the LMC, generating negative in-plane radial velocities. Over the last ~Gyr, as the LMC has fallen into the Milky Way potential (where a higher Milky Way mass is preferred), these stars have been further perturbed, producing the characteristic shape of the northern arm, and the positive out-of-plane velocities observed along its length. Self-gravitating models that are able to more accurately trace the dynamical influence of the SMC over longer timescales will be required to quantitatively test this scenario.

Chapter 5

Kinematics of the disturbed LMC outskirts

A surprising development from a surprising angle.

Yamada Ichiro

This chapter presents the content of **L. R. Cullinane**, A. D. Mackey, G. S. Da Costa, D. Erkal, S. E. Koposov, and V. Belokurov, 2021. *The Magellanic Edges Survey III: Kinematics of the disturbed LMC outskirts.* The paper is the late stages of preparation for submission to the Monthly Notices of the Royal Astronomical Society.

5.1 Abstract

We explore the structural and kinematic properties of the outskirts of the Large Magellanic Cloud (LMC) using data from the Magellanic Edges Survey (MagES) and Gaia EDR3. We find that even at large galactocentric radii ($8^\circ<R<11^\circ$), the north-eastern LMC disk is relatively unperturbed: its kinematics are consistent with a disk of inclination ~36.5° and line-of-nodes position angle ~145° east of north. In contrast, fields at similar radii in the southern and western disk are significantly perturbed from equilibrium, with non-zero radial and vertical velocities, and distances significantly in front of the disk plane implied by our north-eastern fields. Comparison of our observations to simple dynamical models of the Magellanic/Milky Way system reveals that a recent Small Magellanic Cloud (SMC)

crossing of the LMC disk plane ~400 Myr ago, in combination with the LMC's infall to the Milky Way potential, can qualitatively explain most of the perturbations in the outer disk. We additionally find that the claw-like and arm-like structures south of the LMC have similar metallicities to the outer LMC disk ([Fe/H]~ -1), and are likely comprised of perturbed LMC disk material. The claw-like substructure is particularly disturbed, with out-of-plane velocities >60 km s^{-1} and apparent counter-rotation relative to the LMC. No coherent kinematic trends are observed along the southern arm-like feature, indicating its origin is unlikely to be solely due to the same events producing the LMC's northern arm. More detailed models are necessary to elucidate the origin of these southern features, potentially requiring repeated interactions with the SMC prior to ~1 Gyr ago.

5.2 Introduction

At respective distances of ~50 and ~60 kpc (Pietrzyński et al. 2019; Graczyk et al. 2020), the Large and Small Magellanic Clouds (LMC/SMC) are the closest pair of interacting Milky Way (MW) dwarf satellites. This affords us the unique opportunity to study in detail the effects of tidal interactions on both the dynamics and star-formation history of the Magellanic system. As the Clouds are thought to be on their first infall into the Milky Way potential (Kallivayalil et al. 2013), the plethora of unusual features observed in the Clouds are likely the result of repeated interactions between the two galaxies themselves, with the Milky Way affecting their morphology and dynamics only comparatively recently. These features include the extensive Magellanic Stream of HI gas (e.g. Mathewson et al. 1974; Nidever et al. 2008), the irregular morphology and dynamics of the SMC (e.g. Hatzidimitriou and Hawkins 1989; Harris and Zaritsky 2006; Dobbie et al. 2014a; Ripepi et al. 2017; De Leo et al. 2020 and many others), and the tilted, off-centre stellar bar and single spiral arm in the LMC (de Vaucouleurs and Freeman 1972; van der Marel and Cioni 2001).

While the less massive SMC is the more heavily distorted of the two galaxies, the more massive LMC has not escaped from these interactions unscathed. The morphology of the LMC can be broadly described as that of an inclined disk, but it also displays significant deviations from simple ordered rotation in the disk plane. In addition to the unusual properties mentioned above of the stellar bar and spiral arm, which are predominantly comprised of younger stars (e.g. El Youssoufi et al. 2019), older stellar populations also show evidence of perturbation, including multiple warps (Choi et al. 2018b; Olsen and Salyk 2002), ring-like overdensities (Kunkel et al. 1997; Choi et al. 2018a), and offsets between the observed photometric and kinematic centres (see e.g. Table 1 of Wan et al. 2020

for a review), including differences in kinematic centres for different tracer populations. Further, deep photometric studies of the Magellanic periphery (e.g. Mackey et al. 2016, 2018; Pieres et al. 2017), in combination with multi-dimensional phase-space information from Gaia (e.g. Belokurov et al. 2017; Belokurov and Erkal 2019; Gaia Collaboration et al. 2021c), have revealed an abundance of stellar substructure surrounding the Clouds. This includes claw-like structures in the southern LMC outskirts and an apparent truncation in the western edge of the LMC disk (Mackey et al. 2018), diffuse structures to the east of the LMC (El Youssoufi et al. 2021), a diffuse overdensity to the northwest of the SMC (Pieres et al. 2017), a long, thin feature which appears to wrap around the southern LMC, stretching between the eastern outskirts of the SMC and the eastern LMC disk (Belokurov and Erkal 2019), and a ~23° long arm-like feature to the north of the LMC (Mackey et al. 2016; Belokurov and Erkal 2019).

In order to constrain the complex interactions which produce these features, kinematic data are critical. Recently, in Cullinane et al. (2021) we analysed the origin of the LMC's northern arm using 3D kinematics from the Magellanic Edges Survey (MagES: Cullinane et al. 2020) – a spectroscopic survey of red clump (RC) and red giant branch (RGB) stars using the 2dF/AAOmega instrument (Lewis et al. 2002; Sharp et al. 2006) on the 3.9 m Anglo-Australian Telescope (AAT) at Siding Spring Observatory – in conjunction with Gaia astrometry. We found the arm is likely perturbed by a combination of historical interactions with the SMC prior to ~1 Gyr ago, and the LMC's current infall to the Milky Way. This represents the first kinematic evidence that interactions between the Clouds, prior to the recent pericentric passage of the SMC ~150 Myr ago (Zivick et al. 2018), could have produced measurable effects on the present-day structure of the Clouds.

In this paper, we extend our MagES analysis to provide a comprehensive overview of the structural and kinematic properties of the outer LMC disk and surrounding stellar substructures. A summary of the data is presented in §5.3. Section 5.4 describes how red clump photometry is utilised to derive a distance scale to the observed structures, and §5.5 examines the stellar population properties in the outer LMC that allow for such an analysis. The resultant structural and kinematic properties of the LMC outskirts are presented in §5.6. We discuss the properties of each kinematically distinct region, and the implications for interactions between the Clouds and with the Milky Way, in §5.7. Section 5.8 summarises our conclusions.

5.3 Data

5.3.1 Observations

This paper is based on the analysis of eighteen MagES fields targeting the outskirts of the LMC. Ten fields are located in the outer disk between LMC galactocentric radii of $8.5° < R < 11°$, five trace the long arm-like southern substructure discussed in Belokurov and Erkal (2019), and three are located on the claw-like southern substructures discussed in Mackey et al. (2018).

The survey overview for MagES is presented in Cullinane et al. (2020 henceforth referred to as Paper I), and contains details of the target selection procedures, observation characteristics, and data reduction pipeline. Here we briefly summarise salient details for the fields used in this paper. As MagES is an ongoing survey, we note that three additional fields have been observed since the release of Paper I: fields 27-29. These were observed on December 18 and 19 2020, with exposure times of 10800 s, 10055 s, and 10800 s respectively. We show details of these fields, in addition to existing MagES fields discussed in this paper, in Table 5.1. The positions of all MagES fields are presented in Fig. 5.1, with the fields analysed in this paper indicated in blue.

MagES utilises the 2dF multi-object fibre positioner in combination with the dual-beam AAOmega spectrograph on the AAT. The 2dF positioner allows for the observation of ~350 science targets per two-degree diameter field. We configure the blue arm of AAOmega with the 1500V grating, which has resolution R~3700, to provide coverage of the MgIb triplet, and the red arm with the 1700D grating, which has R~10000, to provide coverage of the near-infrared CaII triplet. Reduction of the spectra is performed using the `2dFDR` pipeline (AAO Software Team 2015), and line-of-sight (LOS) velocities are derived using cross-correlation against template spectra. After applying quality cuts, stars with heliocentric velocity estimates are cross-matched against the Gaia EDR3 catalogue, and additional cuts based on Gaia parameters `ruwe`<1.4 (Fabricius et al. 2021) and $C^* < 4\sigma_{C^*}$[27] applied.

5.3.2 Field kinematics

The resulting sample of stars includes both true Magellanic stars and foreground contaminants. We use a statistical framework, described in detail in Paper I, to probabilistically associate stars to either the Clouds, or to one of several possible Milky Way contaminant

[27] C^* and σ_{C^*}, describing the corrected flux excess and thus the consistency between the G, $G_{\rm BP}$, and $G_{\rm RP}$ photometric bands, are defined using Eqs. 6 and 18 of Riello et al. (2021) respectively.

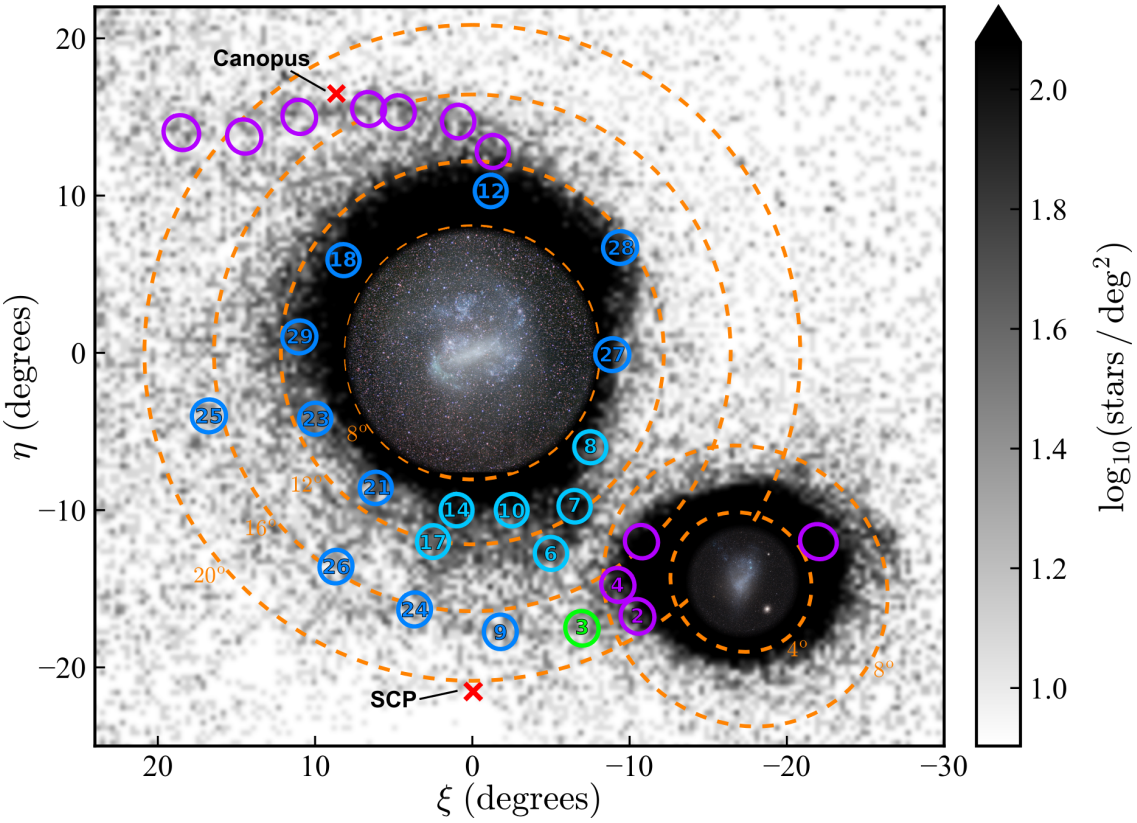

Figure 5.1: Location of observed MagES fields across the Magellanic Periphery. Blue fields are those analysed in this paper, with light and dark blue representing **M** and **G** fields respectively (see §5.3.1 for further detail on these classifications). Purple fields are MagES fields not analysed in this paper, and the green field is field 3, which is initially analysed but is found to be predominantly associated with the SMC, not the LMC. Any field discussed in the text is numbered. The background image shows the density of Magellanic red clump and red giant stars per square degree, selected from Gaia DR2 (the target catalogue from which most MagES stars are drawn) as per Belokurov and Erkal (2019). On this map, north is up and east is to the left; (η, ξ) are coordinates in a tangent-plane projection centred on the LMC ($\alpha_0 = 82.25°$, $\delta_0 = -69.5°$). Orange dashed circles mark angular separations of 8°, 12°, 16° and 20° from the LMC centre and 4°, 8° from the SMC centre. The red x-signs mark the location of Canopus and the south celestial pole.

Table 5.1: MagES fields in the LMC outskirts analysed in this paper. Columns give the field number and classification as described in Paper I; location of the field centre as RA(α), DEC(δ) in J2000.0; on-sky distance of the field from the centre of the LMC ($R_{\rm LMC}$) and position angle (Φ) measured east of north, number of likely Magellanic stars per field, and aggregate kinematic parameters calculated as in §5.3.2. The Magellanic population in field 3 is dominated by SMC stars, whilst all other fields are dominated by LMC stars.

Field (Class)	RA	DEC	$R_{\rm LMC}$ (°)	Φ (°)	$N_{\rm Magellanic}$ (P_i>50%)	$V_{\rm LOS}$ (km s^{-1})	$\sigma_{\rm LOS}$ (km s^{-1})	μ_α (mas yr^{-1})	σ_α (mas yr^{-1})	μ_δ (mas yr^{-1})	σ_δ (mas yr^{-1})
3 (G)	01 20 00	−82 30 00	18.2	201.7	65	185.4 ± 4.1	31.4 ± 3.2	1.41 ± 0.07	0.48 ± 0.05	-1.37 ± 0.04	0.27 ± 0.05
6 (M)	03 22 33	−80 40 55	13.1	201.2	29	174.5 ± 3.5	19.4 ± 3.1	1.78 ± 0.06	0.35 ± 0.06	-0.52 ± 0.04	0.11 ± 0.06
7 (M)	03 26 04	−77 26 18	11.0	213.5	64	167.6 ± 3.3	34.1 ± 2.5	1.61 ± 0.04	0.30 ± 0.03	-0.61 ± 0.03	0.16 ± 0.04
8 (M)	03 39 15	−73 43 48	8.8	231.3	97	197.5 ± 2.6	25.0 ± 2.0	1.77 ± 0.03	0.15 ± 0.03	-0.60 ± 0.02	0.14 ± 0.04
9 (G)	03 40 00	−86 17 13	17.1	185.6	52	198.1 ± 3.4	18.3 ± 2.3	2.50 ± 0.04	0.21 ± 0.03	-0.13 ± 0.05	0.30 ± 0.04
10 (M)	04 36 23	−79 07 17	9.9	193.5	77	211.2 ± 2.4	20.3 ± 1.9	2.02 ± 0.03	0.21 ± 0.04	-0.01 ± 0.03	0.21 ± 0.03
12 (G)	05 20 00	−59 18 00	10.3	355.4	284	287.1 ± 1.5	24.8 ± 1.1	1.78 ± 0.01	0.12 ± 0.01	0.20 ± 0.01	0.19 ± 0.01
14 (M)	05 50 22	−79 21 18	10.0	173.6	85	244.8 ± 2.8	25.2 ± 2.1	1.97 ± 0.03	0.21 ± 0.03	0.80 ± 0.03	0.21 ± 0.04
17 (M)	06 32 16	−80 59 36	12.2	167.7	108	239.6 ± 2.7	26.0 ± 2.1	1.84 ± 0.02	0.17 ± 0.02	1.28 ± 0.03	0.30 ± 0.03
18 (G)	06 40 00	−62 30 00	10.7	55.4	299	324.5 ± 1.2	20.3 ± 0.9	1.49 ± 0.01	0.11 ± 0.01	1.00 ± 0.01	0.12 ± 0.01
21 (G)	07 17 12	−76 36 00	10.9	143.9	149	275.9 ± 1.9	21.6 ± 1.5	1.40 ± 0.02	0.17 ± 0.02	1.57 ± 0.03	0.26 ± 0.02
23 (G)	07 36 00	−71 00 00	11.4	112.7	127	302.2 ± 2.9	30.2 ± 2.0	1.11 ± 0.02	0.13 ± 0.02	1.64 ± 0.02	0.17 ± 0.02
24 (G)	07 58 48	−84 12 00	16.4	167.1	56	225.1 ± 2.1	15.1 ± 1.7	1.09 ± 0.04	0.21 ± 0.03	2.23 ± 0.03	0.16 ± 0.03
25 (G)	08 32 00	−67 00 00	17.5	103.7	37	344.3 ± 2.5	13.7 ± 1.9	0.75 ± 0.02	0.05 ± 0.02	1.97 ± 0.04	0.16 ± 0.03
26 (G)	08 48 00	−79 00 00	16.1	147.3	37	258.4 ± 3.2	18.5 ± 2.3	0.69 ± 0.03	0.11 ± 0.03	2.23 ± 0.03	0.16 ± 0.03
27 (G)	03 52 00	−68 24 00	8.7	266.6	267	222.2 ± 1.3	20.4 ± 1.0	1.83 ± 0.01	0.13 ± 0.01	-0.58 ± 0.01	0.12 ± 0.01
28 (G)	04 06 00	−62 30 00	10.9	301.3	303	210.9 ± 1.1	19.1 ± 0.9	1.78 ± 0.01	0.16 ± 0.01	-0.49 ± 0.01	0.10 ± 0.01
29 (G)	07 16 00	−66 06 00	10.6	84.6	266	324.7 ± 1.1	17.6 ± 0.8	1.29 ± 0.01	0.10 ± 0.01	1.40 ± 0.01	0.12 ± 0.01

P_i>50% of being associated with the Clouds.

Several fields, particularly those located in the southern outskirts of the LMC, could plausibly contain more than one Magellanic population – that is, include stars associated with both the LMC and SMC. To test this idea, we recalculate the above fits assuming a Magellanic population described by two Gaussian components, and compute the Bayesian Information Criterion (BIC: Schwarz 1978) for comparison to that for the fit with a single component. We find that in all cases there is insufficient evidence to prefer the two-Gaussian fit over the single-component fit, and so therefore retain the single-component fit for all fields. We note this does not preclude the existence of both LMC and SMC stars within a field, but simply that any such populations are either i) not kinematically distinct, or ii) strongly mismatched in size (i.e. one population dominates over the other).

In many fields, the number of likely Magellanic stars is significantly lower than the total number of stars observed. In the case of **M** fields (see Paper I for details of these classifications), this is primarily due to the relatively inefficient target selection used, as these fields were observed prior to the release of Gaia DR2. The associated lack of proper motion and parallax information available for the target selection process, in combination with the moderate Milky Way contamination within the CMD selection boxes used to isolate Magellanic red clump stars (see Fig. 3.2), means a significant fraction of the targets observed in these fields are not genuinely Magellanic members. In contrast, MagES fields observed after the release of Gaia DR2 (classified as **G** fields) do incorporate these kinematic priors, and as a result generally suffer less from contamination by non-members. Fields 3, 9, and 24-26 also have comparatively low numbers of likely Magellanic stars, despite their classification as **G** fields. This is due to the inherently low density of Magellanic stars at these locations, as seen in Fig. 5.1.

5.3.2.1 Field 3

Notably, we find that the Magellanic population in field 3 is likely associated with the SMC, rather than the LMC. Comparison of its proper motions to those of nearby fields reveals it is very similar to fields 2 and 4, located in the SMC outskirts (identified in Fig. 5.1 but not explicitly discussed in this paper), and kinematically distinct from fields 6 and 9, each of which have proper motions significantly more likely to be LMC-associated. In addition, the mean metallicity of this field is [Fe/H]~ -1.4: somewhat lower than each of the other analysed fields (discussed further below), and suggestive of a potential origin in the more metal-poor SMC. As such, while we report the observed properties of this field in Table 5.1, we do not analyse it further in the context of the LMC in this paper. However,

we do note that at an SMC galactocentric radius of 9.5°, this is one of the most distant detections of SMC debris to date. It is more remote than the stellar overdensity discussed in Pieres et al. (2017), and may sample the trailing arm of the SMC (cf. Belokurov et al. 2017). A detailed analysis of this field is deferred to a forthcoming paper on the SMC by the MagES collaboration (Cullinane et al. in prep).

5.3.3 Metallicities

MagES additionally reports [Fe/H] estimates for sufficiently bright ($G \gtrsim 18$) red giant branch stars, derived from the equivalent width of the 8542Å and 8662Å CaII triplet lines. These bright RGB stars are not included in the target selection procedure for **M** fields, but are present in all **G** fields. Paper I and Da Costa (2016) describe the equivalent width measurement and [Fe/H] conversion procedure in detail.

For fainter red clump stars (observed in all fields), the S/N is too low to accurately measure the equivalent width of the two lines in any individual stellar spectrum, particularly as the 8662Å line is within a region of the spectrum relatively heavily contaminated by (stochastically over- or under-subtracted) night sky emission. We therefore stack spectra for likely ($P_i > 50\%$) Magellanic RC stars – first shifting these into the rest frame using their (geocentric) LOS velocities – to create a single "representative" RC spectrum for the field. This increases the contrast of the two CaII lines relative to the residual night-sky emission, allowing for equivalent width measurements to be performed. As the stacked clump stars only occupy a small magnitude range (and thus, we assume, a small range in effective temperature and gravity), stacking spectra is not expected to substantially bias the derived equivalent widths, and the resulting [Fe/H] estimates are expected to tend towards the mean metallicity within a given field. All metallicity estimates have uncertainties of 0.2 dex (we refer the interested reader to Paper I for details).

5.3.4 Red Clump properties

Converting the aggregate proper motion for a given field to a physical velocity, as well as placing constraints on the geometry of the outer LMC disk and surrounding features, requires a distance estimate for the Magellanic stars in each field. To obtain these, we use the red clump as a standardisable candle, calibrated to an empirical distance scale as described in the next Section. The properties of the red clump are measured using Gaia EDR3 photometry at the location of each field. In principle, these provide additional information about the thickness and composition of the disk.

For each field, we select all[29] stars within a 1° radius of the field centre, with parallax ϖ<0.15, proper motions within three times the dispersion of the field median motions reported in Table 5.1 (i.e. $\mu_\alpha \pm 3\sigma_\alpha$, and $\mu_\delta \pm 3\sigma_\delta$), and passing the quality cuts `ruwe`<1.4 and C^*<$4\sigma_{C^*}$.

The Gaia G-band photometry is then corrected for the six-parameter solution as described in Riello et al. (2021), and subsequently dereddened using the procedure described in Gaia Collaboration et al. (2021a). This utilises the Schlegel et al. (1998) dust maps, corrected as described in Schlafly and Finkbeiner (2011), in conjunction with the mean extinction coefficients for the Gaia passbands described in Casagrande and VandenBerg (2018). No correction is made for reddening internal to the Clouds as this is not expected to be significant in the low-density peripheral regions targeted by MagES (cf. Choi et al. 2018b). We do, however, restrict our selection to stars with corrected $E(B-V)$<0.25 in order to minimise the effect of any systematic uncertainties in the dereddening procedure on the resultant photometry. To isolate red clump stars, a CMD selection box of 0.8<$(G_{BP}-G_{RP})_0$<1.15, and 18.0<G_0<19.4 is implemented; the large range in G_0 is designed to accommodate any reasonable distance variations between fields.

To this final sample of stars we fit a mixture model describing their distribution on the CMD, within which the red clump takes the form of a two-dimensional Gaussian with five free parameters: a peak at (G_{0c}, $(G_{BP}-G_{RP})_{0c}$), dispersions σ_{BPRP0} in the colour direction and σ_{G0} in the magnitude direction, and a covariance σ_{GBPRP0}. In addition, the background density (accounting for both non-Magellanic populations, and non-RC Magellanic stars including RGB and potentially blue loop stars) is described by linearly varying terms in both colour and magnitude. The relative fraction of contaminants to true RC members is also a free parameter, for a total of ten free model parameters. With on order of ~100 stars per field, there is a sufficient number of data points to robustly determine each of these parameters. The Markov Chain Monte Carlo ensemble sampler EMCEE (Foreman-Mackey et al. 2013) is used to sample the posterior probability distributions for the model parameters. Fig. 5.2 presents the peak red clump colour ($(G_{BP}-G_{RP})_{0c}$) and magnitude (G_{0c}), and associated dispersions, for each field as a function of position angle.

As noted above, all fields except for 25 and 26 have a sufficient number of stars to robustly determine the RC properties. For fields 25 and 26, the Magellanic stellar density is inherently very low, as evidenced by Table 5.1: these fields have amongst the lowest numbers of likely Magellanic stars. For these two fields only, we therefore expand our RC selection criteria to include stars within 3° of the MagES field centre, which increases the number of stars sufficiently to fit the RC properties in these regions. We do note that as

[29] including those for which we do not have line-of-sight velocity measurements.

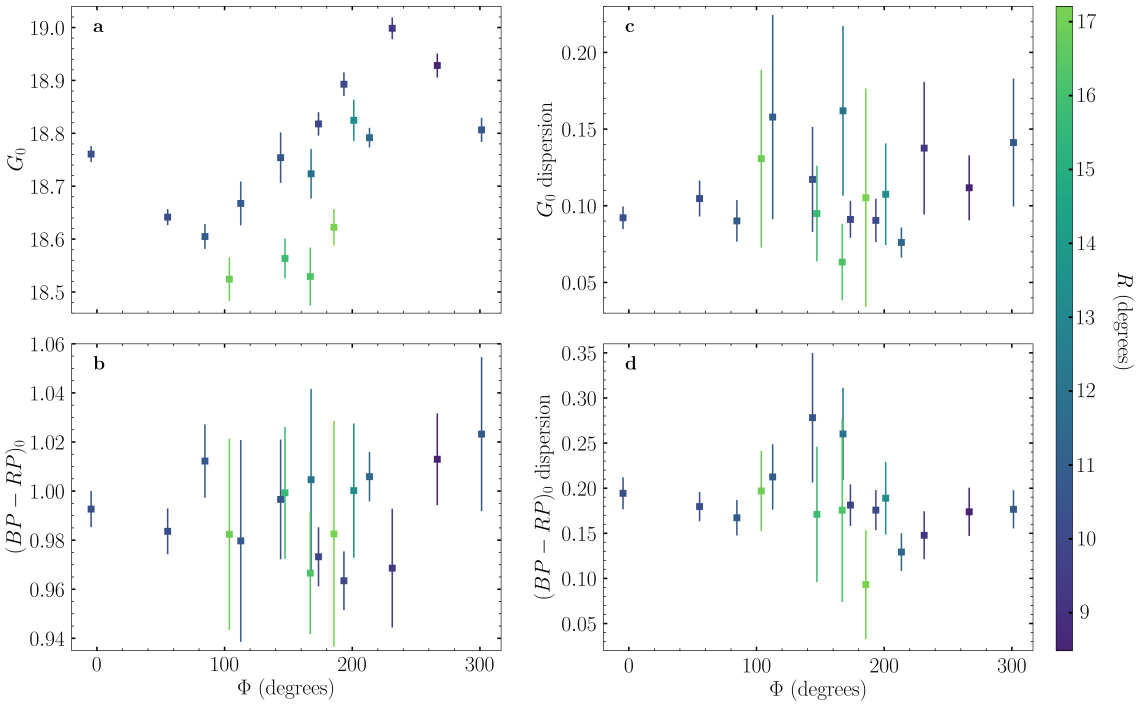

Figure 5.2: Fitted red clump parameters for MagES fields as a function of position angle. Panels show, in order from top to bottom: *a*) the peak G_{0c} magnitude, *b*) the peak $(G_{BP}-G_{RP})_{0c}$ colour, *c*) the G_0 magnitude dispersion σ_{G0}, and *d*) the $(G_{BP}-G_{RP})_0$ colour dispersion σ_{BPRP0}. Points are colour-coded by their LMC galactocentric radius in degrees.

a consequence, it is possible that any distance gradients across these larger regions can potentially inflate σ_{G0} beyond that associated with the line-of-sight depth of the LMC material within the field. Such an effect is expected to be less significant in the other analysed fields, which occupy smaller on-sky areas.

5.4 Anchoring the LMC red clump distance scale

As a standardizable candle, the apparent magnitude of the red clump can be employed to derive distance estimates to each of our observed fields. However, even after dereddening, the apparent magnitude of the clump is not purely governed by its distance: population effects including the age and metallicity of red clump stars affect their intrinsic luminosity (see Girardi 2016 for a review). Consequently, meaningful distance estimates to our fields require a "reference magnitude": the apparent magnitude of a red clump, comprised of an identical stellar population to that of our fields in the LMC outskirts, at a known distance.

However, the geometry of – and therefore absolute distance to – the outer LMC disk (R>8°) is relatively unconstrained. Existing models of the LMC's disk based on kinematic data – such as those from Gaia Collaboration et al. (2021c); van der Marel and Kallivayalil

(2014); Vasiliev (2018) and Wan et al. (2020) – are dominated by data within LMC galactocentric radii of ~8°: smaller than that of even the innermost MagES fields. Given the perturbed appearance of the outer disk, assuming *a priori* these same disk geometries extend to larger radii is not justified. However, in Paper I it was found that the kinematics of MagES field 18 are consistent with predictions of a simple inclined disk model, indicating there are potentially unperturbed regions of the outer LMC disk suitable for calibration of distance estimates. Motivated by this, we seek to fit an inclined disk model to the LMC at galactocentric radii of ~10°, which we can use in conjunction with the measured field-aggregate red clump magnitudes to derive a "reference magnitude" as described above.

Our model is that of a thin disk as described by the framework in van der Marel and Cioni (2001) and van der Marel et al. (2002), with stellar kinematics described purely by a rotational velocity V_θ (i.e. having zero mean radial $\overline{V_r}$ and vertical $\overline{V_z}$ velocities). We fit four model parameters: the inclination (i) and position angle of the line of nodes (LON: Ω)[30], the rotational velocity V_θ, and $G_0^{\rm RC}$: the RC magnitude at the (fixed) centre distance of the LMC. We stress this magnitude is not the actual RC magnitude at the LMC centre, because the RC population at that location is very different to that in the outer disk; but is the magnitude of a population equivalent to that observed in the outer LMC disk, were such a population located at the LMC centre distance of 49.59 kpc (Pietrzyński et al. 2019).

The model additionally requires as inputs the location and kinematics of the LMC centre: we hold these fixed at the values derived by Gaia Collaboration et al. (2021c) for stars with LMC radii >3°, as this is a kinematic centre derived using similar stellar tracers to those we analyse. At the large galactocentric radii analysed, we assume that V_θ is fixed and does not vary with radius (see e.g. Paper I), and there is no precession or nutation of the disk (i.e. the inclination and line of nodes are both fixed: see e.g. van der Marel and Kallivayalil 2014).

As MagES fields do not provide contiguous coverage of the LMC disk, to fit the model we instead select red clump stars (i.e. those within the CMD selection box described in §5.3.4) from Gaia EDR3, passing the quality cuts `ruwe`<1.2 and C^*<3σ_{C^*}[31], to perform the fit. We additionally impose proper motion cuts of 0.4<μ_α<2.5 and −1.6<μ_δ<2.5, and a parallax cut of ϖ<0.15 to isolate likely LMC stars, as seen in Fig. 5.3. We choose stars with LMC galactocentric radii of 9.5°<R<10.5° in order to have a consistent RC population with MagES disk fields (most of which have similar LMC galactocentric radii), and to

[30] the axis along which the plane of the disk intersects the plane of the sky.

[31] These are stricter cuts than applied to general MagES photometry. This is because our aim here is to select the cleanest sample of Magellanic stars, whilst when studying individual fields, we aim to achieve a balance between both clean and complete photometry.

minimise potential population effects such as radial metallicity gradients (e.g. Majewski et al. 2008; Carrera et al. 2011) on the magnitude of the red clump. We later test the validity of the assumption that the RC population is consistent across MagES fields.

As we require the RC magnitude to contribute to the fitting of model distances, we bin the data in position angle ranges of 2.5°, and take the median G_0 magnitude of each bin as the RC magnitude for use in fitting the model. We employ this simpler method, as compared to Gaussian fitting the RC in each bin as described in §5.3.4, in order to simplify the overall fitting process. However, we do test the difference between the explicit RC fitting and the simple median G_0 magnitude, and find for well-populated bins[32], there is no significant difference between the RC magnitude derived using the two methods. For consistency, we then use the median proper motions of each bin, and associated uncertainties, in the fitting process.

To fit the model, we define a chi-squared quantity χ^2 as in Eq. 5.1. Here, $\mu_{\alpha,\mathrm{obs},j}$, $\mu_{\delta,\mathrm{obs},j}$ and $m_{\mathrm{obs},j}$ are the observed proper motions and G_0 magnitude for each bin j; $\mu_{\alpha,\mathrm{err},j}$, $\mu_{\delta,\mathrm{err},j}$ and $m_{\mathrm{err},j}$ are the standard errors in each of those quantities. $\mu_{\alpha,\mathrm{mod},j}$, $\mu_{\delta,\mathrm{mod},j}$ and $m_{\mathrm{mod},j}$ are the proper motions and G_0 magnitude predicted by the model for each bin; these quantities are related to the four fitted model parameters though the framework of van der Marel et al. (2002). We minimize the log-likelihood of χ^2, utilising the Markov Chain Monte Carlo ensemble sampler EMCEE (Foreman-Mackey et al. 2013) to sample the posterior probability distributions for the four fitted model parameters.

$$\chi^2 = \sum_j \left(\left(\frac{\mu_{\alpha,\mathrm{obs},j} - \mu_{\alpha,\mathrm{mod},j}}{\mu_{\alpha,\mathrm{err},j}} \right)^2 + \left(\frac{\mu_{\delta,\mathrm{obs},j} - \mu_{\delta,\mathrm{mod},j}}{\mu_{\delta,\mathrm{err},j}} \right)^2 + \left(\frac{m_{\mathrm{obs},j} - m_{\mathrm{mod},j}}{m_{\mathrm{err},j}} \right)^2 \right) \quad (5.1)$$

Initially, we utilise the full range of position angles around the LMC disk to fit the model. However, we find the resulting model parameters produce a poor fit (i.e. have significant residuals) across most of the disk, indicating our simple model is not an accurate description of the entire outer disk. Consequently, and after some experimentation, we limit our fitting to position angles between $5° < \Phi < 90°$. This region of the disk is not in the immediate vicinity of any known substructures or obvious overdensities – which are indicative of potential perturbations – and includes MagES field 18, which was previously found in Paper I to be kinematically undisturbed.

[32] i.e. containing a large number of genuine Magellanic RC stars, as is the case for LMC disk as opposed to nearby low-density substructures.

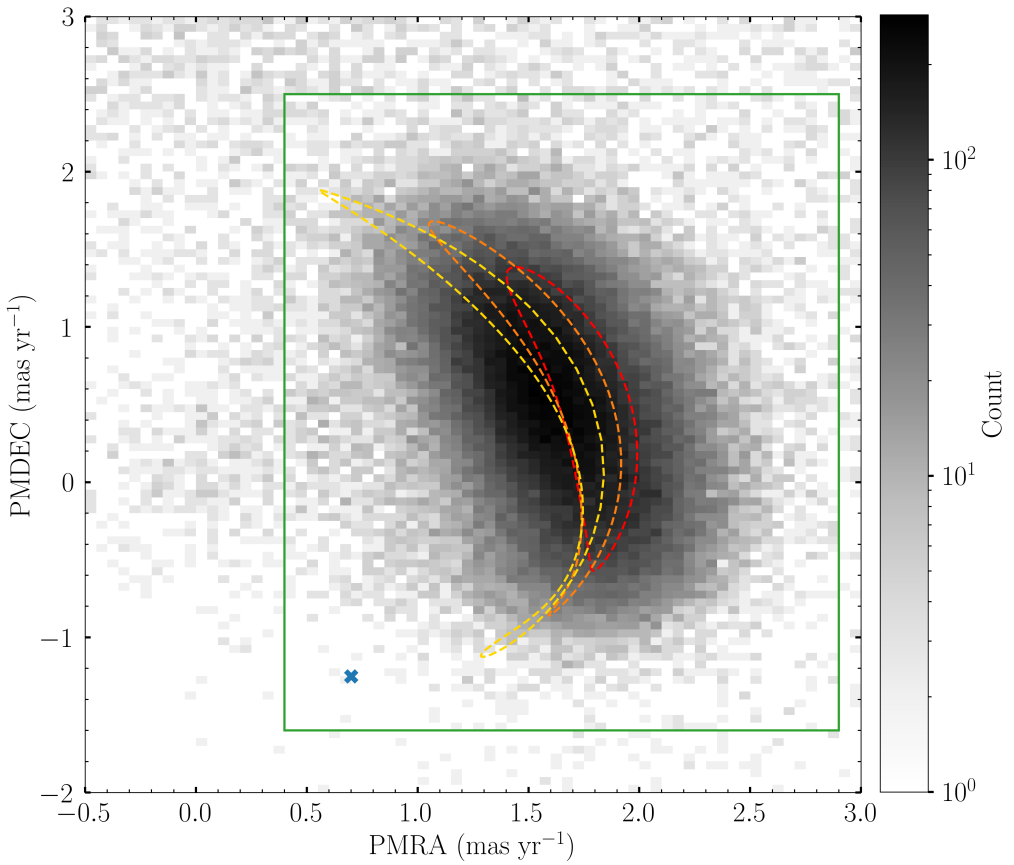

Figure 5.3: 2D density plot of Gaia EDR3 proper motions for red clump stars (selected as described in §5.4) at LMC galactocentric radii between 7 and 12°. Stars associated with the LMC predominantly form a distorted ellipse shape centred at ~(1.5, 0.6). A lower density peak at ~(0, 0) is associated with distant Milky Way halo stars with near-zero proper motions. The blue x-sign marks the mean proper motion of the SMC at ~(0.7, −1.3), though as we only show stars at LMC radii <12°, few SMC stars are present in this plot. Dashed lines show the predicted proper motion tracks for an LMC modelled as an inclined disk with geometry as described in Gaia Collaboration et al. (2021c), at galactocentric radii of 8° (red), 12° (orange), and 16° (gold). The solid green rectangle shows the proper motion selection for likely LMC disk stars used to fit the LMC disk geometry in §5.4. This minimises contamination from the SMC and MW halo, whilst ensuring as complete as possible a sample of LMC stars: the shape of the distribution is such that elliptical selections would omit LMC stars at the large galactocentric radii of interest.

The resultant model parameters for this subset of position angles, presented in Table 5.2, produce a significantly improved fit to the data within this position angle range, with much smaller residuals. The derived inclination and position angle of the line of nodes are similar to literature measurements of the LMC disk at smaller radii derived from both photometric and kinematic fits (such as from Gaia Collaboration et al. 2021c; Vasiliev 2018; van der Marel and Kallivayalil 2014; Olsen and Salyk 2002; van der Marel and Cioni 2001), though we do note our inclination is towards the higher end of the literature range, particularly compared to some purely photometric measurements (e.g. Choi et al. 2018b; Subramanian and Subramaniam 2013; Koerwer 2009). The derived rotation

Table 5.2: Fitted LMC disk model parameters, for position angles between $5°<\Phi<90°$.

Inclination i (°)	LON position angle Ω (°)	V_θ (km s^{-1})	G_0^{RC}
36.5 ± 0.8	145.0 ± 2.5	69.9 ± 1.7	18.90 ± 0.01

velocity is also consistent with literature values (see also Paper I), and using our model parameters on the MagES disk fields with position angles between $5°<\Phi<90°$ reveals these fields obey the expected disk-like kinematics (i.e. $\overline{V_r} \sim \overline{V_z} \sim 0$: see Section 5.6) even when LOS velocity information is included. This indicates our assumption that the north-eastern region of the LMC disk is relatively kinematically unperturbed is reasonable, and our method provides a viable reference red clump magnitude.

5.5 Stellar populations in the LMC outskirts

A critical assumption underpinning our derivation of a "reference" red clump luminosity in §5.4 is that the stellar populations across the outer LMC disk and associated MagES fields are largely homogeneous, such that distance variations are the dominant factor driving differences in the observed red clump magnitude field to field. Here we demonstrate the validity of this assumption by assessing the extent to which age and metallicity may vary in the LMC outskirts given our observations of the stellar populations in this region, and how such variations could affect the red clump luminosity.

We first assess the effect of metallicity, as in optical photmetric bands (such as Gaia G) metal-poor RC stars are intrinsically brighter and bluer than those that are metal-rich (Girardi and Salaris 2001). Fig. 5.4 presents [Fe/H] measurements for stars within MagES fields as a function of position angle and LMC galactocentric radius; square points represent results from stacked red clump spectra, which should approximate the mean metallicity within the field. We find these mean metallicities are, within uncertainty, generally consistent. The median stack metallicity across all fields is [Fe/H]$= -1.01$, with a standard deviation of 0.19. There are no systematic variations in the mean metallicity with galactocentric radius or position angle. We additionally find that, for fields where [Fe/H] estimates of RGB stars are available, the metallicity dispersion within each field is similar, with standard deviations of ~0.5 dex. Consequently, we can infer that metallicity is not a dominant influence on the measured properties of the red clump in MagES fields. Our results are also broadly consistent with literature measurements in the outer LMC disk. Photometric metallicity estimates derived by Grady et al. (2021) using Gaia DR2 data find mean [Fe/H] values between -1 and -1.5 across the outskirts of the LMC

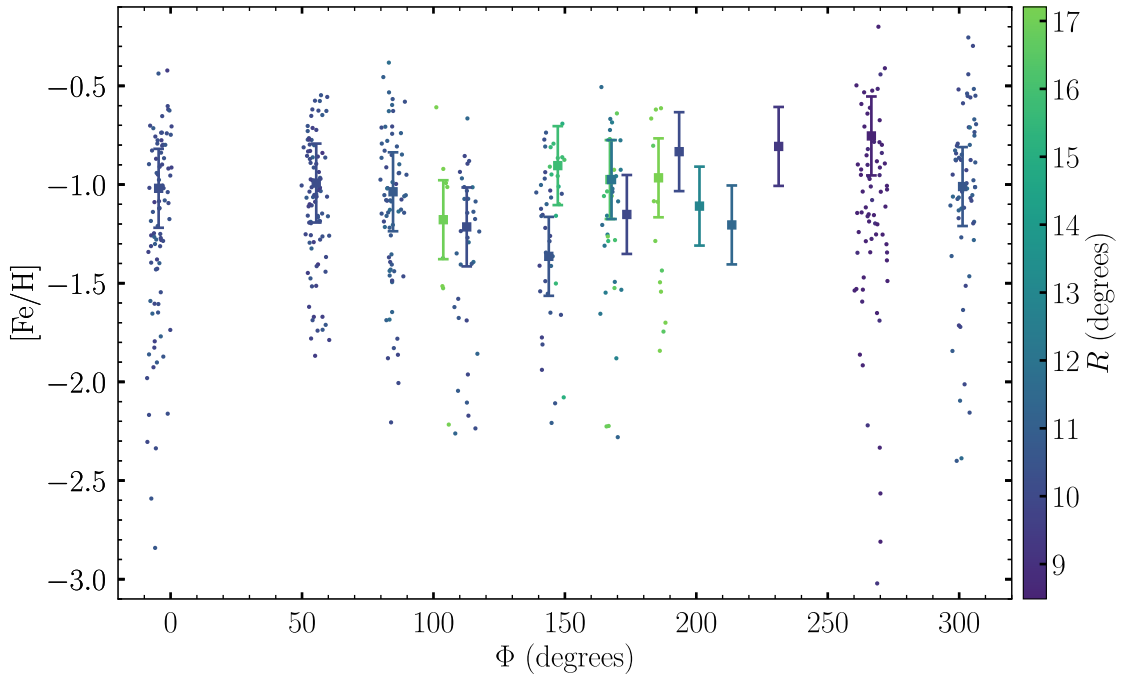

Figure 5.4: [Fe/H] estimates for MagES fields as a function of position angle. Fields are colour-coded by their galactocentric radius from the LMC. Square points represent results from stacked spectra, which approximate the mean metallicity of the field. Errorbars represent 0.2 dex abundance uncertainty. Dots represent [Fe/H] estimates for individual RGB stars within each field; associated uncertainties are omitted for clarity. **M** fields in the southern LMC disk do not include RGB stars, and therefore do not have associated [Fe/H] estimates for individual stars.

disk, with dispersions averaging ~0.5 dex (though we note their derived dispersions vary significantly from point-to-point). Sparse spectroscopic measurements by Carrera et al. (2011) and Majewski et al. (2008), predominantly in the northern outskirts of the disk, also find mean metallicities of approximately −1 dex.

Stellar age also affects the properties of the red clump: young ($\lesssim 2$ Gyr) RC stars are significantly bluer and brighter than older RC stars (Girardi and Salaris 2001). However, DECam photometry in the LMC outskirts shows no evidence for significant populations of main sequence stars above the ancient (~11 Gyr: Mackey et al. 2018) turnoff across the regions studied in this paper, implying a similar lack of young RC stars. We can thus infer age is neither a dominant, nor systematic, influence on the measured properties of the red clump in MagES fields.

Secondary constraints on population effects are also obtainable through analysis of the red clump colour, as changes in age and metallicity also drive changes in this parameter. Panel *b* of Fig. 5.2 shows the fitted $(G_{BP} - G_{RP})_0$ colour of the red clump in each of the MagES fields. We find these are, within uncertainty, consistent at $(G_{BP} - G_{RP})_0 \sim 1.0$, with no systematic variation in colour as a function of either radius or position angle. The

dispersion in colour, presented in panel *d* of Fig. 5.2, is similarly consistent, suggesting a very similar mix of populations across these locations.

The consistent metallicity and RC colour across the MagES fields we are considering, and lack of younger stellar populations in associated photometry at these locations, is indicative that population effects minimally impact the red clump in the LMC outskirts. To quantify this, we use PARSEC isochrones (Bressan et al. 2012)[33] to test the predicted colour and magnitude variations in Gaia EDR3 passbands associated with [Fe/H] variations at the level of the field-to-field dispersion in mean metallicity of ~0.2 dex. The isochrones, for an 11 Gyr population assuming the default parameters for IMF and mass loss, predict that such changes result in $(G_{BP} - G_{RP})_0$ colour variations on the order of ~0.06 mag, consistent with the maximum colour difference across our observations. The implied change in intrinsic red clump luminosity is ~0.04 mag, comparable to the ~0.03 mag uncertainties on the RC magnitude of each field resulting from the fitting process described in §5.3.4. We therefore conclude that distance is indeed the dominant factor impacting the observed RC magnitude. This validates our derivation of a "reference magnitude" for use in the calculation of distance estimates to our fields, and additionally allows us to use the magnitude dispersion of the red clump to draw conclusions about the relative line-of-sight thickness of the disk and nearby substructures.

5.6 Kinematics in the frame of the LMC disk

Having ascertained that the north-eastern LMC outskirts retain a relatively intact disk structure in §5.4, and having validated our assumption of largely homogeneous stellar populations across all the fields we consider in §5.5, we proceed to calculate the kinematics and distances of the fields relative to the frame of the LMC disk. We begin by deriving absolute distances to each field as in Eq. 5.2, where $D_{\rm field}$ is the distance in kpc to each field, D_0 is the distance of the reference red clump magnitude (49.59 ± 0.63 kpc: Pietrzyński et al. 2019), $G_0^{\rm RC}$ is the reference RC magnitude from Table 5.2, and $G_{0,\rm field}$ is the peak RC magnitude for each field as determined in Section 5.3.4. We account for uncertainties in each of D_0, $G_{0,\rm field}$ and $G_0^{\rm RC}$, in derivation of associated uncertainties in $D_{\rm field}$.

$$D_{\rm field} = D_0 \times 10^{\left((G_{0,\rm field} - G_0^{\rm RC})/5.0\right)} \tag{5.2}$$

We then utilise the framework presented in van der Marel et al. (2002), in conjunction with the derived distances to each field, to transform the observed field kinematics

[33] Accessed as version 3.4 of the web form http://stev.oapd.inaf.it/cmd

presented in Table 5.1 into velocities in a cylindrical coordinate system aligned with the LMC disk, with its origin at the LMC centre of mass. In this transformation, we utilise the LMC centre and associated systemic motions reported in Gaia Collaboration et al. (2021c), and the disk inclination and LON angles derived in §5.4 for the outer LMC disk. We subsequently obtain V_θ, the azimuthal streaming or rotation velocity; V_r, the in-plane radial velocity; V_z, the vertical velocity perpendicular to the disk plane; and dispersions $(\sigma_\theta, \sigma_r, \sigma_z)$ in each of these components. We additionally obtain the out-of-plane distance z, describing how far "in front of" or "behind" the expected disk plane stars in each field are located. For fields in the north-eastern disk, these distances are approimately zero by construction, since this is the region used to fit the disk plane (albeit without including line-of-sight velocity information); however fields outside of this region are not required to – and in fact do not – lie within the plane of the disk.

In this coordinate system, a positive V_θ refers to clockwise rotation from north towards west, following the sense of rotation in the LMC, a positive V_r refers to motion in the disk plane radially outward from the LMC centre, and a positive V_z refers to motion perpendicular to the disk plane in a direction predominantly toward the viewer (i.e. "in front of" the LMC disk). For stars obeying equilibrium disk kinematics, the net V_r and V_z within a field are expected to be zero, V_θ is expected to be ~70km s^{-1} as derived in §5.4,[34] and the out-of-plane distance is expected to be zero. Fig. 5.6 plots the resultant disk velocities and their dispersions for all analysed MagES fields, as a function of their position angle around the disk. Points are colour-coded by their radial distance from the LMC centre. Fig. 5.5 plots both the absolute distances to the fields, as well as their out-of-plane distances relative to the LMC disk with geometry assumed as above.

5.6.1 Common properties and literature comparison

In the following subsections, we discuss the derived distances and kinematics of each of the individual regions of the LMC outskirts with distinct kinematic and structural properties. However, possible interpretations of these in the context of interactions between the Clouds are deferred to Section 5.7. We first examine common properties across all studied fields.

With consistent red clump colours, consistent metallicity means and dispersions, and kinematics similar to those predicted by LMC disk models (see Fig. 5.3), we can infer that

[34] We note that the values derived for the north-eastern MagES disk fields are slightly lower than this, though still consistent within uncertainty, due to the inclusion of LOS velocities in this calculation, which are not available for the fitting process in §5.4.

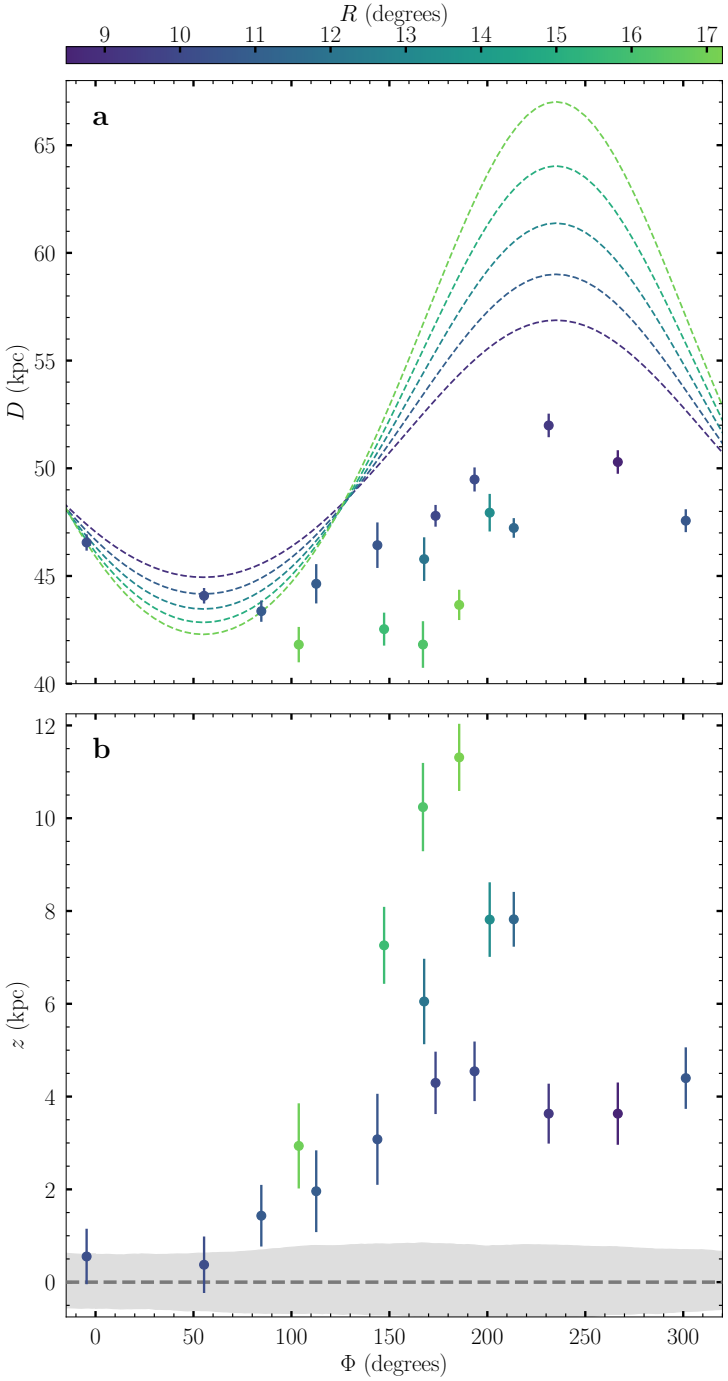

Figure 5.5: Absolute distances $D_{\rm field}$ (top), and out-of-plane distances z (bottom) relative to the LMC disk plane, for MagES fields as a function of position angle. Fields are coloured by their LMC galactocentric radius in degrees. Coloured dashed lines represent the distance predictions based on the inclined disk fit to the north-eastern LMC in §5.4 at the corresponding radii. The dashed grey line in the bottom panel represents the $z = 0$ expectation for stars within the disk plane, with the shaded grey region indicating the distance uncertainty associated with uncertainties in the fitted disk inclination and line of nodes.

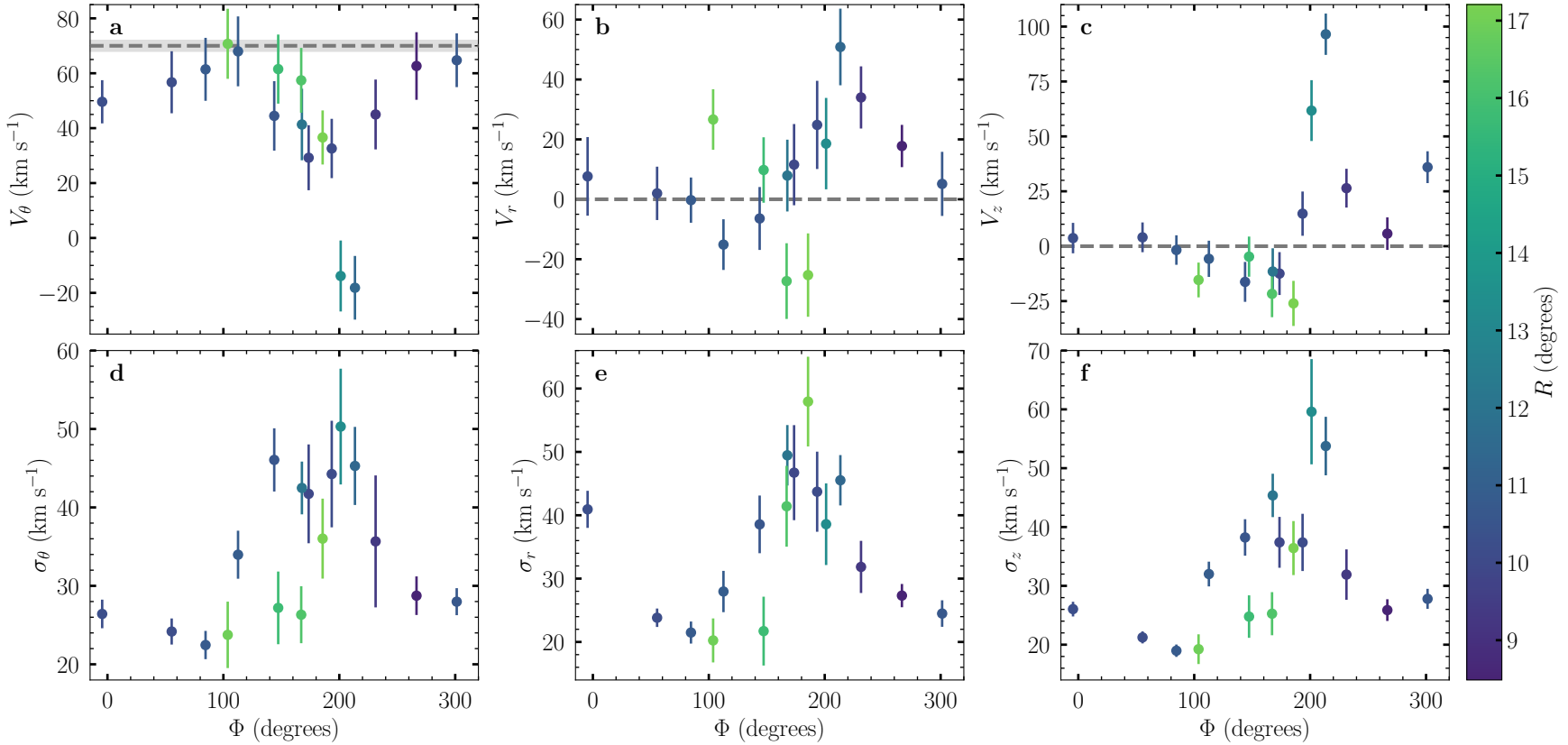

Figure 5.6: Azimuthal (V_θ, left), radial (V_r, centre), and vertical (V_z, right) velocities (top row), and their associated dispersions (bottom row), for MagES fields as a function of position angle. Fields are coloured by their LMC galactocentric radius in degrees. Dashed grey lines represent the expected kinematics for stars in an equilibrium disk.

stars within all MagES fields analysed here[35] are comprised predominantly of LMC disk populations. While we cannot preclude the existence of any SMC stars within our fields, particularly those in the southern LMC outskirts, we can conclude that the majority of stars in each field do not originate with the SMC, as such material would i) be more metal-poor, and ii) have kinematics more consistent with the known SMC proper motion field (as in the case of field 3 as discussed in §5.3.2.1). We can further infer that the majority of stars in our fields are not from an LMC stellar halo, which would be expected to not only be more metal-poor, but also have a lower rotation velocity and significantly larger velocity dispersions in all components than the LMC outer disk. While we cannot completely preclude the presence of LMC halo stars within our fields, the majority of stars are likely disk populations, even at the very large galactocentric radii studied.

El Youssoufi et al. (2021) provide distance estimates to several of the observed structures in the LMC disk outskirts using infrared photometry from the VISTA Hemisphere Survey (VHS) and the VMC survey (Cioni et al. 2011). In that study, RC magnitude estimates are obtained by fitting the dereddened K-band luminosity function of red clump and RGB stars within a defined CMD selection box using a Gaussian distribution (which describes the clump) plus a quadratic polynomial term (which describes the RGB). The magnitudes are converted to distance estimates using the absolute K-band magnitude of solar-neighbourhood RC stars, with a correction factor from Salaris and Girardi (2002) applied to account for the difference in stellar population properties (particularly metallicity) between the two samples.

We thus compare our distance estimates to those provided by El Youssoufi et al. (2021). Specifically, our fields 17 and 14 correspond to their "Southern Substructure 1"; fields 6 and 7 correspond to their "Southern Substructure 2"; fields 9 and 24 correspond to their "Southern Substructure 3"; and field 25 corresponds to their "Eastern Substructure 2". We find the distances estimates from our analysis are systematically smaller than those presented in El Youssoufi et al. (2021), being on average 7.5 ± 1.1 kpc closer, though the relative distances of the different substructures are consistent within uncertainty. At the distance of the LMC, this global offset corresponds to a magnitude difference of ~0.35 mag, larger than our typical photometric uncertainties by a factor of ~10.

The most likely source of this global distance offset is a calibration difference. In particular, we note the Salaris and Girardi (2002) magnitude correction $\delta M_K^{\rm RC} = -0.07$ for the Clouds, used by El Youssoufi et al. (2021), is derived for a younger and more metal-rich population ([Fe/H]~ -0.4, corresponding to an age <5 Gyr: see Table 4 of Girardi and Salaris 2001), which is more representative of the inner regions of the Clouds. However, as

[35] note this excludes field 3 as discussed in §5.3.2.1.

discussed in §5.5, the outskirts of the Clouds are significantly older and more metal-poor, at [Fe/H]~−1. Since Salaris and Girardi (2002) indicate more metal-poor RC stars (with ages >1.5 Gyr) are fainter than more metal-rich stars, this suggests the applied correction factor $\delta M_K^{\rm RC}$ is likely underestimated. Fig. 6 of Salaris and Girardi (2002) indicates for an old (~11 Gyr) population at this metallicity, a more appropriate correction factor is approximtely −0.4: similar to the global magnitude offset between our estimates and those of El Youssoufi et al. (2021). Indeed, applying this alternate correction factor to the El Youssoufi et al. (2021) photometry results in distances consistent within uncertainty to those we derive.

However, we do also note also that the El Youssoufi et al. (2021) distance estimates are calculated for much larger on-sky areas than individual MagES fields, with even their smallest comparable region (Southern Substructure 2) encompassing an on-sky area of ~25 square degrees. This is ~8 times larger than the 3 square degrees covered by MagES fields. As a result, the El Youssoufi et al. (2021) structures have very large associated distance dispersions, on the order of 8 kpc: similar to the offset between the two sets of distance estimates. It is therefore plausible, though we suspect very unlikely, that our fields simply sample the closer end of the distance distribution across each substructure region.

5.6.2 The relatively undisturbed north-eastern disk

As discussed in §5.3.4, Gaia data reveals the north-eastern LMC disk is well-described by an inclined disk with an azimuthal (rotation) velocity of ~70 km s^{-1}. This is supported by the kinematics and structural properties of fields 12, 18 and 29, which span the north-eastern disk (position angles $-5°<\Phi<90°$). We remind the reader that the radial distances and position angles of all fields are given in Table 5.1.

These fields have vertical and radial velocities consistent with zero within uncertainty, as expected in an equilibrium disk, and have velocity dispersions in each component of $20-25$ km s^{-1}, consistent with literature measurements of similar tracer populations at smaller galactocentric radii (Gaia Collaboration et al. 2021c; Vasiliev 2018). While field 12 ($\Phi\sim-5°$) is mildly deviant from these values, with an azimuthal velocity ~1.5σ lower than the canonical value and an elevated radial velocity dispersion of ~40 km s^{-1}, this field is located directly adjacent to the northern arm feature discussed in Paper II. It is therefore unsurprising that minor deviation from equilibrium disk kinematics is observed, likely resulting from the same interactions that formed the nearby substructure. In particular, the elevated in-plane radial velocity dispersion is a known indicator of perturbation (Wan

et al. 2020).

In terms of disk structure, fields 18 and 12 have out-of-plane distances consistent with zero within uncertainty, and the out-of-plane distance for field 29 is only just in excess of a 1σ deviation from zero. We additionally find σ_{G0}, the red clump magnitude dispersion in each field (which is an indication of the line-of-sight thickness of the disk) is consistent across these fields, as expected given the consistent vertical velocity dispersions between these fields.

5.6.3 The "straight-edged" western disk

Fields 8, 27, and 28 are each located in the western outskirts of the LMC disk (with position angles $230°<\Phi<330°$), which appears sharply truncated compared to the north-eastern disk in maps such as Fig. 5.1. Each of these fields are located ~4 kpc in front of the predicted LMC disk plane, and it is thus not surprising that fields 8 and 28 have ~30 km s^{-1} vertical velocities in this direction. The in-plane radial velocity is strongest in field 8, at ~35 km s^{-1} and decreases moving north along the disk edge, reaching ~5 km s^{-1} (consistent with zero within uncertainty) in field 28. We also find the velocity dispersion in each component decreases moving north from field 8 to field 28; however even in field 28 these velocity dispersions are uniformly ~10 km s^{-1} larger than those in the undisturbed north-eastern disk (i.e., fields 18 and 29). Correspondingly, the red clump magnitude dispersion within each of these fields appears mildly elevated compared to the undisturbed disk, though we note the large uncertainties in σ_{G0} mean this difference is not statistically significant.

5.6.4 The disturbed southern disk

The southern outskirts of the LMC disk, including fields 21, 14 and 10 ($100°<\Phi<220°$ and $10°<R<11°$), are significantly disturbed from equilibrium disk kinematics. Velocity dispersions in these fields, typically $40-50$ km s^{-1} in each component, are approximately double those in the undisturbed disk, and the azimuthal velocities of the fields are also ~2σ lower than that in the undisturbed disk. However, we do find that despite the large observed velocity dispersions, these fields do not display elevated red clump magnitude dispersions (σ_{G0}) compared to the undisturbed disk. This is at least partly attributable to projection effects, as σ_{G0} traces only the LOS dispersion of the field. While in the northern outskirts of the LMC, the LOS direction closely maps the V_z direction (such that an elevated vertical velocity dispersion is expected to be observed as an increased LOS velocity dispersion, and thus increased σ_{G0}), in the southern outskirts of the LMC

the line-of-sight projects to a combination of all three (vertical, azimuthal, and radial) disk frame coordinates. Consequently, an increased velocity dispersion in any one of these individual directions will not necessarily introduce a significant increase in σ_{G0}. However, as we observe elevated velocity dispersions in all three components in these fields, it is perhaps surprising we do not see some increase in σ_{G0} in these fields.

Field 23, located in the south-eastern disk (Φ~110°), marks a transition from the relatively ordered kinematics of the north-eastern disk to the disturbed kinematics of the southern disk. The azimuthal and vertical velocities in this field are consistent within uncertainty with those expected for an equilibrium disk, unlike the other southern disk fields. However, its velocity dispersions – each $\sim 30 - 35$ km s^{-1} – are elevated relative to the undisturbed disk, albeit still ~1σ less than the other southern disk fields. We note that while this field does have a large σ_{G0} dispersion, uncertainty on this value is sufficiently large that it is still potentially consistent with the σ_{G0} values measured in the nearby disk fields.

All of the southern disk fields display clear kinematic trends in their radial and vertical velocities as a function of position angle. The in-plane radial velocity of the fields increases from approximately -20 km s^{-1} in field 23 to ~25 km s^{-1} in field 10, with the adjacent field 8 in the south-western disk continuing the observed trend. In addition, the out-of-plane vertical velocity increases from approximately -15 km s^{-1} in field 21 to ~15 km s^{-1} in field 10, with the adjacent field 8 continuing this trend. An increasing vertical velocity is potentially compatible with the observed increase in the out-of-plane distance from ~2 kpc to ~4.5 kpc between fields 21 and 8. Interestingly, we note that Olsen and Salyk (2002) – who fit an LMC disk plane consistent with our measurements – also find stars in the south-western LMC disk have positive out-of-plane distances of up to ~2.5 kpc, though at much smaller galactocentric radii than our fields.

5.6.5 The claw-like southern substructures

The discovery of two "claw-like" substructures in the southern outskirts of the LMC is first described in Mackey et al. (2018), with the more prominent "Substructure 2" located further west than "Substructure 1". MagES fields are located on both substructures, with field 17 (Φ~170°) located on Substructure 1, and fields 6 and 7 (Φ~205°) located on Substructure 2 (see Fig. 5.1). We find the two features are kinematically distinct, and thus discuss each substructure individually.

We compare the kinematics of field 17, located on Substructure 1, with those of field 14, located immediately adjacent in the southern LMC disk. The radial and vertical

velocities in field 17 are very similar to those in field 14, and while the azimuthal velocity is ~10 km s^{-1} higher in field 17, this is still consistent within 1σ with that measured in 14. The azimuthal and radial velocity dispersions are also consistent between the fields. The vertical velocity dispersion is ~8 km s^{-1} (~2σ) larger in field 17, consistent with a very mildly elevated σ_{G0} in this field, though the large uncertainty on this value is such that this is not a statistically significant difference. The only substantial difference between the two fields is their out-of-plane distances: field 17 is ~6 kpc in front of the undisturbed disk plane, a distance ~2 kpc greater than field 14. We therefore suggest field 17 is likely perturbed by the same forces as the nearby southern disk.

In contrast, fields 6 and 7, located on Substructure 2, have distinctively different kinematics to the neighbouring fields 10 and 8. Both fields 6 and 7 have enormous vertical velocities: ~60 km s^{-1} in field 6, and ~100 km s^{-1} in field 7. These are respectively 5 and 8σ higher than that predicted for an equilibrium disk. This potentially explains the very large out-of-plane distances of these fields – both are located ~8 kpc in front of the predicted disk plane, and ~4 kpc further than the nearby fields 10 and 8. The vertical velocity dispersion in the substructure is also 5σ larger (at $\sim 55-60$ km s^{-1}) than the undisturbed disk, and 2σ larger than the nearby disturbed disk ($\sim 35-40$ km s^{-1}). We note that despite the strongly elevated vertical velocity dispersion, σ_{G0} in the substructure is not elevated relative to the nearby disk fields. This is because at this point in the disk, due to projection effects, the vertical velocity dispersion is contributed to most significantly by the dispersion in the PMRA direction (which as per Table 5.1, is elevated in these fields relative to the nearby fields disk fields), and not the LOS direction. The azimuthal and radial velocity dispersions in these fields are not significantly different from those in the nearby southern disk (~45 km s^{-1}), where we similarly do not see an elevated σ_{G0}, despite these velocity dispersions being elevated compared to the undisturbed disk. In sum, this suggests these fields are predominantly perturbed by a force in the z direction, with possibilities for this discussed in greater detail in §5.7.

Unexpectedly, as is evident in panel *a* of Fig. 5.6, fields 6 and 7 are also counter-rotating relative to the rest of the disk, with negative azimuthal velocities. While Olsen et al. (2011) also find a population of counter-rotating stars in the LMC, attributed to SMC debris infalling to the LMC potential, it is unlikely this is also the case for this substructure. As discussed above, the RC colour and mean [Fe/H] for the field are consistent with that of the LMC, while the Olsen et al. (2011) SMC population was found to be significantly more metal-poor than their LMC stars. Further, the Olsen et al. (2011) SMC population was found to be either counter-rotating in a plane closely aligned to that of the LMC disk, or co-rotating in a plane strongly inclined relative to the LMC disk. Both options

are inconsistent with the counter-rotation observed at a very large out-of-plane distance in our fields. We therefore maintain the substructure is comprised of LMC disk material, significantly perturbed from equilibrium kinematics.

5.6.6 The extended southern substructure

The presence of a long, thin arm-like feature in the far southern outskirts of the LMC was first reported in Belokurov and Erkal (2019), and hypothesised as a potential counterpart to the northern arm. Four MagES fields are located along the locus of the feature: fields 9, 24, 25 and 26 (each at R~16.5). However, unlike the northern arm (discussed in Paper II), these fields do not follow consistent kinematic or structural trends along the length of the feature. We thus present the properties of each field individually below, while discussion of implications for the perturbations producing the different features in each field are deferred to §5.7.

Field 25, located ~3 kpc in front of the predicted LMC disk plane in the extreme eastern outskirts of the LMC (Φ~100°), is in the vicinity of "Eastern Substructure 2" in El Youssoufi et al. (2021) (noted also in Gaia Collaboration et al. 2021c). This field has an in-plane radial velocity of ~25 km s^{-1}, and a vertical velocity of approximately -15 km s^{-1}: each of which are ~2σ from the expected kinematics in an equilibrium disk. In contrast, we find the velocity dispersions and red clump magnitude dispersion σ_{G0} for the field, in addition to its azimuthal velocity, are consistent within uncertainty with those in the undisturbed disk.

Field 26 is located in the extreme south-eastern outskirts of the LMC (Φ~150°). Kinematically, it is consistent within uncertainty with the predicted equilibrium disk kinematics, with only mildly elevated velocity dispersions (~5 km s^{-1}: $<1\sigma$ significant) relative to the undisturbed disk, and a consistent red clump magnitude dispersion also. However, this field is located ~7 kpc in front of the predicted LMC disk plane, indicative of a perturbation, which is difficult to reconcile with the effectively undisturbed kinematics in the field.

In contrast to the relatively ordered kinematics of fields 25 and 26, fields 9 and 24 (165°$<\Phi<$185°) are more significantly disturbed. Both fields have in-plane radial velocities of approximately -25 km s^{-1}, indicating inward motion towards the LMC centre. This is the opposite direction to velocities measured in the southern disk and claw-like substructures, but is similar to the negative in-plane radial velocities observed along the northern arm-like feature discussed in Paper II. The fields additionally have vertical velocities of approximately -25 km s^{-1}, despite being located $\geq$ 10 kpc in front of the

predicted LMC disk plane. This is unlike the nearby claw-like Substructure 2, which is similarly located significantly in front of the disk plane, but has correspondingly large and positive vertical velocities. This suggests that different perturbations are likely responsible for the two structures.

The velocity dispersions in these two fields are elevated relative to those in the undisturbed disk, with magnitudes similar to those in the southern disk fields, though field 24 is only significantly elevated in its radial velocity dispersion (~40 km s^{-1}). Field 9 has elevated dispersions in each component, but is also most significantly elevated in its radial velocity dispersion (~55 km s^{-1}). Correspondingly, the red clump magnitude dispersion in field 9 is larger than that in field 24, though the large uncertainties in σ_{G0} due to the comparatively low number of stars in these fields mean these are not statistically significant differences. These elevated velocity dispersions are also unlike the northern arm, which is kinematically cold (with velocity dispersions typically on the order of $\lesssim$ 25 km s^{-1}: see Paper II).

5.7 Discussion

5.7.1 Dynamical models

In order to assist in our interpretation of the disturbed kinematics in the LMC outskirts, we compare our results to a suite of simple dynamical models of the Magellanic system first presented in Paper II. A brief summary of the key model parameters is presented below. We note that these models are designed only as a first exploration of the large and complex parameter space that describes the allowable orbits of the Clouds, and there are consequently associated model limitations. Most significant of these is likely the lack of self-gravity incorporated into the models, which can affect both the orbits of the Clouds, and the response of stars within the Clouds to close interactions. This was discussed in detail in Paper II. As such, here we only perform qualitative, rather than quantitative, comparisons to our observations, and note that more detailed models are required to validate and expand upon our analysis, particularly regarding origins of substructures.

We model the LMC as a collection of test particles within a two-component potential: an exponential disk with mass 2×10^9 $M_\odot$, scale radius 1.5 kpc, and scale height 0.4 kpc; and a Hernquist (Hernquist 1990) dark matter halo of mass 1.5×10^{11} $M_\odot$ (Erkal et al. 2019) and scale radius 20 kpc, such that the circular velocity is ~90 km s^{-1} at 10 kpc (Paper I). The test particle distribution within the disk is initialized using AGAMA (Vasiliev 2019) to account for the velocity dispersion of the LMC disk. The SMC is

modelled as a Hernquist profile with mass 2.5×10^9 $M_\odot$ and scale radius 0.043 kpc, such that the SMC has a circular velocity of 60 km s^{-1} at 2.9 kpc (motivated by the results of Stanimirović et al. 2004)[36]. We do not initialise the SMC potential with tracer particles. The Milky Way is modelled as a three-component system with a bulge, disk, and dark matter halo similar to the `MWPotential2014` from Bovy 2015. As in Erkal et al. (2019), we treat each of the three systems in the model (i.e. the MW, LMC, and SMC) as a particle sourcing a potential, allowing us to account for the motion of the Milky Way in response to the LMC (as in Gómez et al. 2015). We account for the dynamical friction of the Milky Way on the LMC using the results of Jethwa et al. (2016), but do not explicitly account for the effects of dynamical friction between the LMC and SMC.

The LMC and SMC are initialized at their present day locations, then rewound for 1 Gyr in the presence of each other and the Milky Way. At this time, the LMC disk is initialized with $\sim 2.5 \times 10^6$ tracer particles, with a geometry matching that from Choi et al. (2018b). This is a somewhat lower inclination ($i = 25.86° \pm 1.4°$) than that we derive in §5.3.4 ($i = 36.5° \pm 0.8°$), though the LON position angle ($\Omega = 149.23° \pm 8.35°$) is consistent within uncertainty with that we derive ($\Omega = 145.0° \pm 2.5°$). Consequently, when calculating velocities in the frame of the disk for the models, we use the Choi et al. (2018b) geometry to define the disk plane. The system is then evolved to the present. We run multiple model suites in order to probe the range of allowed masses for the LMC, SMC, and MW, but in this paper discuss only two:

- Our fiducial or "base-case" model suite, which utilises our best estimates for the masses of the LMC, SMC, and Milky Way; and
- A "no-SMC" suite, which omits the SMC, but is otherwise identical to the base-case suite. This allows for separation of the effects of the SMC from those of the MW.

Findings from our model suites with increased MW and SMC masses are qualitatively similar to that of our base-case suite.

Within each model suite, we run multiple individual realisations, sampling from literature uncertainties on the current-day distances and systemic velocities of both the LMC and SMC, to explore the allowable parameter space. This results in differing orbits, and thus interaction histories, for the Clouds. As discussed in Paper II, in all model realisations, the SMC has had a recent close pericentric passage around the LMC ~150 Myr ago (in agreement with Zivick et al. 2018), with a total pericentric distance $r_{\rm peri} = 8.0^{+2.4}_{-2.0}$ kpc.

[36] As the entire SMC mass is enclosed within this radius in our models, this results in much smaller scale radii than in e.g. Besla et al. (2012), who model an initially more massive SMC which experiences mass loss through repeated interactions with the LMC.

However, these pericentres occur significantly below the plane of the LMC disk[37], with $z_{\rm peri} = -6.8^{+2.5}_{-2.6}$ kpc: the SMC is only now crossing the LMC disk plane. The projected galactocentric radius of the pericentric passage is ~4 kpc, in a direction toward the south-west of the LMC.

At earlier times, the orbit of the SMC varies significantly depending on how the systemic motions of both Clouds are sampled. Approximately 51% of our base-case realisations have a second SMC crossing of the LMC disk 400^{+85}_{-70} Myr ago, which can occur across a broad range ($28.8^{+11.4}_{-9.2}$ kpc) of in-plane radial distances. The remaining ~49% of orbits remain behind the LMC's disk plane for the 1 Gyr over which our models are run, and include some orbit realisations where the SMC is on its first infall to the LMC potential.

A handful of model realisations (~9%) additionally have a third disk crossing 900^{+60}_{-160} Myr ago, though a larger fraction would experience this crossing if our models were rewound for a greater length of time than 1 Gyr. The particulars of this crossing are much less robustly constrained than the ~400 Myr crossing, with crossing distances of $53.8^{+13.1}_{-46.3}$ kpc permitted due to the increasing uncertainty in the SMC's orbit at earlier times. We additionally find a small fraction (~4%) of our models show a second SMC pericentric passage at around this time, again noting this fraction would increase were our models rewound further than 1 Gyr. These pericentres have similar distances ($r_{\rm peri} = 6.2^{+3.8}_{-2.3}$ kpc) to the most recent pericentric passage, but occur at smaller out-of-plane distances ($z_{\rm peri} = 2.2^{+2.5}_{-1.1}$ kpc) due to the similarly-timed disk crossing in these realisations.

In order to show the qualitative effects of these varying interaction histories on the LMC, Fig. 5.7 presents current-day kinematic maps for four individual model realisations. Each realisation is selected to have a similar orbit of the LMC around the MW (and thus similar effects from MW tides), but varies in its interactions with the SMC. The top row presents a no-SMC realisation, and the second row presents the realisation in the base-case model with identical conditions for the LMC as the top row. This model experiences only the most recent SMC pericentre ~150 Myr ago. The third row presents a base-case realisation which experiences the ~400 Myr disk crossing in addition to the most recent pericentric passage, whilst the last row presents one of the few base-case realisations which experiences a disk crossing ~980 Myr ago in addition to the ~400 Myr disk crossing and ~150 Myr pericentric passage. For each realisation, we show the mean within each spatial bin of, in order: i) ratio of final to initial particle in-plane radius ($R_{\rm final}/R_{\rm initial}$), ii) the in-plane radial velocity (V_r), iii) the out-of-plane vertical velocity (V_z), and iv) the out-of-plane distance (z). We do not show maps for the azimuthal velocity (V_θ) as in our models,

[37] i.e. behind the disk plane relative to us.

this quantity shows an inherent systematic decrease with radius beyond 10 kpc (where we match the observed rotation curve of the LMC) reflecting the Hernquist potential used to model the LMC halo. As a consequence, in our models this velocity component is more difficult to interpret, and thus less useful as a tracer of interaction, compared to the radial and vertical motions.

5.7.2 Predicted effects of interactions in the outer LMC

Fig. 5.7 reveals the broad kinematic trends we expect to result from different perturbations to the LMC disk. We first consider the effect of the MW tides on the LMC disk, shown in the top row of Fig. 5.7. The MW's most significant effect on the LMC is production of a strong vertical velocity gradient across the LMC disk, with a strongly positive V_z in the far northeast, and a strongly negative vertical velocity in the far southwest. This is consistent with our findings in Paper II of an increasingly positive V_z along a long arm-like feature to the north of the LMC. However, we note at the distances of the disk fields analysed in this paper (as opposed to those along the long "arm-like" southern substructure), the magnitude of the V_z perturbation in the model is generally only on the order of ~10 km s^{-1}.

The MW additionally has a (somewhat milder overall) effect on the in-plane radial velocity, acting to compress the LMC disk in the northwest and southeast (marked by both a negative V_r and $R_{\rm final}/R_{\rm initial}<1$), and mildly elongate it in the northeast and southwest (marked by $R_{\rm final}/R_{\rm initial}>1$). Like the vertical perturbation, these effects are strongest at large LMC galactocentric radii, particularly along the long 'arm-like' southern substructure, and comparatively weak (with the magnitude of V_r on the order of ~10 km s^{-1}, and $0.75 \lesssim R_{\rm final}/R_{\rm initial} \lesssim 1.25$) at the radii of the MagES disk fields.

Comparing the MW-only model (top row of Fig. 5.7) to the model which includes only the SMC's most recent pericentre (second row of Fig. 5.7), we see these are not very significantly different. The south-eastern edge of the LMC is more strongly compressed (with $R_{\rm final}/R_{\rm initial}$ smaller than in the MW-only case), though the predicted radial velocity does not change significantly in this region. In addition, there are localised regions in the southwest of the LMC – in the direction of the projected location of the SMC's closest pericentric distance – that have more strongly negative vertical velocities than in the MW-only model. Further, a larger region of the south-western LMC disk in this model has positive radial velocities as compare to the MW-only model. These localised perturbations match the direction of the SMC's gravitational force on the LMC during its recent pericentric passage. However, because the pericentric passage is at a moderate

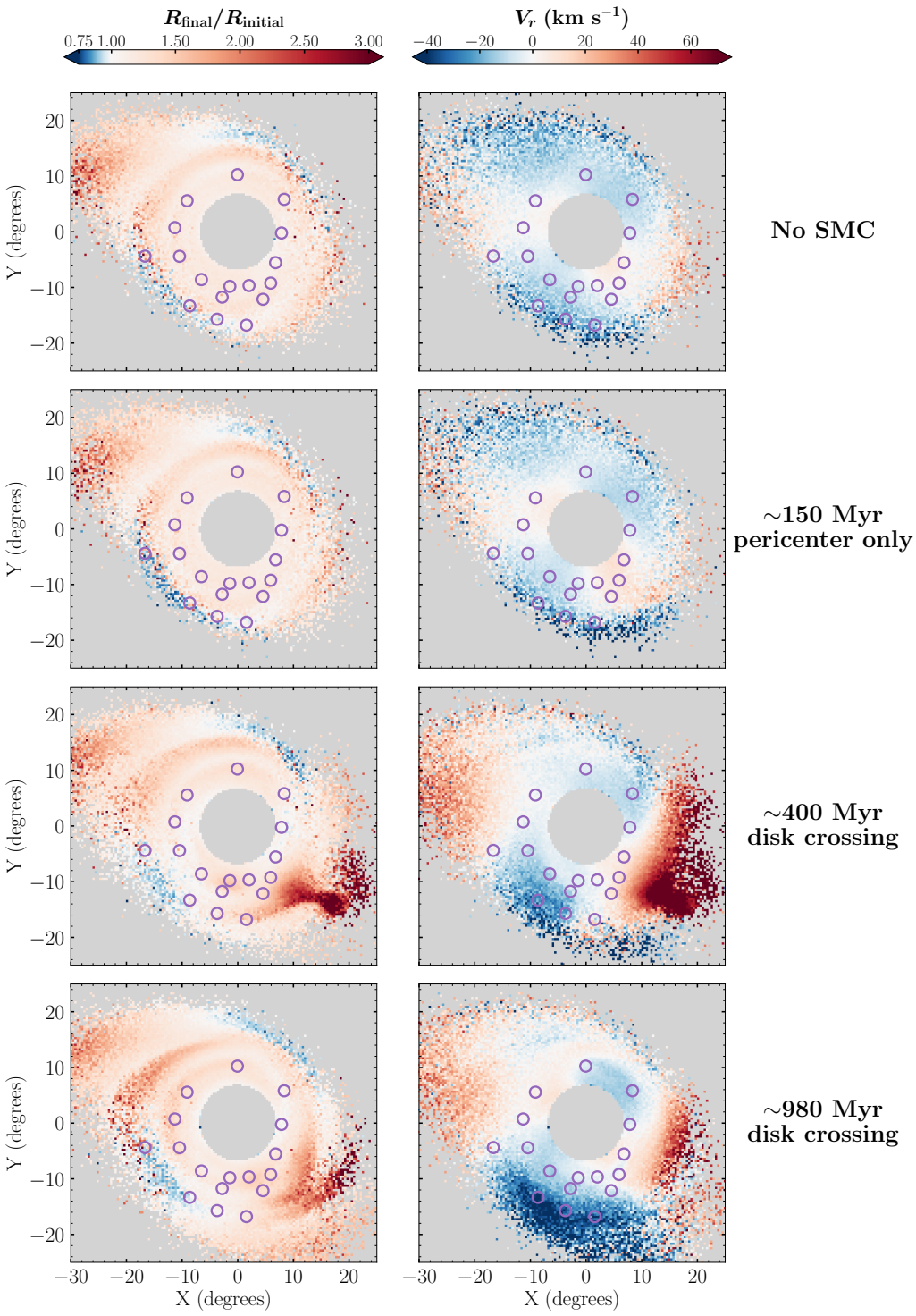

Figure 5.7: Kinematic predictions for four individual model realisations with differing LMC-SMC orbital histories, but similar LMC-MW orbital histories. Rows show model realisations which, in order from top to bottom: i) exclude the SMC entirely, ii) experience only an SMC pericentre ~150 Myr ago, iii) experience an SMC crossing of the LMC disk plane ~400 Myr ago and the SMC pericentre ~150 Myr ago, and iv) experience SMC crossings of the LMC disk plane at both ~980 and ~400 Myr ago, in addition to the SMC's pericentre ~150 Myr ago. Columns show (left) the ratio of final to initial particle in-plane galactocentric radius ($R_{\rm final}/R_{\rm initial}$) and (right) the in-plane radial velocity (V_r).

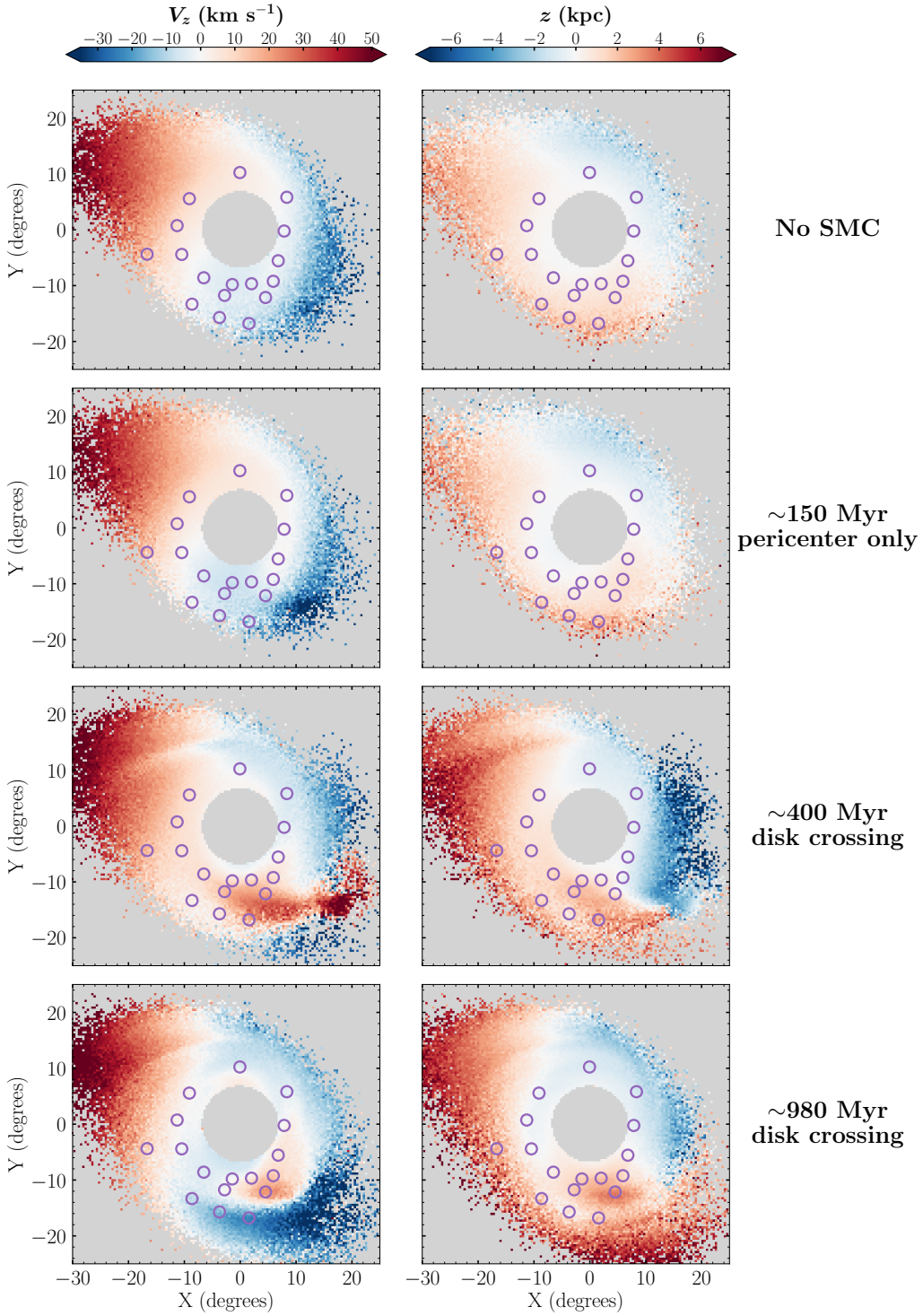

Figure 5.7: – continued. Columns show (left) the out-of-plane vertical velocity (V_z), and (right) the out-of-plane distance (z) for the four model realisations. Purple circles represent the locations of the MagES fields studied in this analysis.

out-of-plane distance (~−9 kpc for this particular model realisation, comparable to the $-6.8^{+2.5}_{-2.6}$ kpc found across the base-case model suite), the kinematic signatures of this perturbation are not as strong as interactions which impact the LMC's disk plane directly, although we note the lack of self-gravity in our models may mean these effects are mildly underestimated (see Paper II).

More dramatic effects on the kinematics of the disk are produced by SMC crossings of the LMC disk plane, as is evident comparing the second row of Fig. 5.7 – which includes only the most recent pericentric passage – to the third row of Fig. 5.7, which displays a model where the SMC additionally crosses the LMC disk plane ~400 Myr ago. In this particular model realisation, the SMC crosses the LMC disk plane in the then-northeast of the LMC, at a radial distance of 17.7 kpc. The material closely perturbed by this interaction has since moved clockwise with the LMC's rotation and is now located in the western outskirts of the LMC. This is evident in the strongly perturbed kinematics of this region in our model, and is also seen in panel *d* of Fig. 4.14 (which shows the same model realisation as in the third row of Fig. 5.7, with the current particle distribution colour-coded by the distance of each particle from the SMC at the time of the disk plane crossing). The in-plane radial velocity is strongly positive ($\geq$ 50 km s^{-1}) across the western LMC disk outskirts, and $R_{\rm final}/R_{\rm initial}$ is strongly positive in the southwest. As the SMC crosses the disk plane at a (radial) distance of 17.7 kpc in this particular realisation, these effects are consistent with the direction of the SMC's gravitational force on the LMC in this region during the crossing. We note the radial distance of the crossing in this particular realisation is at the lower end of the distribution of radial crossing distances for this event seen in our models[38], which means the gravitational force of the SMC (and thus the resultant kinematic signatures in the LMC disk) will be on the stronger end of those allowable.

In terms of vertical perturbations in this model realisation, we see a strongly positive vertical velocity ($\geq$ 40 km s^{-1}) and positive out-of-plane distance (>4 kpc) in the south-western outskirts of the disk, and a strongly negative out-of-plane distance (≤ -4 kpc) along the rest of the western edge of the LMC. However, the vertical velocity in the north-western region is not significantly more negative than that introduced by the Milky Way. This asymmetry in out-of-plane distances, and to some extent vertical velocities (i.e. positive in the southwest, and negative in the northwest) is expected from the SMC crossing the disk in a direction from positive to negative z. This is because material leading the crossing point relative to the sense of (clockwise) rotation in the LMC – today in the southwest – feels a net positive vertical perturbation from the SMC, and material trailing

[38] The median radial crossing distance is 28.8 kpc with 1σ thresholds of 39.8 and 19.6 kpc.

the crossing point – today in the northwest – feels a net negative vertical perturbation from the SMC. We note that the direction of this asymmetry will alternate (i.e. switch between positive and negative) in a given region on a timescale comparable to that of the vertical oscillation period of stars in the disk, due to the restorative force of the LMC disk's gravitational potential. However, as the ~400 Myr disk crossing is comparatively recent, the observed pattern suggests insufficient time has passed for this oscillation to occur, with the resulting velocity and out-of-plane distance still in the direction of the initial perturbation.

In addition to the ~400 Myr disk crossing, which is experienced by ~50% of our model realisations, some model realisations also experience a SMC crossing of the LMC disk plane ~1 Gyr ago. In these cases, the SMC crosses the disk plane in the opposite sense (i.e., from negative to positive z) to that ~400 Myr ago. The particular realisation shown in the bottom row of Fig. 5.7 experiences this additional disk crossing ~980 Myr ago, in the then-southwest of the LMC at a radial distance of 8.2 kpc. This is a distance ~40% smaller than the disk crossing ~400 Myr ago. We thus expect even stronger perturbative effects from the SMC during this crossing.

However, the orbital period of material around the LMC disk is longer at larger radii (due to the approximately constant circular velocity). At the crossing radius, the time since the crossing is comparable to the orbital time, and material closely perturbed in this interaction is in approximately the same location as when the perturbation occurred (i.e. the south-western LMC). In contrast, the shorter orbital period at smaller radii is such that material can complete more than one full disk rotation in the time since the crossing, so material closely perturbed by the interaction appears somewhat mixed (and is even present in the current north-east of the LMC: see panel *f* of Fig. 4.14). Consequently, the kinematic signatures of this earlier perturbation are more difficult to disentangle, with this made even harder by the fact that some material closely affected by this interaction is subsequently perturbed further during the SMC crossing of the disk plane ~400 Myr ago. However, we do still note a more strongly negative in-plane radial velocity and out-of-plane vertical velocity in the extreme southern outskirts of the LMC in this model realisation as compared to that in the third row of Fig. 5.7, which are likely the result of this older disk crossing.

5.7.3 Comparing models to observations

We now perform a qualitative comparison of our measured kinematics to Fig. 5.7 to learn more about the potential origin of the various kinematic signatures observed across

the LMC outskirts. We first note that for the three fields in the north-eastern LMC disk, their kinematics are only very mildly perturbed in each of the model realisations in Fig. 5.7. Even in the most disturbed realisation, which experiences disk crossings at ~980 and ~400 Myr in addition to the SMC's most recent pericentric passage (bottom row of Fig. 5.7), the radial and vertical velocities in fields 18 and 29 (located at X,Y positions $-8.4, 5.8$ and $-10.7, 1.0$ respectively) are approximately zero, as are their out-of-plane distances. This is consistent with our observations, and supports our use of data in this region to fit the LMC disk plane.

Considering next the fields along the western edge of the LMC disk, we find the kinematics in these fields are mostly qualitatively consistent with those resulting from the SMC's crossing of the disk plane ~400 Myr ago (third row of Fig. 5.7), with some effect from the LMC's infall to the Milky Way potential (top row of Fig. 5.7). Fields 27 and 8 (located at X,Y positions of $8.4, -0.5$ and $7.2, -5.8$ respectively) have positive in-plane radial velocities, strongest in field 8 in the south-western disk. This is consistent with the strongly positive radial velocity produced by the disk crossing in this region. The near-zero radial velocity observed in field 17 (located at X,Y position $-2.5, -11.7$) can be interpreted as resulting from the combined effect of the disk crossing, which pulls material radially outward, and the compressive force of the MW tides, which pushes material radially inward in the north-western disk. Fields 8 and 27 are also consistent with the vertical velocity asymmetry resulting from the ~400 Myr crossing (i.e. positive V_z in the southwest and negative V_z in the northwest) if field 27 is located near the current-day position of the disk crossing point itself (where $V_z \sim 0$). From panels *a* and *b* of Fig. 4.14, we see the position angle of field 27 (~270°) is not substantially different to that of the current-day location of the crossing point. In addition, although not shown in Fig. 5.7, we find the velocity dispersions in the western LMC disk outskirts are mildly elevated in the model realisation experiencing the ~400 Myr crossing compared to that which only experiences the SMC's most recent pericentric passage. This is consistent with the elevated velocity dispersions observed in these fields.

However, we do note models which experience only the ~400 Myr disk crossing (as in the third row of Fig. 5.7) predict the vertical velocity and out-of-plane distance in the vicinity of field 28 should be negative. This is inconsistent with the positive values observed. We speculate these may reflect the effects of earlier interactions with the SMC. In particular, the model realisation in the bottom row of Fig. 5.7 (which additionally experiences a disk crossing ~980 Myr ago) has a positive vertical velocity and out-of-plane distance extending to larger position angles – i.e. closer to field 28 – than that in the second row of Fig. 5.7 (which experiences only the ~400 Myr crossing). However, as

the location and timing of older interactions with the SMC are poorly constrained in our simple models, more detailed modelling is required to confirm this.

We next discuss fields in the southern LMC disk. The increasing in-plane radial velocities with position angle observed in this region can be understood as a combination of forces. In the southeast, the compressive forces from the Milky Way tides produce negative radial velocities, as observed in field 23 (located at X,Y$=-10.0, -4.2$). Moving toward the southwest, the gravitational force of the SMC becomes increasingly dominant, pulling material outward and producing positive radial velocities as observed in fields 10 and 8 (located at X,Y positions of $2.3, -9.8$ and $7.2, -5.8$ respectively). In this south-western region, both the ~400 Myr disk crossing (third row of Fig. 5.7) and the SMC's recent pericentric passage (second row of Fig. 5.7) can produce positive radial velocities. However, as seen in the second row of Fig. 5.7, our models predict the recent SMC pericentre also produces negative vertical velocities throughout the southern LMC disk outskirts. This is inconsistent with the positive vertical velocities observed in fields 10 and 8. In fact, the observed transition from negative to positive vertical velocities moving from the southeast to southwest LMC disk is best matched by the model realisation which experiences SMC crossings of the LMC disk plane at ~400 Myr and ~980 Myr ago (the bottom row of Fig. 5.7). This particular realisation additionally replicates the observed increasing out-of-plane distance across these fields. The increased vertical velocity dispersion and (positive) out-of-plane distance observed in field 17 (located at an X,Y position of $-2.5, -11.7$) relative to field 14 (located at an X,Y position of $-1.1, -9.8$) suggest this region is affected by a perturbation strongest in the z-direction – i.e. an SMC crossing of the LMC disk plane. The ~400 Myr disk crossing produces qualitatively similar effects to those observed in both z and V_z. However, more detailed models will be required to confirm the influence of older interactions, and how these combine with the effects of more recent interactions, in this region.

While our simple models provide a reasonable description of the kinematics of fields in the outer LMC disk, they are not able to fully replicate the kinematics of individual substructures in the southern regions. The mildly positive in-plane radial velocities and elevated radial velocity dispersions in fields 6 and 7 (located in the claw-like Substructure 2, at X,Y coordinates $4.8, -12.3$ and $6.2, -9.4$ respectively) are similar to those in the nearby southern disk. This is consistent with an origin in recent interactions with the SMC, be that the ~400 Myr disk-plane crossing (third row of Fig. 5.7) or the pericentric passage ~150 Myr ago (second row of Fig. 5.7). Yet none of our models can replicate their very strongly perturbed azimuthal and vertical velocities, or the distinctive shape of the feature. We thus speculate this substructure is potentially the result of repeated

interactions with the SMC beyond those occurring in the 1 Gyr for which our model suites are run, each having an additive effect. Such a scenario could plausibly produce the large velocity perturbations observed in these fields. However, self-gravitating models will be required to confirm this, as it is possible the lack of self-gravity in our models simply underestimates the effect of recent interactions with the SMC in this region.

Our models are also unable to replicate the effectively unperturbed kinematics of field 26 in the "arm-like" southern substructure (at an X,Y location of $-8.4, -13.1$). Each of our models predicts a strongly negative radial velocity at this location, and also significantly underestimates the out-of-plane distance (z) – though this is perturbed in the correct direction. The enormous out-of-plane distances of fields 9 and 24 (located at X,Y coordinates of $1.7, -16.9$ and $-3.6, -15.6$ respectively) are similarly significantly underestimated in our simple models. However, we do note that the negative vertical and radial velocities in these fields are qualitatively similar to the model realisation which experiences SMC crossings of the LMC disk plane at both ~980 and ~400 Myr ago (bottom row of Fig. 5.7). More detailed modelling is clearly required to understand the origin of these velocity perturbations.

5.8 Summary and Conclusions

In this paper, we have explored the structural and kinematic properties of the LMC outer disk and surrounding substructures. Our analysis utilises spectroscopic data for red clump and red giant branch stars across eighteen MagES fields to obtain [Fe/H] abundances, and in conjunction with Gaia EDR3 astrometry, 3D kinematics for stars across the LMC outskirts. Ten MagES fields probe the outer LMC disk at galactocentric radii of $8.5° < R < 11°$, five trace the long "arm-like" southern substructure discovered in Belokurov and Erkal (2019), and three are located on the claw-like southern substructures discovered in Mackey et al. (2018). We also use Gaia EDR3 photometry of Magellanic red clump stars to probe the structure of the LMC outskirts.

We find field 3, located near the western end of the southern "arm-like" structure, is comprised predominantly of SMC, not LMC, material, owing to its distinct SMC-like kinematics and comparatively low ([Fe/H]~ -1.4) metallicity. At a SMC galactocentric radius of 9.5°, it represents one of the most distant detections of SMC debris. This field is under further investigation by the MagES team, and is not considered further in this paper. The other seventeen fields studied each have properties more consistent with the LMC, and are thus analysed in this context.

We find an approximately constant mean metallicity of [Fe/H]~ -1 across all con-

sidered fields, consistent with previous literature measurements in the outer LMC disk. Where available, [Fe/H] measurements for individual RGB stars reveal an ~0.5 dex standard deviation in each field. RC photometry for each field also shows consistent $(G_{BP} - G_{RP})_0$ colours and colour dispersions across all fields. In combination with the consistent metallicity measurements, this indicates similar stellar populations are present within each field, and that Magellanic stars in all fields are predominantly LMC disk material.

Motivated by previous findings that the north-eastern outskirts of the LMC disk are relatively kinematically undisturbed (Paper I), we utilise Gaia EDR3 astrometry and photometry for RC stars in the north-eastern outskirts of the LMC disk ($9.5°<R<10.5°$, $5°<\Phi<90°$) to fit an inclined disk model as described in van der Marel et al. (2002) to the LMC. In addition to describing the geometry of the disk and the azimuthal velocity of the LMC, our model also outputs a "reference magnitude" which describes the apparent brightness of a red clump, comprised of an identical stellar population to that of our fields in the outskirts, located at the centre distance (49.59 kpc: Pietrzyński et al. 2019) of the LMC.

We find at these large galactocentric radii, the LMC disk has an inclination of $36.5° \pm 0.8°$, a LON position angle of $145.0° \pm 2.5°$, and an azimuthal velocity of 69.9 ± 1.7 km s^{-1}. These are consistent with several literature measurements of the LMC disk at smaller radii. Our "reference magnitude" for the red clump is G_0~18.9, and we utilise this, in conjunction with RC photometry for each of the analysed fields, to derive absolute distance estimates across the LMC outskirts and convert our observed field kinematics into the frame of the LMC disk.

Our results are qualitatively compared to a suite of simple dynamical models of the Magellanic system described in Paper II, sampling from uncertainties in the central locations and systemic motions of the LMC and SMC. This allows investigation of how different interactions between the LMC, SMC, and MW can potentially produce the observed perturbations. Four model realisations are considered, each with similar orbits of the LMC around the MW. The first omits the SMC entirely, the second experiences only the most recent SMC pericentric passage around the LMC ~150 Myr ago. The third and fourth realisations experience SMC crossings of the LMC disk plane in addition to the most recent pericentric passage, with the third realisation having an SMC crossing of the LMC disk plane ~400 Myr ago, and the fourth having disk plane crossings both ~400 and ~980 Myr ago. Findings for each kinematically distinct region of the LMC are summarized below.

As expected, fields in the north-eastern LMC disk display relatively unperturbed kinematics, with radial and vertical velocities consistent with zero, and only minor deviations

in a field near base of an arm-like feature north of the LMC. We note that even in the most disturbed model (i.e. that which experiences disk crossings ~400 and ~980 Myr ago, as well as the pericentric passage ~150 Myr ago) the north-eastern LMC has relatively undisturbed kinematics at the locations of the MagES fields, consistent with our observations.

We find the western outskirts of the LMC disk are most strongly perturbed in an SMC crossing of the LMC disk plane ~400 Myr ago, with the observed kinematics of these fields mostly qualitatively similar to those predicted from this interaction. The in-plane radial velocity uniformly decreases moving northwards along the disk edge, which we find is consistent with the combined effects of the MW tides acting to compress material in the north-western LMC, and the effect of the SMC during the disk crossing, which acts to pull material radially outward along the entire western LMC edge. Our models additionally predict that disk material leading the crossing point during the ~400 Myr crossing (today in the southwestern LMC) feels a net positive vertical perturbation – consistent with our observations in the southwestern disk – but that material trailing the crossing point (today in the northwest) feels a net negative vertical perturbation. This is inconsistent with our observations in the northwest. We speculate the north-western LMC may have been further perturbed by older interactions with the SMC. However, as such interactions are relatively poorly constrained in our simple models, further investigation is required.

Fields in the southern LMC disk also likely feel perturbative effects from multiple interactions with the SMC, with velocity dispersions in these fields approximately double those in the unperturbed north-eastern disk. Clear kinematic trends are observed moving westward around the disk, with both the in-plane radial velocity and out-of-plane vertical velocity increasing from negative to positive values, and the out-of-plane distance also increasing. The in-plane radial velocity trend is consistent with the combined effects of MW tides, which compress material in the southeast, and recent interactions with the SMC, with both the recent pericentric passage and ~400 Myr disk crossing pulling material in the southwest radially outward. However, the increasing vertical velocity and out-of-plane distance is best replicated by the model which experiences disk crossings at both ~400 and ~980 Myr. We additionally find field 17, located in the claw-like Substructure 1, has very similar kinematics to those in the nearby southern disk. This indicates it experiences similar perturbative effects as the nearby southern disk.

In contrast to the LMC disk, the significant perturbations observed in individual substructures in the LMC outskirts are not well described by our models. Fields located on the claw-like Substructure 2 are significantly perturbed in the z direction, with significantly elevated vertical velocities (and dispersions), and out-of-plane distances on the

order of ~8 kpc. Additionally, the feature appears to be counter-rotating relative to the LMC disk, with $V_\theta \sim -20$ km s^{-1}. Our models cannot reproduce these observed kinematics, nor the shape of the feature, and we speculate that additional interactions with the SMC, prior to the 1 Gyr for which our models are run, are required to produce this feature.

Finally, we discuss the "arm-like" southern substructure, which we find does not display coherent kinematic trends along its length. Fields toward the eastern end of the feature are not too significantly ($<2\sigma$) disturbed from the expected disk kinematics, with field 26 appearing almost undisturbed if not for a ~6 kpc out-of-plane distance – qualitatively replicated in each of our models. However, our models suggest these fields should be more significantly disturbed, particularly in terms of their in-plane radial velocity, than is observed. In contrast, fields further west in the substructure do display more disturbed kinematics. While these fields have negative radial and vertical velocities, qualitatively similar and in the correct direction for the feature to be a counterpart to the northern arm-like feature in Paper II, these fields are comparatively much more kinematically hot (with velocity dispersions up to ~40 km s^{-1}) than the northern arm. A qualitative match to the velocities in these fields is given by the model realisation which experiences SMC crossings of the LMC disk plane ~980 and ~400 Myr ago, though the out-of-plane distances (>10 kpc) of these fields are significantly underestimated.

In conclusion, the simple models presented here, in conjunction with our extensive observations, provide a useful first exploration of how interactions in the Magellanic system can potentially produce the perturbed structural and kinematic properties of the LMC outskirts. It is clear from our analysis that different regions and substructures in the outskirts of the Clouds are sensitive to different events in the Magellanic interaction history, such that a joint analysis of each of the observed features can be used to understand the overall interaction history of the Clouds. In particular, our observations of the substructures in the southern outskirts of the LMC, in combination with future self-gravitating models that are able to more accurately trace the dynamical influence of the SMC over longer timescales, will be critical in placing tight constraints on the early orbital history of the Magellanic Clouds, and the consequences for their star formation histories.

Chapter 6

Conclusion

> It's not the end, but the start of a new experience.
>
> Matsuoka Rin

6.1 Thesis summary

The overarching aim of this thesis has been to further the current understanding of the orbital and interaction history of the Magellanic Clouds by performing a detailed study of their stellar outskirts. A key component of this has been the Magellanic Edges Survey (MagES), described in Chapter 3: the first dedicated spectroscopic survey of substructure in the extreme peripheral regions of the Clouds. Targeting red clump and red giant branch stars – which are sufficiently bright to have precise proper motions in Gaia, and in the case of red clump stars, able to be used as standardizable candles to derive distance estimates – the survey has yielded 3D kinematics for ~8700 stars across twenty-nine 3 deg^2 fields to date, as well as spectroscopic [Fe/H] estimates for a subset of sufficiently bright stars. The complete phase-space information provided by the survey is, as demonstrated in the subsequent chapters of the thesis, critical in placing constraints on interactions between the Clouds.

Using the MagES dataset, I have analysed the structural and kinematic properties of stellar structures across the LMC outskirts. In Chapter 4, I study a long, arm-like feature to the north of the LMC. Subsequently, in Chapter 5 I explore the outer LMC disk at radii beyond 8°, as well as two claw-like features to the south of the LMC disk, and a

long arm-like feature which wraps around the south of the LMC at large galactocentric radii. A general finding for each of the studied features is that they have a relatively consistent mean metallicity at [Fe/H]~-1: matching that in the outer LMC disk. In addition, the photometric properties of the red clump (colour and colour dispersion) are equally consistent, indicating each structure is comprised of similar stellar populations – and suggestive that these features share a common origin as disturbed LMC disk material. The one exception to the above is a field in the far east of the long arm-like substructure to the south of the LMC, near to where this structure appears to connect to the SMC. This region has kinematics and metallicities ([Fe/H]~-1.4) significantly more SMC-like, and at a SMC galactocentric radius of 9.5°, represents one of the most distant detections of SMC debris to date.

I compare my observations to a new suite of simple dynamical models of the Magellanic system, which sample from uncertainties in the current systemic positions and motions of both the LMC and SMC, to investigate the recent orbital and interaction histories of the Clouds. In addition to the effect of Milky Way tides on the Clouds, several key events are identified as potentially contributing to the observed perturbations: the recent close passage of the SMC around the LMC ~150 Myr ago (already known from Zivick et al. 2018); a potential SMC crossing of the LMC disk plane ~400 Myr ago in the then-northeast; and a possible, but poorly-constrained, SMC crossing of the LMC disk plane ~900 Myr ago.

Study of the arm-like structure to the north of the LMC in Chapter 4 reveals it follows the inclination of the LMC disk plane. The arm is generally dynamically cold, with velocity dispersions similar to or less than outer-disk-like values ($\lesssim 25$ km s^{-1}), and it maintains an approximately constant azimuthal velocity similar to (if slightly lower than) the LMC disk. An increasing vertical velocity along the arm is likely the result of tides felt by the LMC during its infall to the Milky Way potential. In contrast, the most recent SMC pericentric passage ~150 Myr ago and possible disk crossing ~400 Myr ago likely do not significantly affect the arm: material closely perturbed in these encounters is today predominantly located in the south-western outskirts of the LMC, and there has not yet been sufficient time for this material to phase-mix and reach the arm in the northeast. This, in combination with the fact that none of the simple models can replicate the strongly negative (~-40 km s^{-1}) in-plane radial velocity along the arm, suggests that earlier interactions with the SMC – such as the possible disk crossing ~900 Myr ago or potentially even older interactions not yet probed – may contribute to the formation of the arm.

In contrast to the northern arm, the southern arm-like structure analysed in Chapter 5

does not display clear kinematic trends along its length. Fields toward the eastern end of the feature are not too substantially perturbed, with kinematics similar to (i.e. within 2σ of) those in the relatively undisturbed north-eastern outskirts of the LMC disk. Fields further west in the structure have vertical and in-plane radial velocities qualitatively similar in magnitude and in the correct direction to be a counterpart to the northern arm, but are kinematically much hotter (with velocity dispersions up to ~40 km s^{-1}). A qualitative match to the direction, if not magnitude, of these velocity perturbations is given by model realisations which experience a SMC crossing of the LMC disk plane ~900 Myr ago.

The claw-like Substructure 2 is also significantly perturbed from equilibrium disk kinematics, with large positive vertical velocities (and associated dispersions), and an out-of-plane distance ~8 kpc in front of the predicted LMC disk plane. Additionally, the feature appears to be counter-rotating relative to the LMC disk. None of the dynamical models studied can even qualitatively reproduce these velocities, nor the shape of the feature, leading to speculation that interactions with the SMC occurring prior to the 1 Gyr over which the models are run may be necessary to form this substructure.

The outer LMC disk, at galactocentric radii $8.5° < R < 11°$, also displays perturbations indicative of a variety of different interactions. The north-eastern outskirts of the disk are relatively unperturbed, with near-equilibrium kinematics and a geometry consistent with measurements at much smaller radii. In contrast, analysis of red clump magnitudes suggests the southern and western regions of the disk are located at substantial out-of-plane distances.

The model suites in this thesis indicate the current western outskirts of the LMC disk were most strongly perturbed in a SMC crossing of the LMC disk plane ~400 Myr ago, and the observed kinematics in this region are mostly qualitatively similar to the model predictions. The decreasing in-plane radial velocity moving northwards in this region is consistent with the combined effects of Milky Way tides acting to compress material in the northwest, and the SMC acting to pull material radially outward. Material leading the crossing point, today in the south-western LMC, is predicted to feel a net positive vertical perturbation, consistent with observations. However, material trailing the crossing point, today in the north-western LMC, is predicted to feel a net negative vertical perturbation – which is inconsistent with observations. This indicates the north-western LMC may have been further perturbed by earlier interactions with the SMC not captured in the models.

Fields in the southern LMC disk likely also feel perturbative effects from multiple interactions with the SMC. Moving westward around the disk, both the in-plane radial velocity and out-of-plane vertical velocity increase from negative to positive values. This

is best qualitatively replicated by models which include SMC crossings of the disk plane both ~900 Myr and ~400 Myr ago, in combination with the effect of Milky Way tides (which act to compress material in the southeast). The claw-like Substructure 1 has very similar kinematics to those in the nearby southern disk, indicating it has been perturbed by the same interactions.

From the specific findings outlined above, several more general conclusions about the interaction history of the Clouds can be drawn. Firstly, there is clear evidence for numerous different interactions having shaped the Magellanic system, each of which produces distinct and detectable kinematic signatures. These interactions comprise not only recent infall of the Clouds to the Milky Way potential – which, for example, strongly perturbs the LMC's northern arm – but also multiple SMC pericentric passages and crossings of the LMC disk plane, including disk-plane crossings at ~400 Myr and ~900 Myr ago, and potentially as-yet unexplored interactions prior to 1 Gyr ago. In addition to supporting the hypothesis that the recent bursty star formation history of both Clouds is linked to repeated interactions between them, these are the first direct kinematic constraints on interactions between the Clouds beyond the SMC pericentric passage around the LMC ~150 Myr ago. The model suites presented in this thesis also suggest that disk plane crossings play a particularly significant role in perturbing the LMC disk – potentially even more so than the last SMC pericentric passage, which occured at a significant out-of-plane distance, and is sufficiently recent that perturbed LMC material is still predominantly confined to the south-western disk outskirts.

I have also revealed that different regions of the Clouds are sensitive to different combinations of interactions. One resulting implication is that specific interactions can be efficiently constrained by targeted follow-up of the regions most strongly perturbed, with the dynamical models in this thesis presenting an initial roadmap for such studies. For example, as the ~400 Myr disk crossing most strongly impacts the western outskirts of the LMC disk, further study of this region will provide stronger constraints on the crossing distance of the SMC (which is currently uncertain to within ~10 kpc) – particularly as compared to e.g. analysis of the northern arm, which is not strongly perturbed in this interaction. Perhaps of most importance, however, is the consequence that in order to gain a complete understanding of the interaction history of the Clouds, it is essential to study the Magellanic system as a whole.

Finally, this thesis has confirmed that the stellar outskirts of the Clouds provide the ideal laboratory for studying the interaction history of the system, being both sensitive to a variety of different perturbations, and having sufficiently long dynamical timescales that the resulting kinematic and structural signatures persist for upwards of a Gyr. My analysis

has revealed that the outskirts of the Clouds are extremely complex, both structurally and kinematically, meaning that the use of dynamical models is essential for disentangling the intricate combination of interactions which shape the current properties of the Magellanic periphery.

6.2 Future Work

While the work in this thesis has broken new ground in understanding interactions which can potentially affect different regions of the LMC, there remains scope for significant further study. Here, I explore various possible directions for future work – both experimental and theoretical – which will enhance our knowledge of the orbital and interaction history of the Magellanic system.

6.2.1 Observations

An immediate next step is the continued analysis of MagES fields, in particular extending my analysis to include the SMC. Several MagES fields in the eastern outskirts of the SMC have already been observed (see Fig. 3.1), where the line-of-sight depth of the red clump is known to be large – and given the apparent transition from likely LMC debris to likely SMC debris near field 3 (see §5.3.2.1), study of this region has the strong potential to reveal more about interactions between the two galaxies. In addition, as MagES is ongoing, there are plans to continue observations targeting as-yet spectroscopically unstudied structures around both Clouds – such as e.g. "Northern Substructure 2", an overdensity to the north of the SMC in El Youssoufi et al. (2021). I hope to continue this work in the near future.

Looking further ahead, a key aspiration is to obtain contiguous spectroscopic data for stars across the entire Magellanic periphery. This would better align with the existing comprehensive photometric and astrometric coverage of the system, and provide a more detailed picture of spatial variations in the kinematic and/or chemical properties than is available from isolated MagES fields. Such information is, as is clear from this thesis, critical in placing very precise constraints on the interaction history and evolution of both Clouds. However, the enormous on-sky area occupied by the Clouds – and the associated time necessary for such large-scale observations – means that consortium-level surveys on

dedicated facilities are necessary to achieve this goal[39].

The need for contiguous spectroscopic data has, in fact, already been recognised, and will be met using the planned One Thousand and One Magellanic Fields (1001MC: Cioni et al. 2019) survey on the forthcoming 4-metre Multi-Object Spectroscopic Telescope (4MOST: De Jong et al. 2019) facility. In many respects, this facility is very similar to that which has been successfully been used by MagES: it is a 4m-class telescope with a 4.2 deg^2 field of view, across which 1624 fibres feed a R~6500 spectrograph which includes coverage of the MgIb and CaII triplets (with an additional ~800 fibres simultaneously feeding a R~20000 high-resolution spectrograph). This setup is sufficient to reach a signal-to-noise ratio of 20/pixel for Magellanic red clump stars in ~3 hours[40]: a close match to MagES observation times and data quality, and able to survey the large on-sky area of the Clouds in a tractable timeframe. The 1001MC survey itself, set to begin in 2023, aims to obtain spectra for ~500000 Magellanic stars with $G<19.5$ – of which ~374000 are red clump and RGB stars – across an area of ~1000 deg^2 surrounding the Clouds, including many of the observed outer substructures, as seen in Fig. 6.1. This data set will, in combination with increasingly-precise Gaia astrometry[41], provide a revolutionary dataset of full 3D kinematics across the entire Magellanic system. The resultant ability to consistently and contiguously analyse the inner and outer regions of the Clouds will be ideal for tightly constraining the interaction history of the system. In addition, it will allow for significant reductions in the observational uncertainties on the systemic properties of both Clouds, and hence narrow the allowable parameter space for their orbits: critical for subsequent modelling of the system (discussed further in the next section).

Beyond this, future southern-hemisphere 30m-class telescopes – including the European Extremely Large Telescope (E-ELT: Gilmozzi and Spyromilio 2007) and the Giant Magellan Telescope (GMT: Johns et al. 2012) – each have planned multi-object spectrograph capabilities (GMACS+MANIFEST on the GMT: DePoy et al. 2012; Lawrence et al. 2020, and the ELT-MOS: Padovani 2014) able to observe Magellanic MSTO stars in timeframes comparable to current observations of Magellanic red clump stars using

[39] A back of-the-envelope calculation for the MagES setup, which requires ~3.5 hr exposures for each field, reveals that to obtain single-visit contiguous coverage of on-sky radii within $6°<R<20°$ from the LMC and $4°<R<12°$ from the SMC – a total area of ~1300 square degrees – would take an estimated total of 220 nights. This is a strict minimum requirement for surveying the peripheral regions of the Clouds (and does not account for e.g. weather loss). To further include the central regions of the Clouds, the substantially higher target density in these regions (which significantly exceeds the ~370 fibres per field available in the MagES setup) necessitates repeat visits such that the total time required could be as much as tripled.

[40] calculated using the 4MOST ETC at https://etc.eso.org/observing/etc/fourmost.

[41] https://www.cosmos.esa.int/web/gaia/science-performance indicates an increase in proper motion precision by a factor of ~3.5 for the extended Gaia mission ("DR5") relative to current Gaia EDR3 measurements.

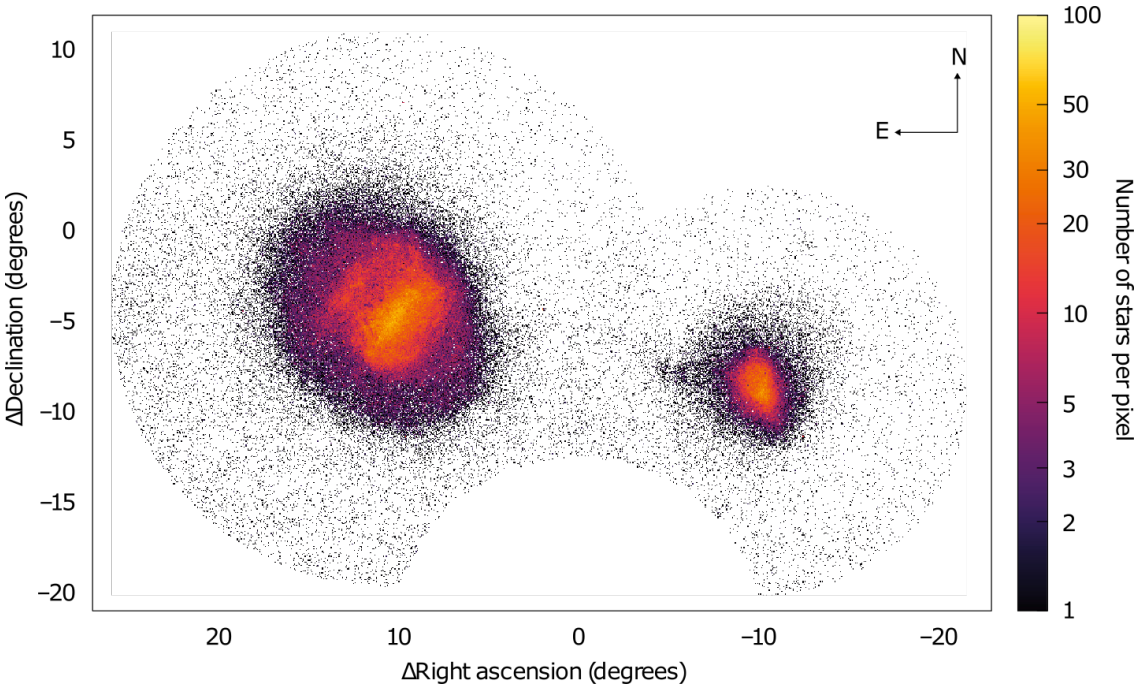

Figure 6.1: Source density distribution of 1001MC target stars, in a zenithal equidistant projection centred at $\alpha_0, \delta_0 = 50°, -67.5°$. Pixels are 0.05 square degrees. The total area is comprised of two circular selections of stars: those with galactocentric on-sky radii R<15° from the LMC COM, and R<10° from the SMC COM. This encompasses much of the extended structure of both Clouds. The circular cutout in the coverage at the bottom of the figure is the result of a declination ≥ -80 degree pointing limit. Taken from Cioni et al. (2019).

4m-class telescopes. While the (comparatively small) fields of view of these instruments make it infeasible to survey the entire Magellanic system in this way, targeted follow-up of regions of interest – including, for example, faint features discovered in forthcoming deep photometric surveys (discussed further below) – will be critical in understanding the early chemical enrichment history of the Clouds, and potentially identifying remnants of smaller systems accreted by the Clouds. Whilst Magellanic MSTO stars are inaccessible to Gaia, observations using future space telescopes – such as the Nancy Grace Roman Telescope (Spergel et al. 2015)[42] – will, in combination with existing HST photometry, have sufficiently long baselines to provide proper motions for these stars, at least for selected fields (The WFIRST Astrometry Working Group et al. 2019).

In addition to kinematic and abundance data provided by spectroscopy, another avenue of investigation useful in understanding the evolution of the Clouds is their star-formation histories. In particular, the development of SFHs with high spatial and temporal resolution can provide synergistic constraints on interactions and their effects on the Magellanic system. There has been significant recent progress in this area, with the use of large

[42] formerly known as the Wide-Field Infrared Space Telescope (WFIRST).

photometric surveys such as VMC and SMASH to derive spatially-resolved SFHs for the LMC body (e.g. Mazzi et al. 2021; Ruiz-Lara et al. 2020). However, further work is needed to 1) understand the links between specific star formation events and dynamical interactions, with the gas-rich inner regions of the Clouds critical targets in constraining bursts linked to recent interactions, and 2) derive SFHs for the outskirts of both galaxies, as well as the inter-Cloud region – the ancient populations of which may help to constrain earlier SF variations, and thus corresponding interactions. Both of these objectives will be advanced by the currently-ongoing DECam Local Volume Exploration survey (DELVE: Drlica-Wagner et al. 2021), which will provide contiguous deep ($g,r,i \geq$ 24.5 mag) optical photometry across an area of ~2200 deg^2, extending to galactocentric on-sky radii of 25° from the LMC COM and 15° from the SMC COM: a larger and more homogeneous dataset than existing photometric surveys. In addition, in the near future the Vera Rubin Observatory (Ivezić et al. 2019)[43] will begin a planned ten-year, six-band *(ugrizy)* photometric survey of the entire southern sky, reaching a coadded depth of 27.5 in the r-band: well below the main sequence turnoff in the Clouds. This dataset will be not only be ideal for the derivation of detailed SFHs as indicated above, but also open the possibility of discovering more faint substructure or Magellanic satellites – each key in adding to our understanding the evolution of the Magellanic system.

6.2.2 Simulations

It is clear from this thesis that significant further work is required in terms of simulations of the Magellanic system. As demonstrated in Chapters 4 and 5, the likely contribution of multiple interaction events to the present structure and kinematics of the Clouds means comparison to dynamical models is necessary to isolate these effects. Given the forthcoming large influx of observational data, as discussed in the preceding subsection, detailed simulation suites are critical in order to fully exploit these data to precisely constrain the orbital and interaction history of the Clouds. However – as evidenced by the relatively few such existing models (e.g. Besla et al. 2010, 2012) – it is computationally expensive to run high-resolution[44] N-body simulations (as would be required) for many Gyr. As such, preliminary work to narrow the allowable parameter space for those models must first be performed.

The new suite of simple dynamical models introduced in this thesis has made some progress in this area, and an immediate next step is to characterise how the varying orbits

[43] formerly known as the Large Synoptic Survey Telescope (LSST).

[44] with comparable simulations to those which would be required utilising total particle numbers of $\sim 2-4\times10^6$ for the two Clouds (Besla et al. 2012; Pardy et al. 2016), and a similar number necessary to model the MW dark halo (Gómez et al. 2015).

in these models depend on the complex observational parameter space of the Clouds. In this case, there are four parameters for each of the two Clouds which are sampled from observational uncertainties – that is, their LOS distance and 3D systemic motion. However, to fully describe this space, an additional two parameters per galaxy (i.e. the on-sky COM position) must be characterised, resulting in a complex 12-dimensional parameter space[45]. By isolating regions of this parameter space which, for example, correspond to scenarios where the SMC has experienced more than one crossing of the LMC disk plane (as likely seems necessary to produce the perturbed features in the southern outskirts of the LMC and the correlated SFHs of the Clouds), these regions can be targeted when running more complex models in the future. Similar work to characterise how these regions do or do not shift when e.g. the LMC and SMC masses are varied within their observational uncertainties is also necessary to further constrain the allowable parameter space.

An example of this is given in Fig. 6.2, which presents several cross-sections of the parameter space varied in the current base-case model suite (i.e. with an LMC mass of 1.5×10^{11} $M_\odot$ and an SMC mass of 2.5×10^9 $M_\odot$), colour coded by orbital parameters including the time and distance of the most recent SMC pericentric passage and crossing of the LMC disk plane. In the top row of this figure, which shows the time since the last SMC crossing of the LMC disk plane (excluding that which is happening approximately now), there is a clear distinction between models in which the SMC has or has not crossed the LMC disk plane ~400 Myr ago. Since this crossing is thought to contribute to the observed perturbation of the western LMC disk (see Chapters 4 and 5), future models could preferentially focus on exploring this region of parameter space.

Once regions of interest in parameter space are identified, further N-body simulations of the Clouds should be performed. As discussed in §4.5.3.1 of this thesis, self-gravitating models are required to capture the deformation of gravitational potentials in response to interactions, which can affect both the global orbits of the Clouds, as well as the specific response of stars within them to each interaction. This is particularly critical in the case of repeated close interactions between the LMC and SMC, which may introduce significant and potentially long-lasting perturbations (such as the formation of the LMC's off-centre bar, or density waves in the LMC disk: e.g. Berentzen et al. 2003; Besla et al. 2012; Yozin and Bekki 2014), the effects of which will compound over time with repeated interactions. These are not captured in the comparatively simple models in this thesis. The goal of targeted N-body models would be to quantitatively, not just qualitatively, match observations of the Clouds, and thus allow for much more precise constraints on the interaction

[45] not including the masses of the LMC, SMC, and Milky Way, each of which also affects the orbits of the Clouds.

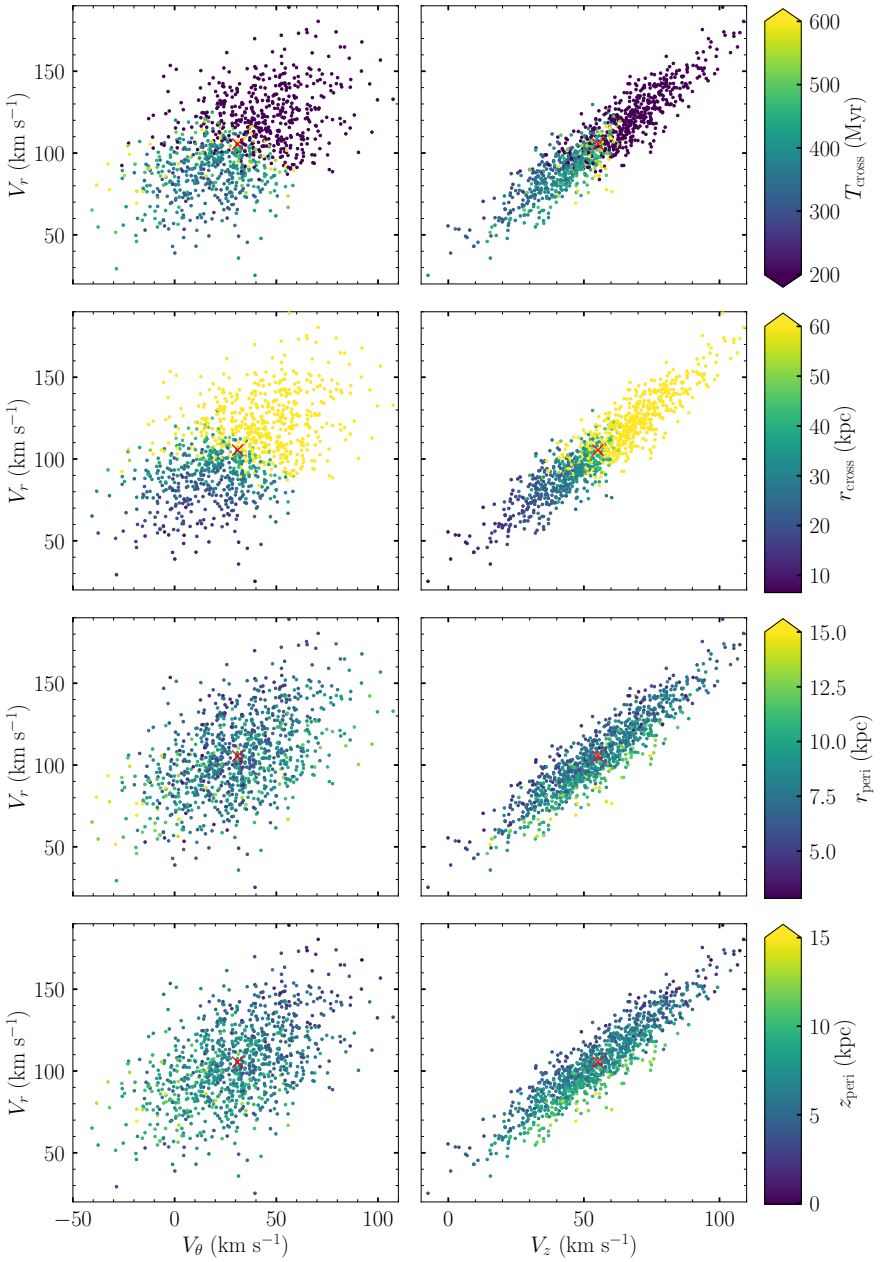

Figure 6.2: Distribution of (left) azimuthal vs. radial velocities and (right) vertical vs. radial velocities of the SMC COM relative to the LMC COM, calculated from sampling the distributions of the observed systemic motions and distances of the LMC and SMC in the "base-case" model suite described in §4.5.3. Panels are colour-coded by, in order from top to bottom: (1) time since the last SMC crossing of the LMC disk plane, excluding the currently-occuring crossing (with models experiencing only the current crossing fixed to a time of zero, and appearing as dark purple points); (2) distance of the SMC COM from the LMC COM at the time of the aforementioned crossing (with models experiencing only the current crossing fixed to a distance of 60 kpc, appearing as yellow points); (3) total distance between the SMC COM and LMC COM during the most recent SMC pericentric passage; and (4) out-of-plane distance of the SMC COM from the LMC disk plane during the most recent SMC pericentric passage. Red crosses mark the locations corresponding to the current best estimates of the systemic location and motions of the Clouds.

history of the system. This includes providing closer constraints on comparatively old interactions (i.e. occurring $\gtrsim 1$ Gyr ago) which are thought to be important in the formation of substructures such as the arm-like features to the north and south of the LMC (see Chapters 4 and 5), but are currently only very weakly constrained. Ultimately, models should be extended to include hydrodynamics such that they can fully and self-consistently replicate both the stellar and gaseous features of the Clouds – the structure and dynamics of which are quite different, thus providing complementary constraints on the orbital and interaction history of the Magellanic system. While such models are ambitious, they are not unachievable, with similar models to those which would be required (e.g. Besla et al. 2012; Pardy et al. 2016) capable of being run on-high-performance computing clusters.

6.3 Final Remarks

In this thesis, I have used the Magellanic Edges Survey – the first dedicated spectroscopic survey of the outskirts of the Large and Small Magellanic Clouds – to perform a detailed study of the structural and kinematic properties of many stellar substructures in the Magellanic periphery. In combination with a suite of new dynamical models, I have made significant progress in linking the observed perturbations to potential interactions in the system, finding in particular that many features are likely shaped by multiple interactions between the LMC and SMC. This has provided the first kinematic constraints on interactions between the Clouds beyond the most recent SMC pericentric passage around the LMC – specifically, probable SMC crossings of the LMC disk plane ~400 Myr and ~900 Myr ago – and demonstrates the importance of full 3D kinematics in placing constraints on dynamical models to understand the orbits of the Clouds and the origin of substructure within them. With further large surveys of the Magellanic system forthcoming, in addition to the promise of detailed dynamical models, we are closer than ever before to unravelling the complex interactions which have shaped the Clouds – a truly exciting time in the history of Magellanic research.

References

AAO Software Team, 2015. *2dfdr: Data Reduction Software (Ascl:1505.015)*.

Abbott, T. M. C.; Abdalla, F. B.; Allam, S.; Amara, A.; Annis, J.; et al., 2018. *The Dark Energy Survey: Data Release 1*. ApJS, 239(2), 18. doi:10.3847/1538-4365/aae9f0.

Alcock, C.; Allsman, R. A.; Alves, D. R.; Axelrod, T. S.; Becker, A. C.; et al., 2000. *The MACHO Project: Microlensing Results from 5.7 Years of Large Magellanic Cloud Observations*. ApJ, 542(1), 281. doi:10.1086/309512.

Alves, D. R. and Nelson, C. A., 2000. *The Rotation Curve of the Large Magellanic Cloud and the Implications for Microlensing*. ApJ, 542(2), 789. doi:10.1086/317023.

Arenou, F.; Luri, X.; Babusiaux, C.; Fabricius, C.; Helmi, A.; et al., 2018. *Gaia Data Release 2: Catalogue Validation*. A&A, 616, A17. doi:10.1051/0004-6361/201833234.

Armandroff, T. E. and Da Costa, G. S., 1991. *Metallicities for Old Stellar Systems from CA II Triplet Strengths in Member Giants*. AJ, 101(4), 1329. doi:10.1086/115769.

Balbinot, E.; Santiago, B. X.; Girardi, L.; Pieres, A.; da Costa, L. N.; et al., 2015. *The LMC Geometry and Outer Stellar Populations from Early DES Data*. MNRAS, 449(1), 1129. doi:10.1093/mnras/stv356.

Battaglia, G.; Taibi, S.; Thomas, G. F.; and Fritz, T. K., 2021. *Gaia Early DR3 Systemic Motions of Local Group Dwarf Galaxies and Orbital Properties with a Massive Large Magellanic Cloud*. arXiv:2106.08819 [astro-ph], 2106.08819.

Bechtol, K.; Drlica-Wagner, A.; Balbinot, E.; Pieres, A.; Simon, J. D.; et al., 2015. *Eight New Milky Way Companions Discovered In First-Year Dark Energy Survey Data*. ApJ, 807(1), 50. doi:10.1088/0004-637X/807/1/50.

Bekki, K., 2009. *Formation of the Off-Center Bar in the Large Magellanic Cloud: A Collision with a Dark Satellite?* MNRAS, 393(1), L60. doi:10.1111/j.1745-3933.2008.00600.x.

Bekki, K. and Chiba, M., 2005. *Formation and Evolution of the Magellanic Clouds - I. Origin of Structural, Kinematic and Chemical Properties of the Large Magellanic Cloud*. MNRAS, 356(2), 680. doi:10.1111/j.1365-2966.2004.08510.x.

Bekki, K. and Chiba, M., 2007. *Dynamical Influences of the Last Magellanic Interaction on the Magellanic Clouds*. PASA, 24(1), 21. doi:10.1071/AS06023.

Bell, C. P. M.; Cioni, M.-R. L.; Wright, A. H.; Rubele, S.; Nidever, D. L.; et al., 2019. *The Intrinsic Reddening of the Magellanic Clouds as Traced by Background Galaxies – I. The Bar and Outskirts of the Small Magellanic Cloud*. MNRAS, 489(3), 3200. doi:10.1093/mnras/stz2325.

Bell, C. P. M.; Cioni, M.-R. L.; Wright, A. H.; Rubele, S.; Nidever, D. L.; et al., 2020. *The Intrinsic Reddening of the Magellanic Clouds as Traced by Background Galaxies – II. The Small Magellanic Cloud*. MNRAS, 499(1), 993. doi:10.1093/mnras/staa2786.

Belokurov, V.; Deason, A. J.; Erkal, D.; Koposov, S. E.; Carballo-Bello, J. A.; et al., 2019. *The Pisces Plume and the Magellanic Wake*. MNRAS, 488(1), L47. doi:10.1093/mnrasl/slz101.

Belokurov, V. and Erkal, D., 2019. *Clouds in Arms*. MNRAS, 482(1), L9. doi:10.1093/mnrasl/sly178.

Belokurov, V.; Erkal, D.; Deason, A. J.; Koposov, S. E.; De Angeli, F.; et al., 2017. *Clouds, Streams and Bridges. Redrawing the Blueprint of the Magellanic System with Gaia DR1*. MNRAS, 466(4), 4711. doi:10.1093/mnras/stw3357.

Belokurov, V. and Koposov, S. E., 2016. *Stellar Streams around the Magellanic Clouds*. MNRAS, 456(1), 602. doi:10.1093/mnras/stv2688.

Berentzen, I.; Athanassoula, E.; Heller, C. H.; and Fricke, K. J., 2003. *Numerical Simulations of Interacting Gas-Rich Barred Galaxies: Vertical Impact of Small Companions*. MNRAS, 341(1), 343. doi:10.1046/j.1365-8711.2003.06417.x.

Bertelli, G.; Mateo, M.; Chiosi, C.; and Bressan, A., 1992. *The Star Formation History of the Large Magellanic Cloud*. ApJ, 388, 400. doi:10.1086/171163.

Besla, G.; Kallivayalil, N.; Hernquist, L.; Robertson, B.; Cox, T. J.; et al., 2007. *Are the Magellanic Clouds on Their First Passage about the Milky Way?* ApJ, 668(2), 949. doi:10.1086/521385.

Besla, G.; Kallivayalil, N.; Hernquist, L.; van der Marel, R. P.; Cox, T. J.; et al., 2010. *Simulations of the Magellanic Stream in a First Infall Scenario*. ApJ, 721(2), L97. doi:10.1088/2041-8205/721/2/L97.

Besla, G.; Kallivayalil, N.; Hernquist, L.; van der Marel, R. P.; Cox, T. J.; et al., 2012. *The Role of Dwarf Galaxy Interactions in Shaping the Magellanic System and Implications for Magellanic Irregulars: The Magellanic System*. MNRAS, 421(3), 2109. doi:10.1111/j.1365-2966.2012.20466.x.

Besla, G.; Martínez-Delgado, D.; van der Marel, R. P.; Beletsky, Y.; Seibert, M.; et al., 2016. *Low Surface Brightness Imaging of the Magellanic System: Imprints of Tidal Interactions Between the Clouds in the Stellar Periphery*. ApJ, 825(1), 20. doi:10.3847/0004-637X/825/1/20.

Binney, J. and Tremaine, S., 2008. *Galactic Dynamics*. 2nd ed., Princeton University Press, Princeton, NJ.

Bland-Hawthorn, J. and Gerhard, O., 2016. *The Galaxy in Context: Structural, Kinematic, and Integrated Properties*. ARA&A, 54(1), 529. doi:10.1146/annurev-astro-081915-023441.

Borissova, J.; Minniti, D.; Rejkuba, M.; Alves, D.; Cook, K. H.; et al., 2004. *Properties of RR Lyrae Stars in the Inner Regions of the Large Magellanic Cloud*. A&A, 423(1), 97. doi:10.1051/0004-6361:20034494.

Bovy, J., 2015. *Galpy: A Python Library for Galactic Dynamics*. ApJS, 216(2), 29. doi:10.1088/0067-0049/216/2/29.

Bovy, J.; Allende Prieto, C.; Beers, T. C.; Bizyaev, D.; da Costa, L. N.; et al., 2012. *The Milky Way's Circular-Velocity Curve Between 4 and 14 Kpc from APOGEE Data*. ApJ, 759(2), 131. doi:10.1088/0004-637X/759/2/131.

Boylan-Kolchin, M.; Besla, G.; and Hernquist, L., 2011. *Dynamics of the Magellanic Clouds in a Lambda Cold Dark Matter Universe: Magellanic Clouds in a ΛCDM Universe*. MNRAS, 414(2), 1560. doi:10.1111/j.1365-2966.2011.18495.x.

Bressan, A.; Marigo, P.; Girardi, L.; Salasnich, B.; Dal Cero, C.; et al., 2012. *PARSEC: Stellar Tracks and Isochrones with the PAdova and TRieste Stellar Evolution Code*. MNRAS, 427(1), 127. doi:10.1111/j.1365-2966.2012.21948.x.

Brüns, C.; Kerp, J.; Staveley-Smith, L.; Mebold, U.; Putman, M. E.; et al., 2005. *The Parkes H I Survey of the Magellanic System*. A&A, 432(1), 45. doi:10.1051/0004-6361:20040321.

Butcher, H., 1977. *A Main-Sequence Luminosity Function for the Large Magellanic Cloud*. ApJ, 216, 372. doi:10.1086/155477.

Caldwell, J. A. R. and Coulson, I. M., 1986. *The Geometry and Distance of the Magellanic Clouds from Cepheid Variables*. MNRAS, 218(2), 223. doi:10.1093/mnras/218.2.223.

Carrera, R.; Conn, B. C.; Noël, N. E. D.; Read, J. I.; and López Sánchez, Á. R., 2017. *The Magellanic Inter-Cloud Project (MAGIC) III: First Spectroscopic Evidence of a Dwarf Stripping a Dwarf*. MNRAS, 471(4), 4571. doi:10.1093/mnras/stx1932.

Carrera, R.; Gallart, C.; Aparicio, A.; Costa, E.; Méndez, R. A.; et al., 2008a. *The Chemical Enrichment History of the Small Magellanic Cloud and Its Gradients*. AJ, 136(3), 1039. doi:10.1088/0004-6256/136/3/1039.

Carrera, R.; Gallart, C.; Aparicio, A.; and Hardy, E., 2011. *Metallicities, Age-Metallicity Relationships, and Kinematics of Red Giant Branch Stars in the Outer Disk of the Large Magellanic Cloud*. AJ, 142(2), 61. doi:10.1088/0004-6256/142/2/61.

Carrera, R.; Gallart, C.; Hardy, E.; Aparicio, A.; and Zinn, R., 2008b. *The Chemical Enrichment History of the Large Magellanic Cloud*. AJ, 135(3), 836. doi:10.1088/0004-6256/135/3/836.

Casagrande, L. and VandenBerg, D. A., 2018. *On the Use of Gaia Magnitudes and New Tables of Bolometric Corrections*. MNRAS, 479(1), L102. doi:10.1093/mnrasl/sly104.

Casetti-Dinescu, D. I.; Vieira, K.; Girard, T. M.; and van Altena, W. F., 2012. *Constraints on the Magellanic Clouds' Interaction from the Distribution of OB Stars and the Kinematics of Giants*. ApJ, 753(2), 123. doi:10.1088/0004-637X/753/2/123.

Cautun, M.; Deason, A. J.; Frenk, C. S.; and McAlpine, S., 2019. *The Aftermath of the Great Collision between Our Galaxy and the Large Magellanic Cloud*. MNRAS, 483(2), 2185. doi:10.1093/mnras/sty3084.

Cerny, W.; Pace, A. B.; Drlica-Wagner, A.; Ferguson, P. S.; Mau, S.; et al., 2021. *Discovery of an Ultra-Faint Stellar System near the Magellanic Clouds with the DECam Local Volume Exploration Survey*. ApJ, 910(1), 18. doi:10.3847/1538-4357/abe1af.

Choi, Y.; Nidever, D. L.; Olsen, K.; Besla, G.; Blum, R. D.; et al., 2018a. *SMASHing the LMC: Mapping a Ring-like Stellar Overdensity in the LMC Disk*. ApJ, 869(2), 125. doi:10.3847/1538-4357/aaed1f.

Choi, Y.; Nidever, D. L.; Olsen, K.; Blum, R. D.; Besla, G.; et al., 2018b. *SMASHing the LMC: A Tidally Induced Warp in the Outer LMC and a Large-Scale Reddening Map*. ApJ, 866(2), 90. doi:10.3847/1538-4357/aae083.

Chomiuk, L. and Povich, M. S., 2011. *Toward a Unification of Star Formation Rate Determinations in the Milky Way and Other Galaxies*. AJ, 142(6), 197. doi:10.1088/0004-6256/142/6/197.

Choudhury, S.; de Grijs, R.; Rubele, S.; Bekki, K.; Cioni, M.-R. L.; et al., 2020. *The VMC Survey – XXXIX. Mapping Metallicity Trends in the Small Magellanic Cloud Using near-Infrared Passbands*. MNRAS, 497(3), 3746. doi:10.1093/mnras/staa2140.

Choudhury, S.; Subramaniam, A.; Cole, A. A.; and Sohn, Y.-J., 2018. *Photometric Metallicity Map of the Small Magellanic Cloud*. MNRAS, 475(4), 4279. doi:10.1093/mnras/sty087.

Cignoni, M.; Cole, A. A.; Tosi, M.; Gallagher, J. S.; Sabbi, E.; et al., 2012. *Star Formation History in Two Fields of the Small Magellanic Cloud Bar*. ApJ, 754(2), 130. doi:10.1088/0004-637X/754/2/130.

Cioni, M.-R.; Clementini, G.; Girardi, L.; Guandalini, R.; Gullieuszik, M.; et al., 2011. *The VMC Survey: I. Strategy and First Data*. A&A, 527, A116. doi:10.1051/0004-6361/201016137.

Cioni, M.-R.; Storm, J.; Bell, C. P. M.; Lemasle, B.; Niederhofer, F.; et al., 2019. *4MOST Consortium Survey 9: One Thousand and One Magellanic Fields (1001MC)*. The Messenger, 175, 54. doi:10.18727/0722-6691/5128.

Cioni, M.-R. L., 2009. *The Metallicity Gradient as a Tracer of History and Structure: The Magellanic Clouds and M33 Galaxies*. A&A, 506(3), 1137. doi:10.1051/0004-6361/200912138.

Cole, A. A.; Tolstoy, E.; Gallagher III, J. S.; and Smecker-Hane, T. A., 2005. *Spectroscopy of Red Giants in the Large Magellanic Cloud Bar: Abundances, Kinematics, and the Age-Metallicity Relation*. AJ, 129(3), 1465. doi:10.1086/428007.

Collins, M. L. M.; Chapman, S. C.; Rich, R. M.; Ibata, R. A.; Martin, N. F.; et al., 2013. *A Kinematic Study of the Andromeda Dwarf Spheroidal System*. ApJ, 768(2), 172. doi:10.1088/0004-637X/768/2/172.

Conroy, C.; Naidu, R. P.; Garavito-Camargo, N.; Besla, G.; Zaritsky, D.; et al., 2021. *All-Sky Dynamical Response of the Galactic Halo to the Large Magellanic Cloud*. Nature, 592(7855), 534. doi:10.1038/s41586-021-03385-7.

Crowl, H. H.; Sarajedini, A.; Piatti, A. E.; Geisler, D.; Bica, E.; et al., 2001. *The Line-of-Sight Depth of Populous Clusters in the Small Magellanic Cloud*. AJ, 122(1), 220. doi:10.1086/321128.

Cullinane, L. R.; Mackey, A. D.; Da Costa, G. S.; Erkal, D.; Koposov, S. E.; et al., 2021. *The Magellanic Edges Survey II. Formation of the LMC's Northern Arm*. arXiv:2106.03274 [astro-ph], 2106.03274.

Cullinane, L. R.; Mackey, A. D.; Da Costa, G. S.; Koposov, S. E.; Belokurov, V.; et al., 2020. *The Magellanic Edges Survey I: Description and First Results*. MNRAS, 497(3), 3055. doi:10.1093/mnras/staa2048.

Cunningham, E. C.; Garavito-Camargo, N.; Deason, A. J.; Johnston, K. V.; Erkal, D.; et al., 2020. *Quantifying the Stellar Halo's Response to the LMC's Infall with Spherical Harmonics*. ApJ, 898(1), 4. doi:10.3847/1538-4357/ab9b88.

Da Costa, G. S., 1991. *The Age-Abundance Relations and Age Distributions for the Star Clusters of the Magellanic Clouds*. In Haynes, R. and Milne, D. (Eds.), *The Magellanic Clouds: Proceedings of the 148th Symposium of the International Astronomical Union*, vol. 148, 193, Kluwer Academic Publishers, Dordrecht.

Da Costa, G. S., 2016. *The Ca Ii Triplet in Red Giant Spectra: [Fe/H] Determinations and the Role of [Ca/Fe]*. MNRAS, 455(1), 199. doi:10.1093/mnras/stv2315.

Da Costa, G. S. and Coleman, M. G., 2008. *A Spectroscopic Survey for ω Centauri Members at and beyond the Cluster Tidal Radius*. AJ, 136(1), 506. doi:10.1088/0004-6256/136/1/506.

De Jong, R. S.; Agertz, O.; Berbel, A. A.; Aird, J.; Alexander, D. A.; et al., 2019. *4MOST: Project Overview and Information for the First Call for Proposals*. The Messenger, 175, 3. doi:10.18727/0722-6691/5117.

De Leo, M.; Carrera, R.; Noël, N. E. D.; Read, J. I.; Erkal, D.; et al., 2020. *Revealing the Tidal Scars of the Small Magellanic Cloud*. MNRAS, 495(1), 98. doi:10.1093/mnras/staa1122.

de Vaucouleurs, G., 1957. *Studies of the Magellanic Clouds. III. Surface Brightness, Colors and Integrated Magnitudes of the Clouds.* AJ, 62, 69. doi:10.1086/107459.

de Vaucouleurs, G.; de Vaucouleurs, A.; Corwin, Jr., H. G.; Buta, R. J.; Pautrel, G.; et al., 1991. *Third Reference Catalogue of Bright Galaxies.* Springer, New York, NY.

de Vaucouleurs, G. and Freeman, K., 1972. *Structure and Dynamics of Barred Spiral Galaxies, in Particular of the Magellanic Type.* Vistas in Astronomy, 14, 163. doi:10.1016/0083-6656(72)90026-8.

Deason, A. J.; Belokurov, V.; Erkal, D.; Koposov, S. E.; and Mackey, D., 2017. *The Clouds Are Breaking: Tracing the Magellanic System with Gaia DR1 Mira Variables.* MNRAS, 467(3), 2636. doi:10.1093/mnras/stx263.

DePoy, D. L.; Allen, R.; Barkhouser, R.; Boster, E.; Carona, D.; et al., 2012. *GMACS: A Wide Field, Multi-Object, Moderate-Resolution, Optical Spectrograph for the Giant Magellan Telescope.* In McLean, I. S.; Ramsay, S. K.; and Takami, H. (Eds.), *Society of Photo-Optical Instrumentation Engineers (SPIE) Conference Series*, 84461N, Amsterdam, Netherlands. doi:10.1117/12.926186.

Di Teodoro, E. M.; McClure-Griffiths, N. M.; Jameson, K. E.; Dénes, H.; Dickey, J. M.; et al., 2019. *On the Dynamics of the Small Magellanic Cloud through High-Resolution ASKAP H* i *Observations.* MNRAS, 483(1), 392. doi:10.1093/mnras/sty3095.

Dias, B.; Angelo, M. S.; Oliveira, R. A. P.; Maia, F.; Parisi, M. C.; et al., 2021. *The VISCACHA Survey: III. Star Clusters Counterpart of the Magellanic Bridge and Counter-Bridge in 8D.* A&A, 647, L9. doi:10.1051/0004-6361/202040015.

Dias, B.; Kerber, L.; Barbuy, B.; Bica, E.; and Ortolani, S., 2016. *SMC West Halo: A Slice of the Galaxy That Is Being Tidally Stripped?: Star Clusters Trace Age and Metallicity Gradients.* A&A, 591, A11. doi:10.1051/0004-6361/201527558.

Diaz, J. and Bekki, K., 2011. *Constraining the Orbital History of the Magellanic Clouds: A New Bound Scenario Suggested by the Tidal Origin of the Magellanic Stream: Tidal Origin of the Magellanic Stream.* MNRAS, 413(3), 2015. doi:10.1111/j.1365-2966.2011.18289.x.

Diaz, J. D. and Bekki, K., 2012. *The Tidal Origin of the Magellanic Stream and the Possibility of a Stellar Counterpart.* ApJ, 750(1), 36. doi:10.1088/0004-637X/750/1/36.

Dobbie, P. D.; Cole, A. A.; Subramaniam, A.; and Keller, S., 2014a. *Red Giants in the Small Magellanic Cloud – I. Disc and Tidal Stream Kinematics*. MNRAS, 442(2), 1663. doi:10.1093/mnras/stu910.

Dobbie, P. D.; Cole, A. A.; Subramaniam, A.; and Keller, S., 2014b. *Red Giants in the Small Magellanic Cloud – II. Metallicity Gradient and Age–Metallicity Relation*. MNRAS, 442(2), 1680. doi:10.1093/mnras/stu926.

D'Onghia, E. and Fox, A. J., 2016. *The Magellanic Stream: Circumnavigating the Galaxy*. ARA&A, 54(1), 363. doi:10.1146/annurev-astro-081915-023251.

D'Onghia, E. and Lake, G., 2008. *Small Dwarf Galaxies within Larger Dwarfs: Why Some Are Luminous While Most Go Dark*. ApJ, 686(2), L61. doi:10.1086/592995.

Drake, A. J.; Cook, K. H.; Alcock, C.; Axelrod, T. S.; and Geha, M., 2001. *A Determination of the Proper Motion of the LMC with MACHO Project Data*. Bulletin of the American Astronomical Society, 33, 1379.

Drlica-Wagner, A.; Bechtol, K.; Allam, S.; Tucker, D. L.; Gruendl, R. A.; et al., 2016. *An Ultra-Faint Galaxy Candidate Discovered in Early Data from The Magellanic Satellites Survey*. ApJ, 833(1), L5. doi:10.3847/2041-8205/833/1/L5.

Drlica-Wagner, A.; Carlin, J. L.; Nidever, D. L.; Ferguson, P. S.; Kuropatkin, N.; et al., 2021. *The DECam Local Volume Exploration Survey: Overview and First Data Release*. ApJS, 256(1), 2. doi:10.3847/1538-4365/ac079d.

Dunlop, J. S., 1828. *A Catalogue of Nebulae and Clusters of Stars in the Southern Hemisphere, Observed at Paramatta in New South Wales*. Philosophical Transactions of the Royal Society of London, 118, 113.

El Youssoufi, D.; Cioni, M.-R. L.; Bell, C. P. M.; de Grijs, R.; Groenewegen, M. A. T.; et al., 2021. *Stellar Substructures in the Periphery of the Magellanic Clouds with the VISTA Hemisphere Survey from the Red Clump and Other Tracers*. MNRAS, 505(2), 2020. doi:10.1093/mnras/stab1075.

El Youssoufi, D.; Cioni, M.-R. L.; Bell, C. P. M.; Rubele, S.; Bekki, K.; et al., 2019. *The VMC Survey – XXXIV. Morphology of Stellar Populations in the Magellanic Clouds*. MNRAS, 490(1), 1076. doi:10.1093/mnras/stz2400.

Epchtein, N.; de Batz, B.; Capoani, L.; Chevallier, L.; Copet, E.; et al., 1997. *The Deep Near-Infrared Southern Sky Survey (DENIS)*. The Messenger, 87, 27.

Erkal, D.; Belokurov, V.; Laporte, C. F. P.; Koposov, S. E.; Li, T. S.; et al., 2019. *The Total Mass of the Large Magellanic Cloud from Its Perturbation on the Orphan Stream*. MNRAS, 487(2), 2685. doi:10.1093/mnras/stz1371.

Erkal, D. and Belokurov, V. A., 2020. *Limit on the LMC Mass from a Census of Its Satellites*. MNRAS, 495(3), 2554. doi:10.1093/mnras/staa1238.

Erkal, D.; Belokurov, V. A.; and Parkin, D. L., 2020. *Equilibrium Models of the Milky Way Mass Are Biased High by the LMC*. MNRAS, 498(4), 5574. doi:10.1093/mnras/staa2840.

Erkal, D.; Deason, A. J.; Belokurov, V.; Xue, X.-X.; Koposov, S. E.; et al., 2021. *Detection of the LMC-Induced Sloshing of the Galactic Halo*. MNRAS, 506(2), 2677. doi:10.1093/mnras/stab1828.

Erkal, D.; Li, T. S.; Koposov, S. E.; Belokurov, V.; Balbinot, E.; et al., 2018. *Modelling the Tucana III Stream - a Close Passage with the LMC*. MNRAS, 481(3), 3148. doi:10.1093/mnras/sty2518.

Evans, C. J. and Howarth, I. D., 2008. *Kinematics of Massive Stars in the Small Magellanic Cloud*. MNRAS, 386(2), 826. doi:10.1111/j.1365-2966.2008.13012.x.

Evans, C. J.; van Loon, J. T.; Hainich, R.; and Bailey, M., 2015. *2dF-AAOmega Spectroscopy of Massive Stars in the Magellanic Clouds: The North-Eastern Region of the Large Magellanic Cloud*. A&A, 584, A5. doi:10.1051/0004-6361/201525882.

Evans, D. W.; Riello, M.; De Angeli, F.; Carrasco, J. M.; Montegriffo, P.; et al., 2018. *Gaia Data Release 2: Photometric Content and Validation*. A&A, 616, A4. doi:10.1051/0004-6361/201832756.

Fabricius, C.; Luri, X.; Arenou, F.; Babusiaux, C.; Helmi, A.; et al., 2021. *Gaia Early Data Release 3: Catalogue Validation*. A&A, 649, A5. doi:10.1051/0004-6361/202039834.

Feast, M. W., 1968. *The Kinematics of Planetary Nebulae in the Magellanic Clouds*. MNRAS, 140(3), 345. doi:10.1093/mnras/140.3.345.

Feitzinger, J. V., 1980. *Galaxien Vom Magellanschen Typ*. Space Science Reviews, 27(1), 35. doi:10.1007/BF00168044.

Flaugher, B.; Diehl, H. T.; Honscheid, K.; Abbott, T. M. C.; Alvarez, O.; et al., 2015. *The Dark Energy Camera*. AJ, 150(5), 150. doi:10.1088/0004-6256/150/5/150.

Foreman-Mackey, D.; Hogg, D. W.; Lang, D.; and Goodman, J., 2013. *Emcee: The MCMC Hammer*. PASP, 125(925), 306. doi:10.1086/670067.

Fox, A. J.; Wakker, B. P.; Barger, K. A.; Hernandez, A. K.; Richter, P.; et al., 2014. *The COS/UVES Absorption Survey of the Magellanic Stream. III. Ionization, Total Mass, and Inflow Rate onto the Milky Way*. ApJ, 787(2), 147. doi:10.1088/0004-637X/787/2/147.

Freedman, W. L.; Madore, B. F.; Gibson, B. K.; Ferrarese, L.; Kelson, D. D.; et al., 2001. *Final Results from the Hubble Space Telescope Key Project to Measure the Hubble Constant*. ApJ, 553(1), 47. doi:10.1086/320638.

Gaia Collaboration; Antoja, T.; McMillan, P. J.; Kordopatis, G.; Ramos, P.; et al., 2021a. *Gaia Early Data Release 3: The Galactic Anticentre*. A&A, 649, A8. doi:10.1051/0004-6361/202039714.

Gaia Collaboration; Babusiaux, C.; van Leeuwen, F.; Barstow, M. A.; Jordi, C.; et al., 2018a. *Gaia Data Release 2: Observational Hertzsprung-Russell Diagrams*. A&A, 616, A10. doi:10.1051/0004-6361/201832843.

Gaia Collaboration; Brown, A. G. A.; Vallenari, A.; Prusti, T.; de Bruijne, J. H. J.; et al., 2018b. *Gaia Data Release 2: Summary of the Contents and Survey Properties*. A&A, 616, A1. doi:10.1051/0004-6361/201833051.

Gaia Collaboration; Brown, A. G. A.; Vallenari, A.; Prusti, T.; de Bruijne, J. H. J.; et al., 2021b. *Gaia Early Data Release 3: Summary of the Contents and Survey Properties*. A&A, 649, A1. doi:10.1051/0004-6361/202039657.

Gaia Collaboration; Helmi, A.; van Leeuwen, F.; McMillan, P. J.; Massari, D.; et al., 2018c. *Gaia Data Release 2: Kinematics of Globular Clusters and Dwarf Galaxies around the Milky Way*. A&A, 616, A12. doi:10.1051/0004-6361/201832698.

Gaia Collaboration; Luri, X.; Chemin, L.; Clementini, G.; Delgado, H. E.; et al., 2021c. *Gaia Early Data Release 3: Structure and Properties of the Magellanic Clouds*. A&A, 649, A7. doi:10.1051/0004-6361/202039588.

Gaia Collaboration; Prusti, T.; de Bruijne, J. H. J.; Brown, A. G. A.; Vallenari, A.; et al., 2016. *The Gaia Mission*. A&A, 595, A1. doi:10.1051/0004-6361/201629272.

Gallart, C.; Stetson, P. B.; Meschin, I. P.; Pont, F.; and Hardy, E., 2008. *Outside-In Disk Evolution in the Large Magellanic Cloud*. ApJ, 682(2), L89. doi:10.1086/590552.

Garavito-Camargo, N.; Besla, G.; Laporte, C. F. P.; Johnston, K. V.; Gómez, F. A.; et al., 2019. *Hunting for the Dark Matter Wake Induced by the Large Magellanic Cloud*. ApJ, 884(1), 51. doi:10.3847/1538-4357/ab32eb.

Garavito-Camargo, N.; Besla, G.; Laporte, C. F. P.; Price-Whelan, A. M.; Cunningham, E. C.; et al., 2021. *Quantifying the Impact of the Large Magellanic Cloud on the Structure of the Milky Way's Dark Matter Halo Using Basis Function Expansions*. arXiv:2010.00816 [astro-ph], 2010.00816.

Gardiner, L. T. and Noguchi, M., 1996. *N-Body Simulations of the Small Magellanic Cloud and the Magellanic Stream*. MNRAS, 278(1), 191. doi:10.1093/mnras/278.1.191.

Geha, M. C.; Holtzman, J. A.; Mould, J. R.; Gallagher III, J. S.; Watson, A. M.; et al., 1998. *Stellar Populations in Three Outer Fields of the Large Magellanic Cloud*. AJ, 115(3), 1045. doi:10.1086/300252.

Gilmozzi, R. and Spyromilio, J., 2007. *The European Extremely Large Telescope (E-ELT)*. The Messenger, 127, 11.

Girardi, L., 2016. *Red Clump Stars*. ARA&A, 54(1), 95. doi:10.1146/annurev-astro-081915-023354.

Girardi, L.; Chiosi, C.; Bertelli, G.; and Bressan, A., 1995. *Age Distribution of LMC Clusters from Their Integrated UBV Colors: History of Star Formation*. A&A, 298, 87.

Girardi, L. and Salaris, M., 2001. *Population Effects on the Red Giant Clump Absolute Magnitude, and Distance Determinations to Nearby Galaxies*. MNRAS, 323(1), 109. doi:10.1046/j.1365-8711.2001.04084.x.

Gómez, F. A.; Besla, G.; Carpintero, D. D.; Villalobos, Á.; O'Shea, B. W.; et al., 2015. *And Yet It Moves: The Dangers Of Artificially Fixing The Milky Way Center Of Mass In The Presence Of A Massive Large Magellanic Cloud*. ApJ, 802(2), 128. doi:10.1088/0004-637X/802/2/128.

Graczyk, D.; Pietrzyński, G.; Thompson, I. B.; Gieren, W.; Pilecki, B.; et al., 2013. *The ARAUCARIA Project. The Distance to the Small Magellanic Cloud from Late-Type Eclipsing Binaries*. ApJ, 780(1), 59. doi:10.1088/0004-637X/780/1/59.

Graczyk, D.; Pietrzyński, G.; Thompson, I. B.; Gieren, W.; Zgirski, B.; et al., 2020. *A Distance Determination to the Small Magellanic Cloud with an Accuracy of Better than Two Percent Based on Late-Type Eclipsing Binary Stars*. ApJ, 904(1), 13. doi:10.3847/1538-4357/abbb2b.

Grady, J.; Belokurov, V.; and Evans, N. W., 2021. *Magellanic Mayhem: Metallicities and Motions*. ApJ, 909(2), 150. doi:10.3847/1538-4357/abd4e4.

GRAVITY Collaboration; Abuter, R.; Amorim, A.; Bauböck, M.; Berger, J. P.; et al., 2019. *A Geometric Distance Measurement to the Galactic Center Black Hole with 0.3% Uncertainty*. A&A, 625, L10. doi:10.1051/0004-6361/201935656.

Grcevich, J. and Putman, M. E., 2010. *HI in Local Group Dwarf Galaxies and Stripping by the Galactic Halo*. ApJ, 721(1), 922. doi:10.1088/0004-637X/721/1/922, 0901.4975.

Grocholski, A. J.; Cole, A. A.; Sarajedini, A.; Geisler, D.; and Smith, V. V., 2006. *CaII Triplet Spectroscopy of Large Magellanic Cloud Red Giants. I. Abundances and Velocities for a Sample of Populous Clusters*. AJ, 132(4), 1630. doi:10.1086/507303.

Guglielmo, M.; Lewis, G. F.; and Bland-Hawthorn, J., 2014. *A Genetic Approach to the History of the Magellanic Clouds*. MNRAS, 444(2), 1759. doi:10.1093/mnras/stu1549.

Guiglion, G.; Recio-Blanco, A.; de Laverny, P.; Kordopatis, G.; Hill, V.; et al., 2015. *The Gaia-ESO Survey: New Constraints on the Galactic Disc Velocity Dispersion and Its Chemical Dependencies*. A&A, 583, A91. doi:10.1051/0004-6361/201525883.

Guo, Q.; White, S.; Li, C.; and Boylan-Kolchin, M., 2010. *How Do Galaxies Populate Dark Matter Haloes?* MNRAS. doi:10.1111/j.1365-2966.2010.16341.x.

Hagen, L. M. Z.; Siegel, M. H.; Hoversten, E. A.; Gronwall, C.; Immler, S.; et al., 2016. *Swift Ultraviolet Survey of the Magellanic Clouds (SUMaC). I. Shape of the Ultraviolet Dust Extinction Law and Recent Star Formation History of the Small Magellanic Cloud*. MNRAS, 466(4), 4540. doi:10.1093/mnras/stw2954.

Hardy, E.; Buonanno, R.; Corsi, C. E.; Janes, K. A.; and Schommer, R. A., 1984. *The Population Structure of the Large Magellanic Cloud Bar*. ApJ, 278, 592. doi:10.1086/161826.

Harris, J. and Zaritsky, D., 2004. *The Star Formation History of the Small Magellanic Cloud*. AJ, 127(3), 1531. doi:10.1086/381953.

Harris, J. and Zaritsky, D., 2006. *Spectroscopic Survey of Red Giants in the Small Magellanic Cloud. I. Kinematics*. AJ, 131(5), 2514. doi:10.1086/500974.

Harris, J. and Zaritsky, D., 2009. *The Star Formation History of the Large Magellanic Cloud*. AJ, 138(5), 1243. doi:10.1088/0004-6256/138/5/1243.

Haschke, R.; Grebel, E. K.; and Duffau, S., 2012. *Three-Dimensional Maps of the Magellanic Clouds Using RR Lyrae Stars and Cepheids. I. The Large Magellanic Cloud*. The Astronomical Journal, 144(4), 106. doi:10.1088/0004-6256/144/4/106.

Hatzidimitriou, D.; Croke, B. F.; Morgan, D. H.; and Cannon, R. D., 1997. *Kinematics of Carbon Stars in the Outer Regions of the Small Magellanic Cloud*. A&AS, 122(3), 507. doi:10.1051/aas:1997150.

Hatzidimitriou, D. and Hawkins, M. R. S., 1989. *Stellar Populations and Large-Scale Structure of the SMC – II. Geometry of the North-Eastern and South-Western Outlying Regions*. MNRAS, 241(4), 667. doi:10.1093/mnras/241.4.667.

Hernquist, L., 1990. *An Analytical Model for Spherical Galaxies and Bulges*. ApJ, 356(2), 359. doi:10.1086/168845.

Hidalgo, S. L., 2017. *Mass-Metallicity Relation of Dwarf Galaxies and Its Dependency on Time: Clues from Resolved Systems and Comparison with Massive Galaxies*. A&A, 606, A115. doi:10.1051/0004-6361/201630264.

Hindman, J.; Kerr, F.; and McGee, R., 1963. *A Low Resolution Hydrogen-Line Survey of the Magellanic System. II. Interpretation of Results*. Aust. J. Phys., 16(4), 570. doi:10.1071/PH630570.

Holtzman, J. A.; Gallagher III, J. S.; Cole, A. A.; Mould, J. R.; Grillmair, C. J.; et al., 1999. *Observations and Implications of the Star Formation History of the Large Magellanic Cloud*. AJ, 118(5), 2262. doi:10.1086/301097.

Hunter, D. A. and Gallagher, III, J. S., 1986. *Stellar Populations and Star Formation in Irregular Galaxies*. PASP, 98, 5. doi:10.1086/131711.

Indu, G. and Subramaniam, A., 2011. *The Recent Star-Formation History of the Large and Small Magellanic Clouds*. A&A, 535, A115. doi:10.1051/0004-6361/201117298.

Inno, L.; Bono, G.; Matsunaga, N.; Fiorentino, G.; Marconi, M.; et al., 2016. *The Panchromatic View of the Magellanic Clouds from Classical Cepheids. I. Distance, Reddening, and Geometry of the Large Magellanic Cloud Disk*. ApJ, 832(2), 176. doi:10.3847/0004-637X/832/2/176.

Iorio, G. and Belokurov, V., 2019. *The Shape of the Galactic Halo with Gaia DR2 RR Lyrae. Anatomy of an Ancient Major Merger*. MNRAS, 482(3), 3868. doi:10.1093/mnras/sty2806.

Irwin, M. J.; Demers, S.; and Kunkel, W. E., 1990. *A Blue Stellar Link between the Magellanic Clouds*. AJ, 99, 191. doi:10.1086/115319.

Ivezić, Ž.; Kahn, S. M.; Tyson, J. A.; Abel, B.; Acosta, E.; et al., 2019. *LSST: From Science Drivers to Reference Design and Anticipated Data Products*. ApJ, 873(2), 111. doi:10.3847/1538-4357/ab042c, 0805.2366.

Jacyszyn-Dobrzeniecka, A. M.; Mróz, P.; Kruszyńska, K.; Soszyński, I.; Skowron, D. M.; et al., 2020a. *OGLE-Ing the Magellanic System: RR Lyrae Stars in the Bridge*. ApJ, 889(1), 26. doi:10.3847/1538-4357/ab61f2.

Jacyszyn-Dobrzeniecka, A. M.; Soszyński, I.; Udalski, A.; Szymański, M. K.; Skowron, D. M.; et al., 2020b. *OGLE-Ing the Magellanic System: Cepheids in the Bridge*. ApJ, 889(1), 25. doi:10.3847/1538-4357/ab61f1.

Jahn, E. D.; Sales, L. V.; Wetzel, A.; Samuel, J.; El-Badry, K.; et al., 2021. *The Effects of LMC-Mass Environments on Their Dwarf Satellite Galaxies in the FIRE Simulations*. arXiv:2106.03861 [astro-ph], 2106.03861.

James, P. A. and Ivory, C. F., 2011. *On the Scarcity of Magellanic Cloud like Satellites: Magellanic Satellite Galaxies*. MNRAS, 411(1), 495. doi:10.1111/j.1365-2966.2010.17695.x.

Jerjen, H.; Conn, B.; Kim, D.; and Schirmer, M., 2018. *On the Nature of Ultra-Faint Dwarf Galaxy Candidates. III. Horologium I, Pictor I, Grus I, and Phoenix II*. arXiv:1809.02259 [astro-ph], 1809.02259.

Jethwa, P.; Erkal, D.; and Belokurov, V., 2016. *A Magellanic Origin of the DES Dwarfs*. MNRAS, 461(2), 2212. doi:10.1093/mnras/stw1343.

Johns, M.; McCarthy, P.; Raybould, K.; Bouchez, A.; Farahani, A.; et al., 2012. *Giant Magellan Telescope: Overview*. In Stepp, L. M.; Gilmozzi, R.; and Hall, H. J. (Eds.), *Society of Photo-Optical Instrumentation Engineers (SPIE) Conference Series*, 84441H, Amsterdam, Netherlands. doi:10.1117/12.926716.

Joshi, Y. and Joshi, S., 2014. *Population I Cepheids and Star Formation History of the Large Magellanic Cloud*. New Astronomy, 28, 27. doi:10.1016/j.newast.2013.10.001.

Joshi, Y. C.; Mohanty, A. P.; and Joshi, S., 2016. *Population I Cepheids and Understanding Star Formation History of the Small Magellanic Cloud*. Research in Astronomy and Astrophysics, 16(4), 009. doi:10.1088/1674-4527/16/4/061.

Joshi, Y. C. and Panchal, A., 2019. *Reddening Map and Recent Star Formation in the Magellanic Clouds Based on OGLE IV Cepheids*. A&A, 628, A51. doi:10.1051/0004-6361/201834574.

Kallivayalil, N.; Sales, L. V.; Zivick, P.; Fritz, T. K.; Del Pino, A.; et al., 2018. *The Missing Satellites of the Magellanic Clouds? Gaia Proper Motions of the Recently Discovered Ultra-Faint Galaxies*. ApJ, 867(1), 19. doi:10.3847/1538-4357/aadfee.

Kallivayalil, N.; van der Marel, R. P.; and Alcock, C., 2006a. *Is the SMC Bound to the LMC? The Hubble Space Telescope Proper Motion of the SMC*. ApJ, 652(2), 1213. doi:10.1086/508014.

Kallivayalil, N.; van der Marel, R. P.; Alcock, C.; Axelrod, T.; Cook, K. H.; et al., 2006b. *The Proper Motion of the Large Magellanic Cloud Using HST*. ApJ, 638(2), 772. doi:10.1086/498972.

Kallivayalil, N.; van der Marel, R. P.; Besla, G.; Anderson, J.; and Alcock, C., 2013. *Third-Epoch Magellanic Cloud Proper Motions. I. Hubble Space Telescope/WFC3 Data And Orbit Implications*. ApJ, 764(2), 161. doi:10.1088/0004-637X/764/2/161.

Kato, D.; Nagashima, C.; Nagayama, T.; Kurita, M.; Koerwer, J. F.; et al., 2007. *The IRSF Magellanic Clouds Point Source Catalog*. PASJ, 59(3), 615. doi:10.1093/pasj/59.3.615.

Kim, S.; Staveley-Smith, L.; Dopita, M. A.; Freeman, K. C.; Sault, R. J.; et al., 1998. *An HI Aperture Synthesis Mosaic of the Large Magellanic Cloud*. ApJ, 503(2), 674. doi:10.1086/306030.

Kim, S.; Staveley-Smith, L.; Dopita, M. A.; Sault, R. J.; Freeman, K. C.; et al., 2003. *A Neutral Hydrogen Survey of the Large Magellanic Cloud: Aperture Synthesis and Multibeam Data Combined*. ApJS, 148(2), 473. doi:10.1086/376980.

Kirby, E. N.; Cohen, J. G.; Guhathakurta, P.; Cheng, L.; Bullock, J. S.; et al., 2013. *The Universal Stellar Mass-Stellar Metallicity Relation for Dwarf Galaxies*. ApJ, 779(2), 102. doi:10.1088/0004-637X/779/2/102.

Koerwer, J. F., 2009. *Large Magellanic Cloud Distance and Structure from Near-Infrared Red Clump Observations*. AJ, 138(1), 1. doi:10.1088/0004-6256/138/1/1.

Koposov, S. E.; Belokurov, V.; Li, T. S.; Mateu, C.; Erkal, D.; et al., 2019. *Piercing the Milky Way: An All-Sky View of the Orphan Stream*. MNRAS, 485(4), 4726. doi:10.1093/mnras/stz457.

Koposov, S. E.; Belokurov, V.; Torrealba, G.; and Evans, N. W., 2015. *Beasts of the Southern Wild: Discovery of Nine Ultra Faint Satellites in the Vicinity of the Magellanic Clouds*. ApJ, 805(2), 130. doi:10.1088/0004-637X/805/2/130.

Koposov, S. E.; Walker, M. G.; Belokurov, V.; Casey, A. R.; Geringer-Sameth, A.; et al., 2018. *Snake in the Clouds: A New Nearby Dwarf Galaxy in the Magellanic Bridge*. MNRAS, 479(4), 5343. doi:10.1093/mnras/sty1772.

Kormendy, J. and Freeman, K. C., 2016. *Scaling Laws for Dark Matter Halos in Late-Type and Dwarf Spheroidal Galaxies*. ApJ, 817(2), 84. doi:10.3847/0004-637X/817/2/84.

Kroupa, P. and Bastian, U., 1997. *The Hipparcos Proper Motion of the Magellanic Clouds*. New Astronomy, 2(1), 77. doi:10.1016/S1384-1076(97)00006-7.

Kroupa, P.; Roser, S.; and Bastian, U., 1994. *On the Motion of the Magellanic Clouds*. MNRAS, 266(2), 412. doi:10.1093/mnras/266.2.412.

Kruk, S. J.; Lintott, C. J.; Simmons, B. D.; Bamford, S. P.; Cardamone, C. N.; et al., 2017. *Galaxy Zoo: Finding Offset Discs and Bars in SDSS Galaxies*. MNRAS, 469(3), 3363. doi:10.1093/mnras/stx1026.

Kunkel, W. E.; Demers, S.; Irwin, M. J.; and Albert, L., 1997. *The Dynamics of the Large Magellanic Cloud Periphery: Mass Limit and Polar Ring*. ApJ, 488(2), L129. doi:10.1086/310930.

Lah, P.; Kiss, L. L.; and Bedding, T. R., 2005. *Red Variables in the OGLE-II Data Base – III. Constraints on the Three-Dimensional Structures of the Large and Small Magellanic Clouds*. MNRAS, 359(1), L42. doi:10.1111/j.1745-3933.2005.00033.x.

Laporte, C. F. P.; Gómez, F. A.; Besla, G.; Johnston, K. V.; and Garavito-Camargo, N., 2018a. *Response of the Milky Way's Disc to the Large Magellanic Cloud in a First Infall Scenario*. MNRAS, 473(1), 1218. doi:10.1093/mnras/stx2146.

Laporte, C. F. P.; Johnston, K. V.; Gómez, F. A.; Garavito-Camargo, N.; and Besla, G., 2018b. *The Influence of Sagittarius and the Large Magellanic Cloud on the Stellar Disc of the Milky Way Galaxy*. MNRAS, 481(1), 286. doi:10.1093/mnras/sty1574.

Law, D. R. and Majewski, S. R., 2010. *The Sagittarius Dwarf Galaxy: A Model for Evolution in a Triaxial Milky Way Halo*. ApJ, 714(1), 229. doi:10.1088/0004-637X/714/1/229.

Lawrence, J. S.; Ben-Ami, S.; Braulio, A.; Colless, M. M.; Contos, A. R.; et al., 2020. *The MANIFEST Pre-Concept Design*. In Evans, C. J.; Bryant, J. J.; and Motohara, K. (Eds.), *Society of Photo-Optical Instrumentation Engineers (SPIE) Conference Series*, 1144728. doi:10.1117/12.2563238.

Le Coarer, E.; Rosado, M.; Georgelin, Y.; Viale, A.; and Goldes, G., 1993. *H-Alpha Survey of the Small Magellanic Cloud*. A&A, 280, 365.

Lewis, I. J.; Cannon, R. D.; Taylor, K.; Glazebrook, K.; Bailey, J. A.; et al., 2002. *The Anglo-Australian Observatory 2dF Facility*. MNRAS, 333(2), 279. doi:10.1046/j.1365-8711.2002.05333.x.

Li, T. S.; Koposov, S. E.; Zucker, D. B.; Lewis, G. F.; Kuehn, K.; et al., 2019. *The Southern Stellar Stream Spectroscopic Survey (S5): Overview, Target Selection, Data Reduction, Validation, and Early Science*. MNRAS, 490(3), 3508. doi:10.1093/mnras/stz2731.

Lucchini, S.; D'Onghia, E.; Fox, A. J.; Bustard, C.; Bland-Hawthorn, J.; et al., 2020. *The Magellanic Corona as the Key to the Formation of the Magellanic Stream*. Nature, 585(7824), 203. doi:10.1038/s41586-020-2663-4.

Lynden-Bell, D., 1976. *Dwarf Galaxies and Globular Clusters in High Velocity Hydrogen Streams*. MNRAS, 174(3), 695. doi:10.1093/mnras/174.3.695.

Mackey, A. D.; Koposov, S. E.; Da Costa, G. S.; Belokurov, V.; Erkal, D.; et al., 2017. *Structured Star Formation in the Magellanic Inter-Cloud Region*. MNRAS, 472(3), 2975. doi:10.1093/mnras/stx2035.

Mackey, A. D.; Koposov, S. E.; Erkal, D.; Belokurov, V.; Da Costa, G. S.; et al., 2016. *A 10 Kpc Stellar Substructure at the Edge of the Large Magellanic Cloud: Perturbed Outer Disc or Evidence for Tidal Stripping?* MNRAS, 459(1), 239. doi:10.1093/mnras/stw497.

Mackey, A. D.; Payne, M. J.; and Gilmore, G. F., 2006. *Photometry of Magellanic Cloud Clusters with the Advanced Camera for Surveys - II. The Unique LMC Cluster ESO 121-SC03: ACS Photometry of ESO 121-SC03*. MNRAS, 369(2), 921. doi:10.1111/j.1365-2966.2006.10342.x.

Mackey, D.; Koposov, S. E.; Da Costa, G.; Belokurov, V.; Erkal, D.; et al., 2018. *Substructures and Tidal Distortions in the Magellanic Stellar Periphery*. ApJ, 858(2), L21. doi:10.3847/2041-8213/aac175.

Majewski, S. R.; Nidever, D. L.; Muñoz, R. R.; Patterson, R. J.; Kunkel, W. E.; et al., 2008. *Discovery of an Extended, Halo-like Stellar Population around the Large Magellanic Cloud*. Proc. IAU, 4(S256), 51. doi:10.1017/S1743921308028251.

Martin, N.; Maurice, E.; and Lequeux, J., 1989. *The Structure of the Small Magellanic Cloud*. A&A, 215, 219.

Martínez-Delgado, D.; Katherina Vivas, A.; Grebel, E. K.; Gallart, C.; Pieres, A.; et al., 2019. *Nature of a Shell of Young Stars in the Outskirts of the Small Magellanic Cloud*. A&A, 631, A98. doi:10.1051/0004-6361/201936021.

Massana, P.; Noël, N. E. D.; Nidever, D. L.; Erkal, D.; de Boer, T. J. L.; et al., 2020. *SMASHing the Low Surface Brightness SMC*. MNRAS, 498(1), 1034. doi:10.1093/mnras/staa2451.

Mastropietro, C.; Burkert, A.; and Moore, B., 2009. *Effects of Ram Pressure on the Gas Distribution and Star Formation in the Large Magellanic Cloud*. MNRAS, 399(4), 2004. doi:10.1111/j.1365-2966.2009.15406.x.

Mastropietro, C.; Moore, B.; Mayer, L.; Wadsley, J.; and Stadel, J., 2005. *The Gravitational and Hydrodynamical Interaction between the Large Magellanic Cloud and the Galaxy*. MNRAS, 363(2), 509. doi:10.1111/j.1365-2966.2005.09435.x.

Mateo, M., 1988. *The Age Distribution and Age-Metallicity Relation of Star Clusters in a Northern Region of the LMC*. In Grindlay, J. and Philip, A. (Eds.), *The Harlow Shapley Symposium on Globular Cluster Systems in Galaxies. Proceedings of the 126th Symposium of the International Astronomical Union*, vol. 126, 557, Kluwer Academic Publishers, Dordrecht.

Mateo, M.; Hodge, P.; and Schommer, R. A., 1986. *CCD Photometry of Large Magellanic Cloud Clusters. III - The Unique, Remote Cluster ESO 121-SC03*. ApJ, 311, 113. doi:10.1086/164757.

Mathewson, D. S.; Cleary, M. N.; and Murray, J. D., 1974. *The Magellanic Stream*. ApJ, 190, 291. doi:10.1086/152875.

Mazzi, A.; Girardi, L.; Zaggia, S.; Pastorelli, G.; Rubele, S.; et al., 2021. *The VMC Survey – XLIII. The Spatially Resolved Star Formation History across the Large Magellanic Cloud*. arXiv:2108.07225 [astro-ph], 2108.07225.

McConnachie, A. W., 2012. *The Observed Properties of Dwarf Galaxies in and around the Local Group*. AJ, 144(1), 4. doi:10.1088/0004-6256/144/1/4.

McMahon, R. G.; Banerji, M.; Gonzalez, E.; Koposov, S. E.; Bejar, V. J.; et al., 2013. *First Scientific Results from the VISTA Hemisphere Survey (VHS)*. The Messenger, 154, 35.

Meatheringham, S. J.; Dopita, M. A.; Ford, H. C.; and Webster, B. L., 1988. *The Kinematics of the Planetary Nebulae in the Large Magellanic Cloud*. ApJ, 327, 651. doi:10.1086/166222.

Meschin, I.; Gallart, C.; Aparicio, A.; Hidalgo, S. L.; Monelli, M.; et al., 2014. *Spatially Resolved LMC Star Formation History – I. Outside in Evolution of the Outer LMC Disc*. MNRAS, 438(2), 1067. doi:10.1093/mnras/stt2220.

Minniti, D., 2003. *Kinematic Evidence for an Old Stellar Halo in the Large Magellanic Cloud*. Science, 301(5639), 1508. doi:10.1126/science.1088529.

Miszalski, B.; Shortridge, K.; Saunders, W.; Parker, Q. A.; and Croom, S. M., 2006. *Multi-Object Spectroscopy Field Configuration by Simulated Annealing*. MNRAS, 371(4), 1537. doi:10.1111/j.1365-2966.2006.10777.x.

Miyamoto, M. and Nagai, R., 1975. *Three-Dimensional Models for the Distribution of Mass in Galaxies.* PASJ, 27, 533.

Monteagudo, L.; Gallart, C.; Monelli, M.; Bernard, E. J.; and Stetson, P. B., 2018. *The Origin of the LMC Stellar Bar: Clues from the SFH of the Bar and Inner Disc*. MNRAS, 473(1), L16. doi:10.1093/mnrasl/slx158.

Moster, B. P.; Somerville, R. S.; Maulbetsch, C.; van den Bosch, F. C.; Macciò, A. V.; et al., 2010. *Constraints on the Relationship between Stellar Mass and Halo Mass at Low and High Redshift*. ApJ, 710(2), 903. doi:10.1088/0004-637X/710/2/903.

Munari, U.; Sordo, R.; Castelli, F.; and Zwitter, T., 2005. *An Extensive Library of 2500–10 500 Å Synthetic Spectra*. A&A, 442(3), 1127. doi:10.1051/0004-6361:20042490.

Munoz, R. R.; Majewski, S. R.; Zaggia, S.; Kunkel, W. E.; Frinchaboy, P. M.; et al., 2006. *Exploring Halo Substructure with Giant Stars. XI. The Tidal Tails of the Carina Dwarf Spheroidal Galaxy and the Discovery of Magellanic Cloud Stars in the Carina Foreground*. ApJ, 649(1), 201. doi:10.1086/505620.

Mutlu-Pakdil, B.; Sand, D. J.; Carlin, J. L.; Spekkens, K.; Caldwell, N.; et al., 2018. *A Deeper Look at the New Milky Way Satellites: Sagittarius II, Reticulum II, Phoenix II, and Tucana III*. ApJ, 863(1), 25. doi:10.3847/1538-4357/aacd0e.

Nadler, E. O.; Wechsler, R. H.; Bechtol, K.; Mao, Y.-Y.; Green, G.; et al., 2020. *Milky Way Satellite Census. II. Galaxy–Halo Connection Constraints Including the Impact of the Large Magellanic Cloud*. ApJ, 893(1), 48. doi:10.3847/1538-4357/ab846a.

Navarrete, C.; Belokurov, V.; Catelan, M.; Jethwa, P.; Koposov, S. E.; et al., 2019. *Stellar Streams around the Magellanic Clouds in 4D*. MNRAS, 483(3), 4160. doi:10.1093/mnras/sty3347.

Navarro, J. F.; Frenk, C. S.; and White, S. D. M., 1997. *A Universal Density Profile from Hierarchical Clustering*. ApJ, 490(2), 493. doi:10.1086/304888.

Nayak, P. K.; Subramaniam, A.; Choudhury, S.; and Sagar, R., 2018. *Star Clusters in the Magellanic Clouds: II. Age-Dating, Classification, and Spatio-Temporal Distribution of the SMC Clusters*. A&A, 616, A187. doi:10.1051/0004-6361/201732227.

Neistein, E.; Weinmann, S. M.; Li, C.; and Boylan-Kolchin, M., 2011. *Linking Haloes to Galaxies: How Many Halo Properties Are Needed?: Linking Haloes to Galaxies*. MNRAS, 414(2), 1405. doi:10.1111/j.1365-2966.2011.18473.x.

Nidever, D. L.; Majewski, S. R.; and Burton, W. B., 2008. *The Origin of the Magellanic Stream and Its Leading Arm*. ApJ, 679(1), 432. doi:10.1086/587042.

Nidever, D. L.; Majewski, S. R.; Burton, W. B.; and Nigra, L., 2010. *The 200 Degree-Long Magellanic Stream System*. ApJ, 723(2), 1618. doi:10.1088/0004-637X/723/2/1618.

Nidever, D. L.; Monachesi, A.; Bell, E. F.; Majewski, S. R.; Muñoz, R. R.; et al., 2013. *A Tidally Stripped Stellar Component of the Magellanic Bridge*. ApJ, 779(2), 145. doi:10.1088/0004-637X/779/2/145.

Nidever, D. L.; Olsen, K.; Choi, Y.; de Boer, T. J. L.; Blum, R. D.; et al., 2019. *Exploring the Very Extended Low-Surface-Brightness Stellar Populations of the Large Magellanic Cloud with SMASH*. ApJ, 874(2), 118. doi:10.3847/1538-4357/aafaf7.

Nidever, D. L.; Olsen, K.; Walker, A. R.; Vivas, A. K.; Blum, R. D.; et al., 2017. *SMASH - Survey of the MAgellanic Stellar History*. MNRAS, 154(5), 199. doi:10.3847/1538-3881/aa8d1c.

Nikolaev, S.; Drake, A. J.; Keller, S. C.; Cook, K. H.; Dalal, N.; et al., 2004. *Geometry of the Large Magellanic Cloud Disk: Results from MACHO and the Two Micron All Sky Survey.* ApJ, 601(1), 260. doi:10.1086/380439.

Noël, N. E. D.; Aparicio, A.; Gallart, C.; Hidalgo, S. L.; Costa, E.; et al., 2009. *Old Main-Sequence Turnoff Photometry in the Small Magellanic Cloud. II. Star Formation History and Its Spatial Gradients.* ApJ, 705(2), 1260. doi:10.1088/0004-637X/705/2/1260.

Noël, N. E. D.; Conn, B. C.; Carrera, R.; Read, J. I.; Rix, H.-W.; et al., 2013. *The MAGellanic Inter-Cloud Project (MAGIC). I. Evidence for Intermediate-Age Stellar Populations in between the Magellanic Clouds.* ApJ, 768(2), 109. doi:10.1088/0004-637X/768/2/109.

Noël, N. E. D.; Conn, B. C.; Read, J. I.; Carrera, R.; Dolphin, A.; et al., 2015. *The MAGellanic Inter-Cloud (MAGIC) Project – II. Slicing up the Bridge.* MNRAS, 452(4), 4222. doi:10.1093/mnras/stv1614.

Noël, N. E. D.; Gallart, C.; Costa, E.; and Méndez, R. A., 2007. *Old Main-Sequence Turnoff Photometry in the Small Magellanic Cloud. I. Constraints on the Star Formation History in Different Fields.* AJ, 133(5), 2037. doi:10.1086/512668.

Noordermeer, E.; Merrifield, M. R.; and Aragn-Salamanca, A., 2008. *Exploring Disc Galaxy Dynamics Using Integral Field Unit Data.* MNRAS, 388(3), 1381. doi:10.1111/j.1365-2966.2008.13487.x.

Odewahn, S. C., 1991. *Properties of the Magellanic-Type Spirals. I - Surface Photometry of NGC 4618 and NGC 4625.* AJ, 101, 829. doi:10.1086/115728.

Odewahn, S. C., 1994. *Properties of the Magellanic Type Spirals. 2: The Frequency of Companion Galaxies.* AJ, 107, 1320. doi:10.1086/116945.

Olsen, K. A. G., 1999. *Star Formation Histories from Hubble Space TelescopeColor-Magnitude Diagrams of Six Fields of the Large Magellanic Cloud.* AJ, 117(5), 2244. doi:10.1086/300854.

Olsen, K. A. G. and Massey, P., 2007. *Evidence for Tidal Effects in the Stellar Dynamics of the Large Magellanic Cloud.* ApJ, 656(2), L61. doi:10.1086/512484.

Olsen, K. A. G. and Salyk, C., 2002. *A Warp in the Large Magellanic Cloud Disk?* AJ, 124(4), 2045. doi:10.1086/342739.

Olsen, K. A. G.; Zaritsky, D.; Blum, R. D.; Boyer, M. L.; and Gordon, K. D., 2011. *A Population of Accreted Small Magellanic Cloud Stars in the Large Magellanic Cloud*. ApJ, 737(1), 29. doi:10.1088/0004-637X/737/1/29.

Olszewski, E. W.; Schommer, R. A.; Suntzeff, N. B.; and Harris, H. C., 1991. *Spectroscopy of Giants in LMC Clusters. I - Velocities, Abundances, and the Age-Metallicity Relation*. AJ, 101, 515. doi:10.1086/115701.

Omkumar, A. O.; Subramanian, S.; Niederhofer, F.; Diaz, J.; Cioni, M.-R. L.; et al., 2020. *Gaia View of a Stellar Sub-Structure in Front of the Small Magellanic Cloud*. MNRAS, 500(3), 2757. doi:10.1093/mnras/staa3085.

Padovani, P., 2014. *E-ELT Programme Top Level Requirements for the ELT-MOS. ESO-204696 V1.*

Pardy, S. A.; D'Onghia, E.; Athanassoula, E.; Wilcots, E. M.; and Sheth, K., 2016. *Tidally Induced Offset Disks in Magellanic Spiral Galaxies*. ApJ, 827(2), 149. doi:10.3847/0004-637X/827/2/149.

Pardy, S. A.; D'Onghia, E.; and Fox, A. J., 2018. *Models of Tidally Induced Gas Filaments in the Magellanic Stream*. ApJ, 857(2), 101. doi:10.3847/1538-4357/aab95b.

Pardy, S. A.; D'Onghia, E.; Navarro, J. F.; Grand, R.; Gómez, F. A.; et al., 2019. *Satellites of Satellites: The Case for Carina and Fornax*. MNRAS, stz3192. doi:10.1093/mnras/stz3192.

Parisi, M. C.; Grocholski, A. J.; Geisler, D.; Sarajedini, A.; and Clariá, J. J., 2009. *Ca II Triplet Spectroscopy of Small Magellanic Cloud Red Giants. I. Abundances and Velocities for a Sample of Clusters*. AJ, 138(2), 517. doi:10.1088/0004-6256/138/2/517.

Patel, E.; Kallivayalil, N.; Garavito-Camargo, N.; Besla, G.; Weisz, D. R.; et al., 2020. *The Orbital Histories of Magellanic Satellites Using Gaia DR2 Proper Motions*. ApJ, 893(2), 121. doi:10.3847/1538-4357/ab7b75.

Paudel, S. and Sengupta, C., 2017. *UGC 4703 Interacting Pair Near the Isolated Spiral Galaxy NGC 2718: A Milky Way Magellanic Cloud Analog*. ApJ, 849(2), L28. doi:10.3847/2041-8213/aa95bf.

Paudel, S.; Smith, R.; Yoon, S. J.; Calderón-Castillo, P.; and Duc, P.-A., 2018. *A Catalog of Merging Dwarf Galaxies in the Local Universe*. ApJS, 237(2), 36. doi:10.3847/1538-4365/aad555.

Pawlowski, M. S., 2018. *The Planes of Satellite Galaxies Problem, Suggested Solutions, and Open Questions*. Modern Physics Letters A, 33(6), 1830004. doi:10.1142/S0217732318300045.

Pearson, S.; Besla, G.; Putman, M. E.; Lutz, K. A.; Fernández, X.; et al., 2016. *Local Volume TiNy Titans: Gaseous Dwarf–Dwarf Interactions in the Local Universe*. MNRAS, 459(2), 1827. doi:10.1093/mnras/stw757.

Pedreros, M. H.; Anguita, C.; and Maza, J., 2002. *Proper Motion of the Large Magellanic Cloud Using QSOs as an Inertial Reference System: The Q0459-6427 Field*. AJ, 123(4), 1971. doi:10.1086/339554.

Pejcha, O. and Stanek, K. Z., 2009. *The Structure of the Large Magellanic Cloud Stellar Halo Derived Using OGLE-III RR Lyr Stars*. ApJ, 704(2), 1730. doi:10.1088/0004-637X/704/2/1730.

Peñarrubia, J.; Gómez, F. A.; Besla, G.; Erkal, D.; and Ma, Y.-Z., 2016. *A Timing Constraint on the (Total) Mass of the Large Magellanic Cloud*. MNRAS, 456(1), L54. doi:10.1093/mnrasl/slv160.

Petersen, M. S. and Peñarrubia, J., 2020. *Reflex Motion in the Milky Way Stellar Halo Resulting from the Large Magellanic Cloud Infall*. MNRAS, 494(1), L11. doi:10.1093/mnrasl/slaa029.

Petersen, M. S. and Peñarrubia, J., 2021. *Detection of the Milky Way Reflex Motion Due to the Large Magellanic Cloud Infall*. Nature Astronomy, 5(3), 251. doi:10.1038/s41550-020-01254-3.

Pieres, A.; Santiago, B. X.; Drlica-Wagner, A.; Bechtol, K.; van der Marel, R. P.; et al., 2017. *A Stellar Overdensity Associated with the Small Magellanic Cloud*. MNRAS, 468(2), 1349. doi:10.1093/mnras/stx507.

Pietrzyński, G.; Graczyk, D.; Gallenne, A.; Gieren, W.; Thompson, I. B.; et al., 2019. *A Distance to the Large Magellanic Cloud That Is Precise to One per Cent*. Nature, 567(7747), 200. doi:10.1038/s41586-019-0999-4.

Poggio, E.; Laporte, C. F. P.; Johnston, K. V.; D'Onghia, E.; Drimmel, R.; et al., 2020. *Measuring the Vertical Response of the Galactic Disc to an Infalling Satellite*. arXiv:2011.11642 [astro-ph], 2011.11642.

Price-Whelan, A. M.; Nidever, D. L.; Choi, Y.; Schlafly, E. F.; Morton, T.; et al., 2019. *Discovery of a Disrupting Open Cluster Far into the Milky Way Halo:*

A Recent Star Formation Event in the Leading Arm of the Magellanic Stream? ApJ, 887(1), 19. doi:10.3847/1538-4357/ab4bdd.

Putman, M. E.; Gibson, B. K.; Staveley-Smith, L.; Banks, G.; Barnes, D. G.; et al., 1998. *Tidal Disruption of the Magellanic Clouds by the Milky Way.* Nature, 394(6695), 752. doi:10.1038/29466.

Putman, M. E.; Staveley-Smith, L.; Freeman, K. C.; Gibson, B. K.; and Barnes, D. G., 2003. *The Magellanic Stream, High-Velocity Clouds, and the Sculptor Group.* ApJ, 586(1), 170. doi:10.1086/344477.

Rafelski, M. and Zaritsky, D., 2005. *The Star Clusters of the Small Magellanic Cloud: Age Distribution.* AJ, 129(6), 2701. doi:10.1086/424938.

Ramachandran, V.; Oskinova, L. M.; and Hamann, W.-R., 2021. *Discovery of O Stars in the Tidal Magellanic Bridge: Stellar Parameters, Abundances, and Feedback of the Nearest Metal-Poor Massive Stars and Their Implication for the Magellanic System Ecology.* A&A, 646, A16. doi:10.1051/0004-6361/202039486.

Reiprich, T. H.; Basu, K.; Ettori, S.; Israel, H.; Lovisari, L.; et al., 2013. *Outskirts of Galaxy Clusters.* Space Science Reviews, 177, 195. doi:10.1007/s11214-013-9983-8.

Rezaei kh., S.; Javadi, A.; Khosroshahi, H.; and van Loon, J. T., 2014. *The Star Formation History of the Magellanic Clouds Derived from Long-Period Variable Star Counts.* MNRAS, 445(3), 2214. doi:10.1093/mnras/stu1807.

Richter, P.; Fox, A. J.; Wakker, B. P.; Lehner, N.; Howk, J. C.; et al., 2013. *The COS/UVES Absorption Survey of the Magellanic Stream. II. Evidence for a Complex Enrichment History of the Stream from the Fairall 9 Sightline.* ApJ, 772(2), 111. doi:10.1088/0004-637X/772/2/111.

Riello, M.; De Angeli, F.; Evans, D. W.; Montegriffo, P.; Carrasco, J. M.; et al., 2021. *Gaia Early Data Release 3: Photometric Content and Validation.* A&A, 649, A3. doi:10.1051/0004-6361/202039587.

Ripepi, V.; Cioni, M.-R. L.; Moretti, M. I.; Marconi, M.; Bekki, K.; et al., 2017. *The VMC Survey. XXV. The 3D Structure of the Small Magellanic Cloud from Classical Cepheids.* MNRAS, 472(1), 808. doi:10.1093/mnras/stx2096.

Robin, A. C.; Reylé, C.; Derrière, S.; and Picaud, S., 2003. *A Synthetic View on Structure and Evolution of the Milky Way.* A&A, 409(2), 523. doi:10.1051/0004-6361:20031117.

Robotham, A. S. G.; Baldry, I. K.; Bland-Hawthorn, J.; Driver, S. P.; Loveday, J.; et al., 2012. *Galaxy And Mass Assembly (GAMA): In Search of Milky Way Magellanic Cloud Analogues*. MNRAS, 424(2), 1448. doi:10.1111/j.1365-2966.2012.21332.x.

Rubele, S.; Pastorelli, G.; Girardi, L.; Cioni, M.-R. L.; Zaggia, S.; et al., 2018. *The VMC Survey – XXXI: The Spatially Resolved Star Formation History of the Main Body of the Small Magellanic Cloud*. MNRAS, 478(4), 5017. doi:10.1093/mnras/sty1279.

Ruiz-Lara, T.; Gallart, C.; Monelli, M.; Nidever, D.; Dorta, A.; et al., 2020. *The Large Magellanic Cloud Stellar Content with SMASH: I. Assessing the Stability of the Magellanic Spiral Arms*. A&A, 639, L3. doi:10.1051/0004-6361/202038392.

Sacchi, E.; Richstein, H.; Kallivayalil, N.; van der Marel, R.; Libralato, M.; et al., 2021. *Star Formation Histories of Ultra-Faint Dwarf Galaxies: Environmental Differences between Magellanic and Non-Magellanic Satellites?* arXiv:2108.04271 [astro-ph], 2108.04271.

Saha, A.; Olszewski, E. W.; Brondel, B.; Olsen, K.; Knezek, P.; et al., 2010. *First Results from the NOAO Survey of the Outer Limits of the Magellanic Clouds*. AJ, 140(6), 1719. doi:10.1088/0004-6256/140/6/1719.

Salaris, M. and Girardi, L., 2002. *Population Effects on the Red Giant Clump Absolute Magnitude: The K Band*. MNRAS, 337(1), 332. doi:10.1046/j.1365-8711.2002.05917.x.

Sales, L. V.; Navarro, J. F.; Cooper, A. P.; White, S. D. M.; Frenk, C. S.; et al., 2011. *Clues to the 'Magellanic Galaxy' from Cosmological Simulations: The Magellanic Clouds*. MNRAS, 418(1), 648. doi:10.1111/j.1365-2966.2011.19514.x.

Sales, L. V.; Navarro, J. F.; Kallivayalil, N.; and Frenk, C. S., 2017. *Identifying True Satellites of the Magellanic Clouds*. MNRAS, 465(2), 1879. doi:10.1093/mnras/stw2816.

Sales, L. V.; Wang, W.; White, S. D. M.; and Navarro, J. F., 2013. *Satellites and Haloes of Dwarf Galaxies*. MNRAS, 428(1), 573. doi:10.1093/mnras/sts054.

Sanders, D. B.; Soifer, B. T.; Elias, J. H.; Madore, B. F.; Matthews, K.; et al., 1988. *Ultraluminous Infrared Galaxies and the Origin of Quasars*. ApJ, 325, 74. doi:10.1086/165983.

Schlafly, E. F. and Finkbeiner, D. P., 2011. *Measuring Reddening with Sloan Digital Sky Survey Stellar Spectra and Recalibrating SFD*. ApJ, 737(2), 103. doi:10.1088/0004-637X/737/2/103.

Schlegel, D. J.; Finkbeiner, D. P.; and Davis, M., 1998. *Maps of Dust Infrared Emission for Use in Estimation of Reddening and Cosmic Microwave Background Radiation Foregrounds*. ApJ, 500(2), 525. doi:10.1086/305772.

Schommer, R. A.; Suntzeff, N. B.; Olszewski, E. W.; and Harris, H. C., 1992. *Spectroscopy of Giants in LMC Clusters. II - Kinematics of the Cluster Sample*. AJ, 103(2), 447. doi:10.1086/116074.

Schönrich, R.; Binney, J.; and Dehnen, W., 2010. *Local Kinematics and the Local Standard of Rest*. MNRAS, 403(4), 1829. doi:10.1111/j.1365-2966.2010.16253.x.

Schwarz, G., 1978. *Estimating the Dimension of a Model*. Ann. Statistics, 6(2). doi:10.1214/aos/1176344136.

Scowcroft, V.; Freedman, W. L.; Madore, B. F.; Monson, A.; Persson, S. E.; et al., 2016. *The Carnegie Hubble Program: The Distance and Structure of the SMC as Revealed by Mid-Infrared Observations of Cepheids*. ApJ, 816(2), 49. doi:10.3847/0004-637X/816/2/49.

Scudder, J. M.; Ellison, S. L.; Torrey, P.; Patton, D. R.; and Mendel, J. T., 2012. *Galaxy Pairs in the Sloan Digital Sky Survey - V. Tracing Changes in Star Formation Rate and Metallicity out to Separations of 80 Kpc*. MNRAS, 426(1), 549. doi:10.1111/j.1365-2966.2012.21749.x.

Shao, S.; Cautun, M.; Deason, A. J.; Frenk, C. S.; and Theuns, T., 2018. *Evolution of LMC/M33-Mass Dwarf Galaxies in the Eagle Simulation*. MNRAS, 479(1), 284. doi:10.1093/mnras/sty1470.

Shapley, H., 1940. *An Extension of the Small Magellanic Cloud*. Harvard Bulletin, 914, 8.

Sharp, R.; Saunders, W.; Smith, G.; Churilov, V.; Correll, D.; et al., 2006. *Performance of AAOmega: The AAT Multi-Purpose Fiber-Fed Spectrograph*. In McLean, I. S. and Iye, I. (Eds.), *Society of Photo-Optical Instrumentation Engineers (SPIE) Conference Series*, 62690G. doi:10.1117/12.671022.

Shipp, N.; Erkal, D.; Drlica-Wagner, A.; Li, T. S.; Pace, A. B.; et al., 2021. *Measuring the Mass of the Large Magellanic Cloud with Stellar Streams Observed by S5*. arXiv:2107.13004 [astro-ph], 2107.13004.

Simon, J. D.; Li, T. S.; Erkal, D.; Pace, A. B.; Drlica-Wagner, A.; et al., 2020. *Birds of a Feather? Magellan/IMACS Spectroscopy of the Ultra-Faint Satellites Grus II, Tucana IV, and Tucana V*. ApJ, 892(2), 137. doi:10.3847/1538-4357/ab7ccb.

Skowron, D. M.; Jacyszyn, A. M.; Udalski, A.; Szymański, M. K.; Skowron, J.; et al., 2014. *OGLE-ING the Magellanic System: Stellar Populations in the Magellanic Bridge*. ApJ, 795(2), 108. doi:10.1088/0004-637X/795/2/108.

Skowron, D. M.; Skowron, J.; Udalski, A.; Szymański, M. K.; Soszyński, I.; et al., 2021. *OGLE-Ing the Magellanic System: Optical Reddening Maps of the Large and Small Magellanic Clouds from Red Clump Stars*. ApJS, 252(2), 23. doi:10.3847/1538-4365/abcb81.

Skrutskie, M. F.; Schneider, S. E.; Stiening, R.; Strom, S. E.; Weinberg, M. D.; et al., 1997. *The Two Micron All Sky Survey (2MASS): Overview and Status*. In Garzón, F.; Epchtein, N.; Omont, A.; Burton, B.; and Persi, P. (Eds.), *The Impact of Large Scale Near-IR Sky Surveys*, vol. 210, 25–32, Springer Netherlands, Dordrecht. doi:10.1007/978-94-011-5784-1_3.

Smecker-Hane, T. A.; Cole, A. A.; Gallagher III, J. S.; and Stetson, P. B., 2002. *The Star Formation History of the Large Magellanic Cloud*. ApJ, 566(1), 239. doi:10.1086/337985.

Soszyński, I.; Udalski, A.; Szymański, M. K.; Skowon, D.; Pietrzyński, G.; et al., 2015. *The OGLE Collection of Variable Stars. Classical Cepheids in the Magellanic System*. Acta Astronomica, 65(4), 297.

Spergel, D.; Gehrels, N.; Baltay, C.; Bennett, D.; Breckinridge, J.; et al., 2015. *Wide-Field InfrarRed Survey Telescope-Astrophysics Focused Telescope Assets WFIRST-AFTA 2015 Report*. arXiv:1503.03757 [astro-ph], 1503.03757.

Stanimirovic, S.; Staveley-Smith, L.; Dickey, J. M.; Sault, R. J.; and Snowden, S. L., 1999. *The Large-Scale HI Structure of the Small Magellanic Cloud*. MNRAS, 302(3), 417. doi:10.1046/j.1365-8711.1999.02013.x.

Stanimirović, S.; Staveley-Smith, L.; and Jones, P. A., 2004. *A New Look at the Kinematics of Neutral Hydrogen in the Small Magellanic Cloud*. ApJ, 604(1), 176. doi:10.1086/381869.

Stewart, K. R.; Bullock, J. S.; Wechsler, R. H.; Maller, A. H.; and Zentner, A. R., 2008. *Merger Histories of Galaxy Halos and Implications for Disk Survival*. ApJ, 683(2), 597. doi:10.1086/588579.

Stierwalt, S.; Besla, G.; Patton, D.; Johnson, K.; Kallivayalil, N.; et al., 2015. *TiNy TITANS: The Role Of Dwarf–Dwarf Interactions In Low-Mass Galaxy Evolution*. ApJ, 805(1), 2. doi:10.1088/0004-637X/805/1/2.

Strantzalis, A.; Hatzidimitriou, D.; Zezas, A.; Antoniou, V.; Lianou, S.; et al., 2019. *Discrete Star Formation Events in the Central Bar of the Small Magellanic Cloud*. MNRAS, 489(4), 5087. doi:10.1093/mnras/stz2540.

Stryker, L. L., 1984. *Faint Star Studies in the Magellanic Clouds. II - Field Regions 9 Deg Northeast of the Large Magellanic Cloud Bar*. ApJS, 55, 127. doi:10.1086/190950.

Subramaniam, A., 2003. *Large Magellanic Cloud Bar: Evidence of a Warped Bar*. ApJ, 598(1), L19. doi:10.1086/380556.

Subramaniam, A. and Subramanian, S., 2009. *The Mysterious Bar of the Large Magellanic Cloud: What Is It?* ApJ, 703(1), L37. doi:10.1088/0004-637X/703/1/L37.

Subramanian, S.; Rubele, S.; Sun, N.-C.; Girardi, L.; de Grijs, R.; et al., 2017. *The VMC Survey - XXIV. Signatures of Tidally Stripped Stellar Populations from the Inner Small Magellanic Cloud*. MNRAS, 467(3), 2980. doi:10.1093/mnras/stx205.

Subramanian, S. and Subramaniam, A., 2010. *An Estimate of the Structural Parameters of the Large Magellanic Cloud Using Red Clump Stars*. A&A, 520, A24. doi:10.1051/0004-6361/201014201.

Subramanian, S. and Subramaniam, A., 2012. *The Three-Dimensional Structure of the Small Magellanic Cloud*. ApJ, 744(2), 128. doi:10.1088/0004-637X/744/2/128.

Subramanian, S. and Subramaniam, A., 2013. *Structure of the Large Magellanic Cloud from near Infrared Magnitudes of Red Clump Stars*. A&A, 552, A144. doi:10.1051/0004-6361/201219327.

Tamfal, T.; Mayer, L.; Quinn, T. R.; Capelo, P. R.; Kazantzidis, S.; et al., 2021. *Revisiting Dynamical Friction: The Role of Global Modes and Local Wakes*. arXiv:2007.13763 [astro-ph], 2007.13763.

Tatton, B. L.; van Loon, J. T.; Cioni, M.-R. L.; Bekki, K.; Bell, C. P. M.; et al., 2021. *The VMC Survey – XL. Three-Dimensional Structure of the Small Magellanic Cloud as Derived from Red Clump Stars*. MNRAS, 504(2), 2983. doi:10.1093/mnras/staa3857.

The WFIRST Astrometry Working Group; Sanderson, R. E.; Bellini, A.; Casertano, S.; Lu, J. R.; et al., 2019. *Astrometry with the Wide-Field Infrared Space Telescope*. JATIS, 5(04), 1. doi:10.1117/1.JATIS.5.4.044005.

Tollerud, E. J.; Boylan-Kolchin, M.; Barton, E. J.; Bullock, J. S.; and Trinh, C. Q., 2011. *Small-Scale Structure in the Sloan Digital Sky Survey and ΛCDM: Isolated ˜L * Galaxies with Bright Satellites*. ApJ, 738(1), 102. doi:10.1088/0004-637X/738/1/102.

Torrealba, G.; Belokurov, V.; Koposov, S. E.; Bechtol, K.; Drlica-Wagner, A.; et al., 2018. *Discovery of Two Neighbouring Satellites in the Carina Constellation with MagLiteS*. MNRAS, 475(4), 5085. doi:10.1093/mnras/sty170.

Udalski, A.; Szymanski, M.K.; Soszynski, I.; and Poleski, R., 2008. *The Optical Gravitational Lensing Experiment. Final Reductions of the OGLE-III Data*. Acta Astronomica, 58, 69.

van der Marel, R. P., 2001. *Magellanic Cloud Structure from Near-Infrared Surveys. II. Star Count Maps and the Intrinsic Elongation of the Large Magellanic Cloud*. AJ, 122(4), 1827. doi:10.1086/323100.

van der Marel, R. P.; Alves, D. R.; Hardy, E.; and Suntzeff, N. B., 2002. *New Understanding of Large Magellanic Cloud Structure, Dynamics, and Orbit from Carbon Star Kinematics*. AJ, 124(5), 2639. doi:10.1086/343775.

van der Marel, R. P. and Cioni, M.-R. L., 2001. *Magellanic Cloud Structure from Near-Infrared Surveys. I. The Viewing Angles of the Large Magellanic Cloud*. AJ, 122(4), 1807. doi:10.1086/323099.

van der Marel, R. P. and Kallivayalil, N., 2014. *Third-Epoch Magellanic Cloud Proper Motions. II. The Large Magellanic Cloud Rotation Field In Three Dimensions*. ApJ, 781(2), 121. doi:10.1088/0004-637X/781/2/121.

van der Marel, R. P.; Kallivayalil, N.; and Besla, G., 2008. *Kinematical Structure of the Magellanic System*. Proc. IAU, 4(S256), 81. doi:10.1017/S1743921308028299.

Vasiliev, E., 2018. *Internal Dynamics of the Large Magellanic Cloud from Gaia DR2*. MNRAS, 481(1), L100. doi:10.1093/mnrasl/sly168.

Vasiliev, E., 2019. *AGAMA: Action-Based Galaxy Modelling Architecture*. MNRAS, 482(2), 1525. doi:10.1093/mnras/sty2672.

Vasiliev, E.; Belokurov, V.; and Erkal, D., 2021. *Tango for Three: Sagittarius, LMC, and the Milky Way*. MNRAS, 501(2), 2279. doi:10.1093/mnras/staa3673.

Vera-Ciro, C. and Helmi, A., 2013. *Constraints on the Shape of the Milky Way Dark Matter Halo from the Sagittarius Stream*. ApJ, 773(1), L4. doi:10.1088/2041-8205/773/1/L4.

Wan, Z.; Guglielmo, M.; Lewis, G. F.; Mackey, D.; and Ibata, R. A., 2020. *A SkyMapper View of the Large Magellanic Cloud: The Dynamics of Stellar Populations*. MNRAS, 492(1), 782. doi:10.1093/mnras/stz3493.

Wang, J.; Hammer, F.; Yang, Y.; Ripepi, V.; Cioni, M.-R. L.; et al., 2019. *Towards a Complete Understanding of the Magellanic Stream Formation*. MNRAS, 486(4), 5907. doi:10.1093/mnras/stz1274.

Weinberg, M. D. and Nikolaev, S., 2001. *Structure of the Large Magellanic Cloud from 2MASS*. ApJ, 548(2), 712. doi:10.1086/319001.

Weisz, D. R.; Dolphin, A. E.; Skillman, E. D.; Holtzman, J.; Dalcanton, J. J.; et al., 2013. *Comparing the Ancient Star Formation Histories of the Magellanic Clouds*. MNRAS, 431(1), 364. doi:10.1093/mnras/stt165.

Wilcots, E. M. and Prescott, M. K. M., 2004. *H* i *Observations of Barred Magellanic Spirals. II. The Frequency and Impact of Companions*. AJ, 127(4), 1900. doi:10.1086/381293.

Williamson, D. and Martel, H., 2021. *The Evolution of Magellanic-like Galaxy Pairs and the Production of Magellanic Stream Analogs in Simulations with Tides, Ram Pressure, and Stellar Feedback*. ApJ, 907(1), 9. doi:10.3847/1538-4357/abceb5.

Willmer, C. N. A., 2018. *The Absolute Magnitude of the Sun in Several Filters*. ApJS, 236(2), 47. doi:10.3847/1538-4365/aabfdf.

Wolf, C.; Onken, C. A.; Luvaul, L. C.; Schmidt, B. P.; Bessell, M. S.; et al., 2018. *SkyMapper Southern Survey: First Data Release (DR1)*. PASA, 35, e010. doi:10.1017/pasa.2018.5.

Yanchulova Merica-Jones, P.; Sandstrom, K. M.; Johnson, L. C.; Dolphin, A. E.; Dalcanton, J. J.; et al., 2021. *Three-Dimensional Structure and Dust Extinction in the Small Magellanic Cloud*. ApJ, 907(1), 50. doi:10.3847/1538-4357/abc48b.

Yozin, C. and Bekki, K., 2014. *Tidal-Induced Lopsidedness in Magellanic-Type Galaxies*. MNRAS, 439(2), 1948. doi:10.1093/mnras/stu075.

Yozin, C. and Bekki, K., 2015. *Local Ultra Faint Dwarves as a Product of Galactic Processing during a Magellanic Group Infall*. MNRAS, 453(3), 2303. doi:10.1093/mnras/stv1828.

Zaritsky, D.; Harris, J.; Grebel, E. K.; and Thompson, I. B., 2000. *The Morphologies of the Small Magellanic Cloud*. The Astrophysical Journal, 534(1), L53. doi:10.1086/312649.

Zaritsky, D.; Harris, J.; Thompson, I. B.; and Grebel, E. K., 2004. *The Magellanic Clouds Photometric Survey: The Large Magellanic Cloud Stellar Catalog and Extinction Map*. AJ, 128(4), 1606. doi:10.1086/423910.

Zhang, D.; Luo, Y.; and Kang, X., 2019. *The Effect of the Large Magellanic Cloud on the Satellite Galaxy Population in Milky Way Analogous Galaxies*. MNRAS, 486(2), 2440. doi:10.1093/mnras/stz957.

Zhao, H.; Ibata, R. A.; Lewis, G. F.; and Irwin, M. J., 2003. *Kinematic Outliers in the Large Magellanic Cloud: Constraints on Star–Star Microlensing*. MNRAS, 339(3), 701. doi:10.1046/j.1365-8711.2003.06208.x.

Zivick, P.; Kallivayalil, N.; Besla, G.; Sohn, S. T.; van der Marel, R. P.; et al., 2019. *The Proper-Motion Field along the Magellanic Bridge: A New Probe of the LMC–SMC Interaction*. ApJ, 874(1), 78. doi:10.3847/1538-4357/ab0554.

Zivick, P.; Kallivayalil, N.; and van der Marel, R. P., 2021. *Deciphering the Kinematic Structure of the Small Magellanic Cloud through Its Red Giant Population*. ApJ, 910(1), 36. doi:10.3847/1538-4357/abe1bb.

Zivick, P.; Kallivayalil, N.; van der Marel, R. P.; Besla, G.; Linden, S. T.; et al., 2018. *The Proper Motion Field of the Small Magellanic Cloud: Kinematic Evidence for Its Tidal Disruption*. ApJ, 864(1), 55. doi:10.3847/1538-4357/aad4b0.